Experimental Analysis and Modeling Investigation of Precipitation Kinetics and Hardening in two Al-Zn-Mg-Cu Alloys

by

Atekeh Abolhasani

A thesis
presented to the University of Waterloo
in fulfilment of the
thesis requirement for the degree of
Doctor of Philosophy
In
Mechanical and Mechatronics Engineering

Waterloo, Ontario, Canada, 2023

Examining Committee Membership

The following served on the Examining Committee for this thesis. The decision of the Examining Committee is by majority vote.

Supervisor(s)	Shahrzad Esmaeili, PhD Professor, University of Waterloo
	Mary A. Wells, PhD Professor, University of Waterloo
External Examiner	Hatem S. Zurob, PhD Professor, McMaster University
Internal Member	Michael J. Worswick, PhD Professor, University of Waterloo
Internal Member	Adrian Gerlich, PhD Associate Professor, University of Waterloo
Internal-external Member	Boxin Zhao Professor, University of Waterloo

Author's Declaration

This thesis consists of material all of which I authored or co-authored: see Statement of Contributions included in the thesis. This is a true copy of the thesis, including any required final revisions, as accepted by my examiners.

I understand that my thesis may be made electronically available to the public.

Statement of Contributions

This research was conducted at the University of Waterloo by Atekeh Abolhasani under the supervision of Professor Shahrzad Esmaeili and Professor Mary A. Wells.

The materials and experiments detailed in this work have partly come about through the contributions and assistance of others.

Dr. Babak Shalchi Amirkhiz performed Transmission Electron Microscopy (TEM) observations and supervised the analysis of the TEM results. TEM sample preparations were performed by CanmetMaterials staff. Dr. Brian Langelier performed Atom Probe Tomography (APT) experiments and the analysis of APT results. Dr. Massimo DiCiano contributed to designing and performing the Gleeble experiments and the Gleeble sample preparation.

Research presented in Sections 4.1.1 and 5.1.1 has been published as follows:

Citation: A. Abolhasani, B. Langelier, M. J. Worswick, M. A. Wells, and S. Esmaeili, "Experimental analysis and modelling of natural aging evolution in AA7xxx Al alloys". J. Alloys Compd. 2022. doi: 10.1016/j.jallcom.2022.164344

The contributions of the authors for this publication are as follows:

Atekeh Abolhasani: Formal analysis, Investigation, Validation, Conceptualization, Methodology, Writing - original draft.
Brian Langelier: Formal analysis, Investigation, Writing - review & editing.
Michael J. Worswick: Funding acquisition, Resources, Writing - review & editing.
Mary A. Wells*:* Supervision, Funding acquisition, Resources, Writing - review & editing.
Shahrzad Esmaeili: Supervision, Funding acquisition, Resources, Conceptualization, Methodology, Writing - review & editing.

Abstract

The effects of various thermal processing routes on the precipitation hardening behavior and microstructural characteristics of AA7075 and a developmental AA7xxx alloy (D-7xxx) are investigated using multi-scale characterization and modeling techniques. For the AA7075 alloy, two general thermal processing histories are investigated: (a) solutionizing and water-quenching (WQ), or (b) die-quenching (DQ) or forced-air quenching (FAQ) process, all of which were followed by either natural aging or multi-step aging treatments. The multi-step aging treatments include natural aging, followed by intermediate-temperature aging, to achieve pre-aged tempers prior to the final artificial aging step. To investigate natural aging, the strengthening behavior of the water-quenched D-7xxx alloy and the natural aging of water-quenched and pre-aged AA7075 are also studied. The primary precipitation process during the natural aging of the as-water-quenched AA7075 alloy is the nucleation of natural aging Zn-Mg precipitates. The pre-aging process, prior to natural aging, reduces the capacity for precipitate formation and hardening rate of the AA7075 alloy during the room-temperature holding period. Similarly, the die-quenching process applied to AA7075 results in slower kinetics of subsequent natural aging and higher hardness in the as-quenched state compared to the WQ and FAQ conditions. These changes in material behavior are related to the effects of pre-aging precipitation or the presence of dislocations formed during the die-quenching process, which affect the rate of nuclei formation at room temperature. A modeling methodology is introduced to analyze the precipitation kinetics and yield strength evolution during the natural aging of variously processed Al-Zn-Mg-(Cu) alloys. The analysis of the combined modeling and experimental results for the multi-step aging treatments of the AA7075 alloy in DQ, FAQ, and WQ tempers suggests that dislocations formed during the die-quenching process enhance the hardening response of the DQ alloy after a pre-aging treatment (DQ+PA) compared to the similarly aged material after water-quenching or forced-air quenching. After the final stage of aging, the material in the DQ+PA condition exhibits a lower hardness value than the similarly aged WQ and FAQ samples. The recovery of dislocations and the interactions between solutes, vacancies, and fine precipitates with dislocations reduce the hardening response of the alloy in the DQ+PA condition during the subsequent aging treatment. The kinetics of precipitation hardening during the final aging step are also highly affected by dislocation-enhanced precipitation. Microstructure-strength modeling relationships are introduced to predict the evolution of microstructure and the strengthening response of the AA7075-WQ alloy in pre-aged conditions, as well as during subsequent artificial aging treatments. These modeling approaches are further expanded to include the effects of dislocation-enhanced precipitation and dislocation recovery on the kinetics of precipitation and the strengthening behavior during the artificial aging treatment of the alloy in the DQ+PA condition. The validity of these models is verified by the good agreement between the model predictions and the results from the experimental investigations.

Acknowledgements

I would like to acknowledge and sincerely thank the numerous people whose contributions in time, effort, and expertise made it possible to accomplish this work.

First and foremost, I would like to express my sincere gratitude to my supervisor, Professor Shahrzad Esmaeili. Her patience, guidance, encouragement, and support were invaluable for the completion of this study. She has taught me so much, not only what to learn but also, most importantly, how to learn. I would also like to thank my co-supervisor, Professor Mary A. Wells, who has patiently guided and endlessly supported me throughout my time as her student. I am truly grateful that I have had the opportunity to work under your supervision over the last few years.

I would like to thank my PhD committee members: Professor Hatem Zurob from McMaster University, Professor Boxin Zharo, Professor Michael J. Worswick, and Professor Adrien Gerlich from the University of Waterloo for generously dedicating your time, expertise, and providing valuable feedback to enhance the quality of this thesis.

My heartfelt appreciation goes to Professor Michael J. Worswick, who helped me tremendously throughout this study. Working with you has been a great honor for me.

I gratefully acknowledge my direct collaborators, Dr. Babak Shalchi Amirkhiz and Dr. Brian Langelier, for their invaluable contributions to this work. This work would also not have been possible without the assistance of Dr. Massimo DiCiano, who assisted me in designing and conducting the Gleeble experiments.

I would like to express my gratitude to Honda R&D Americas Inc., Arconic Ground Transportation Group, Promatek Research Centre, the Natural Sciences and Engineering Research Council (NSERC), the Canada Foundation for Innovation, the Ontario Research Fund, the Ontario Centres of Excellence, and the Ontario Advanced Manufacturing Consortium for their financial support of this research.

Many thanks and appreciation go to the technical and research staff at the University of Waterloo, in particular, Dr. Yuquan Ding, Laurie Wilfong, Mark Griffett, Eckhard Budziarek,

Tom Gawel, and Mark A. Whitney. I would also like to thank the rest of the staff and researchers at the University of Waterloo, the Canadian Centre for Electron Microscopy, and CanmetMATERIALS for their assistance.

A very important mention goes to my fellow researchers and friends, including Dr. Kaab Omer, Dr. Li Hua Liao, and Dr. Sante DiCecco, who have generously helped me throughout my research. I would like to acknowledge the contributions of the co-op students and undergraduate research assistants, Hannah Van Rooyen and Ariana Montazeri, who assisted me with experimental analysis. A huge “thank you” goes to my dearest friend, Negar Baghbanaghaei, for her friendship, help, and contributions. I would also like to thank Dr. Tirdad Niknejad for kindly sharing his tensile testing results on the D-7xxx alloy to help me with the analysis of the natural aging behavior.

My heartfelt gratitude goes to my loving family, particularly my parents, sister, and brother, for their boundless love and encouragement throughout my PhD journey. They showed me how distance can be overcome by being present even from thousands of miles away. Mom, Dad, you are the sole reason I am standing in this place today.

Last but not least, I would like to express my deepest appreciation to my caring, loving, and supportive husband, Ali, though no words can adequately convey my gratitude for your endless love, patience, inspiration, and unwavering support that made all of this possible. Thank you for everything! Incredibly special thanks go to my lovely son, Arad, who has continually provided me with the requisite breaks from research and has brought a smile to my face even during the most challenging times.

Table of Contents

List of Figures

List of Tables

Nomenclature

a	An equivalent growth rate constant; also used as a constant factor
a_c	Cross-sectional area of the dislocation core
A	A constant
b	Magnitude of the Burgers vector; also used as a constant factor
b_1	A constant factor
C, C_2, C_{AA}	Constant factors
C_t	Main alloying elements percentage (*i.e.*, wt.%: Zn+Mg+Cu) of the alloys
D	Diffusion coefficient of the solute in the matrix
D_0	Proportionality constant for the diffusivity equation
D_{0c}	Pre-exponential factors for dislocation core diffusion
D_{0s}	Pre-exponential factor for self-diffusion
D_{0sc}	Pre-exponential factor for self-diffusion through dislocation cores
D_{0v}	Pre-exponential factors for lattice diffusion
D_s	Self diffusivity coefficient
D_{s-eff}	Effective self-diffusion coefficient
D_{sc}	Self-diffusion coefficient in the presence of dislocation cores
f	Volume fraction of precipitates
f_{peak}	Volume fraction of precipitates at the peak-aged condition
f_r	Relative volume fraction of precipitates
f_r^0	Relative volume fraction of precipitates at the beginning of the artificial aging process
f_r^{NA}	Relative volume fraction of precipitates during natural aging

f_r^{SNA}	Relative volume fraction of natural aging precipitates during natural aging of the pre-aged material
F	Obstacle strength
F_{peak}	Average obstacle strength at the peak age condition
G	Shear modulus
I	Nucleation rate per unit volume
k, k_1, k_3, k_4	A constant
k_0	A proportionality constant
k_B	Boltzmann constant
k_r	Rate constant
k_v	Temperature dependent constant describing the reaction rate in the absence of dislocations
k_{eff}	Temperature dependent constant describing the reaction rate in the presence of dislocations
L	Effective obstacle spacing on the slip plane
L_{strong}	Average spacing between strong obstacles
L_{weak}	Average spacing between weak obstacles
m	A constant
M	Taylor factor
n	A numerical exponent for the JMAK relationship
p	A dimensionless number between 1 and 2
P^*	Normalized time
Q_A	An apparent activation energy
Q_c^{diff}	Activation energies for dislocation core diffusion
Q_v^{diff}	Activation energy for lattice diffusion

Q_s	Activation energy for self-diffusion
Q_{sc}	Activation energy for self-diffusion through dislocation cores
r	Radius of a spherical particle; also, radius of the circular cross sectional area of a precipitate on the slip plane
r_{peak}	Radius of precipitates at the peak-aged condition
r_t	Radius of precipitates at time *t*
R	Universal gas constant (see text)
t	Time
t_0	Time for the onset of the exothermic event in isothermal calorimetry
t_f	Time to reach zero heat evolution (approximately) during the isothermal calorimetry experiment
t_{NA}	Natural aging time
t_{SNA}	Natural aging time for the natural aging of pre-aged materials
t_{peak}	Time to peak-age condition
T	Temperature
α	A dimensionless constant
β	A generic time exponent
Γ	Dislocation line tension
ε	True strain
φ_c	The critical angle between the adjacent arms of a dislocation when it overcomes the obstacle
ρ	Dislocation density
ρ_{AA}	Dislocation density during artificial aging of the DQ+PA temper
ρ_{DQ}	Dislocation density of the DQ material
ρ_f	Dislocation density of the final condition

ρ_i	Immobilized dislocation density
ρ_{NA}	Dislocation density of the material in the DQ+naturally-aged condition
ρ_{PA}	Dislocation density of the material in the DQ+PA condition
σ	True stress
σ_d	Contribution of dislocation strengthening to the yield strength
σ_i	Frictional stress of the lattice
$\sigma_{initialdis}$	Contribution of dislocations to yield strength right after deformation
σ_p	Peak strength
σ_{ppt}	Contribution of precipitation strengthening to the yield strength
σ_{rec}	The amount of recovery
σ_{0ss}	Contribution of solid solution strengthening to yield strength for the as-quenched material
σ_{ss}	Contribution of solid solution strengthening to the yield strength
σ_{ss}^{PA+SNA}	Contribution of solid solution strengthening to the yield strength for natural aging of pre-aged material
σ_{ss}^{PA}	Contribution of solid solution strengthening to the yield strength of the pre-aged material
σ_{ppt}^{PA}	Contribution of precipitation strengthening to the yield strength of the pre-aged material
σ_t	Yield strength at time t during artificial aging
σ_y^{AQ}	Yield strength of as-quenched material
σ_y^{DQ+NA}	Yield strength of the material in die-quenched+naturally-aged condition
τ	Critical resolved shear stress strengthening

1. Introduction

Over the years, Al-Zn-Mg-(Cu) (7xxx series) alloys have been widely used in aerospace and aircraft industries for their high strength-to-weight ratio and desirable mechanical properties and performance [1,2]. To date, the use of AA7xxx alloys for applications in the automotive industry has been limited for a variety of reasons [3–5]. However, the high specific strength of AA7xxx alloys continues to generate interest for exploring their use in automotive applications. AA7xxx alloys are wrought aluminum alloys that can be heat-treated to significantly increase their strength through precipitation hardening. The formation of precipitates from the supersaturated solid solution effectively strengthens these alloys during the aging treatments to the peak-aged condition. To develop tailored mechanical properties in final automotive products, proper control of the distribution, size, and density of precipitates in the microstructure of these alloys is crucial. This can be achieved through an enhanced understanding of the linkages between thermomechanical history, precipitate formation, and properties, and the use of this understanding to design appropriate thermal processing routes for typical automotive processing routes, such as paint bake cycling.

The main drawback of using AA7xxx for automotive applications is their poor formability at room temperature. One promising solution to overcome this limitation is the combination of hot forming and quenching using a cold die (*i.e*. die-quenching) [6]. High-temperature forming at solutionizing temperatures has previously been applied to AA7xxx alloys for aeronautical applications [7–9]. The use of high-temperature forming processes for automotive components has the capacity to not only exploit the higher formability of the alloys at high temperatures, but can also lead to high final yield strength values through the subsequent age hardening processes that occur during paint bake cycling (PBC) [6]. In the die-quenching process, the solutionized material is simultaneously formed and quenched to room temperature to achieve a supersaturated solid solution, which has the highest driving force for subsequent precipitation [10], while minimizing any distortion in the final manufactured parts [6,11]. Existing literature provides valuable information on certain aspects of the age hardening behavior of solutionized and water-quenched AA7xxx alloys [12–15]. However, there are key knowledge gaps regarding the effect of the aging history on the precipitation hardening behavior of these alloys, which is of importance for automotive applications. These include understanding the natural aging behavior after quenching and the effect of initial lower-temperature aging treatments (pre-aging) on mechanical properties (formability and strength). Improving our knowledge of the age hardening response after the die-quenching processes and the pre-aging treatments of these alloys allows the design of thermomechanical routes to take advantage of the paint-bake cycle (PBC) as a final precipitation heat treatment for these alloys. The current study aims to increase our understanding of some of these knowledge gaps.

Previous experimental and theoretical investigations have led to the introduction of physically based process models, which are useful tools for the efficient optimization of thermomechanical processes, microstructures, and properties and can reduce the necessity of significant experimental work. Using physically based relationships, the process models can predict the microstructural evolution and final properties of the material after different thermomechanical processing routes. This research aims to introduce microstructure-strength modeling relationships to predict the precipitation kinetics and age hardening behavior of AA7xxx alloys in water- and die-quenched conditions, during natural aging, and multi-step aging treatments. The results of this research will provide useful information for the development and design of industrially relevant thermomechanical processing routes to exploit the age-hardening potential of AA7xxx alloys for future automotive applications.

1.1 Objectives and Scope

This research fulfills the following two main objectives:

(1) To investigate the effect of industrially relevant thermal processing routes, which include water-quenching, forced-air quenching, or die-quenching followed by natural aging or multi-step aging treatments, on the precipitation hardening behavior of two Al-Zn-Mg-Cu alloys (AA7075 and D-7xxx),

(2) To analyze and predict the effect of the thermal histories of interest on the microstructural evolution and precipitation hardening response of these alloys.

A number of process routes after hot forming were investigated for the AA7075, including water-quenching, forced-air quenching, and die-quenching, followed by: (a) natural aging; (b)

2-day natural aging followed by an intermediate temperature aging (pre-aging) prior to final aging; (c) secondary natural aging of pre-aged tempers; and (d) artificial aging of a pre-aged material.

The strengthening behavior and microstructure characteristics of the AA7075 alloy during the thermal processing routes of interest were investigated using a combination of microhardness measurement, tensile testing, transmission electron microscopy, differential scanning calorimetry, isothermal calorimetry, and atom probe tomography.

The second alloy studied is a developmental AA7xxx alloy (D-7xxx). For this alloy, natural aging behavior was studied through experimental (tensile testing) and modeling investigations. Models of the natural aging process were developed based not only on the measured data from the D-7xxx and AA7075 alloys, but also on experimental data taken from the literature for five different Al-Zn-Mg-(Cu) alloys.

2. Literature Review

In the current chapter, a brief review of the wrought aluminum categories and second-phase particles in AA7xxx alloys will be given. Then, the precipitation sequence in Al-Zn-Mg-(Cu) alloys and their precipitation hardening behavior after various thermal processing treatments that are pertinent to the current research will be reviewed. Finally, an overview of previous studies on modeling the precipitation hardening behavior of heat-treatable aluminum alloys relevant to the current research will be presented.

2.1 Wrought Aluminum Alloys Categories

Wrought aluminum alloys are aluminum alloys that are initially cast as ingots or billets and subsequently, hot and/or cold worked into the desired form. These alloys are subdivided into two categories: heat-treatable and non-heat-treatable. Wrought heat-treatable alloys can be strengthened through thermal heat treatments (aging treatments). In contrast, non-heat-treatable alloys do not respond to thermal heat treatments for strengthening and are primarily strengthened through various types of cold working and strain hardening processes. The classification of wrought aluminum alloys is schematically presented in Table 2-1.

Table 2-1 Designation of wrought aluminum alloys.

Alloy designation	Alloying element	Heat treatment
1xxx	99% pure aluminum	Non-heat treatable
2xxx	Cu containing alloy	Heat-treatable
3xxx	Mn containing alloy	Non-heat treatable
4xxx	Si	Non-heat treatable
5xxx	Mg	Non-heat treatable
6xxx	Mg and Si	Heat-treatable
7xxx	Zn	Heat-treatable
8xxx	Others (Li, Sn, Fe)	Heat-treatable/Non-heat treatable

2.2 Second-Phase Particles in AA7xxx Aluminum Alloys

Second-phase particles that can form in wrought heat-treatable aluminum alloys are classified into three different types which appear in the following order during the processing sequence [16,17]:

1. The constituent phases are relatively large Si- or Fe-rich particles (with diameters ranging from 2 to 5μm). These brittle particles form during the solidification of the ingot and due to the interaction of alloying elements with impurity elements (such as Fe or Si). These particles are difficult to dissolve at high temperatures.
2. The dispersoids are Cr, Zr, or Mn-rich particles (with diameters ranging from 0.05 to 2μm). They form during solidification or subsequent homogenizing solution treatment of the ingot. These elements are added to inhibit and retard recrystallization, as well as enhance the stress corrosion resistance of aluminum.
3. The hardening precipitates are nano-sized particles that form through the aggregation of the main alloying elements (*i.e.*, Zn, Mg, and Cu in AA7xxx alloys) during heat treatment, specifically at low temperatures after solutionizing, known as aging treatments. These particles are responsible for the high strength of the AA7xxx alloys.

Dispersoids and constituent phases are not associated with age hardening processes and, therefore, will not be further discussed. Further information on these particles can be found in Ref [18].

2.3 Precipitation Behavior of AA7xxx Alloys

Precipitation hardening in metallic alloys is a thermally activated phenomenon where the purposeful formation of precipitates with a different composition from the matrix hardens the material by impeding the movement of dislocations [19–21]. Precipitation hardening is the most significant strengthening mechanism utilized by heat-treatable Al-Zn-Mg-(Cu) alloys (7xxx series). These alloys can be strengthened through a sequence of heat treatments that result in the formation of hardening precipitates within the matrix. The heat treatment processes for precipitation hardening of these alloys involve three steps: (1) solution heat treatment, in which the material is heated to an elevated temperature to dissolve all second-phases dissolve into the matrix and transform the aluminum matrix into a single phase; (2) quenching from the elevated temperature to room temperature to suppress any solute from precipitating from the solid solution and create a supersaturated solid solution; and (3) subsequent age hardening at a lower temperature to precipitate second phases in a controlled manner. These alloys can be heat-treated by aging either at room temperature (natural aging) or at one or more elevated temperatures (artificial aging), which are usually in the range of 100-190°C [22].

The composition range of the AA7xxx alloys includes Zn (3-7 wt.%), Mg (0.8-3 wt.%), and Cu (0-2.8 wt.%) [23,24]. The minimum content of Zn+Mg alloying elements required for precipitation hardening to occur (minimum supersaturation) falls within the range of 4.5-8.5 wt.% [23,24]. Several factors, including the alloy composition, aging parameters (temperature and time), and initial material condition, can influence the nature of precipitates, the rate of nucleation, growth, and coarsening of precipitates, and the overall kinetics of precipitation. The precipitation sequence in AA7xxx alloys and the effect of various aging practices on their precipitation hardening will be discussed in the following sections.

2.3.1 Precipitation Sequence

The precipitation reactions that occur in AA7xxx alloys during age hardening treatments are complex and depend on multiple factors, such as solutionizing temperature, quench rate, aging time and temperature, and various microstructural features (*e.g.,* presence of dispersoids, dislocations, impurities, and grain boundaries). The precipitation sequence of Al-Zn-Mg-(Cu) alloys has been extensively studied using various investigation methods, including electrical resistivity, calorimetry experiments, electron microscopy, and X-ray-based methods [18,25–32]. Figure 2-1 illustrates the general precipitation sequence during the aging treatments of Al-Zn-Mg-(Cu) alloys at various temperatures. This schematic sequence has been created using the vast information present in the literature (*e.g.,* [33–36]). The temperature range for the precipitation of different phases in the precipitation sequence of the Al-Zn-Mg-(Cu) alloys is depicted in Figure 2-2. This schematic diagram has been created based on the information reported in references [19,25,37–40]. It should be noted that Cu atoms can replace Zn or Mg atoms in the precipitates during the aging treatments of copper-containing AA7xxx alloys. However, it is generally believed that this replacement does not alter the type of hardening precipitates or the sequence of precipitation in these alloys [41–43]. In Al-Zn-Mg-Cu alloys, the formation of Cu-containing particles, such as S (Al_2CuMg), θ (Al_2Cu), and T ($Al_2Mg_3Zn_3$), phases may occur during heat treatments at higher temperatures, depending on the alloy's composition (mainly Mg content) and the thermal processing route [44,45].

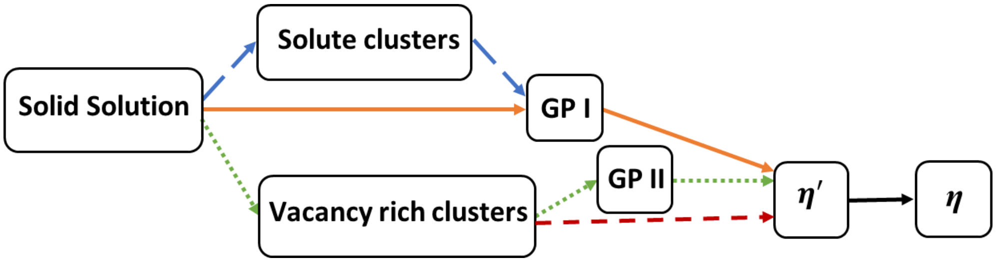

Figure 2-1 Precipitation sequence in Al-Zn-Mg-(Cu) alloys.

After solution treatment and quenching, the AA7xxx alloy matrix becomes supersaturated with vacancies and alloying elements [33]. During the early stages of decomposition of the supersaturated solid solution in AA7xxx alloys, three types of zones and clusters can form in the microstructure: vacancy-rich clusters (VRCs), solute clusters, and GP I zones. The formation of solute clusters during the natural aging of Al-Zn-Mg alloys has been reported by several researchers [34,46–48]. These clusters are reported to be Zn-rich solute aggregates/clusters, which transform into GP zones with increasing time during the natural aging of the investigated Al-Zn-Mg alloys [34,46–48]. GP I zones are another early-stage precipitate that form in the microstructure of AA7xxx alloys during natural or artificial aging treatments. It is generally accepted that spherical GP I zones are the first precipitates to form in an as-quenched (AQ) Al-Zn-Mg-(Cu) alloy when kept at room temperature [33]. GP I zones are small precipitates containing Zn, Mg, and Cu [36]. These zones can form over a wide range of temperatures from room temperature to 150°C [37], as shown in Figure 2-2. These precipitates have a tendency to dissolve within the temperature range of 100-140°C, which varies based on the duration of the holding time [36,49,50]. Vacancy-rich clusters (VRCs) are assumed to form during or immediately after quenching to room temperature from temperatures above 450°C. This temperature is associated with the critical value of vacancy supersaturation [50–52]. These clusters are believed to remain stable during natural aging and do not impact the formation of natural aging precipitates [35].

Many authors have reported the presence of two types of GP zones (GP I and GP II) in both naturally and artificially aged AA7xxx alloys [5,36,50,53]. The existence of different types of GP zones was first proposed by Schmalzried and Gerold in an Al-Zn-Mg alloy [53]. Later, Ungar *et al.* [25] used small-angle X-ray scattering (SAXS) experiments to report the presence of two types of GP zones with different sizes in an Al-Zn-Mg alloy. They found that the smallest GP zones disappeared during aging of the alloy above 90°C. GP II zones are reported to form from VRCs during aging at higher temperatures (*i.e.*, above 70°C) [19,38,39] or after prolonged aging at room temperature [34,46,54,55]. These zones are mostly reported to form as thin plates with a thickness of 1-2 {1 1 1} atomic planes and a diameter of 3-6 nm [50–52]. The dissolution of GP II zones begins at a higher temperature (125°C) than GP I zones [55].

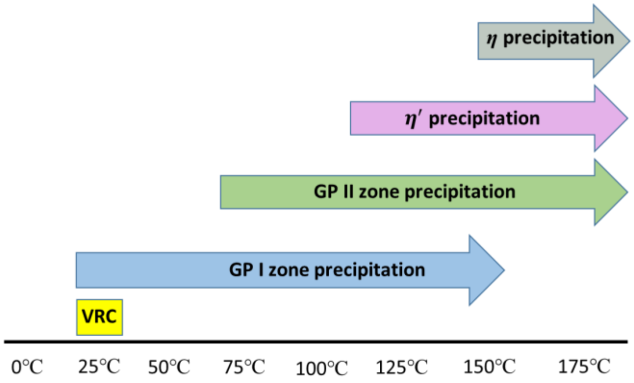

Figure 2-2 Temperature ranges for the formation of different precipitates in Al-Zn-Mg-(Cu) alloys (Note: GP II zones may also form during aging at lower temperatures for a very long time).

There are three different routes for the formation of η'precipitates, as shown in Figure 2-1. The GP I and GP II zones can serve as nucleation sites for the next phase in the precipitation sequence, which are η' precipitates [35]. During aging at higher temperatures (above the solvus line of GP zones, which is higher than 100°C according to Ungar et al. [25]), GP II zones transform to the η' phase, while GP I zones either dissolve or transform to η'. The direct nucleation of η' can also occur at temperatures of approximately 120-150°C [56]. Furthermore, some researchers have reported the nucleation of η' precipitates on VRCs [36,57,58]. According to their results, in a two-step aging treatment (*e.g.*, at 100°C and 150°C), VRCs do not affect the formation of precipitates (GP zones) during natural aging or artificial aging below the temperature range of 80-100°C but they can act as precursors of η' precipitates during the subsequent aging treatment at a higher temperature (*e.g.,* 150°C). In AA7xxx alloys, as the aging process continues and η' precipitates grow, there will be a range of precipitate sizes in the microstructure. As a consequence of precipitate growth, coherency is gradually lost by increasing the coherency strains, and the incoherent η ($MgZn_2$ *or* $Mg(Zn,Al,Cu)_2$) phase forms [52]. The transformation of η' to η and coarsening of precipitates begins at temperatures around 150ºC in the AA7075 alloy [40].

The T phase ($Mg_3Zn_3Al_2$ or $Mg_{32}(Zn,Al)_{49}$) is another type of precipitate found in AA7xxx alloys with higher levels of Mg (*i.e.,* higher Mg/Zn ratios in the alloy) [41,44]. Cu-bearing phases, such as S ($CuMgAl_2$) or θ (Al_2Cu), can also form in copper-containing AA7xxx alloys during high-temperature heat treatments [44,59]. To identify the phases present in the microstructure of the alloys studied in this research, **Error! Reference source not found.** d isplays a section of the Al-Zn-Mg-Cu phase diagram at 1.5 wt.% Cu (which closely matches the copper content of the AA7075 alloy) at a temperature of 460°C [41]. The composition of the AA7075 alloy falls near the boundary of the $Al+\eta$ ($MgZn_2$)+S ($CuMgAl_2$) region in the Al-Zn-Mg-Cu phase diagram (Figure 2-1). Please note that η, T, and the Cu-bearing phases are not associated with age hardening processes and will not be discussed further. Further information on the η and T precipitates can be found in References [30,52,60,61] and [44,52,62], respectively.

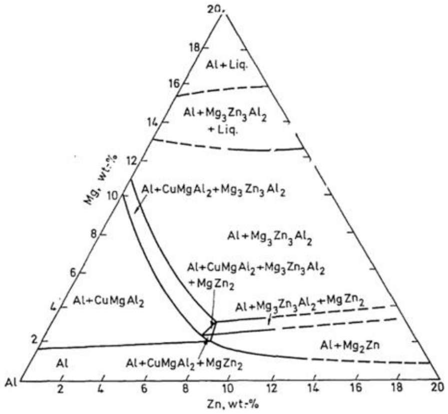

Figure 2-3 Section through the Al-Zn-Mg-Cu phase diagram at a Cu concentration of 1.5 wt.% and a temperature of 460°C [41]**.**

To gain a better understanding of the evolution of precipitates during aging treatments of the AA7075 alloy, the calculated time-temperature-transformation (TTT) diagram for this alloy is shown in Figure 2-4. This figure shows the calculated time-temperature-transformation (TTT) diagram for the AA7075 alloy for the start of noticeable transformation (0.5% amount of phase formed) of the various phases from the supersaturated Al matrix [40]. The TTT diagram can be utilized to determine a test matrix for the aging heat treatment of age-hardenable alloys. According to this figure, GP zones form in the temperature range of 0-170°C in the AA7075 alloy, with the nose of the curve occurring at approximately 150°C. The η' phase forms within a temperature range of 70-370°C, with the nose of the curve lying at approximately 325°C.

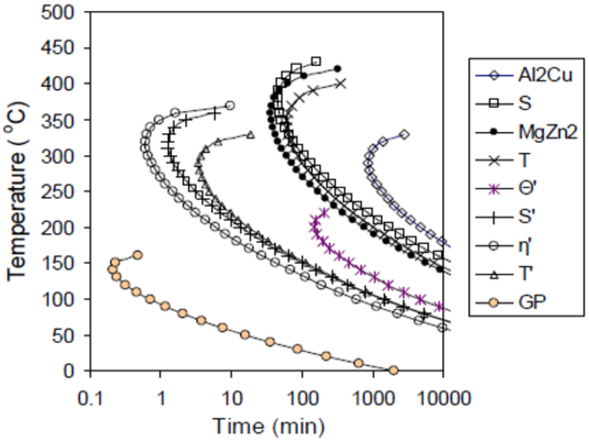

Figure 2-4 Calculated TTT diagram for AA7075 alloy [40]**.**

Figure 2-5 shows the TEM micrographs of all the phases listed in Figure 2-1. It should be noted that there is no direct observation of VRC available in the literature. Figure 2-5 (a) shows small particles, measuring 1–2 nm diameter, identified as solute clusters within the matrix of an Al-Zn-Mg alloy [47]. The GP I and GP II zones in an AA7xxx alloy which have different shapes and are fully coherent with the matrix, are shown in Figure 2-5 (b). The η' phase has been reported to be either coherent [44,63] or semi-coherent [60,63] with the matrix. The projections of the η' phase, with round or plate-shaped morphologies, under different habit planes are shown in Figure 2-5 (c). Figure 2-5 (d) shows the rod-shaped incoherent η phase in the microstructure of an AA7xxx alloy. GP zones have been reported to have spherical AuCu (I)-type, tetragonal, or orthorhombic crystal structures [36,50]. The η' phase has been reported to form into platelets on {1 1 1} planes and is mostly reported to have a hexagonal crystal structure [26,27,52,64]. The η precipitates have a hexagonal structure, and their composition is generally $MgZn_2$, according to the literature [52].

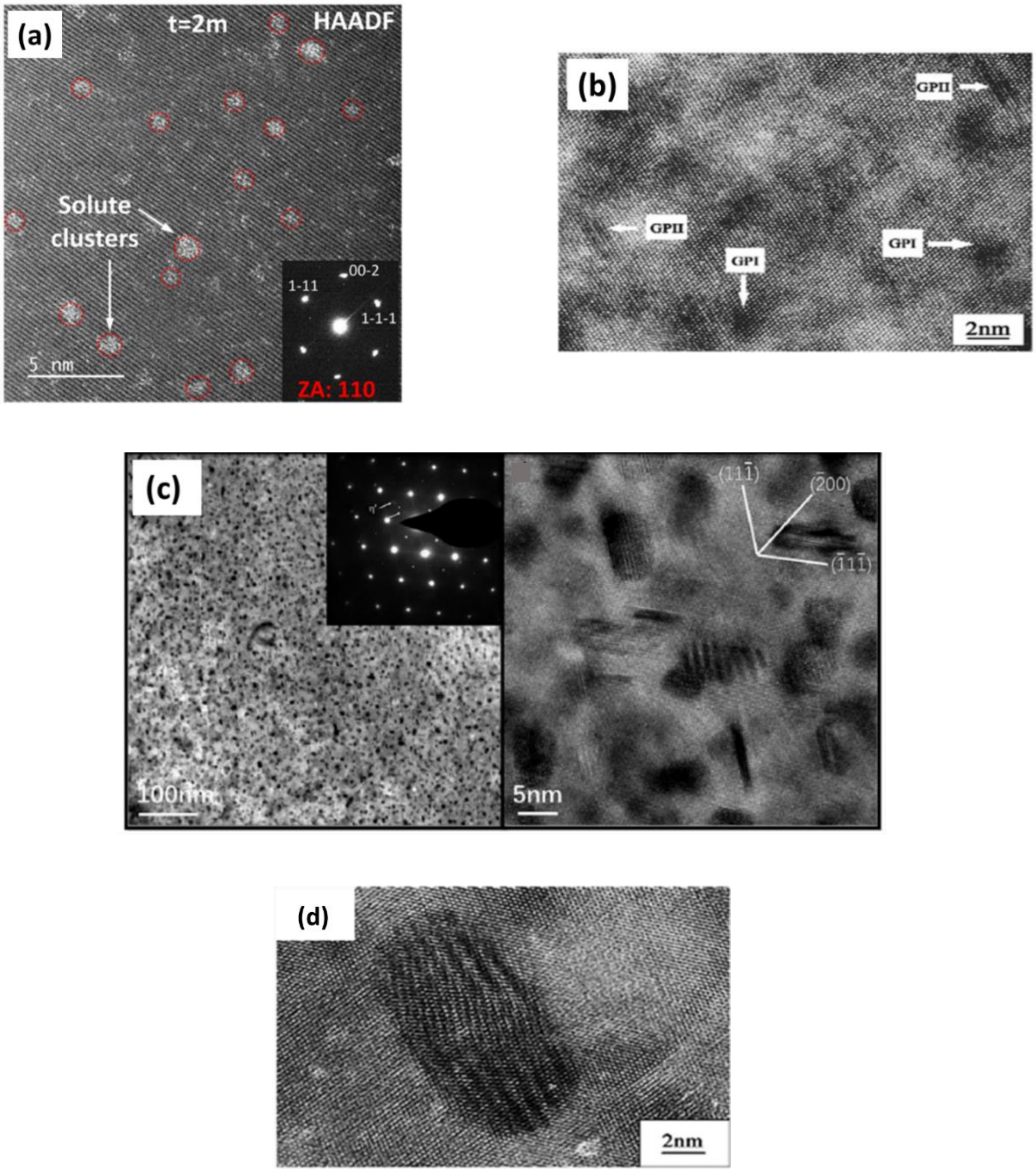

Figure 2-5 (a) HAADF-STEM image of a 2-min naturally aged Al-Zn-Mg alloy showing solute clusters [47]**, (b) HREM images in [110]Al projection of a AA7xxx alloy** [60] **aged for 7 h at 115°C (showing GP I and GP II zones), (c) BF image, and HRTEM image in [110] Al projection of AA7085 alloy aged at 150°C for 8 h (showing η' precipitates with different cross-sectional morphologies)** [65] **and (d) HREM images in [110]Al projection of a AA7xxx alloy** [60] **aged for 7 h at 115°C plus 12 h at 160°C (showing a rod-shaped η phase)** [60]**.**

2.3.2 Age Hardening Behavior

2.3.2.1 Effect of the Aging Route

The age hardening behavior of AA7xxx alloys has been investigated in several studies [13,51,61,66–68]. Due to complexity of the precipitation processes, it is essential to consider multiple microstructures and processing factors when aging AA7xxx alloys. In this section, the effect of various factors on the age hardening behavior of AA7xxx alloys is reviewed.

Natural Aging

AA7xxx alloys will naturally age harden at room temperature, leading to an increase in their hardness with time. The increase in hardness that occurs during natural aging has been reported to be due to the nucleation and growth of GP zones [55,69,70]. As shown in Figure 2-6 [69], the yield strength of an Al-Zn-Mg-Cu alloy (wt.%: 7.55Zn–2.65Mg–1.97Cu) increases as the natural aging time increases up to 3 years. A similar observation was also reported by Staley [69] for AA7075 and AA7050 alloys, where the yield strength was found to increase continuously with increasing the natural aging time up to two years. Lee *et al.* [55] found that the increase in hardness during the natural aging of this alloy was caused by the nucleation of GP I zones and an increase in their size and volume fraction. These have caused the increase in hardness during the natural aging of this alloy and these zones grow and transform into GP II zones after aging for 1500 hours. The growth of GP zones during natural aging has been attributed to the further diffusion of Zn and Mg atoms into these zones [28,46,71]. Some researchers have found that the formation of GP zone during the natural aging of Al-Zn-Mg-(Cu) alloys is preceded by the formation of solute aggregates/clusters, which then transform into GP zones [34,46–48,72]. These natural aging clusters have been reported to have the same crystal structure as the aluminum matrix and are Zn-rich [46,47]. Zhang *et al.* [48] suggested, based on APT analysis, that the migration of Zn atoms controls the kinetics of solute clustering in an Al-Zn-Mg alloy. They observed that the average Zn/Mg ratio of solute clusters increased after natural aging from 120 h to 1440 h. In a recent study, Chatterjee *et al.* [47] found that GP II zones form from both solute clusters and GP I zones during early stages of natural aging in an AA7xxx alloy. They also observed that these zones grow with increasing natural aging time. Liu *et al.* [46] reported that after more than three months of natural aging in an Al-Zn-Mg alloy, GPI and GPII zones formed with Zn/Mg atomic ratios of 1.2 and 1.3–1.4, respectively. The presence of semicoherent η' precipitates has also been reported after one month of natural aging in Al-Zn-Mg alloys with a high Zn concentration [73]. Although the presence of solute clusters, GP I, GP II zones, and η' precipitates has been reported in the microstructure of naturally aged Al-Zn-Mg-(Cu) alloys, there are many uncertainties regarding their early-stage precipitation phenomena. This is due to the complicated precipitation behavior of these alloys. Also, limited information has been reported on the differences in the kinetics of natural aging in Al-Zn-Mg-(Cu) alloys. Furthermore, the relationship between the microstructural characteristics and resultant strengthening behavior of these alloys is not well understood. A better understanding of the microstructure evolution during natural aging of Al-Zn-Mg-(Cu) alloys is of great importance in optimizing the precipitation structure and improving the final strength of the alloy for automotive applications where the occurrence of natural aging is inevitable in the manufacturing process chain.

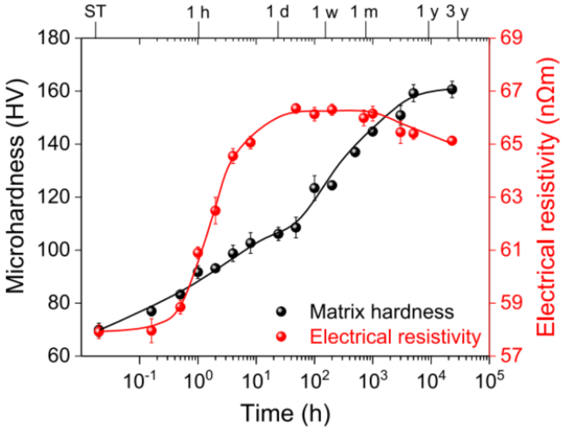

Figure 2-6 The evolution of microhardness and electrical resistivity during natural aging of an Al-Zn-Mg-Cu alloy [55]**.**

Artificial aging of Naturally-Aged Alloy

Aluminum alloys that are used for automotive body structures are typically subjected to natural aging after solutionizing and quenching, and prior to the paint-bake cycle treatment [74]. Natural aging prior to artificial aging affects the nucleation of the η' phase and the hardening potential of AA7xxx alloys. Both positive and negative effects of natural aging prior to artificial aging on the hardening potential of AA7xxx alloys have been reported in the literature. In AA7178 alloy, an increase in the natural aging time prior to T6 heat treatment resulted in a reduction of the yield strength values [75]. Similarly, any natural aging time above 4 hours is reported to have a negative impact on the aging response of AA7075-T6 [75]. In this alloy, delays of 4 to 30 hours before T6 heat treatment are reported to be more detrimental than longer delays [75]. The formation of clusters and GP zones during natural aging, as well as their dissolution during subsequent artificial aging, have been reported as the reasons for the detrimental effect on the hardening potential of an AA7xxx alloy subjected to the initial natural aging step [52]. This phenomenon is called reversion, wherein the volume fraction of GP zones decreases as they dissolve in the matrix and rendering them incapable of serving as nucleation sites for the formation of η' precipitates. On the other hand, according to Staley's analysis of AA7050 and AA7075 alloys [69], GP zones formed during the natural aging stage can grow during slow heating to subsequent artificial aging temperature, and as a result, they act as nuclei for the formation of η' precipitates.

Natural Aging of Pre-Aged Alloy

The pronounced natural aging of AA7xxx alloys after quenching can lead to unpredictable final strengths of automotive-manufactured parts and the poor formability of these alloys. Applying an intermediate-temperature aging treatment (pre-aging) prior to final artificial aging process can assist in minimizing or suppressing the natural aging of these alloys after quenching. A few experimental studies have explored pre-aging treatments to minimize or inhibit the natural aging process of AA7xxx alloys. Österreicher *et al.* [76] found that application of a pre-aging treatment at 90°C or 120°C for one hour can inhibit the secondary natural aging process in the AA7021 alloy but it cannot stabilize AA7075 alloy. The observed behavior in the AA7021 alloy has been attributed to the formation of stable GP II zones during the pre-aging treatment, which prevents the subsequent formation of GP I zones. Wan *et al.* [77] have studied the effect of natural aging prior to the pre-aging process (in a temperature range of 120 to 170°C) on the subsequent (secondary) natural aging behavior of an Al-Zn-Mg alloy. They reported that the application of 72 hours of natural aging prior to pre-aging treatments can significantly reduce the strengthening effect during subsequent natural aging.

According to their microstructure analysis (using SAXS and TEM), this inhibition of natural aging is due to the formation of precipitates during a pre-aging treatment. These precipitates are reported to be precursors of the η' phase and are stable at room temperature. For the application of AA7xxx alloys in the automotive industry, it is of key importance to design a pre-aging treatment that will prevent or minimize natural aging at room temperature and is beneficial for achieving the desired mechanical properties after the final paint-bake processes.

Artificial Aging of Pre-Aged Alloy

The application of a pre-aging treatment prior to final artificial aging (PBC) process can enhance the precipitation kinetics and hardening potential of AA7xxx alloys. For AA7xxx alloys, the T6 heat treatment is a commonly used process that significantly enhances the age hardening response of these alloys. This heat treatment, which typically results in maximum peak hardness, involves solutionizing followed by artificial aging at 120°C for 24 hours [78]. η' is the main precipitate phase present in the microstructure of AA7xxx alloys in the T6 condition, and it is the main contributor to the age hardening response of these alloys [79]. However, for automotive applications of these alloys, T6 treatment (where the material is peak-aged) is not suitable for achieving the optimal strength after PBC treatment. As shown in Figure 2-4, for the AA7075 alloy, the kinetics of GP zone formation are rapid at temperatures ranging from 100-120ºC. Saunders [40] reported that if aging continues in this temperature range, these GP zones will grow and transform into η'. This transformation can be accelerated by a subsequent aging treatment at temperatures ranging from 140-180ºC. During the aging process at low temperatures up to 120°C, the nucleation and growth of GP zones become more dominant [51,80]. These precipitates can serve as nuclei or heterogeneous nucleation sites for the formation of η' precipitates during the subsequent aging step at higher temperatures, typically in the range of 140-180°C, which results in an enhanced strengthening effect [25]. Cao *et al.* [81] used TEM analysis to demonstrate a fine distribution of GP zones in the matrix of an Al-Zn-Mg-Cu aluminum alloy after pre-aging treatment (80°C for 12 hours). Their results showed a closely spaced distribution of strengthening η' precipitates following the subsequent artificial aging process at 180°C (peak-aged condition). In contrast, a microstructure consisting of coarse needle-like or lath-like precipitates was observed for the alloy which was artificially aged (peak-aged) at 180°C without a pre-aging treatment. Similar results have been also observed by other researchers [40,51,82], where a multi-step aging process resulted in the formation of finer and more closely spaced η' precipitates in AA7xxx alloys. This led to an improved hardening and strengthening response compared to a single artificial aging process. Therefore, to exploit the precipitation hardening potential of AA7xxx alloys in automotive applications, several factors, such as the pre-aging time and temperature, as well as the effect of different pre-aging treatments on subsequent natural aging of these alloys prior to PBC treatment, should be considered.

2.3.2.2 Effect of Deformation

The effect of deformation on the age hardening response and precipitation kinetics is another subject of interest in studying the precipitation hardening behavior of AA7xxx alloys. The presence of dislocations in the microstructure of the deformed material has various effects on the precipitation process of these alloys. Previous studies using the small-angle X-ray scattering (SAXS) method have shown that deformation can accelerate the kinetics of dynamic precipitation of GP zones at room temperature by enhancing the nucleation of these zones [83]. This stems from dislocations acting as favorable heterogeneous nucleation sites, thereby reducing the energy barrier for nucleation [10,83]. Deformation can also accelerate the growth rate and coarsening of precipitates during artificial aging [84], which is the result of dislocations providing fast diffusion paths, known as pipe diffusion [10,84]. Poole *et al.* [85] reported an accelerated rate of growth and coarsening of precipitates during artificial aging (at 150°C) of pre-aged AA7030 (wt.%: 5.45Zn–1.22Mg–0.3Cu) and AA7108 (wt.%: 5.45Zn–1.2Mg–0.27Cu) alloys for up to 60 days (in the over-aged region) by increasing the level of pre-deformation at room temperature. Dislocations can facilitate the formation of more stable precipitates on their cores. Deschamps *et al.* [86] found, through DSC and TEM analyses, that pre-deformation resulted in the direct formation of the η phase on dislocations during the artificial aging (at 160°C) of a naturally aged Al-Zn-Mg (wt.%: 6.1Zn–2.35Mg) alloy. They suggested that the alteration in the precipitation sequence was linked to the reduction in activation energy required for the formation of these precipitates because of the relaxation of their elastic misfit energy at the dislocation cores. However, dislocations can cause the annihilation of vacancies, acting as sinks due to the interaction of their elastic fields [6,87]. This process can hindering the homogeneous nucleation and growth of precipitates [6,87]. Poole *et al.* [85] attributed the reduction in hardening kinetics during natural aging of pre-deformed AA7030 and AA7108 alloys to the progressive annihilation of vacancies by dislocations, which reduced the formation of GP zones in the matrix of the alloys. Dislocations can also serve as solute sinks, thereby reducing the amount of solutes that are available for homogeneous precipitation. Deschamps *et al.* [86] reported the presence of large precipitate-free zones (PFZs) around dislocations in the microstructure of a naturally aged and deformed Al-Zn-Mg alloy (wt.%: 6.1Zn–2.35Mg) during subsequent artificial aging at 160°C, mainly in the later stages of aging. The formation of the PFZ was attributed to the flux of solutes towards the dislocations, leading to a rapid growth and coarsening of precipitates during over-aging. The annihilation of vacancies and solutes on dislocations can adversely affect the precipitation process and mechanical properties of AA7xxx alloys [6,87].

In both the aircraft and automotive (bumper applications) industries, pre-stretching operations are applied after solutionizing and quenching AA7xxx alloys and prior to aging treatments. Pre-stretching is utilized to remove quenching stress and distortion from manufactured parts, and the effect of this deformation process has been the subject of a few studies [13,85,87]. By applying the hot stamping or die-quenching (DQ) process, also known as hot form quenching (HFQ), the residual stresses associated with the quenching process are significantly reduced. This allows for the exploitation of the higher formability of AA7xxx alloys at high temperatures. The DQ process is a novel metal-forming process in which forming (deformation) and quenching occur simultaneously. A simple schematic representation of the die-quenching process sequence and the corresponding time-temperature profile are shown in Figure 2-7 (a) and (b), respectively. In the die-quenching process, a blank is heated to the solutionizing temperature, then quenched and formed in cold tooling. The formed parts are then subjected to age hardening processes to increase the final strength of the manufactured parts. This process has the potential to improve the limited cold formability of AA7xxx alloys by forming them at elevated temperatures. This expands the application of these alloys in the automotive industry and results in a higher final strength of manufactured automotive parts through the application of subsequent aging processes.

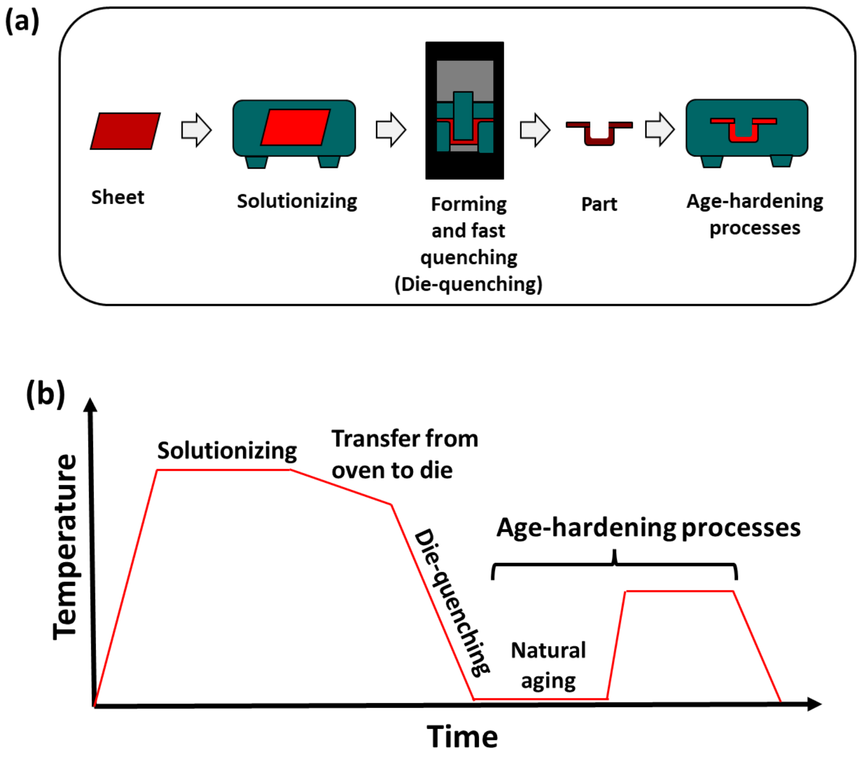

Figure 2-7 (a) A schematic presentation of process steps in the die-quenching process and (b) a time-temperature profile of the die-quenching process chain.

By employing the DQ process, it is possible to minimize the residual stresses associated with the quenching process. This, in turn, allows for the utilization of the enhanced formability of AA7xxx alloys at elevated temperatures. However, it has been reported that loss of vacancies and the formation of residual strain in die-quenched parts can affect the microstructural evolution of the material after subsequent aging treatments [6]. Kumar and Ross [6] investigated the post-form age hardening response of the AA7921 alloy (wt.%: 7.28Zn–2.63Mg–0.13Cu) after hot stamping (from the side-wall section of a deep drawn sample). They reported that the hardness of the alloy in the T4 temper (solutionized, water-quenched, and naturally aged for 2 weeks) was higher (~28%) than that of the hot-formed (at 470°C) and die-quenched parts after two weeks of natural aging. This difference was explained by the fact that dislocations act as vacancy sinks, thereby annihilating the quenched-in vacancies that are available for the formation of GP zones during natural aging. Furthermore, the hardness of the die-quenched material increased by 29% after two weeks of natural aging and 1-step PBC, attributed to the formation of η' [6]. However, as seen in Figure 2-8, the hardness of the material after the aforementioned heat treatments, and even after a 3-step PBC (20-minute heat treatments at temperatures of 180, 160, and 140°C), was still lower than that of the initial T6 condition (~520 MPa) [6]. They attributed this trend in the hardness values to the decreasing stability of η' precipitates in the following order: T6, 3-step PBC, and 1-step PBC [6]. Omer *et al.* [88] found that high strength values, close to the T6 strength, can be achieved in the die-quenched AA7075 alloy by application of a pre-aging treatment (120°C for 8 h) and performing a PBC treatment (177°C for 30 min). Schuster *et al.* [89] found that the HFQ process increased the hardness of die-quenched AA7021 and AA7075 alloys (compared to the hardness of the undeformed materials in the W-temper) due to strain aging. According to their results, the hardness evolution during the 21-day natural aging of both alloys after the HFQ process followed a trend parallel to that of the undeformed material (W-temper). They also investigated the effect of a stabilization (pre-aging) treatment, specifically at 80°C for 1 hour after HFQ process, on the hardness of the AA7021 alloy. They concluded that the hardness of the stabilized alloy remained unchanged during subsequent natural aging for up to 21 days.

Another factor that has been the subject of a few investigations in the aging treatments of die-quenched AA7xxx alloys is the effect of the quench rate. Omer *et al.* [88] investigated the effect of quench rate on the hardening potential of die-quenched AA7075. They revealed that by applying a quench rate of more than 30°C/s during the die-quenching process, a maximum hardening potential could be achieved during the subsequent natural aging (up to two weeks) of the die-quenched AA7075. Zheng *et al.* [90] reported that the quench-sensitive temperature range for the AA7075 alloy is between 250 to 400°C. In this range the formation of coarse η precipitates, both in the matrix and on grain boundaries, decreased the amount of solutes available for precipitation of η' phase during subsequent T6 treatment [90]. They also found that 350 °C was the most critical temperature at which the T6 strength of the alloy decreased by 45% within 10 seconds of being held. Zhu *et al.* [91] investigated a new method of hot stamping for the AA7075 alloy. The method involves applying a pre-cooling treatment prior to the start of deformation during die-quenching. They found that the critical cooling rate during die-quenching of the AA7075 alloy to achieve the maximum volume fraction of hardening precipitates during subsequent T6 treatment was 30°C/s. Reportedly, by decreasing the pre-cooling temperature, the hardness of the alloy decreased after the subsequent T6 treatment due to the formation of more *η* particles during quenching [91].

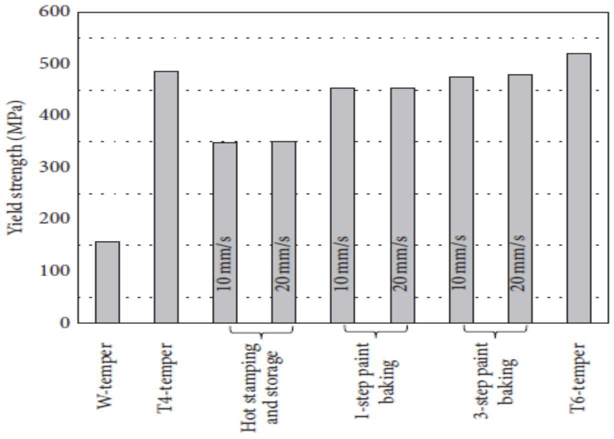

Figure 2-8 Effect of the processing history on the yield strength of AW-7921 sheet in the warm forming. All measurements were made at room temperature except for the preheat treatment measurements, which were measured at 230°C [6] **(Note: W-temper=solution heat treated).**

The abovementioned results show that there are various possible interactions that can affect the precipitation hardening behavior of die-quenched AA7xxx alloys. In the literature, there is a lack of comprehensive understanding of the nature of precipitation processes and their evolution during subsequent multi-step aging treatments, which are relevant to automotive applications, of hot-formed and die-quenched AA7xxx alloys. This proves the necessity of optimizing the thermal routes to achieve high strength levels after age hardening processes for automotive AA7xxx alloys. In this study, the precipitation hardening behavior of AA7xxx alloys after various thermal processing heat treatments have been investigated. The experimental results will be presented in Chapter 4, concerning the factors and phenomena discussed in Section 2.3.2.

2.4 Process Modelling Applied to Age-Hardenable Aluminum Alloys

The process modeling methods applied to the thermal treatment of age-hardenable aluminum alloys, such as AA6xxx and AA7xxx alloys, have been the subject of several studies [20,33,67,92–97]. The objectives of such models are to predict the microstructural changes or the mechanical properties of aluminum alloys, which will help in optimizing the process and the properties of these alloys and also achieve a better scientific understanding of processing-structure-property relationships. This review mostly concentrates on the literature related to the modeling approaches, which is pertinent to the current study.

2.4.1 Modeling of Precipitation Kinetics

The overall kinetics of the phase transformations during aging treatments of AA6xxx alloys, which have a history of intermediate aging (*i.e.*, pre-aging) prior to the final artificial aging treatment, have been modeled by Esmaeili and Lloyd [98], as follows:

$$f_r = 1 - (1 - f_r^0) \exp\left[- \int_0^t aIt^{\beta} dt\right] \quad \textbf{Eq. 2-1}$$

where f_r^0 is the relative volume fraction of precipitates in the pre-aged material, a is the equivalent growth rate constant, I is the nucleation rate per unit volume, and β is a generic time exponent. According to their study [98], for an isokinetic system, aI is a single function of temperature ($aI = f(T)$). Such a formulation for isothermal transformations (where $f(T)$ is constant) simplifies to [98]:

$$f_r = 1 - (1 - f_r^0) \exp(-kt)^n \quad \textbf{Eq. 2-2}$$

where:

$$n = (1 + \beta) \quad \textbf{Eq. 2-3}$$

and:

$$k = [\frac{f(T)}{n}]^{1/n} \quad \textbf{Eq. 2-4}$$

For non-isothermal aging treatments, Eq. 2-1 is expressed as:

$$f_r = 1 - (1 - f_r^0) \exp\left[- \sum_i k_i^n (t_i^n - t_{i-1}^n)\right] \quad \textbf{Eq. 2-5}$$

where k_i is the temperature dependent rate constant and has an Arrhenius type relationship with temperature, as in Eq. 2-8. The parameters k and n in Eq. 2-2 have been obtained for AA6xxx alloys using calorimetry experiments [98].

For aging treatments of the materials without a pre-aging history (*i.e.,* an as-quenched condition), f_r^0 is equal to zero, and thereby Eq. 2-5 reduces to a generalized form of the Johnson-Mehl, Avrami, Kolmogorov (called JMAK) formulation [99–101]. According to this modelling approach, the relative volume fraction of precipitates that form isothermally at time *t*, f_r , is described as:

$$f_r = 1 - \exp\,(-kt)^n \qquad \textbf{Eq. 2-6}$$

where k is the temperature-dependent kinetic parameter related to both nucleation and growth rates, and *n* is a numerical exponent independent of temperature, on the condition that there is no change in the nucleation mechanism. *n* can vary from ~0.5 to 4 depending on the assumptions made regarding the nucleation and growth processes [102,103]. The JMAK formulation has been used by Shercliff and Ashby [104] and Esmaeili *et al.* [105] to model the microstructural evolution during aging treatments of AA6xxx alloys. Poole *et al.* [85] have also used this formulation to model the kinetics of age hardening during aging treatments of AA7xxx alloys. The kinetic parameters k and n are usually obtained by experimental measurement of f_r as a function of temperature. Then plotting the $ln\,ln(\frac{1}{1-f_r})$ vs. $ln\,t$ and finding the slop and y-axis intercept of the resultant line, as Eq. 2-7 shows:

$$\ln\ln\left(\frac{1}{1-f_r}\right) = \ln k + n\ln t \qquad \textbf{Eq. 2-7}$$

Having the k values for at least three different temperatures, the Arrhenius type relationship of $k\,(\,s^{-1})$ as a function of temperature is found [98]:

$$k = k_0 \exp\,(-\frac{Q_A}{RT}) \qquad \textbf{Eq. 2-8}$$

The parameter k_0 is the proportionality constant, Q_A (kJ mol^{-1}) is the equivalent activation energy, and *R* is universal gas constant. This approach was adopted by Esmaeili and co-workers

[105] to describe the precipitation kinetics in the AA6111 alloy, where isothermal calorimetry was used for experimental analysis of f_r.

Baghbanaghaei [106] has further expanded the kinetic model developed by Esmaeili and Lloyd [98] to account for the effect of deformation on the precipitation kinetics during the final artificial aging of a pre-aged and warm-formed (PA+WF) material. Accordingly, the evolution of f_r during the final artificial aging treatment has been formulated as follows [106]:

$$f_r(tot) = 1 - (1 - f_r^0)\ \exp\left[-\sum_i\ (t_i^n - t_{i-1}^n)((k_{iv})^n + (k_{ieff})^n)\right] \qquad \textbf{Eq. 2-9}$$

where k_{iv} is the temperature-dependent constant describing the reaction rate in the absence of dislocations, and k_{ieff} is the temperature dependent constant describing the reaction rate in the presence of dislocations (during the warm-forming stage and the final aging treatment). In developing Eq. 2-9, it is assumed that dislocations enhance the kinetics of precipitation by increasing the solute diffusivity through the effect of dislocation core diffusion (pipe diffusion). Thereby, the effective precipitation rate parameter (k_{eff}) is defined as follows [106]:

$$k_{eff} = k_v \left(1 + \rho a_c \frac{D_{0c}}{D_{0v}} \exp(\frac{Q_v^{diff} - Q_c^{diff}}{RT})\right) \qquad \textbf{Eq. 2-10}$$

in which, ρ is the dislocation density, a_c is the cross-sectional area of the dislocation core, D_{0v}, and D_{0c} are the pre-exponential factors for lattice and core diffusion, respectively. Q_v^{diff}, Q_c^{diff} are the activation energies for lattice and core diffusion, respectively. Baghbanaghaei's model has been implemented to predict the evolution of f_r during warm-forming of the pre-aged AA7075 alloy and also during subsequent aging of the PA+WF alloy at four different aging temperatures. The evolution of f_r obtained through modeling and experiments (IC analysis) is shown in Figure 2-9 [106]. The comparison of the two results showed their good agreement beyond the earliest stage of the final artificial aging process. The discrepancy between the initial modeled and experimental values for f_r was ascribed to precipitate dissolution due to the change in aging temperature (*i.e.,* from the WF to the final artificial aging temperature), possible dissolution of some “pre-aging zones” during the warm-forming cycle, and annihilation of the VRCs.

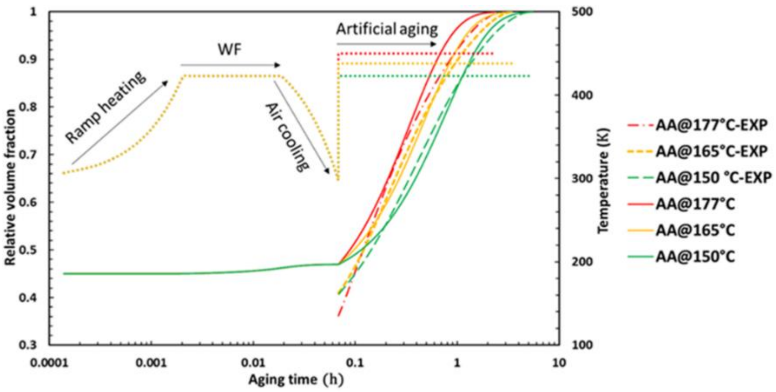

Figure 2-9 The comparison of the predicted and measured values of f_r during non-isothermal processing of AA7075, which includes the WF sequence and final aging treatment at three artificial aging temperatures of 150 ℃, 165℃ or 177℃ (AA = artificial aging) [106]**.**

2.4.2 Modeling of Yield Strength

Over the years, various yield strength models based on the microstructural evolution have been developed for aging treatments of age-hardenable aluminum alloys. The most common approach is to use the concept of process modeling [107] combined with the internal state variable approach (originally proposed by Richmond [108]) which relates the material response of interest to microstructural variables. Process modeling which was first introduced by Shercliff and Ashby [107] is “a mathematical relation between the process variables (alloy composition and heat treatment temperature and time) and the alloy strength or hardness, based on physical principles (thermodynamics, kinetic theory, dislocation mechanics, and so on). This section has been concentrated on the modelling approaches used in the literature that are related to the current investigation.

For the modeling of precipitation hardening in aluminum alloys, it is generally accepted that during aging treatments, the yield strength of the material (σ_y) is contributed by the intrinsic strength of the aluminum matrix (σ_i), dislocation (σ_d), precipitation (σ_{ppt}), and solid solution (σ_{ss}) hardening [97,106,109,110]:

$$\sigma_y = \sigma_i + \sigma_{ss} + \left(\sigma_{ppt}^m + \sigma_d^m\right)^{1/m}$$ **Eq. 2-11**

m value can vary between 1 and 2. For the cases where there is a high density of weak obstacles, m is equal to 1, and for strong obstacles, m is equal to 2 [109,110]. For intermediate cases, m falls between 1 and 2 [101]. Esmaeili *et al.* [105] assumed that the yield strength of an aged alloy in the absence of dislocations (pre-deformation) can be obtained using a linear addition law, as follows:

$$\sigma_y = \sigma_i + \sigma_{ss} + \sigma_{ppt}$$ **Eq. 2-12**

The basis of modeling of σ_{ppt} in Eq. 2-12 is the interaction between precipitates and moving dislocations, where the precipitates act as obstacles to dislocation movement. Accordingly, the contribution of precipitation strengthening, σ_{ppt}, to the yield strength depends on the average obstacle spacing and strength, as follows [105]:

$$\sigma_{ppt} = \frac{MF}{bL}$$ **Eq. 2-13**

where M is the Taylor factor, F (nN) is the maximum interaction force between an average-size precipitate and dislocation, b (nm) is the magnitude of the Burgers vector, and L (nm) is the average spacing between obstacles. In Eq. 2-13, F and L change with aging time and temperature and are functions of microstructural variables. Based on a simple force balance, F has been defined as [96,111]:

$$F = 2\Gamma \cos\left(\frac{\varphi_c}{2}\right)$$ **Eq. 2-14**

in which φ_c is the critical breaking angle and Γ $(GPa\ nm^2)$ is the dislocation line tension. F increases with increasing the precipitate size for shearable precipitates, while it is constant for non-shearable ones (*i.e.*, 2*Γ*). When the dislocation breaking angle while encountering an obstacle, φ_c (Figure 2-10), is small, the dislocation movement becomes harder. Esmaeili *et al.* [105] have described shearable obstacles with $120^{\circ} > \varphi_c \geq 0^{\circ}$, as strong obstacles, while for $180^{\circ} \geq \varphi_c > 120^{\circ}$, obstacles are considered weak. Accordingly, non-shearable obstacles, which interact with dislocations according to the Orowan mechanism (*i.e.*, $\varphi_c = 0^{\circ}$) are always strong obstacles. It has been reported that the average spacing between strong obstacles can be related to the total volume fraction of precipitates after an aging treatment, as [96,105,112]:

$$L_{strong} = \sqrt{\frac{2\pi}{3f_v}}r \qquad \textbf{Eq. 2-15}$$

where f_v is the volume fraction of precipitates and r (nm) is the radius of an average-sized obstacle. The average spacing between weak obstacles is found as [96,105,112]:

$$L_{weak} = (\frac{F}{2\Gamma})^{-1/2}L_{srtong} \qquad \textbf{Eq. 2-16}$$

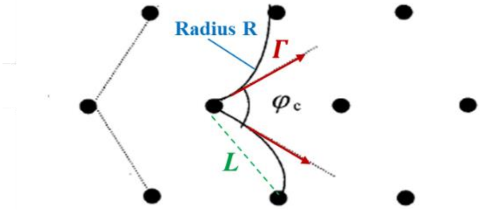

Figure 2-10 The interaction between dislocations and obstacles in a triangular array of obstacles [105]**.**

σ_{ppt} for materials in the under-aged and peak-aged conditions can be obtained by replacing the corresponding relationships for *F* and *L* in Eq. 2-13. The theoretical relationships for σ_{ppt}, using weak and strong-obstacle assumptions, developed by Esmaeili and co-workers [105], are outlined in Table 2-2. The weak obstacle model in Ref. [105] was further used by Sepehrband and Esmaeili [112] to derive a simplified equation for modeling of σ_{ppt} (see Table 2-2) which eliminates the need to have the precipitate radius *r* as a function of aging time. Sepehrband and Esmaeili reported that pure growth of precipitates (and not nucleation) was assumed to be the dominant controlling mechanism of precipitation (in the presence of pre-existing precipitates).

For the modeling of the evolution of precipitate size (r) during aging processes in which concurrent nucleation and growth of precipitates happen, Baghbanaghaei [106] developed a modeling equation (described as the "nucleation-affected growth" model), as follows:

$$r_t = \sqrt{f_r(t)} \times r_{peak} \qquad \textbf{Eq. 2-17}$$

in which r_{peak} is the radius of precipitates at the peak-aged condition and r_t and $f_r(t)$ are the radius and the relative volume fraction of precipitates at time *t* during aging treatment. As described in Baghbanaghaei's work, this equation would better define nucleation-dominated aging processes (*e.g.,* the earlier stages of aging during artificial aging of pre-aged materials). By substituting Eq. 2-17 in Eq. 2-13, Baghbanaghaei also developed a theoretical formulation for σ_{ppt} (described as "modified-weak obstacle" model), for nucleation-dominated aging processes, as listed in Table 2-2.

Table 2-2 Formulations for precipitation strengthening contribution.

Assumption for σ_{ppt}	Formula	Symbols	Reference
Weak obstacle	$\sigma_{ppt\|Weak} = C_2(rf_r)^{1/2}$	C_2, and C are proportionality factors related to the microstructure-strength relationship for the peak-aged material.	[105]
Weak obstacle	$\sigma_{ppt\|Weak} = C(f_r)^{2/3}$		[112]
Strong obstacle	$\sigma_{ppt\|Strong} = C(f_r)^{1/2}$		[105]
Modified-weak obstacle	$\sigma_{ppt\|Modified-Weak} = C(f_r)^{3/4}$		[106]

The yield strength modeling relationships reviewed in this section were implemented in References [96,98,105,106,112,113] to predict the precipitation hardening behavior of AA6xxx and AA7xxx alloys during various aging paths. Using Eq. 2-12, Esmaeili *et al.* [105] modeled the yield strength evolution during artificial aging of (a) solutionized [105], (b) naturally aged [113], and (c) pre-aged AA6xxx alloys [98]. The methodology developed by Esmaeili and Lloyd [98] was also implemented on the modelling of precipitation hardening for a pre-aged AA7030 alloy during artificial aging by Sepehrband and Esmaeili [112]. The evolution of yield strength during aging at 150°C, obtained through modeling and experiment, is shown in Figure 2-11 (b). In this work, they used the results of isothermal calorimetry and DSC experiments to analyze the evolution of f_r (as shown in Figure 2-11 (a)) and to model the evolution of σ_y during final aging step. The yield strength modeling results showed that the weak obstacle model better suits the earlier stages of aging during artificial aging of pre-aged AA7030 alloy.

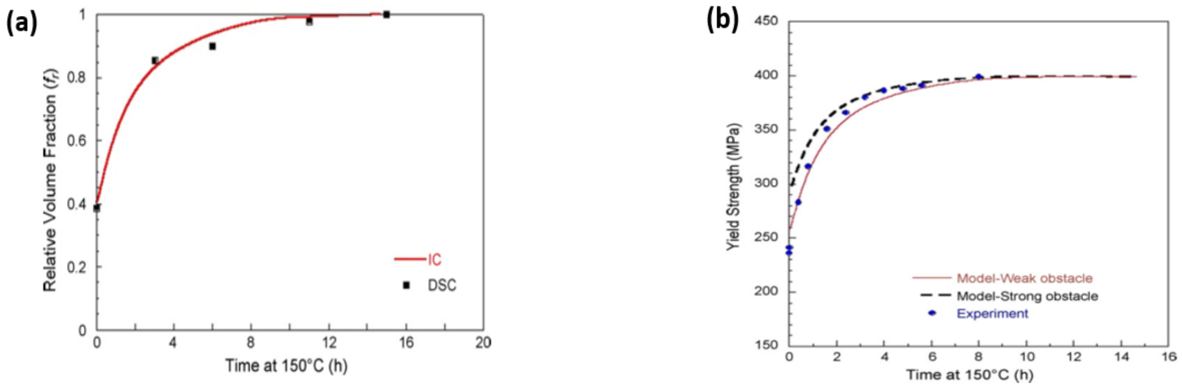

Figure 2-11 (a) The evolution of f_r using DSC vs. IC approach and (b) comparison of the experimental and modeling results for yield strength evolution [112]**.**

There are a few process models for predicting the yield strength evolution of AA7xxx alloys after pre-straining (in the presence of dislocations) and aging treatments in which the radius, volume fraction of precipitates, and relative volume fraction of precipitates are used as variables [13,85,97,106]. In a study by Baghbanaghaei [106], the evolution of yield strength during artificial aging of a PA+WF AA7075 alloy at 177℃ was modeled using Eq. 2-11 and assuming *m*=1, and the results are shown in Figure 2-12. The overestimation of yield strength during the final aging treatment (as seen in Figure 2-12) was attributed to the effect of dislocation recovery reducing the strengthening potential of the alloy, which has not been considered in their model [106].

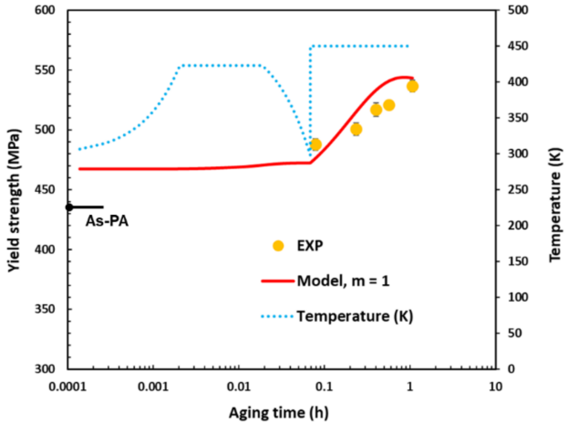

Figure 2-12 Comparison of the modeling and the experimental results for the evolution of yield strength during artificial aging of the PA+WF AA7075 at 177℃ [106]**.**

The investigation of recovery processes during aging treatments of age-hardenable aluminum alloys has been very limited. In a study by Poole *et al.* [85], a "simplified decay law" was used to incorporate the effect of annihilation/recovery of dislocations to σ_d (in Eq. 2-11) during a two-step artificial aging treatment of solutionized and pre-deformed AA7030 alloy, as follows:

$$\sigma_d = \sigma_{initialdis} + \sigma_{rec}(\exp(-k_3 P^*) - 1) \qquad \textbf{Eq. 2-18}$$

where P^* is a normalized time, $\sigma_{initialdis}$ is the contribution of dislocations to yield strength right after deformation, and k_3 is a constant. In this equation, the amount of recovery (σ_{rec}) was reported to be related to the pre-strain level as [85]:

$$\sigma_{rec} = A(1 - \exp(k_4 \varepsilon)) \qquad \textbf{Eq. 2-19}$$

where A and k_4 are constants. In their work, the constant parameters were estimated by fitting the model to the experimental yield-stress values (60-day overaged yield strength values) for artificial aging of pre-deformed AA7030 alloy deformed at different pre-strain levels, and the total amount of recovery was modeled as a function of pre-strain level, as seen in Figure 2-13 [85]. The authors further stated that more experimental work would be needed to further analyze the level of accuracy of their recovery modeling approach [85].

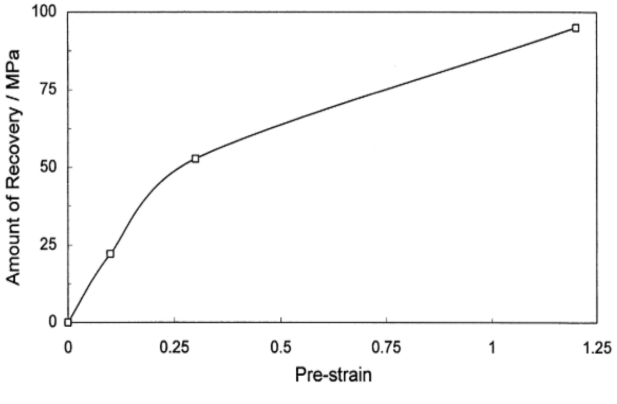

Figure 2-13 Predicted values for total static recovery vs. pre-strain level [85].

In regard to process modeling of precipitation hardening in pre-deformed AA7xxx alloys, there are two shortcomings within the current literature: (1) there is a lack of modeling work to predict microstructural and yield strength evolution of AA7xxx alloys after hot-forming and die-quenching processes, and (2) the effect of static recovery during aging treatments has been neglected in the current models. Therefore, the precipitation hardening behavior of AA7xxx alloys after hot-forming and die-quenching needs to be further investigated, and relevant process modeling should be developed for successful application of these alloys in the automotive industry.

3. Experimental Methodology

In this chapter, the materials, heat treatment, thermo-mechanical procedures, and experimental methods of investigation, which include hardness measurements, tensile tests, atom probe tomography (APT), transmission electron microscopy (TEM), isothermal calorimetry, and differential scanning calorimetry, will be described.

3.1 Materials

The materials used in this study were AA7075 and a developmental alloy, denoted here as D-7xxx. The alloys were provided by Arconic in sheet form, measuring 2 mm in thickness, and in the industrially processed T6 and T76 conditions, respectively. The composition of the AA7075 sheet was tested using inductively coupled plasma atomic emission spectrometry, according to ASTM E1097-12 [114]. The resultant data, along with the nominal composition of the D-7xxx alloy, are provided in Table 3-1.

Table 3-1 Chemical compositions for AA7075 and D-7xxx [106] **(wt.%).**

Alloys	Al	Zn	Mg	Cu	Zr	Fe	Cr
AA 7075	90.07	6.35	1.92	1.46	Negligible	0.1	0.1
D-7xxx	87.6-90.4	7.0-8.0	1.2-1.8	1.3-2.0	0.08-0.15	0.08	0.04

3.2 Thermo-Mechanical Processing

The solution treatment process was conducted in two ways: (a) sand bath heating followed by water quenching and (b) heating in a thermomechanical simulator (Gleeble) followed by hot-form quenching. The following sections describe the heat treatments and thermomechanical processing routes related to these solutionizing processes.

3.2.1 Aging Treatments on Solutionized and Water-Quenched Alloys (In Relevance to Sections 4.1 and 5.15.1)

The alloy samples were solutionized at 470℃ for 10 minutes in a Techne FB-08C fluidized bed furnace (sand bath) with temperature fluctuations within ±1°C and a heating rate of 7ºC/min and then quenched in water. The overall heat treatment profiles used in this investigation for the solutionized and water-quenched samples are schematically presented in Figure 3-1 for the (a) natural aging, (b) pre-aging, (c) secondary natural aging of pre-aged samples, and (d) artificial aging of pre-aged alloy.

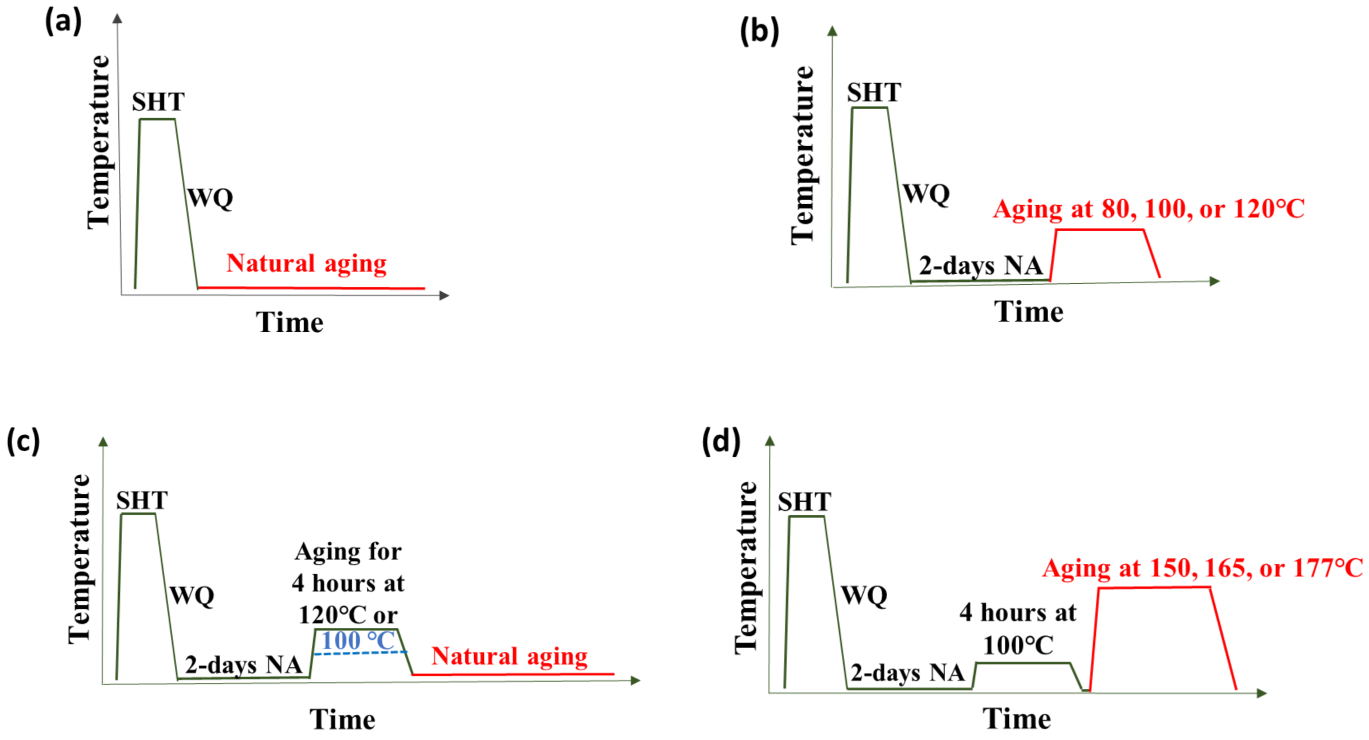

Figure 3-1 Heat treatment profiles of (a) natural aging treatment, (b) artificial aging of 2-day naturally aged samples (pre-aging treatment), (c) secondary natural aging treatment of pre-aged samples and (d) artificial aging treatments of pre-aged samples (SHT = Solutionizing Heat Treatment, WQ=Water-Quenching and NA=Natural Aging).

To assess the natural aging behavior of AA7075 and D-7xxx alloys (Figure 3-1 (a)), samples were kept at room temperature (~25°C) for different times after solution treatment and water quenching, as summarized in Table 3-2.

Table 3-2 Heat treatment conditions for experimental analyses of natural aging for AA7075 and D-7xxx.

Test type	Heat treatment			
		AA7075		D-7xxx
Microhardness		NA for 1 h to 1 year		-
Tensile testing	#1	AQ (6 min NA)	#1	AQ (6 min NA)
	#2	As-received T6	#2	NA for 1, 2, 7, and 30 days
DSC	#1	AQ (2 min NA)		-
	#2	NA for 1, 2, 3, 14, and 28 days		-
APT	#1	1-day natural aging		-
	#2	2-days natural aging		
	#3	4-days natural aging		
	#4	14-days natural aging		

*Note: NA=Naturally-Aged, AQ=As-Quenched, SHT=Solution Heat-Treated, WQ=Water-Quenched. The initial condition for all heat treatments (except as-received T6) was SHT + WQ.

An analysis of the effect of pre-aging treatments at three different temperatures (Figure 3-1 (b)) on the microstructure evolution and yield strength of the AA7075 alloy was conducted, and the heat treatment details for various samples are summarized in Table 3-3. For this purpose, the as-received (T6) samples were first solutionized and then naturally aged for two days (NA2 condition) before the subsequent artificial aging step. It should be noted that this preliminary two-step aging treatment in the current study is considered a pre-aging treatment before the final aging step. The fluidized sand bath furnace was used for all aging treatments in this study.

Table 3-3 Heat treatment conditions for experimental analyses of pre-aging for AA7075.

Test type		Heat treatments		Designation
Microhardness		Initial condition	SHT + WQ + 2-days NA	2NA
	#1	Aging	80℃ for 0.5, 1, 2, 4 hours	PA80
	#2		100℃ for 0.5, 1, 2, 4 hours	PA100
	#3		120℃ for 1, 2, 4 hours	PA120
IC	#1	Initial condition	SHT + WQ	WQ
		Aging during IC	2-days at room temperature	-
	#2	Initial condition	SHT + WQ + 2-days NA	2NA
		Aging during IC	*t* at 80, 100, and 120℃	-

* Note: NA=Naturally-Aged, PA=Pre-Aged, SHT=Solution Heat Treated, WQ=Water-Quenched.

Secondary natural aging of two different pre-aged AA7075 samples (Figure 3-1 (c)) was analyzed to assess the stability of these tempers after storage at room temperature, as summarized in Table 3-4.

Table 3-4 Heat treatment conditions for experimental analyses of secondary natural aging for pre-aged AA7075 samples.

Test type		Heat treatments		Designation
Microhardness	#1	Initial condition	SHT + WQ + 2-days NA + 4 h at 100℃	PA
		Aging	Natural aging at room temperature for 6 to 4320 hours	SNA
	#2	Initial condition	SHT + WQ + 2-days NA + 4 h at 120℃	PA120-4
		Aging	Natural aging at room temperature for 6 to 5040 hours	SNA
DSC	#1	SHT + WQ + 2-days NA + 4 h at 100℃		PA
	#2	SHT + WQ + 2-days NA + 4 h at 120℃		PA120-4

	#3	SHT + WQ + 2-days NA + 4 h at 100℃ + Natural aging for 2 or 4 weeks	-
	#4	SHT + WQ + 2-days NA + 4 h at 120℃ + Natural aging for 2 or 4 weeks	-

* Note: NA=Naturally-Aged, PA=Pre-Aged, SHT=Solution Heat Treated, WQ=Water-Quenched, SNA= Secondary Natural Aged.

The aging kinetics and evolution of the yield strength during artificial aging treatments of AA7075 alloy samples in the PA condition (Figure 3-1 (d)) were investigated. The first two steps of aging (PA) were chosen based on the preliminary tensile testing results. As a preliminary investigation, different pre-aging treatments were employed to examine the effect of different natural aging times during the first step and different artificial aging times and temperatures during the second step of aging on the evolution of the yield strength in the D-7xxx alloy. The yield strength values obtained from the tensile testing results (not reported here) showed that a maximum yield strength value similar to that of a conventional T6 temper can be achieved by employing the pre-aging treatment, as shown in Figure 3-1 (d).

Table 3-5 Heat treatment conditions for experimental analyses of artificial aging of AA7075 samples in PA condition.

Test type		Heat treatments	Designation
Microhardness	Initial condition	SHT + WQ + 4 h at 100℃	PA
	Aging	Final stage aging at 150, 165 or 177℃	MSA
IC	Initial condition	SHT + WQ + 4 h at 100℃	PA
	Aging during IC	*t* at 150, 165 or 177℃	-
DSC	#1	SHT + WQ + 2-days NA + 4 h at 100℃ + 6h at 150 ℃	-
	#2	SHT + WQ + 2-days NA + 4 h at 100℃ + 0.5 h at 177 ℃	PB

* Note: NA=Naturally-Aged, PA=Pre-Aged, SHT=Solution Heat Treated, WQ=Water-Quenched, MSA=Multi-Step Aged, PB=Paint-Baked, For the IC tests, *t* was selected as the time required to achieve peak strength.

3.2.2 Thermo-Mechanical Processing History and Aging Treatments of Die-Quenched and Forced-Air Quenched AA7075 (In Relevance to Sections 4.2 and 5.2)

To simulate the hot forming and die-quenching processes, the AA7075 samples were simultaneously heat-treated and deformed using a thermomechanical simulator (Gleeble-3500, Dynamic Systems Inc.). A modified version of the standard ASTM subsize tensile sample was used (Figure 3-2). The sample size modification was applied to minimize the thermal gradients along the length of the coupons. Further details regarding the sample geometry and thermal gradient profile have been given in Ref. [115].

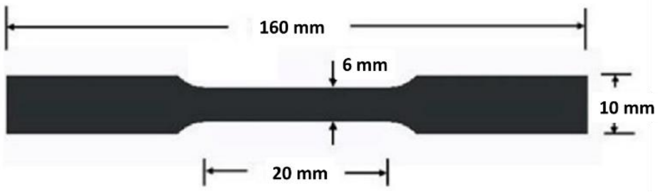

Figure 3-2 Gleeble sample dimensions.

For the simulated die quenching process, the samples were first heated to a solutionizing temperature of 470±1℃ in 35 s and held at this temperature for 10 min. They were then forced-air quenched with compressed air using a pair of air nozzles pointing at the center of the sample and simultaneously pulled (deformed) at a constant stroke rate. Deformation was applied non-isothermally during the quenching process in the temperature range of 400-225℃ in 4 s. The temperature range was chosen to simulate the temperature variation that occurs in the sheet during actual die-quenching processes [116]. The deformed regions of the samples, with pre-determined maximum strain levels of ~15% and 26% equivalent true strains, were used for further experimental analyses. Figure 3-3 (a) shows the temperature/stroke (displacement)-time profile for the entire solutionizing and quenching processes in the Gleeble for the simulated die-quenched samples.

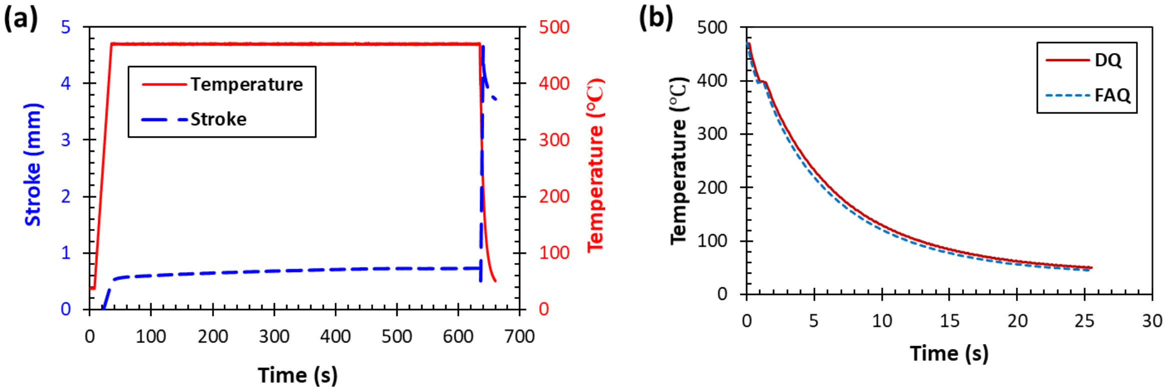

Figure 3-3 (a) Typical temperature and displacement measurements for the DQ (simulated die-quenched) samples and (b) temperature-time profile for the DQ and FAQ (forced-air quenched) samples during quenching step in Gleeble.

The tensile strains during the hot forming process were monitored using an in-situ digital image correlation (DIC) technique. Two 4-megapixel, 140 frames per second, Gazelle cameras were used for this purpose. A 10mm long virtual extensometer was used at the center of the gauge section for strain measurements. The raw load-displacement data were obtained and analyzed by data processing of the captured images using the Correlated Solutions Vic 3D© software. For displacement measurement using the DIC technique, samples were prepared as follows: they were first sandblasted with glass beads, cleaned using ethanol, and etched with a 10 wt.% NAOH solution for 5-6 seconds. Then, one side of the sample's cross-sectional surface was painted with a fine, random, black-speckle pattern for surface strain mapping via DIC. To track the thermal gradient across the samples, two thermocouples were spot-welded to the center of the non-painted sides of the samples using a voltage set point of 25 V.

To investigate the effect of the sole cooling rate during simulated die-quenching on the precipitation hardening behavior of the AA7075 alloy during subsequent aging treatments, some samples were solutionized and forced-air quenched in the Gleeble simulator without any deformation. All the samples were subjected to an approximate true strain of 0.006 during the heating and holding periods. The cooling curves of the DQ and FAQ samples are shown in Figure 3-3 (b). The DQ and FAQ samples were placed in dry ice (-78.5°C) for up to 8 hours, immediately after quenching. Two square-shaped samples sized 5×5×2 mm^3 were then cut from the center of the gauge length of the Gleeble samples using a Struers Accutom-5 precision saw for calorimetry, hardness measurements, and TEM. The cutting process took less than 10 minutes.

All aging treatments carried out on the FAQ and DQ samples were conducted in a sand bath furnace. A schematic representation of the heat treatment profiles used for the analysis of aging treatments on the die-quenched samples is shown in Figure 3-4.

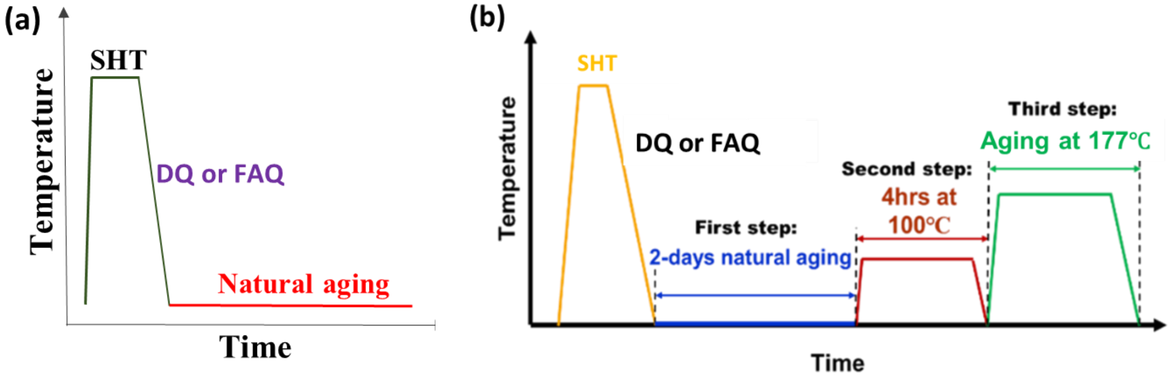

Figure 3-4 Schematic presentation of the ageing treatment routes for (a) naturally-aged and (b) multi-step aging treated samples in the DQ temper.

For the analysis of the natural aging behavior, the DQ and FAQ samples were kept at room temperature (~25°C) for different times after solutionizing (Figure 3-4 (a)). A summary of the thermal processing routes and the experiments conducted on AA7075 for the analysis of natural aging are outlined in Table 3-6.

Table 3-6 Heat treatment conditions for experimental analyses of natural aging of AA7075-DQ.

Test type	Thermal processing route			Designation
Microhardness	#1	Initial condition	SHT + Forced-air quenched	FAQ
		Aging	Natural aging for different times	-
	#2	Initial condition	SHT + Simulated die-quenched (15% deformed)	DQ
		Aging	Natural aging for different times	-

* Note: SHT=Solution Heat Treated, FAQ=Forced-Air Quenched, DQ=Die-Quenched. SHT, DQ and FAQ were conducted in Gleeble.

For the multi-step aging treatment (Figure 3-4 (b)), the artificial aging behavior of the FAQ or DQ samples was investigated after three aging sequences in a multi-step aging route, as shown schematically in Figure 3-4 (b). For some analyses, the third aging step was chosen as 30 min at 177°C [115], in accordance with the automotive paint-baking process [74]. A summary of the thermal processing routes and the experiments conducted on AA7075 alloy is presented in Table 3-7.

Table 3-7 Heat treatment conditions for experimental analyses of multi-step aging in AA7075-DQ.

Test type		Thermal processing route		Designation
Microhardness	#1	SHT + Forced-air quenched + 2-days natural aging		FAQ + 2NA
	#2	SHT + Die-quenched (15% deformed)		DQ + 2NA
	#3	SHT + Forced-air quenched + 2-days natural aging + 4h at 100°C		FAQ + PA
	#4	SHT + Die-quenched (15% deformed) + 2-days natural aging + 4h at 100°C		DQ + PA
	#5	SHT + Forced-air quenched + 2-days natural aging + 4h at 100°C+ 0.5h at 177°C		FAQ + PB
	#6	SHT + Die-quenched (15% deformed) + 2-days natural aging + 4h at 100°C + 0.5h at 177°C		DQ + PB
IC	#1	Initial condition	SHT + Die-quenched (15% deformed)	DQ
		Aging during IC	*t* at 177°C	-
	#2	Initial condition	SHT + Die-quenched (15% deformed) + 2-days natural aging + 4h at 100°C	DQ + PA
		Aging during IC	*t* at 177°C	-
TEM	#1	SHT + Die-quenched (15% deformed) + 2-days natural aging + 4h at 100°C		DQ + PA
	#2	SHT + Water-quenched + 2-days natural aging + 4h at 100°C		WQ + PA

	#3	SHT + Die-quenched (15% deformed) + 2-days natural aging + 4h at 100℃ + 0.5 h at 177 ℃	DQ + PB
	#4	SHT + Die-quenched (26% deformed) + 2-days natural aging + 4h at 100℃ + 0.5 h at 177 ℃	DQ (26%) + PB
	#5	SHT + Water-quenched + 2-days natural aging + 4h at 100℃ + 0.5 h at 177 ℃	WQ + PB
DSC	#1	SHT + Forced-air quenched	FAQ
	#2	SHT + Die-quenched (15% deformed)	DQ

* Note: NA=Naturally-Aged, PA=Pre-Aged, SHT=Solution Heat Treated, WQ=Water-Quenched, MSA=Multi-Step Aged, PB=Paint-Baked, FAQ=Forced-Air Quenched, DQ=Die-Quenched. For the IC tests, *t* was selected as the time required to achieve peak strength. SHT, DQ and FAQ were conducted in Gleeble.

3.3 Experimental Methods of Investigation

3.3.1 Mechanical Testing

3.3.1.1 Hardness Testing

Microhardness measurements were conducted using a Wilson 402MVD Vickers hardness tester using a 300 g load. Square-shaped samples, 7mm ×7mm ×2mm in size, were cut from the as-received AA7075 sheet for microhardness measurements. The samples were prepared and tested as per the ASTM-E384 standard. The hardness measurements were performed on the surfaces of the polished samples. The reported hardness for each condition is the average value obtained from at least five indentations on a single sample. The error bars included in the hardness plots represent one standard deviation, assuming a normal distribution. Microhardness data for the AA7075 alloy was used to estimate the evolution of yield strength during different aging treatments of this alloy by assuming that the yield strength in MPa was approximately equivalent to the measured Vickers Hardness Number (VHN) multiplied by 3 [56].

3.3.1.2 Tensile Testing

For tensile testing, the D-7xxx and AA7075 samples were cut from the as-received sheet in the rolling direction according to the ASTM E8 standard, solutionized in the sand bath (at

470°C for 10 min), and then quenched in water. The samples were put in dry ice for up to 6 hours, immediately after quenching. Tensile tests were conducted at room temperature using a screw-driven MTS Criterion 49 machine and an initial strain rate of $0.001s^{-1}$. A commercial stereoscopic digital image correlation (DIC) system was used for displacement measurements according to the methodology reported in Ref. [88]. The raw load-displacement data was obtained by data processing of the captured images using the Vic-7 software (Correlated Solutions, Inc.). The load-displacement data was then converted to true stress-strain values. The yield strength values were obtained based on the 0.2% offset method using the true stress-strain curves. The test repeatability was confirmed by conducting at least three tests for each aging condition. The reported yield strength values for these alloys are the average of all repeatable measured values.

3.3.2 Microstructure Characterization

3.3.2.1 Atom Probe Tomography

Samples for atom probe tomography (APT) were prepared by creating 'matchstick' samples 0.5×0.5×10 mm^3 in size. The matchstick samples were solutionized in a sand bath, quenched in water, and then stored at room temperature before testing. The samples were then electropolished to obtain sharp tips (less than 150 nm in diameter) using a standard 2-stage electropolishing method and perchloric acid solutions [117]. APT data acquisition was performed using a Cameca LEAP4000X HR operating in voltage pulse mode with a pulse fraction of 20%, a pulse frequency of 200 kHz, and a nominal detection rate of 0.03 ion/pulse (3%). The sample chamber was kept in a vacuum environment below 4×10^{-11} Torr, and the sample stage at a temperature of approximately 38 K. APT data reconstruction was done using IVAS 3.8.2 (CAMECA Instruments, Inc.). Reconstructions were spatially-calibrated using the crystal poles, which were apparent on the detector desorption maps, and well-known plane spacings for FCC-Al [117]. To visualize and quantify solute clustering in each dataset, the maximum separation method [117,118] was used. The cluster search algorithm used Mg and Zn as target solutes with a 1st order, d_{max} of 0.52 nm, N_{min} of 13, and both envelope and erosion distances as 0.26 nm [119].

3.3.2.2 Transmission Electron Microscopy

Sub-microstructural analysis was performed using FEI’s (Thermo Fisher Scientific) Tecnai Osiris transmission electron microscope (TEM) equipped with an X-FEG gun operating at 200 keV. Foil samples were prepared by polishing plates down to approximately 100 µm and punching out 3 mm disks. These discs were subsequently thinned electrolytically until perforation with the A2 electrolyte using Struers twin-jet TenuPol-5 to create an electron-transparent region around the perforation. Conventional bright field (BF) and dark field (DF) imaging, selected area diffraction (SAD), and convergent beam electron diffraction (CBED) techniques have been used for phase identification and crystallography. STEM mode using bright field (BF) and high-angle annular dark field (HAADF) detectors was used in combination with energy-dispersive X-ray spectroscopy (EDS). EDS mapping was performed using the ESPRIT software. The precipitate size distributions in different samples were analyzed by image analysis of the TEM-BF and HAADF images using ImageJ 1.53e software. Image analysis was performed on the TEM images at the locations where the precipitates did not interfere with each other. To verify the consistency of the results, the size (diameter) of at least 800 precipitates was measured for each heat-treatment condition studied here. The measurement was performed on at least four different TEM images (at similar magnifications) for each condition. For the elongated (plate-shaped) precipitates, the size of the precipitate’s long axis was approximately treated as a measure of the precipitate diameter ([011] in this study). To measure the volume of the measured area, the thicknesses of the samples were measured for each mapped area by electron energy loss spectroscopy (EELS) using the Malis/Egerton log ratio formula [120]. Thickness measurements were also used to analyze the dislocation density measurements. For dislocation density measurements, the technique described in Ref. [121] was used in this study. For this purpose, STEM images were taken at a low-index zone axis (*i.e.*, [011]), where all dislocations were visible. The reported values for dislocation density are the average of at least five measurements.

3.3.3 Calorimetry

Calorimetry experiments were conducted using a SETARAM C80 calorimeter (see Figure 3.5) in an air atmosphere. Calorimetry experiments measured the materials’ response, *i.e.*, heat flow, to heating. In isothermal calorimetry (IC) tests, the heat flow was recorded as a function of the aging time at a constant aging temperature. For differential scanning calorimetry (DSC) experiments, the heat flow was recorded as a function of temperature using a constant heating rate. The heat released or absorbed resulted in exothermic and endothermic peaks, corresponding to precipitation and dissolution reactions, respectively.

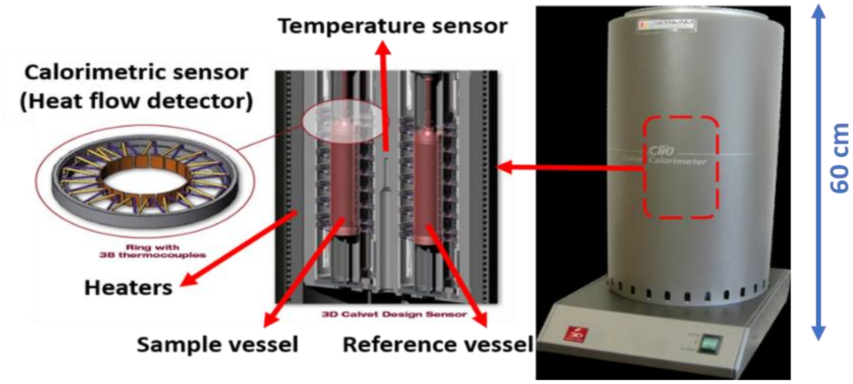

Figure 3.5 Schematic diagram of C80 calorimeter [122]**.**

Multiple-piece samples with an approximate total mass of ~930 mg (7 mm×7 mm×2 mm in size) for the WQ condition and ~670 mg (5 mm×5 mm×2 mm in size) for the DQ or FAQ condition were used for each IC or DSC test.

3.3.3.1 Differential Scanning Calorimetry

DSC experiments were carried out on the heat-treated samples, using a heating rate of 1°C/min and in the temperature range of 30-300°C. A second DSC test was run on a pure aluminum sample with the same mass as the alloy sample, in order to obtain a baseline trace. The net DSC trace was obtained by subtracting the pure aluminum baseline data from the test data of the alloy sample. The DSC runs for each condition were repeated at least three times to confirm the test repeatability. In Chapter 4, all of the DSC traces were plotted with a y-axis shift so that all traces coincided at the third exothermic peak at ~200°C. The DSC traces of the alloy in the FAQ and DQ conditions in Chapter 4.2.2.2.1 were also corrected so that all traces coincide at the fourth exothermic peak at ~230°C.

3.3.3.2 Isothermal Calorimetry

For the IC runs, the SETARAM C80 calorimeter was first stabilized at the test temperatures. For each test, the sample pieces were dropped simultaneously into the test vessel 50 s after data acquisition started, while the reference vessel was kept empty. The IC tests were conducted at the temperature of interest until the heat flow was reduced to the approximate baseline level (*i.e.*, ~$(1.2 - 2) \times 10^{-4}$ W/g). An isothermal run was also performed at each test temperature on pure aluminum samples (*i.e.*, blank runs) with approximately equal mass to the alloy samples. Subtraction of the resultant data of the blank run from the data obtained from testing the alloy sample (test run) for each temperature yielded the net heat evolution data. The initial calorimeter disturbance, which is inherent in the sample drop procedure, requires the exclusion of the data acquired within the time range of 450-900 s. This correction is based on the methodology introduced by Esmaeili and Lloyd [25]. Multiple IC tests were conducted for each heat-treatment condition to establish reproducibility.

4. Experimental Analysis

In this section, the results of the investigation on the precipitation hardening behavior of the two AA7xxx alloys of this study are presented and discussed. The applied thermal processing histories for each section of this chapter are shown schematically in Figure 4-2.

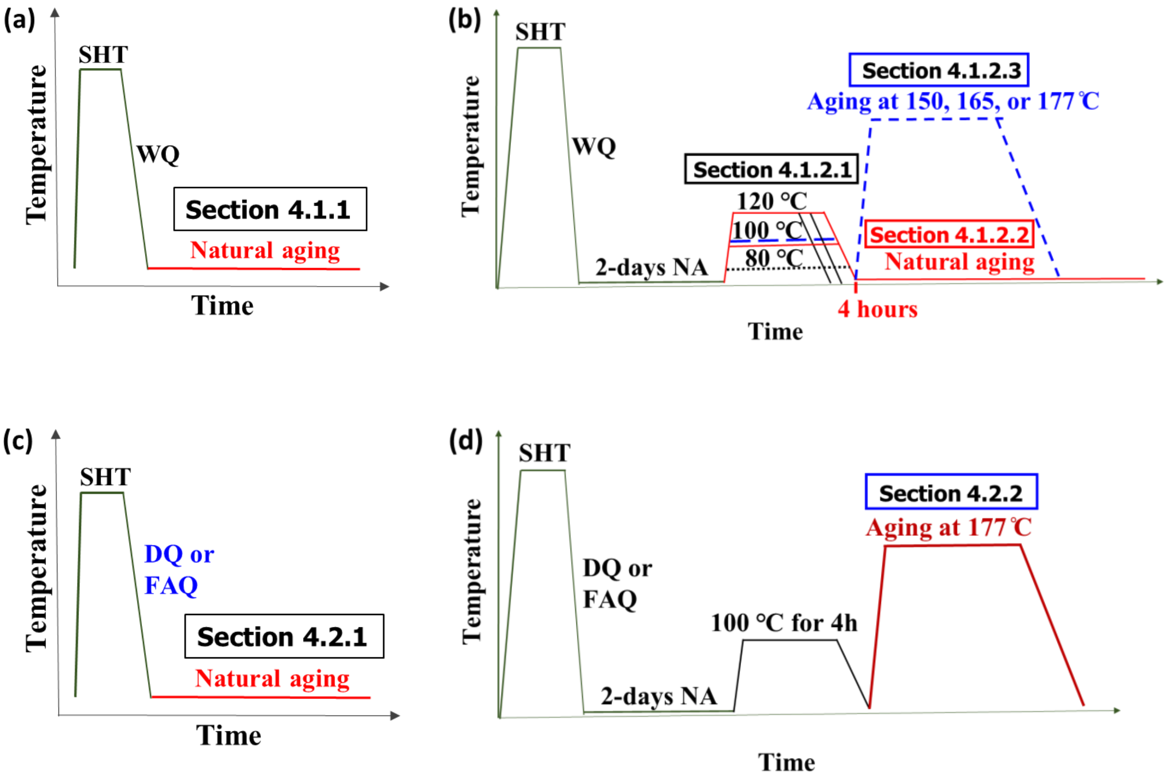

Figure 4-1 Schematic presentations of the thermal processing routes studied for the AA7075 alloy including: a) WQ + Natural Aging, b) WQ + Natural Aging + Pre-Aging + PBC, c) DQ or FAQ + Natural Aging, and d) DQ or FAQ + Natural Aging + Pre-Aging + PBC. .

4.1 Precipitation Hardening Behavior of the Water-Quenched Materials

In this section, precipitation hardening behavior during natural aging of AAA7xxx alloys (Section 4.1.1) and multi-step aging of AA7075 (Section 4.1.2) is presented. The natural aging behavior (Section 4.1.1) has been published in a journal paper [123].

4.1.1 Natural Aging of AA7xxx Alloys

4.1.1.1 Mechanical Testing

The strengthening behaviors of AA7075 and D-7xxx alloys are evaluated by analyzing the yield strength evolution with natural aging time. As Figure 4-2 (a) shows, the yield strength values for both alloys follow linear relationships with the logarithm of time beyond the earliest stage. The quick rise in yield strength during early-stage natural aging can be observed, that then trails off slowly as the natural aging time increases (*i.e.*, logarithmic trendline). This behavior is representative of natural aging in not only these AA7xxx alloys but also in AA6xxx alloys, as previously reported by Lloyd and Gupta [124] and Esmaeili and co-workers [113,125]. The observed trends in the natural aging rate reduction can be described based on consideration of the thermodynamics and kinetics of the decomposition of the supersaturated solid solution. The highest rate of solid solution decomposition occurs in the as-quenched condition of the alloy, the condition for which the alloy experiences the highest driving force for precipitation. As natural aging progresses, more of the excess solutes and vacancies are lost from the matrix, decreasing the driving force for precipitation and thus the rate of natural aging.

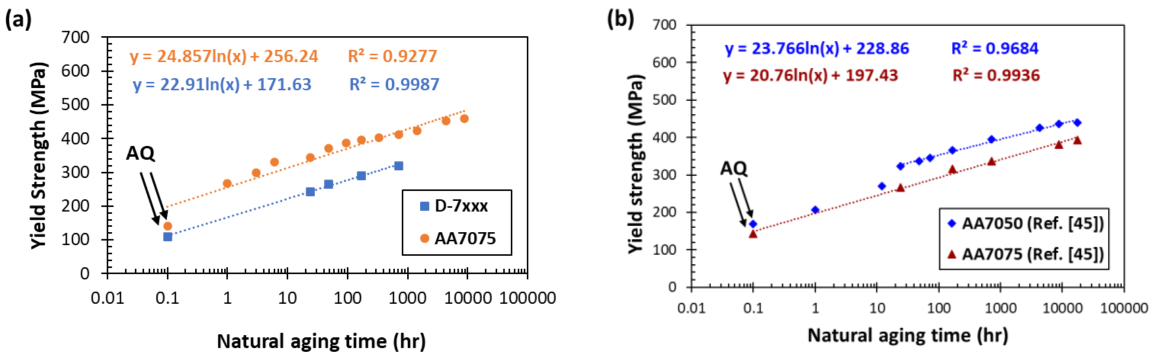

Figure 4-2 The evolution of yield strength during natural aging of (a) AA7075 (YS data for naturally-aged AA7075 has been calculated assuming YS= hardness×3) and D-7xxx (experimental results) and (b) AA7075 [45] and AA7050 alloys [45].

As suggested by their parallel strength-time trends shown in Figure 4-2 (a), the two alloys studied in this research, appear to have similar rates of natural aging beyond the earliest stage. Examining the yield strength data reported by Staley [69] (Figure 4-2 (b)), a similarity in the strength-time trends is revealed for on AA7050 and AA7075 alloys, as well. The parallel trends are proposed to stem from the compositional similarity of the alloys, particularly the proportional Zn, Mg, and Cu alloy content, and the potential presence of composition-dependent "quenching clusters", as previously suggested by Esmaeili and Lloyd [125] in explaining the similar natural aging trends in AA6xxx alloys. In AA7xxx alloys, copper has been reported to accelerate the rate of precipitation of GP zones and to increase their number density during low temperature (20-90°C) aging processes [43]. Accordingly, the parallel strength-time trend observed in Figure 1 can be rationalized based on the similarity in the copper content in the composition of the alloys investigated in Figure 4-2. This compositional similarity can result in similar driving forces for formation of natural aging precipitates and similar rates of precipitation during natural aging.

4.1.1.2 Differential Scanning Calorimetry Analysis

DSC experiments were performed on the AA7075 alloy to better understand the effect of the natural aging time on the precipitation (*i.e.*, exothermic) and dissolution (*i.e.*, endothermic) reactions. Figure 4-3 shows the results of the tests (*i.e.*, traces) for the as-quenched as well as naturally-aged samples.

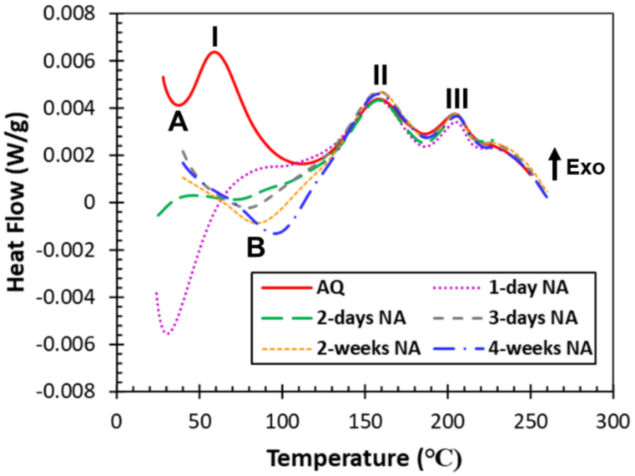

Figure 4-3 DSC traces of as-quenched and naturally-aged AA7075 for different times.

Considering the temperature range for the formation of GP zones during DSC [54,126], the first exothermic peak (*i.e.*, peak I) is associated with the precipitation of GP zones during the DSC test. The second and third exothermic peaks, II, and III are considered precipitation events associated with the formation of η' and η phases, respectively [54,126]. Figure 4-3 also highlights two endothermic events A and B, which are attributed to precipitate dissolution events [29]. The important observations from DSC traces in Figure 4-3 are as follows:

1. An increase in the magnitude of the endothermic heat associated with peak A is observed in the DSC trace of the 1-day naturally-aged sample, compared to that of the as-quenched (AQ) sample. Peak A disappears as the material is naturally-aged beyond 1-day.
2. The exothermic peak I is not present on the DSC traces of any of the naturally-aged alloy samples.
3. The traces for the samples naturally-aged for 3 days and beyond reveal the presence of a second endothermic event, *i.e.*, peak B, which occurs in the temperature range well above 50°C. By increasing the natural aging time peak B increases in magnitude and moves to higher temperatures.

The presence of event A on the DSC traces of the as-quenched (AQ) AA7075 and 1-day naturally-aged alloy suggests that the microstructure of these samples contains very fine primary precipitates that dissolve as soon as the DSC heating process starts. Such early-stage precipitates are suggested to be primary clusters or GP zones that form immediately after quenching (*i.e.*, the earliest stage of natural aging). The increase in the magnitude of the endothermic heat associated with peak A in the DSC trace of the 1-day naturally-aged sample, compared to that of the AQ sample, indicates that more of the “primary precipitates” form during the early stages of natural aging of this alloy. As the material is naturally-aged beyond 1-day, the endothermic event A disappears, suggesting that the stability of precipitates drastically increases beyond 1-day natural aging.

Reporting the DSC traces for as-quenched AA7020 and AA7150 alloys, Dupasquier *et al.* [34] and Ghosh and Gao [93] have related the endothermic peaks that appear at the lowest temperature ranges during ramp heating to the dissolution of small GP zones formed before the DSC scan. Their interpretation is consistent with the observation of peak A in the current DSC traces (Figure 4-3) suggesting the presence of primary precipitates that become thermodynamically unstable during the DSC scan. Evidence for the homogeneous formation of nano-sized precipitates prior to the start of natural aging, *i.e.*, during fast cooling, has also been reported in AA7449 [127]. Schloth *et al.* [127] have identified these early precipitates as quench-induced GP I zones with a smaller Guinier radius and volume fraction compared to GP I zones formed during natural aging. These independent observations all attest to the presence of "primary precipitates" which form during or immediately after quenching of AA7xxx alloys.

The absence of the first exothermic peak (Peak I) on the traces of all naturally-aged alloy samples is primarily due to the formation of natural aging precipitates (*i.e.*, solute clusters/GP zones) during natural aging. The overlapping effects with endothermic events, and/or the changes to the driving force for the formation of natural aging precipitates, associated with Peak I, can also promote the shift or disappearance of that peak on DSC traces of the samples naturally-aged for relatively short times.

Endothermic peak B, the magnitude of which increases with increasing natural aging time, appears to be equivalent to the endothermic event analyzed by Riontino and Massazza [128]. The increase in the magnitude of the endothermic event B with natural aging time is attributed to the increase in the volume fraction of natural aging precipitates (solute clusters/GP zones) and matches well with the strengthening observed in Figure 4-2 during natural aging of the alloys, and the analysis by Riontino and Massazza [128]. The absence of event B on the DSC traces of the samples naturally-aged for 1- and 2-days (Figure 4-3) might be due to the overlapping effect of this event with the small exothermic event around 80℃.

By increasing the natural aging time, endothermic event B moves to higher temperatures. This is commonly attributed to the increase in the temperature stability of the precipitates formed during natural aging with increased natural aging time. The increase in the temperature stability of these precipitates can also be due to a combination of factors such as changes in the size, chemistry, and structural evolution of precipitates during natural aging as well as the overlapping effect of the exothermic event B with the endothermic event I. The evolution of size and chemistry of these precipitates during natural aging will be discussed in section

4.1.1.3. On the basis of the observed trends in the evolution of the DSC peaks by increasing natural aging time (Figure 4-3), the overlapping effect of peaks B and I during natural aging of the alloy is schematically represented in Figure 4-4. This figure shows the deconvolution of DSC traces for transformation peaks I and B assuming that the start, peak, and finish temperatures for events I (*i.e.*, T_{SI}, T_{PI}, and T_{FI}) and B (*i.e.*, T_{SB}, T_{PB}, and T_{FB}) do not change by increasing natural aging time and $T_{PI} < T_{SB} < T_{FI}$. Note that the same increasing trend in the endothermic peak B would be observed in the event of other scenarios for the starting, peak, and finish temperatures for the events I and B (considering the overlapping stability ranges of different peaks). In the cumulative DSC curve shown in Figure 4-4, the temperature at which the exothermic event I and endothermic event B come together (*i.e.*, T_C) is assumed to be constant with an increase in the natural aging time. This trend is also observed in Figure 4-3 in which all of the DSC traces of the naturally-aged AA7075 alloy intersect at around 65℃ at which point heat flow is equal to zero. Figure 4-4 demonstrates that the endothermic peak B inevitably moves to higher temperatures by decreasing the magnitude of exothermic peak I and the concomitant increase in the magnitude of peak B. Therefore, the overlapping effect of these peaks can lead to the experimentally observed increase in the peak temperature of endothermic event B, by increasing the natural aging time.

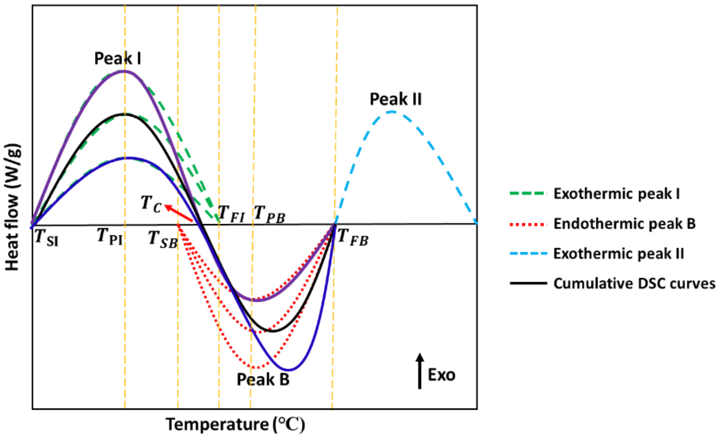

Figure 4-4 Schematic illustration showing the overlapping effects of exothermic and endothermic events on the resultant Peak B where T_{SB}>T_{PI} (T_{SB} is the starting temperature of endothermic event B, and T_{PI} is the temperature of peak I).

4.1.1.3 Atom Probe Tomography Analysis

To better understand the microscopic aspects of natural aging, particularly the evolution of size, number density, and chemistry of precipitates, APT analysis has been employed on AA7075 that was naturally-aged for 1-, 2-, 4-days, and 2-weeks.

4.1.1.3.1 General Findings

The microstructure of the 2-week naturally-aged sample is introduced here so that a broad picture of the multi-scale particle population is demonstrated. Zn-Mg precipitates with significantly different average size ranges (0.8±0.1 and 2.2±0.1 nm), and Cr-rich particles (approximate composition of $Al_{68}Mg_{15}Cr_9Zn_6Cu_2$, and 50-200 nm in size) are present in the microstructure of the naturally-aged alloy sample (Figure 4-5 (a)). A high number density of fine Zn-Mg precipitates, homogeneously distributed in the matrix, as well as less-common larger Zn-Mg precipitates, are notable in Figure 4-5 (a). The latter precipitates appear to be more heterogeneously-formed on the Cr-rich particles (see black arrows in Figure 4-5 (b)), although they are also observed in the matrix. It is well established that both homogeneously and heterogeneously distributed precipitates can form in the microstructure of the quench-sensitive AA7xxx alloys during quenching from high temperatures (*i.e.*, solutionizing temperature) [11,88,127,129–131]. Formation of precipitates on pre-existing second phase particles during quenching in AA7xxx alloys has been previously reported [43,132,133]. The incoherent Cr-rich particles (referred to as E phase [134] in the literature), due to their high interfacial energy, can act as preferential nucleation sites for Zn-Mg precipitates. The heterogeneous precipitation of large Zn-Mg particles on the Cr-rich particles causes the depletion of solutes in the adjacent matrix, resulting in the formation of an apparent precipitate-free zone (PFZ). Also, Cr-rich particles can act as vacancy sinks at their interface with the matrix during quenching, reducing the possibility of the formation of Zn-Mg precipitates in the vicinity (*i.e.*, PFZ). Due to the effect of these particles on the clustering and precipitation in their vicinity, the datasets including Cr-rich particles (*e.g.*, dataset in Figure 4-5) have not been used for clustering analysis and quantification purposes.

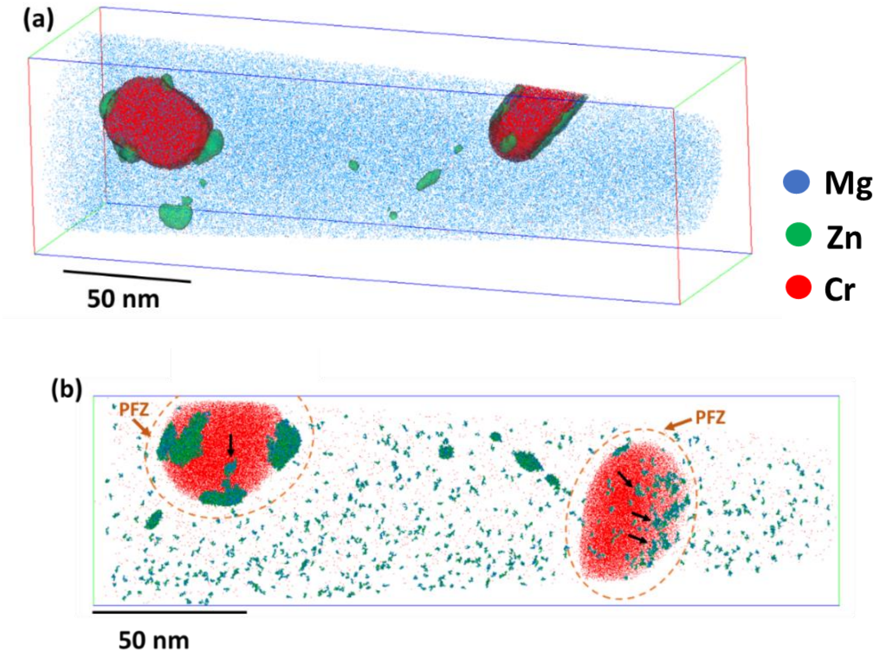

Figure 4-5 APT analysis results of 2-week naturally-aged AA7075 showing (a) Cr-rich particles and Zn-Mg precipitates highlighted by 2 at.% Cr and 10 at.% Zn iso-concentration surfaces, respectively (magnified 60×80×275 nm^3 volume) and (b) Zn-Mg precipitates and PFZs in the vicinity of the Cr-rich particles defined by cluster-search analyses.

APT atom maps representing the results of cluster search algorithm (*i.e.*, 3D reconstructions of Zn and Mg solutes in precipitates) for different natural aging times are presented in Figure 4-6. The aggregation of Zn and Mg atoms into fine Zn-Mg precipitates continues by increasing the natural aging time, as shown in Figure 4-6. The number density of fine Zn-Mg precipitates increases by increasing the natural aging time from 1-day to 2-weeks. Although both fine and large-type Zn-Mg precipitates are observed in the microstructure of the 1-day, 2-day, and 2-week naturally-aged samples, larger Zn-Mg precipitates are not observed in the atom map of the 4-day naturally-aged alloy, as seen in Figure 4-6 (c). AA7075 is a quench-sensitive alloy [11,88,90,135,136], for which a small change in the quenching conditions may entail changes in the formation of these quenching precipitates during cooling from high temperatures. Therefore, the lack of large-type Zn-Mg precipitates in the atom map of the 4-day naturally-aged sample can be related to the quench sensitivity of this alloy. The evolution of Zn-Mg precipitates with natural aging time is further analyzed in the following section.

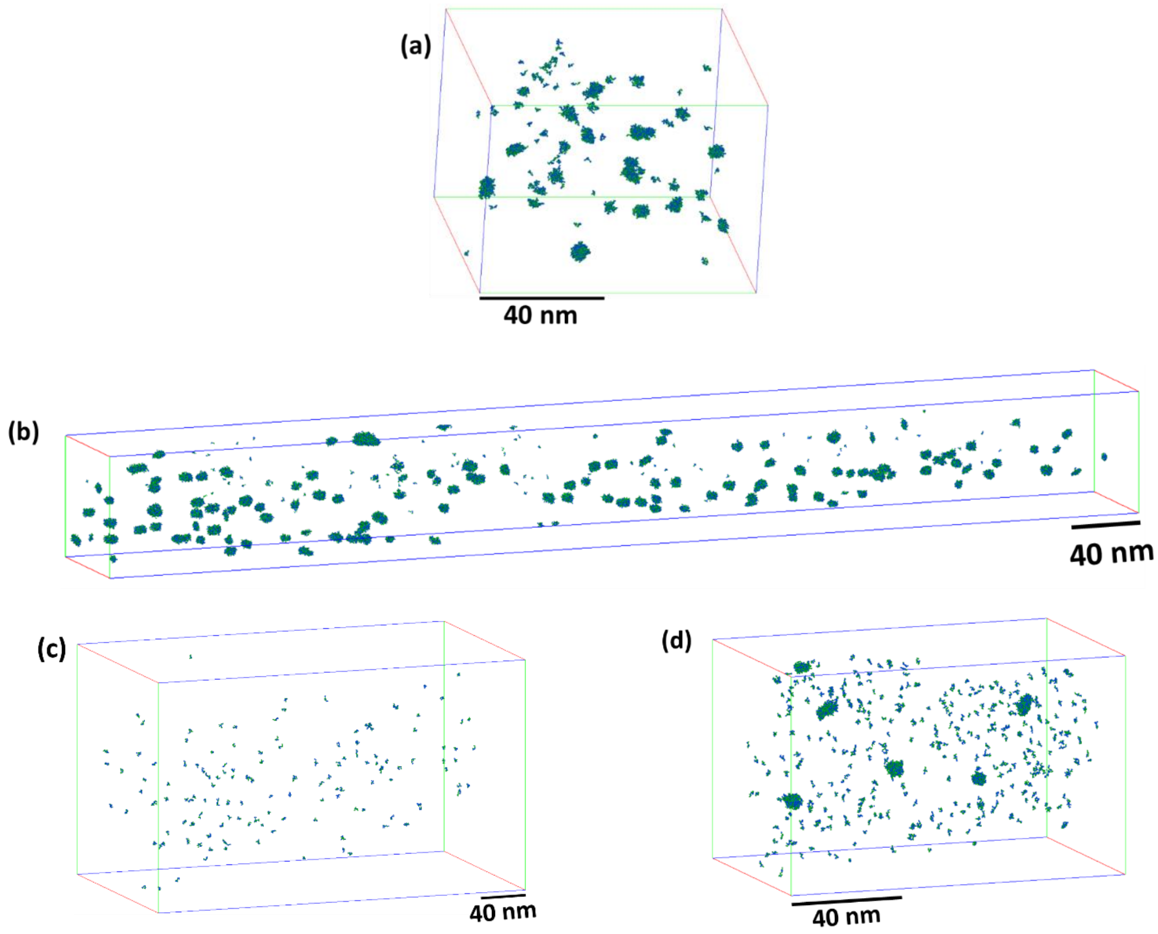

Figure 4-6 Reconstructed microstructure (cluster analysis) showing the 3D atom distribution of Zn-Mg clusters in AA7075 alloy naturally-aged for (a) 1-day, (b) 2-day, (c) 4-day and (d) 2-week.

4.1.1.3.2 Zn-Mg Precipitate Analysis

The size distribution of Zn-Mg precipitates for all four naturally-aged conditions is shown in Figure 4-7. It should be noted that the diameter of smaller precipitates, found by the cluster search algorithm, was defined as twice the average radius of gyration, defined by the ranged ions detected within the cluster. The bi-modal size distribution of Zn-Mg precipitates is evident in Figure 4-7 (b). In Figure 4-7 (a), (c) and (d), one clear peak can be seen at a diameter of approximately 0.8 nm. The presence of numerous precipitates with a diameter of 1.2 nm < d < 3 nm, beyond the main peak in Figure 4-7 (a), and (d), is indicative of the bimodal distribution of precipitates in these naturally-aged conditions (as in the case of 2-day NA condition). No bimodal size distribution is observed in the APT results of 4-day naturally-aged alloy (Figure 4-7 (c)), due to the absence of larger size Zn-Mg particles (as seen in Figure 4-6 (c)). As seen in Figure 4-7 (b), the two peaks overlap in a size range of 1.2-1.6 nm. The lowest limit of this overlap range (1.2 nm) is the largest size of precipitates in 4-day naturally-aged alloy (Figure 4-7 (c)). Therefore, this boundary is selected as the threshold from fine (F) to large (L) Zn-Mg precipitates.

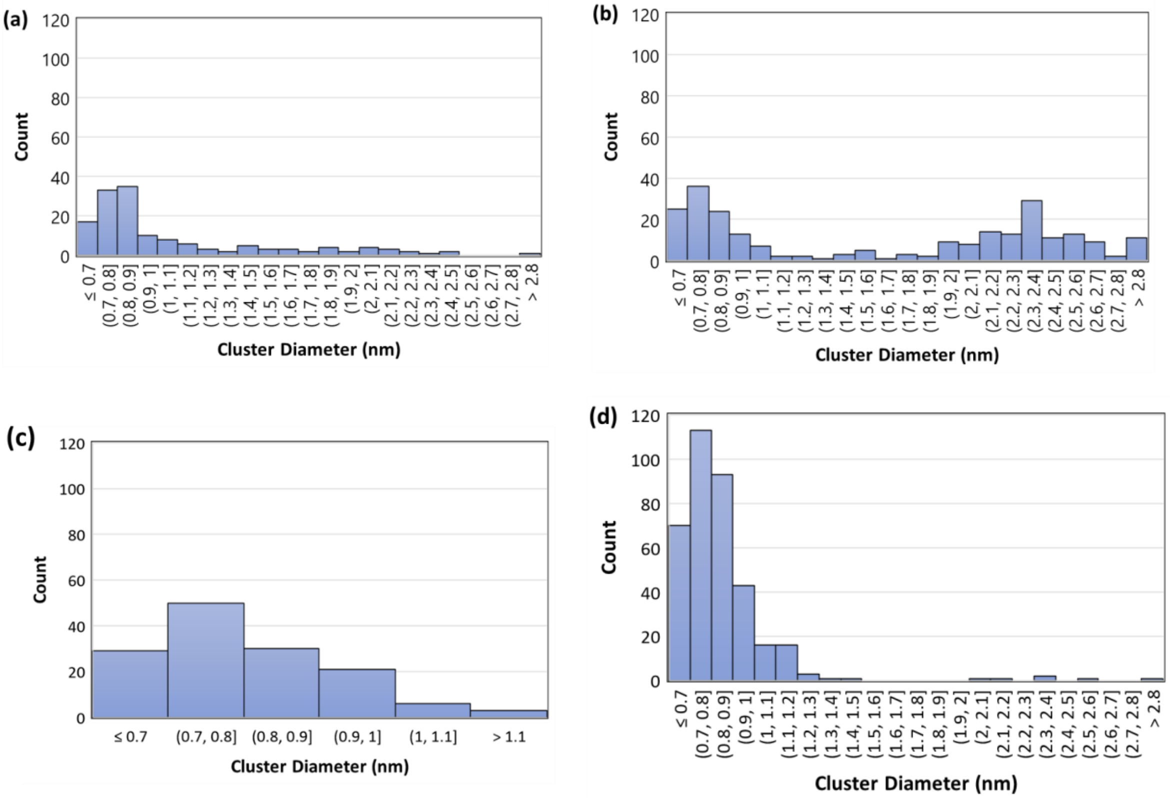

Figure 4-7 Precipitates size distribution in the (a) 1-day, (b) 2-day, (c) 4-day and (d) 2-week naturally-aged AA7075.

The statistical analysis of APT data also reveals the presence of two size ranges of Zn-Mg precipitates within the matrix of 2-day and 2-week naturally aged samples. To investigate the trends of solute segregation, the first approach taken is to analyze the nearest-neighbor (NN) distribution of solutes [117]. Figure 4-8 shows the 10th nearest-neighbor (10NN) distributions data for different phases present in the microstructures of 2-day and 2-week NA samples (Figure 4-8 (a) and (b)), as well as the superposition of all these distributions in 2-day and 2-

week NA datasets (Figure 4-8 (c)). It should be noted that in Figure 4-8 (c) the overall 10NN distribution heights are normalized based on total solutes.

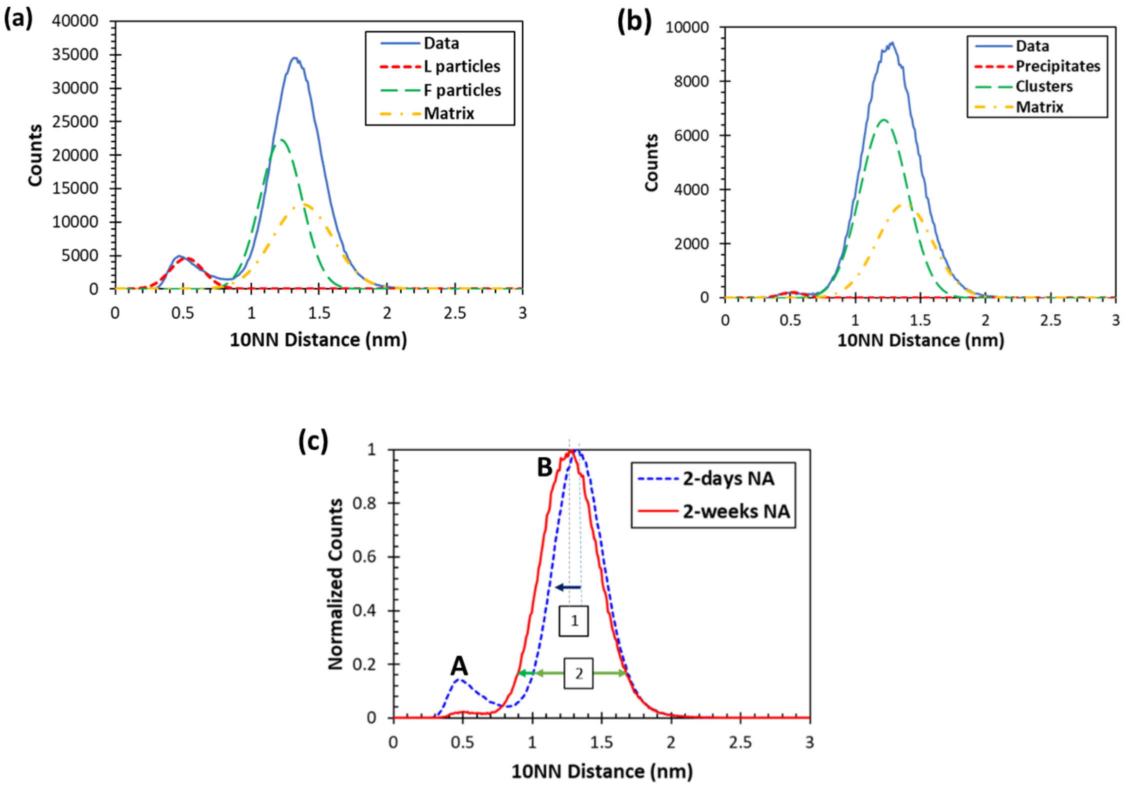

Figure 4-8 Distribution of the 10th nearest neighbour distance for (a) different phases in 2-day NA alloy, (b) different phases in 2-week NA alloy and (c) Zn+Mg solutes in 2-day and 2-week NA dataset.

The bimodal nature of the 10NN distribution in Figure 4-8 (c) and the evolution of peak B by increasing natural aging time reveal the presence of two size range of particles in the microstructures of 2-day and 2-week NA alloy. Peak A, in Figure 4-8 (c), is due to the L particles and the identical distribution distance of this peak in both naturally aged conditions indicates that the concentration of these particles does not change after two weeks of natural aging. The main observations that can be drawn from the shape of peak B in Figure 4-8 (c) are: (1) a shift of the peak to shorter distribution distances and (2) a broadening of the distribution, with increasing natural aging time. Both phenomena are caused by solute ordering within the matrix due to the increase in the number density of F particles in the alloy by increasing the natural aging time.

The quantitative information about F and L particles for the four natural aging conditions is given in Table 4-1 and Table 4-2. The average sizes of F and L precipitates are about 0.8 nm and 2.3 nm, respectively, and do not change significantly with increasing natural aging time up to two weeks, as reported in Table 4-1 and Table 4-2.

4.1.1.3.2.1 L particles

The chemical composition of L particles is investigated for the 1-day, 2-day, and 2-week naturally-aged samples by the results of the proximity histograms (proxigrams) [137]. The proxigrams in Figure 4-9 (a), (b), and (c) demonstrate significant Zn and Mg segregation within the L particles, whereas the copper content of these particles is very small. Note that the zero distance in the proxigrams represents the particle interface (defined by the 6 at.% Zn isosurface) and the positive values (upper bounds) represent the interior of a precipitate. Due to the small size and evaporation field of L particles (which is lower than the surrounding Al matrix), it is believed that the high Al content detected within the particles in the proxigrams (Figure 4-9) is an artifact of the evaporation process. The chemistry of these particles (*i.e.*, the ratio of solutes, excluding Al) for different natural aging conditions is reported in Table 4-1. According to the literature, the diameter of the GP zones has been reported to range from about 1 to 6 nm [35,138,139] with a Zn:Mg ratio ranging from 1 to 1.4 in different Al-Zn-Mg-(Cu) alloys under various aging conditions [27,46,140–142]. Considering the size range and chemistry of the L particles (as listed in Table 4-1), these precipitates are regarded as GP zones. The chemistry data reported in Table 3 as well as the narrow composition distribution for L particles observed in Figure 4-9 (d) indicate that the composition of these particles does not change significantly during this duration of natural aging.

Table 4-1 Average size, chemistry, and number density of L particles in the microstructure of AA7075 naturally-aged for different times measured via APT.

Natural aging time	Chemistry of the average size particle (Mean Zn: Mg solute ratio)	Number density (clusters / nm3)	Average size (nm)
1-day	1.2±0.3	0.5×10^{-4}	2.2±0.1
2-day	1.2±0.3	0.8×10^{-4}	2.3±0.1
4-day	-	-	-
2-week	1.2±0.3	0.1×10^{-4}	2.3±0.1

As shown in Table 4-1, the evolution of number density of L particles with natural aging time does not follow an increasing (or decreasing) trend. It should be noted that the reported number densities of both F and L particles for the alloy in 1-day NA condition are the weighted average of three datasets (since the acquired data in each dataset was smaller than that for other natural aging conditions) obtained from three different samples (each solutionizied and quenched separately). The result of the APT analyses for the 1-day NA samples also shows the presence of different number densities of L particles in each case. These observations suggest that L particles form during quenching and their formation is highly dependent on the minor variation in the quenching condition (*i.e.*, the quench rate). The higher yield strength of AA7075 in the as-quenched condition, compared to the D-7xxx alloy, can be attributed to the presence of these quenching precipitates (L particles) in the AA7075 microstructure.

The observation of the constant size of the L particles during natural aging, as well as the insignificant change in their composition (in contrast to the wide range of composition distribution for F particles as presented in the next section), further suggests that the L particles are precipitates that form during quenching. Therefore, they do not evolve during aging at low temperatures (*e.g.*, natural aging). Gerlach and Löffler [143] have also reported that the size of GP zones does not remarkably increase during aging of an Al-Zn-Mg alloy at low temperatures (<70 °C). The insignificant change in the size of L particles can stem from the very slow growth rate of these precipitates during natural aging when the diffusion rate of solutes is low.

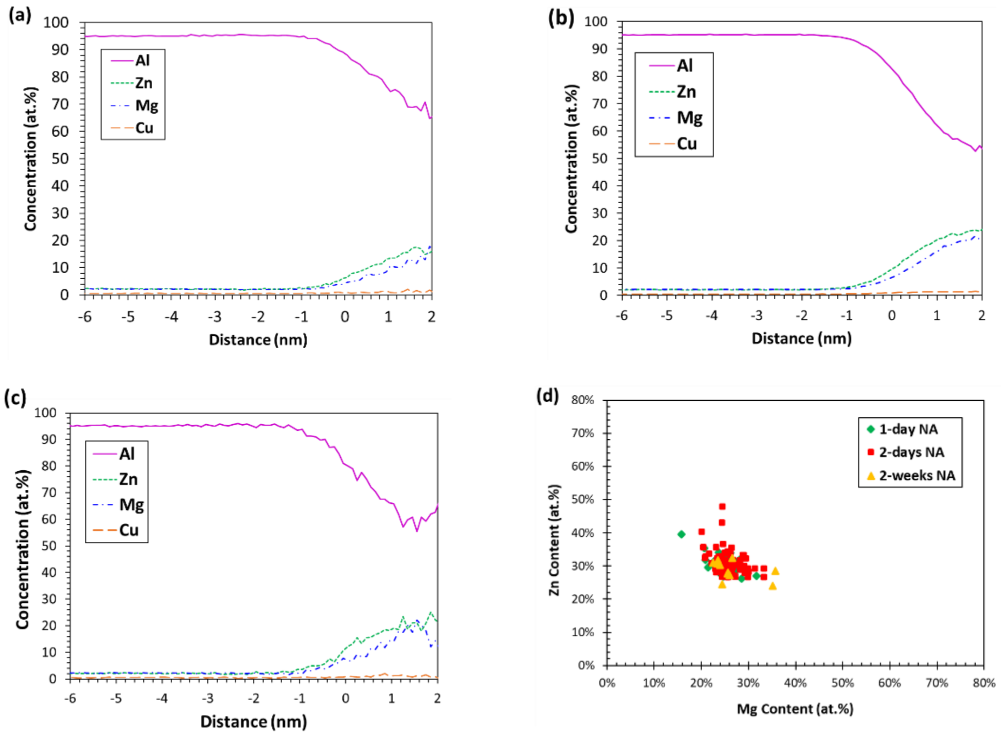

Figure 4-9 Proxigrams of L particles in (a) 1-day, (b) 2-day, and (c) 2-week naturally-aged alloy, taken from the averaged total across all precipitates, yielding 1D concentration profiles normal to the particle interface and (d) the distribution of composition of L particles in 1-, 2-day, and 2-week naturally-aged AA7075.

4.1.1.3.2.2 F particles

The evolution of the chemical composition of the F particles during natural aging (*i.e.*, atomic ratios of Zn vs. Mg) is analyzed using the composition distribution charts, as shown in Figure 4-10. A wide range of Zn:Mg ratios for these particles can be seen in the microstructure of the alloy for the natural aging conditions shown in Figure 4-10 (a) and (b). The highest population of F particles has a Zn:Mg atomic ratio in a range of 0.8 to 1.2 in the microstructure of the alloy in both 1-day and 2-weeks natural aging conditions. The distribution data charts for Zn:Mg solute ratios of F particles, *i.e.*, APT datasets in Figure 4-10 (a), and (b), as well as the APT datasets for the other two natural aging conditions, are then used to obtain Figure 4-10 (c). This figure shows the distribution of Zn vs. Mg content in F particles in comparison with that for the L particles (Figure 4-9 (d)). There is a wide distribution of composition for F particles, influenced by the greater degree of variation in APT measurement that comes with lower total solute counts per cluster, as well as a limited detection efficiency (*i.e.*, approximately 0.36 in this case). This high degree of variability leaves significant uncertainty in determining a mean solute ratio for these particles and raises a question as to how representative it may be of their true chemistry. Any change in the chemistry for F particles with increasing natural aging time is not significant enough, relative to the measurement uncertainty, to be reflected in the solute ratio distributions, as seen in Figure 4-10 (c). This is also consistent with previous observation of a very slow rate of compositional change in the natural aging precipitates during natural aging of an Al-Zn-Mg alloy, where a Zn:Mg ratio convergence was obtained after 3-months of natural aging [46]. The wide range of composition distribution of F particles for all the natural aging conditions (Figure 4-10 (c)) is also consistent with nucleation of F particles and the evolution of their chemical composition being an ongoing process within 2-weeks of natural aging.

Table 4-2 Average size, chemistry, and number density of F particles in the microstructure of AA7075 naturally-aged for different times measured via APT.

Natural aging time	Chemistry of the average size particle (Zn: Mg solute ratio range)	Number density (clusters / nm3)	Average size (nm)
1-day	0.15-3	1.6 $\times 10^{-4}$	0.8±0.1
2-day	0.16-2.1	6.6 $\times 10^{-5}$	0.8±0.1
4-day	0.18-3.3	1.3 $\times 10^{-4}$	0.8±0.1
2-week	0.08-4	7.5 $\times 10^{-4}$	0.8±0.1

The number densities of F particles for all four natural-aging conditions have been determined and reported in Table 4-2. The results show that for 1-day naturally-aged sample, the estimated number density of F particles is slightly higher than those for the 2- and 4-day naturally-aged conditions. This observation implies the presence of primary precipitates in the microstructure of 1-day naturally-aged alloy as suggested by peak A in the DSC trace of 1-day naturally-aged alloy (Figure 4-3). Primary precipitates are regarded as fine F particles (*i.e.*, Zn-Mg particles with a diameter of $<$0.7 nm in Figure 4-7). The observed increase followed by a decrease in the number density of F particles has been similarly reported for the evolution of number density of Mg-Si clusters during natural aging of Al-Mg-Si alloys where the subsequent decrease in the number density of clusters has been ascribed to the dissolution of early-stage clusters upon further natural aging [144]. As natural aging evolves, the number density of F particles increases more than one order of magnitude with increasing the natural aging time from 2 days to 2 weeks (see Table 4-2). This is consistent with the observed increase in the magnitude of peak B in the DSC traces of the naturally-aged alloy (Figure 4-3). Considering the size and chemistry of F particles in the current APT results, the natural aging precipitates are categorized as F particles, observed in the microstructure of naturally-aged AA7075 alloy.

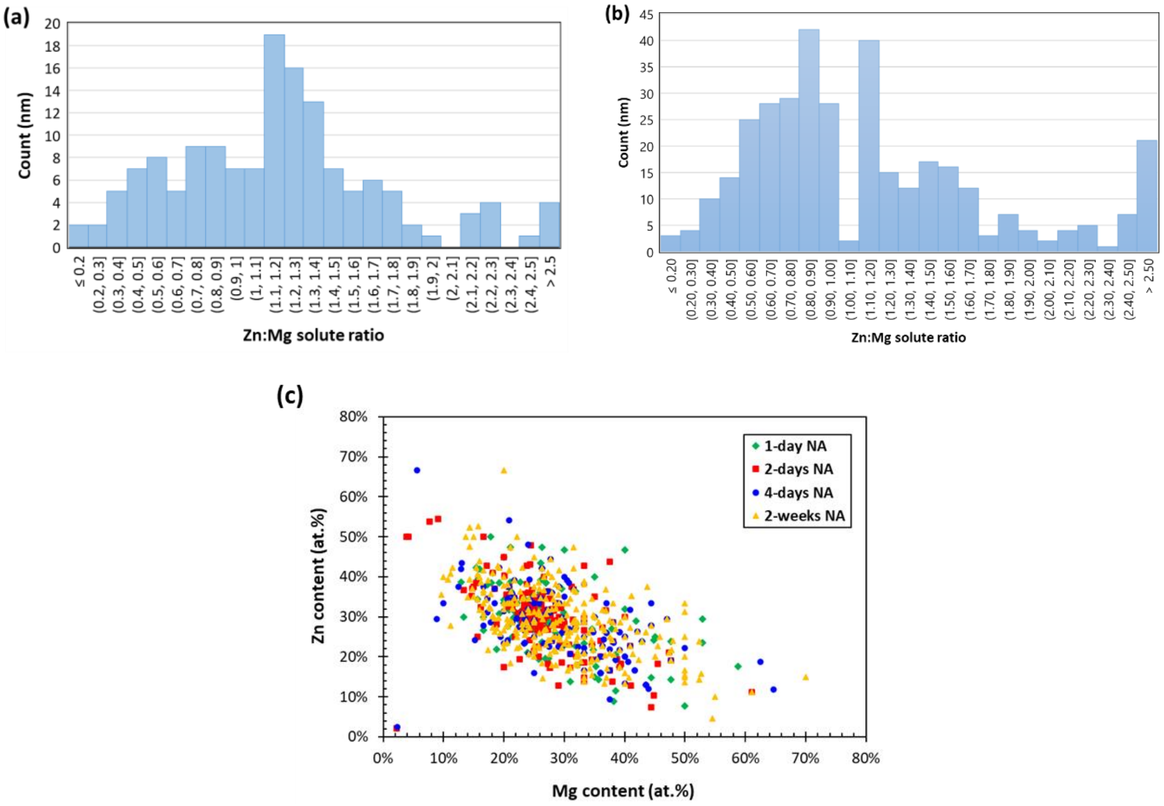

Figure 4-10 The distribution of atomic ratios of F particles in (a) 1-day, and (b) 2-week naturally-aged alloy and (c) the distribution of composition of F particles in 1-, 2-, 4-day, and 2-week naturally-aged AA7075.

The average size of the natural aging precipitates (*i.e.*, F particles) does not evolve significantly during natural aging of AA7075 up to 2 weeks, as listed in Table 4-2. Further diffusion of Zn and Mg atoms is needed for the growth of natural aging precipitates during natural aging of AA7xxx alloys. The lower migration energy of Zn compared to that of Mg [46] can cause the very slow growth rate of natural aging precipitates during natural aging of these alloys. Considering the observed trend in the number density as well as the insignificant size evolution of the natural aging precipitates, it is concluded that the formation of these precipitates should be mainly in the nucleation regime during natural aging up to two weeks.

4.1.2 Multi-Step Aging of AA7075 Alloy

In this section precipitation hardening behavior during (a) artificial aging of naturally-aged (Section 4.1.2.1), (b) secondary natural aging of pre-aged (Section 4.1.2.2), and (c) artificial aging of pre-aged (Section 4.1.2.3) AA7075 alloy is presented.

4.1.2.1 Pre-Aging Treatments of AA7075

4.1.2.1.1 Hardening Response

Microhardness measurements were conducted on samples that had been naturally aged for two days (2NA) after undergoing artificial aging at three different temperatures. This was done to better understand the effect of different intermediate-temperature aging treatments on the hardening behavior. Figure 4-11 shows that the hardness of the 2NA samples increased with increasing the artificial aging time and temperature. It has been reported that natural aging precipitates (clusters/GP I zones) formed during room-temperature pre-aging can act as precursors of the next precipitates (*i.e.*, GP zones and η') during subsequent artificial aging treatments (*i.e.*, the intermediate-temperature aging treatments in this study), and the formation of η' is facilitated by the heterogeneous nucleation of these precipitates [145]. As seen in Figure 4-11, the increase in hardness is more significant with aging of the 2NA samples at 120°C. The higher increase in hardness during aging at 120°C is attributed to the formation of η' precipitates in the microstructure of the PA120 alloy. On the other hand, GP zones are identified as the dominant precipitates in the microstructure of the PA100 sample after 4 hours of aging, as reported in the TEM results in Section 4.2.2.2.3. Likewise, previous studies have reported that the microstructure of the AA7075 alloy artificially aged at 120°C for 2 hours, contains significant amounts of the η' precipitates [76]. The results of the hardness measurements in this section have been further used for modeling validation purposes in Section 5.1.2.1.

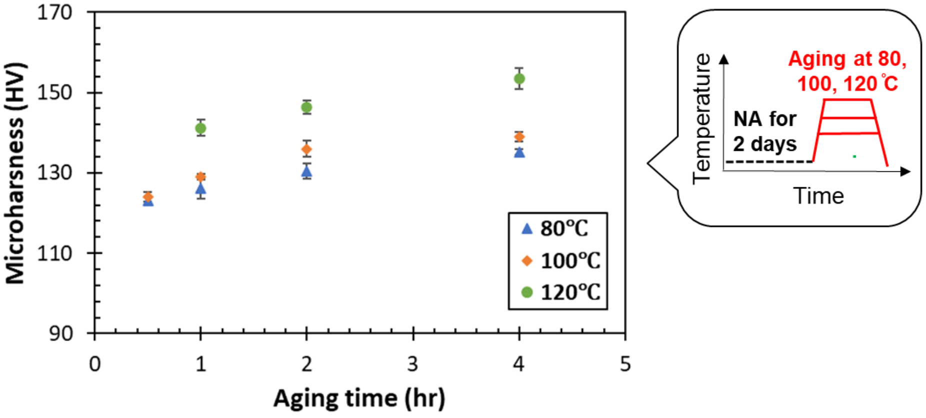

Figure 4-11 Measured evolution of hardness during aging of water-quenched and 2-day naturally aged AA7075 samples at 80, 100, and 120°C.

4.1.2.1.2 Isothermal Calorimetry

The objective of the IC tests was to study the evolution of the relative volume fraction of precipitates during aging, through which the yield strength values of the aged material could be estimated. To calculate the relative volume fraction of precipitates at the end of the intermediate temperature aging treatments (f_r^0), IC results for the two-step isothermal aging associated with pre-aging, as well as the aging of the as-WQ material at 177°C, are required. The IC result of the first aging step, which shows the aging history of the samples before the intermediate aging step, is shown in Figure 4-12 (a). The result of the IC test on the as-quenched sample at 177°C is shown in Figure 4-12 (b).

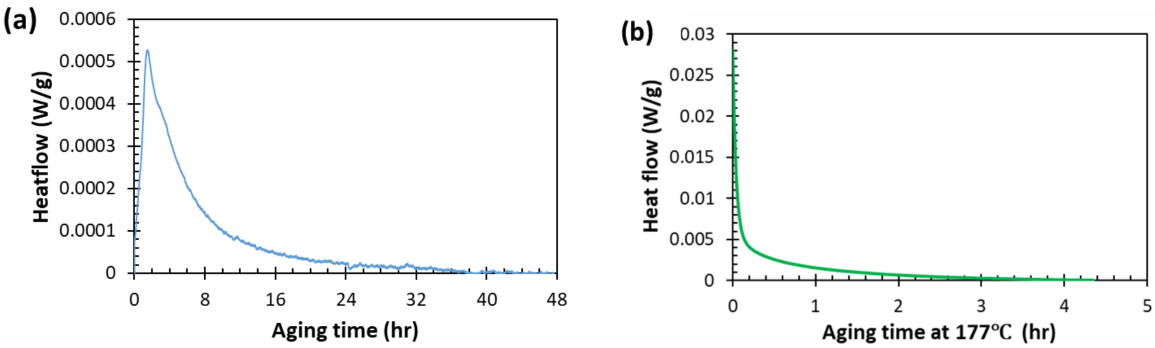

Figure 4-12 Isothermal calorimetry traces of AA7075-WQ alloy (a) aged at room temperature for 48h (b) during aging at 177°C.

IC tests were conducted at three different temperatures on the 2-day naturally aged AA7075 samples. The results of these tests are shown in Figure 4-13 (b). The IC traces in Figure 4-13 show an exothermic heat flow that rapidly increases to a maximum level and then drops back to the baseline level.

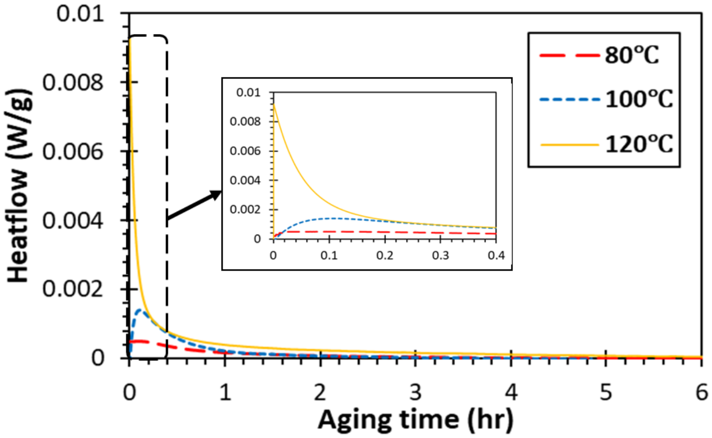

Figure 4-13 Isothermal calorimetry traces of AA7075-WQ alloy after 2-days of NA at three different temperatures.

The calculated areas under the IC traces (Figure 4-13), which represent the total heat evolved after a certain aging time at the aging temperatures due to precipitation reactions, are tabulated in Table 4-3.

Table 4-3 The evolution of total heat for AA7075 after 2-days natural aging at different temperatures.

Aging temperature (°C)	Total heat effect after aging at different times (*J/g*)				
	0.5 h	1 h	2 h	4 h	6h
80	0.4	0.8	1.3	2.1	2.5
100	0.7	1.6	2.3	2.9	-
120	3.1	3.9	4.7	6	7.2

The total area under the IC traces of the as-quenched material and during the first step of aging has been calculated for the AA7075 alloy, and the results are presented in Table 4-4.

Table 4-4 The total heat evolved during aging treatments of AA7075.

Heat treatment	Total heat effect (*J/g*)
As-quenched aged at 177℃	20.9 (±0.5)
1st step	8.7 (±0.8)

4.1.2.1.3. Estimation of the Relative Volume Fraction of Precipitates

The total volume fraction of precipitates at the end of the intermediate temperature aging (*i.e.*, after the 2-step pre-aging treatments), $f_v|_{PA}$, can be expressed as:

$$f_v|_{PA} = f_v|_{step\ 1} + f_v|_{step\ 2} \qquad \textbf{Eq. 4-1}$$

To estimate the total relative volume fraction of precipitates in pre-aged samples, f_r^0, Eq. 4-1 is divided by the fraction of precipitates at the peak-aged condition, *i.e.*, f_{peak}. f_r^0 is then formulated as:

$$f_r^0 = \frac{f_v|_{step\ 1} + f_v|_{step\ 2}}{f_{peak}} \qquad \textbf{Eq. 4-2}$$

where $f_r^0 = \frac{f_v|_{PA}}{f_{peak}}$.

<u>Analyses of the Calorimetry Results</u>

The evolution of the relative volume fraction of precipitates during aging treatments of interest is quantified using calorimetry results and the analytical methodology developed by Esmaeili *et al.* [98,146,147]. To analyze and model the evolution of f_r during the aging treatments of heat-treated material in under-aged conditions, it is assumed that the precipitation process is complete at the peak-age condition, *i.e.,* f_r=1 when t=t_{peak} [146].

According to the general methodology [146], the area under the IC trace at aging time *t* divided by the total area under the IC trace will provide f_r as a function of the aging time:

$$f_r = \frac{\int_0^t \frac{dQ}{dt}dt}{\int_0^{t_{peak}} \frac{dQ}{dt}dt} \qquad \textbf{Eq. 4-3}$$

According to Eq. 4-2, f_r^0 can be obtained by calculating the fraction of the total heat evolution due to precipitation during the first two steps of aging (pre-aging) in a 3-step aging route. f_{peak} can be found from isothermal calorimetry experiments at the artificial aging temperature of interest (*i.e.*, the aging temperature of the third step) on as-quenched material. Hence:

$$f_r^0 = \frac{\int_0^{t_{s1}} \frac{dQ}{dt} dt|_{step\ 1} + \int_0^{t_{s2}} \frac{dQ}{dt} dt|_{step\ 2}}{\int_0^{t_{peak}} \frac{dQ}{dt} dt|_{AQ+AA}} \qquad \textbf{Eq. 4-4}$$

Using the heat flow values reported in Table 4-3 and Table 4-4 in Eq. 4-4, the evolution of f_r^0 after certain aging times at temperatures of 80, 100, and 120°C is quantified for the AA7075 alloy, as shown in Figure 4.14.

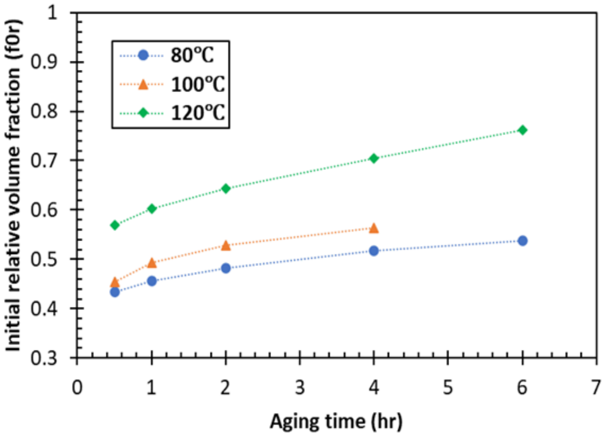

Figure 4.14 Predicted relative volume fraction of precipitates after aging at particular times and temperatures based on IC measurements.

4.1.2.1.4 Calculation of Yield Strength

The main objective of this section is to estimate the yield strength values of the AA7075 alloy in pre-aged conditions. For this purpose, first, the values of f_r^0 (the relative volume fraction of precipitates after pre-aging treatment) for the pre-aged samples are determined through the experimental analysis of IC tests, as described in the previous section. Then, the yield strength values for the pre-aged samples are calculated using the experimentally obtained f_r^0 values and the yield strength modeling formulations. The modeling framework is the approach developed by Esmaeili *et al*. [105], and the equations applied for this purpose are reported in the chart shown in Figure 4-15. To calculate σ_{ppt} for a pre-aged material (in an underaged condition), it is assumed that precipitates act as weak shearable obstacles, and thus, the modified-weak obstacle modeling equation has been used. This is also in accordance with the initial assumption for using the modified-weak obstacle model, in which the concurrent nucleation and growth of precipitates are considered to be the precipitation mechanisms that occur during the investigated aging times and temperatures.

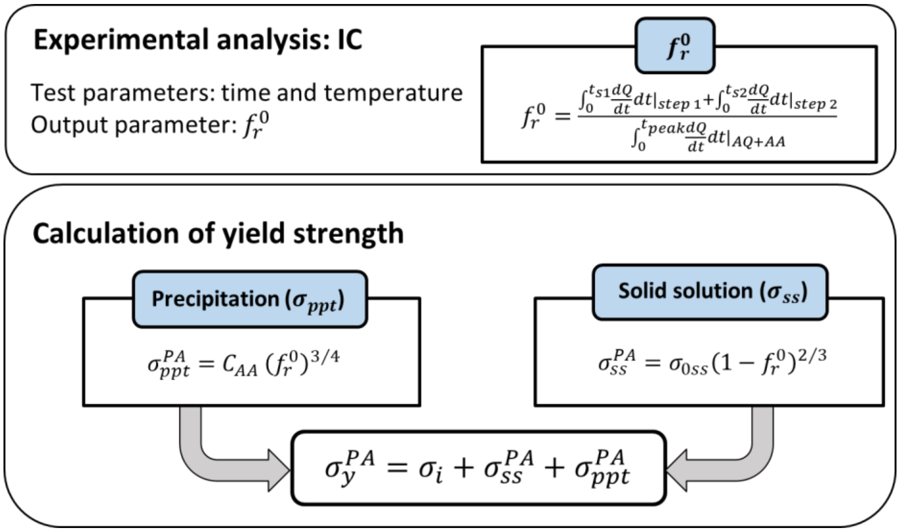

Figure 4-15 Schematic outline of the calculation of yield strength for pre-aged materials (PA=Pre-Aged).

The calibration parameters are listed in Table 4-5. The values of the relative volume fraction of precipitates for pre-aged conditions, shown in Figure 4.14, are then used to calculate σ_{ss} and σ_{ppt}, as outlined in Figure 4-15. The yield strength values during the second step of aging at different aging temperatures and times for the AA7075 alloy are then estimated using the equation for σ_y, listed in Figure 4-15.

Table 4-5 Input parameters for modeling of the yield strength of AA7075 after pre-aging treatments.

Parameter	Value	Remarks
σ_i(MPa)	10	From Ref. [97]
C_{AA} (MPa)	488	Obtained from experiments (Ref. [123])
σ_{0ss}(MPa)	130	Obtained from experiments (Ref. [123])

The results of the yield strength model predictions are compared with the experimental values for artificial aging at three different temperatures for the 2-day naturally aged AA7075 in Figure 4-16. It is evident that the model provides excellent predictions for the investigated aging times, with a difference of up to 11%. The obtained f_r^0 values can be further used as input for modeling the evolution of microstructure and yield strength during artificial aging treatments of the pre-aged AA7075 (reported in Section 5.1.2.2).

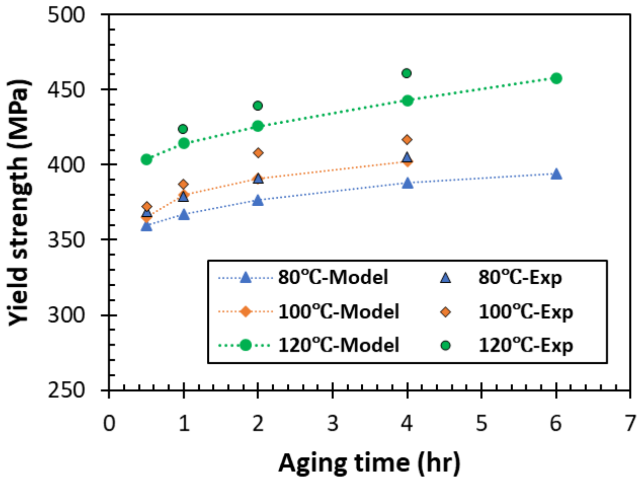

Figure 4-16 Comparison of the modeling predicted yield strength to the measurements after the second aging step at three different temperatures.

4.1.2.2 Secondary Natural Aging of Pre-Aged AA7075

4.1.2.2.1 Hardening Response

The evolution of hardness during the natural aging of AA7075 alloy with different pre-aging histories (secondary natural aging) is shown in Figure 4-17. It appears that a linear logarithmic trend, as also found for the natural aging of AA7xxx alloys [123], holds for the natural aging that follows pre-aging treatments of AA7075. However, the rate of hardness increase is lower for the pre-aged materials compared to materials without pre-aging (Section 4.1.1.1). This reduction in the rate is more significant when pre-aging includes intermediate aging at 120°C for 4 hours. The increase in hardness of the PA material (2-day NA+4h at 100°C) is more significant during natural aging for up to 14 days compared to the later stage of aging (up to 365 days). However, the hardness of the alloy in the PA120-4 condition, however, does not change significantly at room temperature during the investigated time period. This increase in the stability of the AA7075 alloy at room temperature is attributed to the reduction in supersaturation caused by the formation of precipitates (GP zones and η') during pre-aging. The DSC results reported in Section 4.1.2.2.2 further support this finding. In addition, the TEM results reported in Section 4.2.2.1.2.2, show that GP zones are the main precipitates in the microstructure of the alloy in the PA condition, while η' precipitates have been reported to form at intermediate temperatures of typically 120°C-180°C [25,56]. The above results are in agreement with the findings of Wan *et al.* [77] who reported that the hardness of the pre-aged AA7003 samples, which are strengthened by η' precipitates and their precursors, does not change significantly during subsequent natural aging.

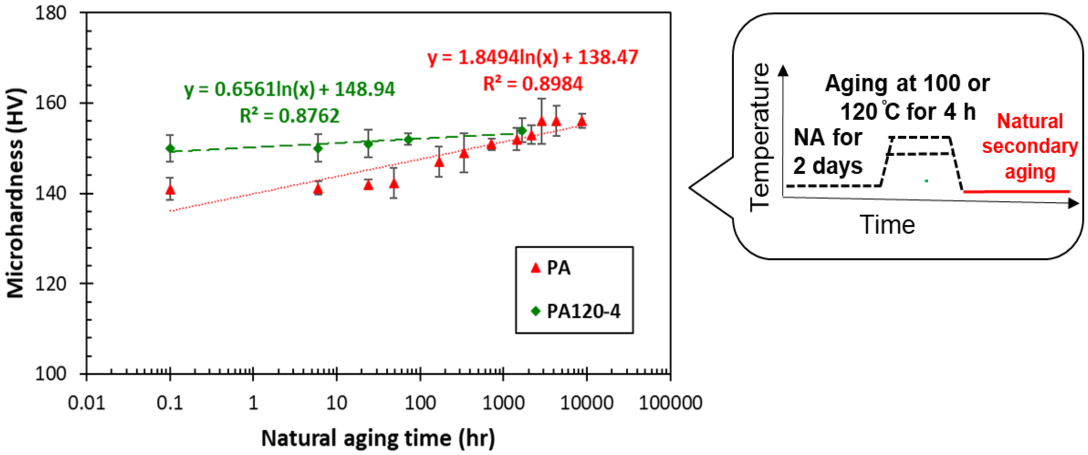

Figure 4-17 Measured microhardness changes over time showing the kinetics of the natural aging of AA7075 alloy in the PA (2-days NA+4h at 100ºC) and PA120-4 (2-day naturally aged+4h at 120ºC) conditions.

4.1.2.2.2 Differential Scanning Calorimetry Results for Secondary Natural Aging of Pre-Aged AA7075

To investigate the evolution behavior of precipitates during the non-isothermal heating of PA and PA120-4, DSC experiments were conducted on AA7075 samples that were held at room temperature for different times. The corresponding DSC thermograms are shown in Figure 4-18. Peaks I, II, and III are similar to the peaks observed in the DSC traces of the as-quenched and naturally aged materials, as reported in Section 4.1.1.2. Peak I, observed in the range of 50-80°C, decreases in magnitude as the natural aging time increases up to 2 weeks after pre-aging at 100°C. In other words, after two weeks of natural aging, the PA sample shows a reduced capacity for GP zone formation during DSC. The samples that were naturally aged for 2 and 4 weeks after the PA treatment have similar DSC traces. This observation is consistent with the hardness data in Figure 4-17, which indicates that the hardness of the PA sample does not significantly increase when the natural aging time is increased from 2 to 4 weeks. It should be noted that the changes in the second and third peaks (peaks II and III) due to natural aging after pre-aging are not significant, as seen in Figure 4-18 (a).

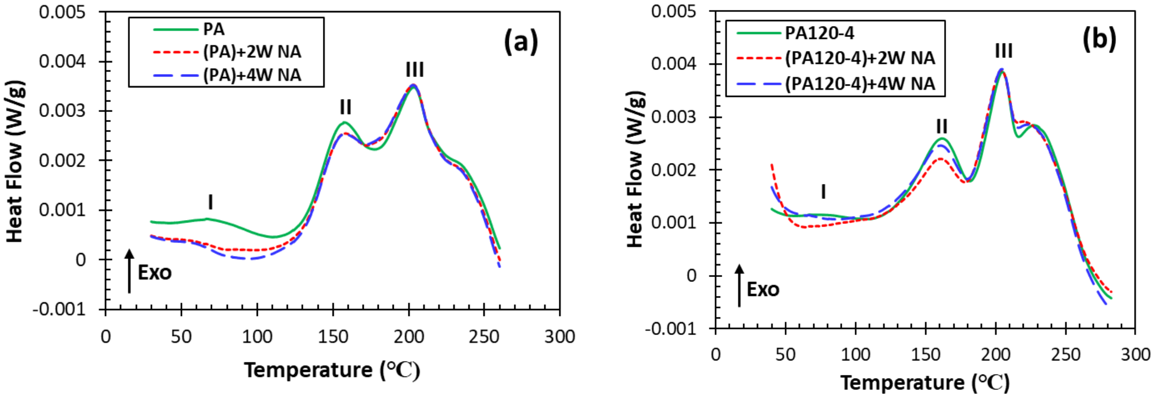

Figure 4-18 DSC traces of pre-aged AA7075 alloy at (a) 100°C and (b) 120°C after natural aging for different times.

Figure 4-18 (b) shows the DSC traces of the PA120-4 samples kept at room temperature for different times up to 4 weeks. There is not a significant change in the first peak, peak I, in the DSC traces of the three heat-treated samples, as shown in Figure 4-18 (b). The DSC results match well with the microhardness measurements, where there was not significant increase in the hardness of the PA120-4 samples kept at room temperature. The negligible change in peak I confirms that the material is microstructurally stable at room temperature after pre-aging at 120°C for 4 hours. To predict the extent of natural aging that occurs after pre-aging, a modeling approach has been formulated, as reported in Section 5.1.2.1.

4.1.2.3 Artificial Aging of Pre-Aged AA7075

4.1.2.3.1 Hardening Response

The two-step aging process (reported in Section 4.1.2.1) is designed and employed to generate a high density of GP zones so that they can act as nucleation sites for the formation of η' precipitates during the subsequent high-temperature aging process. Figure 4-19 shows the effect of artificial aging at 150, 165, and 177°C on the yield strength of AA7075 in PA condition (2-days NA+4h at 100°C). There is a rapid increase in the yield strength during the first 2 hours of aging at 150°C, followed by a smaller increase at a slower rate up to 6 hours of aging. As expected, age hardening occurs more quickly during aging at higher temperatures of 165 and 177°C. Figure 4-19 also shows that artificial aging to the peak-aged condition of the pre-aged material at all three temperatures of 150, 165, and 177°C results in hardness values comparable to the T6 hardness value of the AA7075 alloy (~173HV). Thus, the application of the pre-aging treatment is found to be beneficial for the accelerated hardening response of AA7075 alloy (as compared to single-step T6 heat treatment), which is more notable during aging at higher temperatures such as 177°C.

A slow drop in the yield strength evolution is observed during the aging of pre-aged AA7075 at 150°C (Figure 4-19) for 8 hours, implying a slow-rate precipitate coarsening process. On the other hand, during aging at the higher temperatures of 165 and 177°C, the yield strength decreases at a faster rate after the peak hardness is achieved. Similar behavior has been reported for a 7055 alloy during aging at 120 and 160°C, where the peak strength is plateaued during aging at 120°C between 300 min to 48 h [148]. The presence of this plateau was explained by TEM observation, where there was little change in the volume fraction and radius of η' during aging for more than 300 min compared to the early stage of aging, suggesting that the precipitates remained shearable during aging at this time period [148]. The absence of significant coarsening after a long aging time at 150°C might be due to the small size distribution of precipitates after the pre-aging treatment because of the enhanced nucleation phenomenon occuring at the low temperatures used for pre-aging.

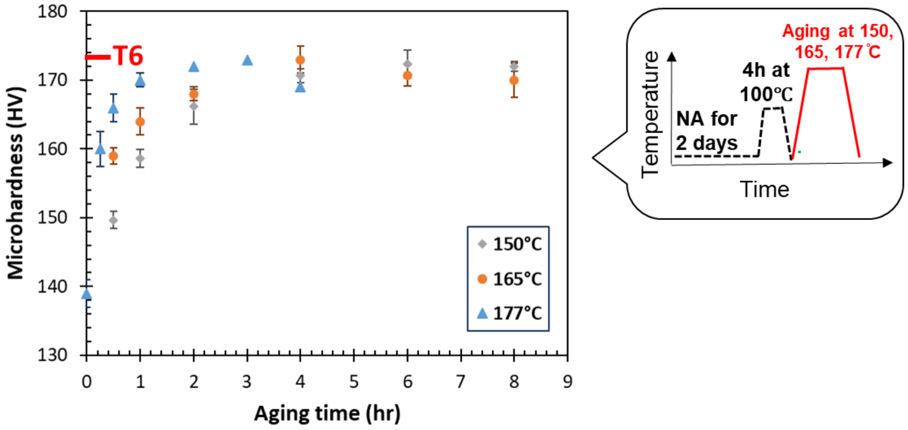

Figure 4-19 The evolution of yield strength during aging of the pre-aged AA7075 at 150, 165, and 177°C.

4.1.2.3.2 Isothermal Calorimetry

The IC results are used to study the precipitation kinetics and then model the precipitation hardening response during the aging of the pre-aged AA7075 alloy. For this purpose, IC tests were conducted on AA7075-PA in the temperature range of 150-177°C. The resultant IC test data were analyzed using the approach of Esmaeili *et al*. [146]. Figure 4-20 shows the IC traces at three aging temperatures of 150, 165, and 177℃. It is observed that the times to reach the zero heat effect during the IC tests are similar to the peak-aged times found using hardness measurements (Figure 4-19) during aging treatments of the PA material. This confirms the fact that the time to reach the ignorable heat release corresponds to the time to reach the peak-aging condition [98,105,146].

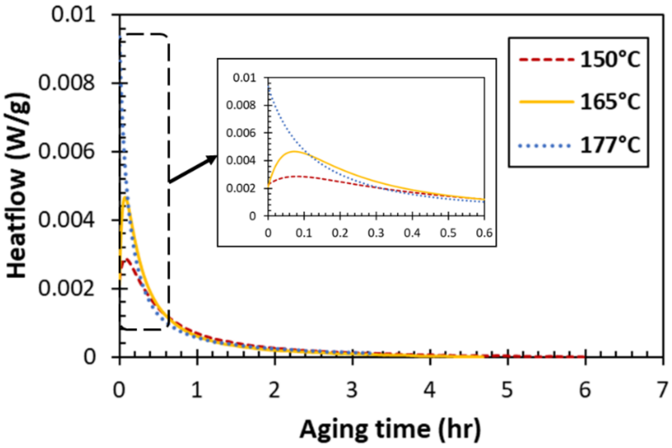

Figure 4-20 The isothermal calorimetry results for artificial aging of AA7075-PA samples at different temperatures.

Analyses of the Calorimetry Results

The calculation of the relative volume fraction of precipitates (f_r) for the final stage artificial aging of pre-aged alloys (*i.e.*, three-step aging routes) is based on the assumption that the volume fraction of precipitates in peak-aged conditions in an artificially aged material is independent of its pre-aging path [98]. To quantify the precipitate evolution during the artificial aging of pre-aged alloys, first, this assumption should be checked using the following equation [98]:

$$f_v = f_v|_{PA} + f_v|_{AA} \qquad \textbf{Eq. 4-5}$$

where f_v is the volume fraction of precipitates which form during the artificial aging of pre-aged alloys up to the peak-aged condition, $f_v|_{PA}$ is the volume fraction of precipitates of the pre-aged materials, and $f_v|_{AA}$ is the volume fraction of precipitates that form during the final step of aging (*i.e.*, the third step of aging). For a three-step aging route, Eq. 4-5 is rewritten as [112]:

$$\int_0^{t_{peak}} \frac{dQ}{dt}\mathrm{dt}|_{AQ+AA} \cong \int_0^{t_{s1}} \frac{dQ}{dt}dt|_{step\ 1} + \int_0^{t_{s2}} \frac{dQ}{dt}dt|_{step\ 2} + \int_0^{t_{s3}} \frac{dQ}{dt}dt|_{step\ 3} \qquad \textbf{Eq. 4-6}$$

where *dQ/dt* is the heat flow per unit mass (*J/g*) and the integration limits t_{s1}, t_{s2} and t_{s3} represent the times for the three sequential steps of aging, and AQ+AA represents the artificial aging of the as-quenched (as-WQ) alloy.

Eq. 4-6 is examined here using the integrated heat effects for the three steps of aging (*i.e.*, PA+artificial aging at 177°C) and the aging of the as-WQ material at 177°C (IC tests were reported in Sections 4.1.2.1.2 and 4.1.2.3.2) which are listed in Table 4-6. The result, with the left-hand side of Eq. 4-6 being ~20.9 *J/g* and the right-hand side being 21.5 *J/g*, and the levels of the measurement errors suggest that Eq. 4-6 is a valid assumption.

Table 4-6 The total heat evolved during aging treatments of AA7075.

Heat treatment	**Total heat effect (*J/g*)**
As-quenched aged at 177℃	20.9 (±0.5)
1st step	8.7 (±0.8)
2nd step	3 (±0.2)
3rd step (aging at 177℃)	9.8 (±0.3)

Following the validation of Eq. 4-6, f_r is obtained as follows [98]:

$$f_r = f_r^0 + \frac{\int_0^t \left(\frac{dQ}{dt}\right) dt|_{\mathrm{PA+AA}}}{\int_0^{t_{peak}} \left(\frac{dQ}{dt}\right) dt|_{AQ+AA}} \qquad \textbf{Eq. 4-7}$$

where:

$$f_r^0 = \frac{\int_0^{t_{peak}} \left(\frac{dQ}{dt}\right) dt|_{AQ+AA} - \int_0^{t_{peak}} \left(\frac{dQ}{dt}\right) dt|_{\mathrm{PA+AA}}}{\int_0^{t_{peak}} \left(\frac{dQ}{dt}\right) dt|_{AQ+AA}} \qquad \textbf{Eq. 4-8}$$

where $\int_0^t \left(\frac{dQ}{dt}\right) dt|_{PA+AA}$ is the area under the IC trace up to time *t* for artificial aging of the pre-aged alloy. The evolution of f_r during artificial aging of the AA7075-PA at the three aging temperatures of 150, 165, and 177°C is shown in Figure 4.21. It is observed that the time to reach the peak-aged condition (*i.e.*, when $f_r = 1$) has a decreasing trend with respect to the aging temperature. The obtained data for the evolution of f_r will be used to model the precipitation kinetics during aging of the PA material in Section 5.1.2.2.1.

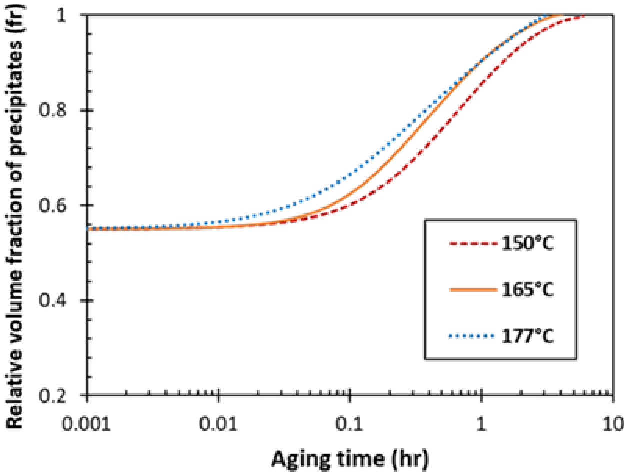

Figure 4.21 The calculated evolution of the relative volume fraction of precipitates during aging of the AA7075-PA alloy.

4.2 Precipitation Hardening Behavior of Die-Quenched and Forced-Air Quenched AA7075

The following section focuses on the precipitation hardening behavior of the die-quenched (DQ) and forced-air quenched (FAQ) AA7075 during natural aging (Section 4.2.1), after a pre-aging treatment, and during the subsequent artificial aging treatment associated with automotive paint-bake cycling (Section 4.2.2). To isolate the effect of quench rate from deformation, FAQ samples were quenched by forced air at the same rate as in the die-quenching process.

4.2.1 Natural Aging

4.2.1.1 Results

4.2.1.1.1 Hardening Response

The hardening behavior of the AA7075 samples in the DQ condition during subsequent natural aging is evaluated by analyzing the evolution of hardness with natural aging time, as shown in Figure 4-22. To investigate the effect of the quench rate used in the die-quenching process (without deformation) on the subsequent natural aging behavior of the AA7075 alloy, the hardness evolution of the FAQ samples with the natural aging time is also examined (Figure 4-22). The hardness measurements of the WQ sample during natural aging reported in Ref. [123] are included in Figure 4-22 for comparison. The DQ samples have higher hardness values in the as-quenched and naturally aged conditions than the FAQ and WQ samples. The hardness values increase as the natural aging time increases in all three cases, and their evolutions follow linear relationships with the logarithm of the natural aging time. The hardness evolution in the FAQ and WQ samples is nearly identical, while the rate of hardening in the DQ sample is slightly slower, suggesting slower kinetics of natural aging in this sample.

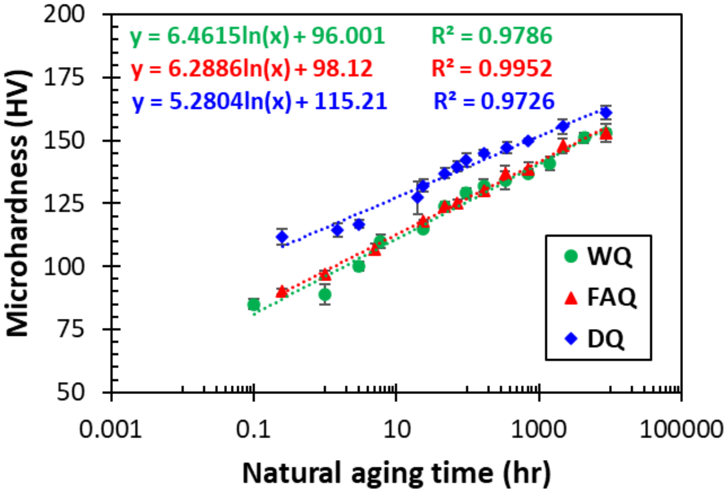

Figure 4-22 The evolution of hardness during natural aging of AA7075 with different quenching conditions.

4.2.1.1.2 Differential Scanning Calorimetry (Analysis of As-Quenched Conditions)

DSC results (Figure 4-23) are analyzed to investigate the effect of forced-air quenching and die-quenching on the microstructure evolution of the as-quenched AA7075 alloy during heating in a DSC experiment. This analysis can help us gain a better understanding of the changes in the transformation sequence and kinetics that occur due to the effects of the quench rate applied in the die-quenching process (FAQ condition) and deformation in the DQ material. Figure 4-23 shows the DSC traces of the FAQ, DQ, and WQ samples. The first endothermic peak (peak A) is attributed to the dissolution of primary quenching clusters, which form immediately after quenching in the alloy [123]. The first exothermic peak (peak I) is associated with the precipitation of GP zones, as indicated by previously reported DSC results [54,126]. The second exothermic peak (peak II), ranging from ~110 to ~190°C, results from the formation of η' during DSC [54,126]. The third and fourth peaks (peaks III and IV) can be associated with the formation of η and T phases, respectively [44,54,126].

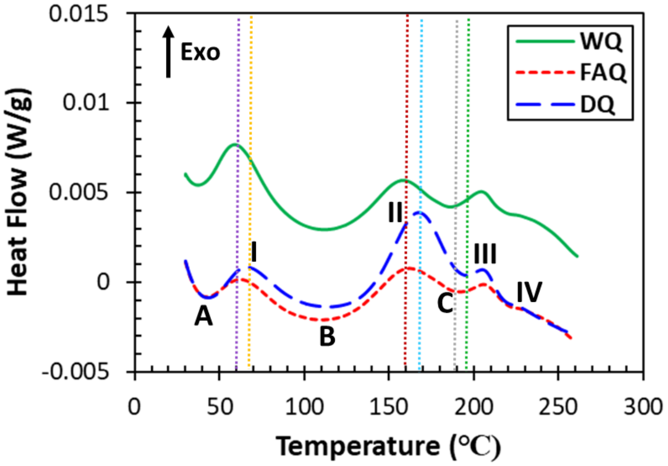

Figure 4-23 DSC traces of AA7075 alloy in the WQ, FAQ and DQ conditions.

The important observations from the DSC traces in Figure 4-23 are as follows:

1. Peak I shifts to higher temperatures on the DSC traces of the DQ sample (indicated by the yellow dotted line) compared to those of the WQ and FAQ samples (indicated by the purple dotted line).

2. Peak II is the most prominent peak on the DSC trace of the alloy in the DQ condition. The magnitude of peak II appears to be higher than those of the WQ and FAQ conditions. In addition, this peak occurs at a noticeably higher temperature (indicated by the blue dotted line) than that in the WQ and FAQ samples (indicated by the red dotted line).

3. The peak temperature of peak C is higher on the DSC trace of the DQ sample (green dotted line) than those of the WQ and FAQ samples (grey dotted line).

4. Peak III does not show any noticeable change on the DSC traces of the DQ and FAQ samples compared to the WQ sample.

4.2.1.2 Discussion of Experimental Results

In this section, the effects of the quench type (applied during forced-air quenching) and deformation (applied during die-quenching) on the natural aging behavior of the AA7075 alloy are discussed using the combination of hardness and DSC results.

Effect of Quench Type

The increase in the hardness of the FAQ and DQ samples during natural aging (Figure 4-22) is due to the formation of fine Zn-Mg precipitates and an increase in their number density, as previously reported for the natural aging of AA7075 in the WQ conditions (Section 4.1.1 [123]). A slow quench rate after solutionizing in some alloys may lead to the loss of vacancies due to their annihilation during quenching and/or the loss of solutes due to quench-induced precipitation [149,150]. The lower magnitude of the exothermic heat associated with peak I on the DSC trace of the FAQ and DQ samples compared to that of the WQ sample (Figure 4-23) indicates that fewer GP zones form in the microstructures of the FAQ and DQ samples. This observation may reflect the effect of the quench rate and the loss of vacancies and/or solutes during quenching, which reduces the potential for the precipitation of GP zones in these two samples. Furthermore, the FAQ and DQ samples have been stored at room temperature for a longer time before conducting the DSC runs, which also affects both the peak temperature and the magnitude of peak I. The similarity in the hardness values of the as-WQ and as-FAQ samples indicates that forced-air quenching does not cause noticeable increase in hardness in the as-quenched material. This suggests that the amount of solutes lost during forced-air quenching, due to precipitation during quenching, is negligible. Additionally, the similarity in the rates of natural aging for the WQ and FAQ samples suggests that the quench rate applied during forced-air quenching has been sufficient to prevent the significant loss of vacancies and/or solutes. As a result, the supersaturation of solutes in the as-FAQ sample or the formation of fine Zn-Mg precipitates during subsequent natural aging is not affected.

Effect of Deformation

The natural aging behavior of the alloy in DQ condition can be influenced by both the deformation and quench rate applied during the die-quenching process. To investigate the effect of deformation and the combined effects of deformation and quench rate, the natural ageing behavior of the DQ sample is compared with that of the FAQ and WQ samples in this section. As discussed in the previous section, the quench rate applied during the die-quenching process does not significantly affect the evolutions of microstructure and hardness for the DQ sample during subsequent natural aging. Therefore, the higher hardness values of the DQ sample in the as-quenched and naturally-aged conditions (Figure 4-22), compared to those for the WQ and FAQ samples, are attributed to the effect of deformation applied during the die-quenching process. The persistent formation and accumulation of dislocations in the microstructure of the alloy during die-quenching result in the strain hardening of the as-DQ sample. Owing to this strain hardening effect, the hardness value of the DQ sample remains higher during natural aging compared to those for the FAQ and WQ conditions (see Figure 4-22).

The slightly lower rate of natural aging of the DQ sample compared to the WQ sample (Figure 4-22) is attributed to the consistent annihilation of vacancies on dislocations during the natural aging processes. Similarly, a decrease in the precipitation kinetics has been reported during the natural aging of a hot-formed quenched AA7921 alloy [6]. In aluminum alloys, the formation of solute clusters and/or natural aging precipitates in the early stages is affected and facilitated by the excess vacancies obtained after quenching [151,152]. The loss of vacancies in the DQ sample can increase the energy barrier for the nucleation of natural aging precipitates. This results in a lower nucleation rate of natural aging precipitates and a lower hardening rate during the natural aging of the DQ sample, as shown in Figure 4-22. The shift of peak I to higher temperatures on the DSC trace of the DQ sample, compared to the WQ and FAQ samples (as seen in Figure 4-23), is also attributed to the effect of the presence of dislocations on GP zone precipitation. During the DSC experiment, GP zones form at a higher temperature in the microstructure of the DQ sample, compared to the WQ and FAQ samples, due to the annihilation of vacancies on dislocations and the reduction of the vacancy supersaturation.

4.2.2 Multi-step Aging

In this section, the precipitation hardening response and microstructural evolution of the AA7075 alloy in the DQ and FAQ conditions and after a multi-step aging treatment are presented, as schematically shown in Figure 4-24.

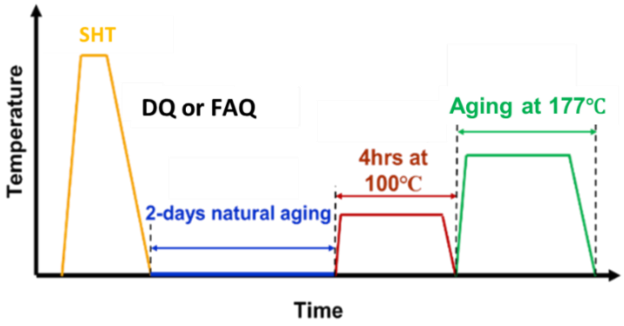

Figure 4-24 Schematic of the multi-step aging process.

4.2.2.1 Results

4.2.2.1.1 Hardening Response

The effect of the thermal processing history (*i.e.*, different quenching conditions) on the age hardening response of AA7075 alloy during a multi-step aging treatment is investigated, as shown in Figure 4-25. The important observations from these measurements can be summarized as follows:

(1) The difference in hardness values of the alloy samples in the FAQ and WQ conditions is relatively insignificant in the AQ, 2NA, and PA conditions. However, the hardness value of the FAQ sample in the PB condition is lower than that of the WQ sample.

(2) The DQ samples in the AQ, 2NA, and PA conditions exhibit higher hardness values as compared to those for the WQ and FAQ samples. However, the DQ sample achieves a lower hardness value after the PBC treatment than the FAQ and WQ samples.

(3) The increase in the hardness of the DQ sample after each aging step is lower than that of the other two quenching conditions.

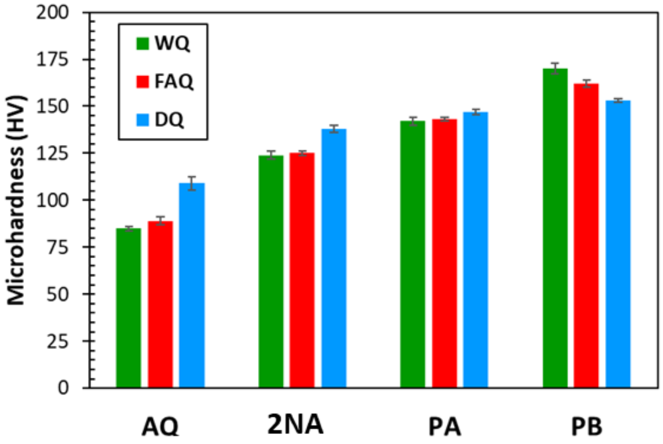

Figure 4-25 Measured microhardness values of the WQ (Water Quenched), FAQ (Forced-Air Quenched), and DQ (Die-Quenched) AA7075 alloy after different aging steps. (AQ=As-Quenched, NA=2-day Naturally Aged, PA=Pre-Aged, PB=Paint Baked).

The hardness evolution of the samples in the PA (WQ+PA condition) and DQ+PA conditions during the final artificial aging at 177°C is shown in Figure 4-26. Although the hardness value of the DQ sample is higher than that of the WQ sample in the as-PA condition, the lower peak hardness (~22 HV difference) is achieved during the artificial aging of the sample in the DQ+PA condition. Figure 4-26 also shows that the peak hardness in the DQ+PA condition is achieved faster than in the PA condition during aging at 177°C.

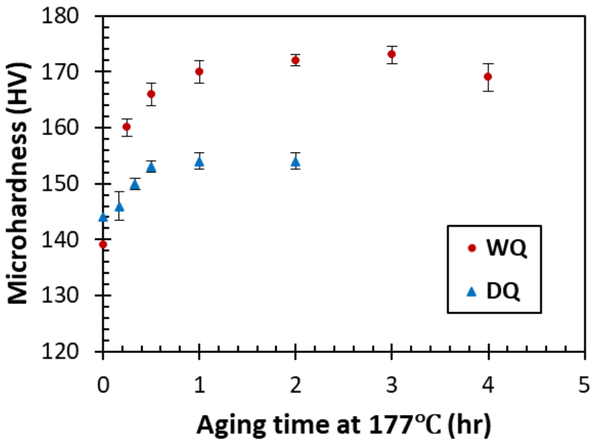

Figure 4-26 Measured microhardness values of AA7075 alloy in the PA and DQ+PA tempers during aging at 177°C.

4.2.2.1.2 Microstructural Evolution

4.2.2.1.2.1 Isothermal Calorimetry Analysis (Analysis of Multi-Step Aged Conditions)

The evolution of the relative volume fraction of precipitates during the aging treatments of interest is quantified using the calorimetry results and the analytical methodology developed by Esmaeili *et al.* [98,146,147]. The analytical methods applied in this section also require IC tests of the as-quenched samples at 177°C, as shown in Figure 4-27 (b). The results of the IC test conducted on alloy samples in the DQ+PA and PA conditions at 177°C are presented in Figure 4-27 (a). As shown in Figure 4-27 (b), the time to reach the peak-aged condition during the aging of AA7075-PA at 177°C is approximately 2.5 hours. This confirms the fact that the time to reach the zero heat effect corresponds to the time to reach the peak-aged condition in this sample, as shown in Figure 4-26 [98,105,146].

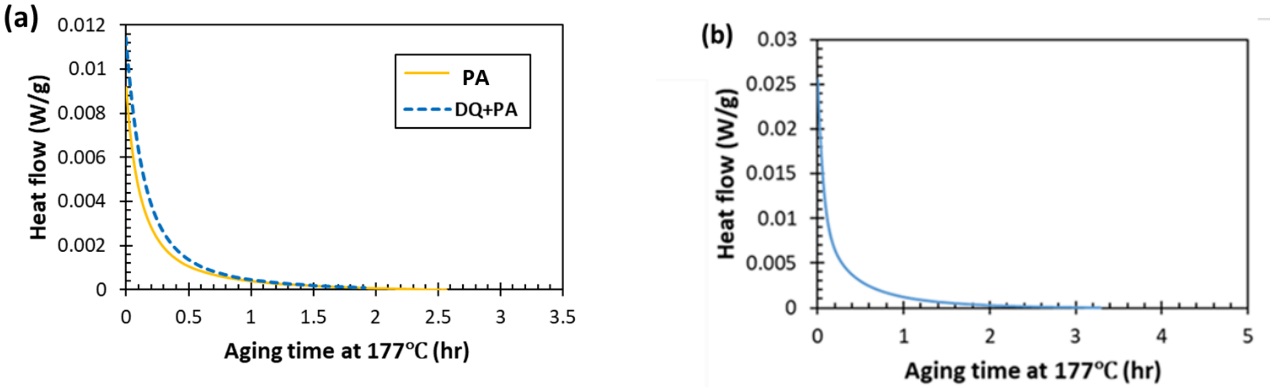

Figure 4-27 IC results for artificial aging of AA7075 in the (a) PA and DQ+PA conditions, and (b) DQ condition, during aging at 177°C.

Analysis of the Calorimetry Results

For the analysis of f_r during artificial aging of AA7075-DQ+PA, the total areas under the IC traces for the as-DQ and DQ+three-step aged conditions, have been calculated and are presented in Table 4-7. The respective areas under the IC traces for the DQ samples are slightly smaller than those of the WQ material (Table 4-6). The slight decrease in the total heat effects in the DQ sample indicates a slight reduction in the volume fraction of precipitates that form during the IC run. It should be noted that this difference can also be attributed to the potential errors involved in analyzing the IC results [98].

Table 4-7 The values of the total heat evolved during aging treatments of AA7075-DQ.

Heat treatment	Total heat effect (J/g)
As-DQ sample aged at 177℃	19.6 (±0.7)
DQ+PA sample aged at 177℃	9.2 (±0.3)

The areas under the IC traces (Figure 4-27) are used according to Eq. 4-2 and Eq. 4-4 to obtain the evolution of f_r during aging of the AA7075 alloy in the PA and DQ+PA tempers at 177°C. The results of the IC analysis are shown in Figure 4-28. It is evident that f_r reaches 1 faster during artificial aging of the material in the DQ+PA condition as compared to the PA condition.

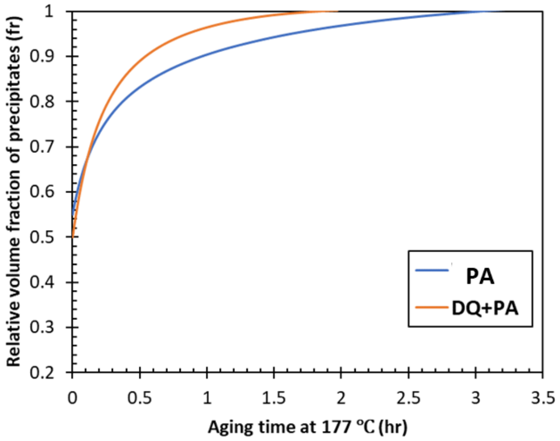

Figure 4-28 The calculated evolution of relative volume fraction of precipitates for the materials in the PA and DQ+PA conditions during aging at 177°C.

4.2.2.1.2.2 Transmission Electron Microscopy Analysis of Multi-Step Aged AA7075 Alloy Samples

TEM imaging has been employed on selected AA7075 samples with different processing histories to capture the effect of die-quenching and subsequent aging treatments (including PBC) on the microstructural characteristics of the alloy in comparison with water-quenched samples. The TEM micrographs of the PA and DQ+PA samples are reported here, respectively, as shown in Figure 4-29. As seen in Figure 4-29 (a) and (b), nano-sized spherical precipitates (in an approximate size range of ~0.5-3.9 nm) are homogeneously distributed in the microstructures of the sample in the PA condition. It should be noted that the measurements of the size distribution for the nano-sized precipitates for the samples in the PA and DQ+PA conditions are not reported here due to the very small size of the precipitates and the resultant errors of measurements.

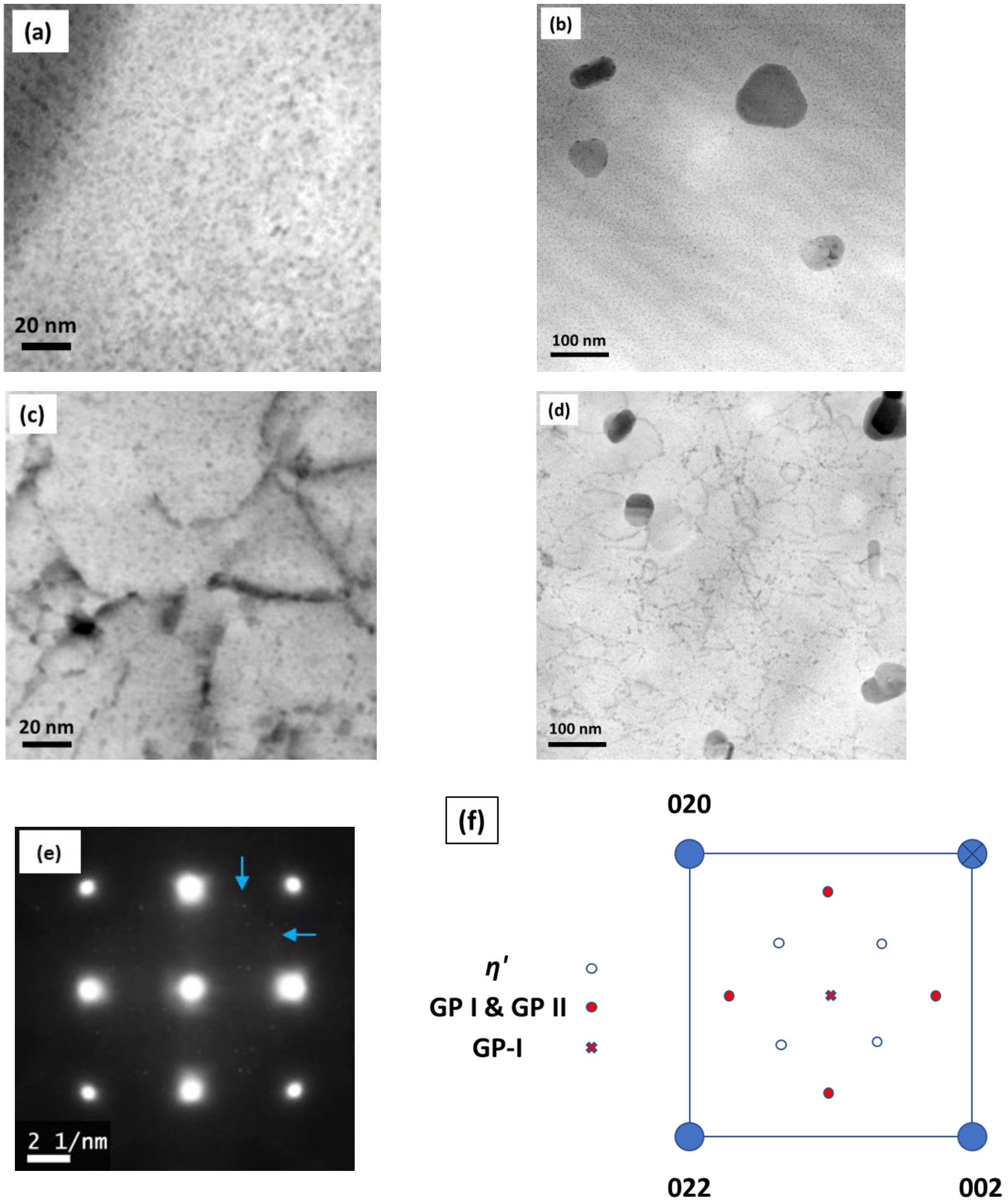

Figure 4-29 Bright field TEM micrographs for samples with different heat treatment histories: (a), (b) PA, (c), (d) DQ+PA, and (e) diffraction patterns for PA condition along <001>Al zone axis and (f) schematic diagram of diffraction pattern from different precipitates in [001]Al zone axis.

Previous TEM studies [140,153,154] have shown that nano-sized precipitates in the microstructure of AA7xxx alloys can be revealed in the [001] Al matrix orientations by characteristic diffuse scattering patterns, as shown schematically in Figure 4-29 (f). This schematic diagram has been prepared and used to readily identify the types of precipitates in the microstructure of the alloy after different thermal processing histories; the analysis results are presented in Table 4-8. GP zones are found to be the dominant precipitates in the microstructure of the alloy in the PA condition. According to the EDS results (refer to Appendix A), these precipitates contain Zn, Mg, and Cu. It should be noted that the very small, sharp diffraction spots present in the diffraction patterns shown in Figure 4-29 (e), Figure 4-30 (e), and (f) are assigned to Cr-rich particles. Some nano-sized precipitates are heterogeneously formed on the large dispersoids, as shown in Figure 4-29 (b). According to the EDS results (Appendix A), these dispersoids are Cr-rich particles (with an approximate composition of $Al_{68}Mg_{15}Cr_9Zn_6Cu_2$ [123] and an FCC crystal structure [155]), which are also observed in the microstructures of the AA7075 alloy with other thermal processing histories (Figure 4-29 and Figure 4-30). General information regarding these particles is provided in Section 4.1.1.3. The heterogeneous formation of nano-sized precipitates on Cr-rich particles, which has also been reported by Bai *et al.* [123], has been observed in all AA7075 samples with different thermal processing histories.

Table 4-8 Summary of scattering spots observed in the diffraction patterns of thermally treated AA7075 alloy.

Heat treatment condition	Diffraction spots in $[001]_{Al}$ Zone Axis
PA	Weak spots from GP zones (indicated by blue arrows)
PB	Spots from GP II (indicated by blue arrow), and η' (indicated by red arrow)
DQ+PB	Spots from GP I (indicated by green arrow), GP II (indicated by blue arrow), and η' (indicated by red arrow)

Bright-field TEM micrographs of the alloy in the DQ+PA condition are shown in Figure 4-29 (c) and (d). In these figures, an inhomogeneous distribution of precipitates can be observed, with arrays of larger precipitates present along the dislocation lines. Precipitates that are far from dislocations are homogeneously distributed, and their size range is found to be similar to that of the sample in the PA condition. The presence of precipitate-free zones (PFZ) around dislocations is evident in Figure 4-29 (c) and (d). It should be noted that clear diffraction spots from the precipitates were not obtained in the diffraction patterns of the sample in the

DQ+PA condition. This can be attributed to the effect of dislocations, which can cover the local elastic strain contrast of small nano-sized precipitates [156], leading to extremely weak diffraction spots.

Figure 4-30 shows the TEM micrographs of the samples in the PB and DQ+PB conditions. Compared to the as-PA sample (Figure 4-29 (a) and (b)), the precipitates in the microstructures of the PB sample (Figure 4-30 (a) and (b)) are larger. Nano-sized precipitates with two different cross-sectional morphologies (*i.e.*, plate and lath-shaped) are homogeneously distributed in the microstructure of the PB sample (Figure 4-30 (a) and (b)). The analysis of DP in the [001]Al zone axis revealed the presence of GP zones and η' precipitates in the microstructure of the PB sample (Table 4-8).

For the DQ+PB sample (Figure 4-30 (c) and (d)), precipitates that are far from dislocations are homogeneously distributed with two distinct cross-sectional morphologies, similar to the PB sample. In addition, some relatively larger precipitates have formed heterogeneously along the dislocation lines in the microstructure of the DQ+PB sample (Figure 4-30 (c) and (d)). Similar to the DQ+PA sample, PFZs can be readily observed around the dislocations in the microstructure of this sample. As listed in Table 4-8, GP zones and η' are present in the microstructures of the DQ+PB sample. The absence of spots from GP I zones in the diffraction pattern of the alloy in the PB condition can be attributed to either the absence of these zones or the smaller volume fraction of these precipitates in the microstructure of the PB sample. Similarly, Stiller *et al.* [140] have previously reported the dissolution of GP I zones during the artificial aging of a pre-aged (100°C for 6 hours) Al-Zn-Mg alloy at 150°C. The presence of diffraction spots from GP I zones in the microstructure of the DQ+PB sample, on the other hand, may suggest an increase in the stability of these zones. This increase is likely due to the larger size range of precipitates that result from their enhanced growth on dislocations.

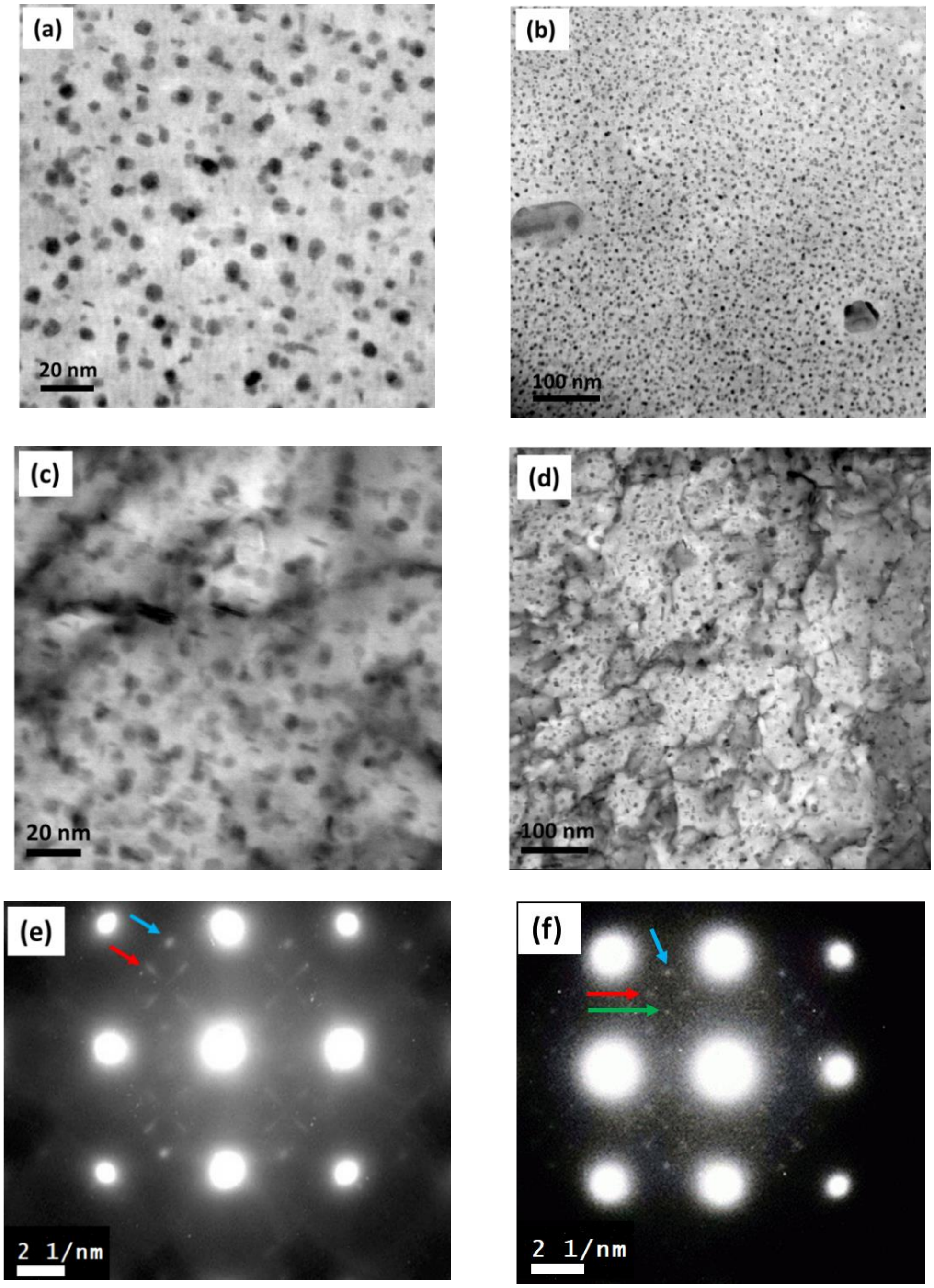

Figure 4-30 Bright field TEM micrographs along <011>Al zone axis for samples with different heat treatment histories: (a), (b) PB, (c), (d) DQ+PB, and <001>Al diffraction patterns for (e) PB and (f) DQ+PB conditions.

To further investigate the nano-sized precipitates with two different cross-sectional morphologies in the microstructure of the PB sample, a TEM micrograph of the sample in the [110]Al zone axis, along with the corresponding DP and Fast Fourier Transform (FFT) diffraction images are further analyzed, as shown in Figure 4-31. The corresponding DP (Figure 4-31 (b)) shows diffraction spots assigned to η' precipitates, which are identified by red arrows. The FFT diffraction image (Figure 4-31 (c)) shows that the precipitates are coherent with the matrix. Furthermore, the edge-on configurations of these precipitates reveal that they possess two different $(1\bar{1}1)$Al and $(\bar{1}11)$Al habit planes. The precipitates shown by the red dashed line are suspected to be GP II zones or a precursor of η', based on the aspect ratio of the precipitate (thickness of ~1 nm and a diameter of ~5.5 nm) [44], whereas the precipitate shown by the dotted blue line appears to be η' (thickness of ~2 nm and a diameter of ≥7 nm). Considering the size range of the precipitates in comparison with the reported size range for η' (*i.e.*, 5-10 nm [157]) and their presence on {111}Al when observed in the [110]Al zone axis and the DP analysis, it can be concluded that η' precipitates are the major precipitates in the microstructure of the alloy in the PB condition.

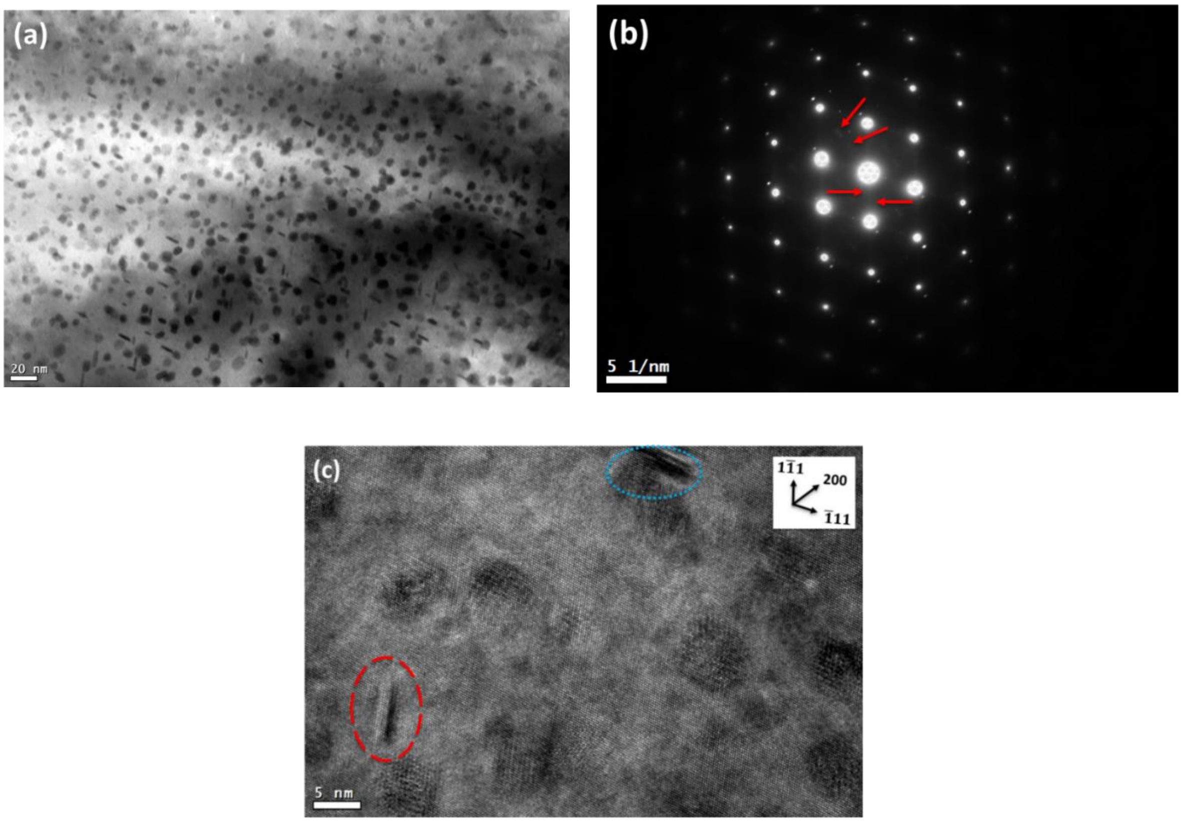

Figure 4-31 (a) The TEM micrograph taken from the PB sample along the [110]Al zone axis, (b) corresponding diffraction pattern and (c) corresponding HRTEM micrograph.

Figure 4-32 shows histograms of the size distribution of precipitates for the AA7075 alloy in the PB and DQ+PB conditions. The average and maximum sizes of the precipitates for both conditions are reported in this figure. Both the average and maximum sizes of precipitates in the DQ+PB sample are larger than the corresponding data for the PB condition. Figure 4-32 also shows that there is a notable increase in the population of larger precipitates with diameters larger than 10 nm in the DQ+PB sample.

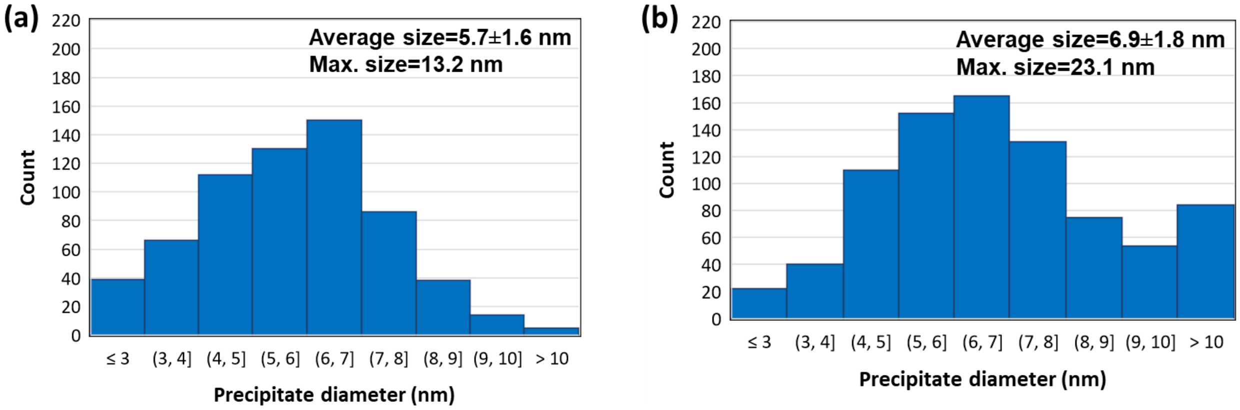

Figure 4-32 Measured size distribution of precipitates in AA7075 alloy in the (a) PB and (b) DQ+PB conditions.

4.2.2.2 Discussion of Experimental Results

The precipitation hardening behavior of aluminum alloys is affected by microstructural parameters, including size, volume fraction, and types of precipitates. The combination of hardness, DSC, IC, and TEM results are used to discuss the effects of quench type (applied during forced-air quenching) and deformation (applied during die-quenching) on the microstructure and hardening response of AA7075 alloy after different aging steps (*i.e.*, pre-aging and final artificial aging).

4.2.2.2.1 Effect of Quench Type

The similarity in hardness values obtained for the FAQ and WQ samples in the PA conditions, as seen in Figure 4-25, suggests a similarity in the microstructures of these samples. According to the TEM results, the GP zones are the primary precipitates in the microstructure of the WQ+PA sample. It can be concluded that forced-air quenching does not significantly affect the formation of GP zones in the microstructure of the PA samples. The lower quench rate for the FAQ sample, compared to the WQ sample, can reduce the number of excess vacancies and VRCs in the microstructure by allowing them to annihilate on defects. As discussed in Section 4.2.1.2, for NA conditions, the similarity in the hardness values of the samples in the WQ+PA and FAQ+PA conditions suggests that the quench rate during forced-air quenching has been sufficient to inhibit the significant loss of vacancies and/or solutes during quenching. Furthermore, this similarity may imply that the loss of VRCs does not affect the formation of GP zones during the pre-aging treatment. Similar observations were made by other researchers [36,57,58] regarding VRCs and their effect on the formation of GP zones. They concluded that VRCs do not significantly affect the formation of GP zones in the low-temperature region (*i.e.,* below 80–100°C), and they remain stable enough to act as nucleation sites for precipitation of η' at higher temperatures (*e.g.,* 150°C).

The lower hardness value obtained for the FAQ+PA sample, compared to that for the WQ+PA sample, after the PBC treatment, is attributed to the loss of vacancies and/or the formation of less vacancy-rich clusters (VRC) during or immediately after quenching as a result of the slower quench rate. VRCs are reported to be precursors of the η' phase [36,57,58]; therefore, a decrease in their number density reduces the amount of η' precipitates that form during the PBC (suppressed precipitation of η'). This, in turn, results in a decrease in the hardening potential of the FAQ+PA sample during subsequent aging treatments at higher temperatures (*e.g.,* PBC).

4.2.2.2.2 Effect of Deformation

Microstructural Evolution

The deformation applied during die-quenching has several effects on the microstructural evolution and hardening behavior of the alloy during the subsequent aging treatments. Dislocations stored in the microstructure of the DQ sample serve as heterogeneous nucleation sites for the formation of hardening precipitates during subsequent aging steps. Furthermore, the enhanced diffusion of solutes through the dislocation paths can ultimately lead to the formation of larger precipitates, as observed in the TEM images of the DQ+PA and DQ+PB samples (Figure 4-29 (c), (d) and Figure 4-30 (c), (d)). For the DQ+PB sample, this is confirmed by the observation of larger values of average and maximum size of precipitates, as well as a higher population of larger precipitates (which are heterogeneously formed precipitates) in the histograms of the size distribution of precipitates (Figure 4-32 (b)), compared to the PB sample (Figure 4-32 (a)). The reduced time taken to reach the peak aging time during artificial aging of the DQ+PA sample at 177℃, as compared to the WQ+PA sample, is evident in Figure 4-26 and Figure 4-27. This is attributed to an increase in the nucleation, growth, and coarsening rate of the precipitates, which is caused by the presence of dislocations.

To gain a better understanding of the effect of dislocations on the transformation sequence in the DQ samples, it is worthwhile to examine the DSC results reported in Section 4.2.1.1.2. The higher magnitude of peak II on the DSC trace of the DQ sample (Figure 4-23), compared to those of the WQ and FAQ samples, indicates that dislocations in the DQ sample promote the formation of η' precipitates during heating to higher temperatures, close to the PBC temperature. This DSC observation also suggests that dislocations act as heterogeneous sites for the direct formation of η' precipitates during the DSC run. The heterogeneous precipitation of η' on dislocations has been previously reported during aging treatments in deformed Al-Zn-Mg and AA7050 alloys [158,159]. The shift of the dissolution peak for η' precipitates (Peak C) to a higher temperature on the DSC trace of the DQ sample, compared to the WQ and FAQ samples, suggests the presence of a larger population of larger η' precipitates in the microstructure of the DQ sample. This also indicates an increase in their stability during the DSC run. This shift could also be caused by the overlapping effects of peak C and exothermic events.

Dislocations not only cause the nucleation and growth of larger precipitates, but they can also act as vacancy sinks, which affects the formation of precipitates in their surrounding area. The higher magnitude of Peak II on the DSC trace of the DQ sample, indicating the enhanced formation of η' precipitates, can be attributed to the microstructure evolution resulting from vacancy annihilation on dislocations. Trapping and annihilation of vacancies on dislocations can decrease the volume fraction of GP zones that form during the DSC run in the DQ sample (as discussed in Section 4.2.1.2). As a result, a higher concentration of solute remains in the matrix of the alloy sample. This, in turn, results in a higher driving force for the formation of η' precipitates and a higher magnitude of Peak II on the DSC trace of the DQ sample compared to the FAQ and WQ samples. The occurrence of Peak II at a higher temperature in the DSC trace of the DQ sample, compared to those of the WQ and FAQ samples, can be attributed to the annihilation of vacancies on dislocations, which can delay the formation of η' precipitates. The presence of a narrow PFZ around dislocations, as seen in the TEM images of the DQ+PA and DQ+PB samples in Figure 4-29 and Figure 4-30, further suggests the annihilation of vacancies on dislocations and the depletion of vacancies in the vicinity of dislocations right after quenching and during natural aging (as discussed in Section 4.2.1).

Hardening Response

The deformation applied during die-quenching affects the hardening response of the material in DQ condition during subsequent heat treatments by influencing the precipitation characteristics and strain hardening caused by dislocation accumulation. The reduced hardening potential of the DQ material after the PA and PA+PBC treatments, compared to the similarly aged WQ samples (Figure 4-25), can be ascribed to the annihilation of vacancies on dislocations and the depletion of vacancies in the vicinity of dislocations immediately after quenching and during natural aging. Due to the annihilation of vacancies, the formation of precipitates around the dislocations is inhibited during the subsequent aging steps, namely PA and PBC. Furthermore, the heterogeneous formation of precipitates on dislocations, such as η' precipitates in the microstructure of the DQ+PB sample, may have resulted in the depletion of solutes from the surrounding matrix. Both of the aforementioned phenomena lead to the formation of a PFZ in the vicinity of dislocations and widen the size distribution of the precipitates. The formation of the PFZ leads to a reduction in the volume fraction of homogeneous precipitates in the DQ+PB sample compared to the WQ+PB temper. The lower value for the total heat released during the IC experiment (*i.e.*, the volume fraction of precipitates) associated with the aging of the DQ+PA sample at 177℃ (Table 4-7), as compared to that of the WQ+PA sample (Table 4-6), is also consistent with the above-mentioned interpretation. The lower volume fraction of precipitates results in a decrease in the strengthening contribution due to precipitation. As a result, the DQ+PA sample exhibits lower hardness values during artificial aging at 177°C (Figure 4-26) compared to the WQ+PA sample. In addition, the widening of the size distribution of precipitates can potentially decrease the hardening capacity of the DQ+PA material during the aging at 177°C and after the PBC treatment (refer to Figure 4-25 and Figure 4-26). In the presence of a precipitate size distribution (*i.e.*, in DQ+PB), only a fraction of the precipitates has a critical size (assuming that the peak strength occurs at a precipitate size, r_c) in the peak-aged condition. As a result, not all of the precipitate populations simultaneously contribute to the yield strength at the same time. Deschamps and Bréchet [97] have theoretically studied this effect and showed that widening the size distribution of precipitates reduces the peak strength of a pre-deformed and artificially aged Al-Zn-Mg alloy.

The smaller increase in the hardness values of the DQ sample after the PA and PBC treatments, compared to the WQ sample, can also be rationalized by the effect of the rearrangement of dislocations and partial recovery during these artificial aging treatments. During the die-quenching process, dislocations form in the microstructure of the DQ sample; thus, the stored energy of the material increases. This provides the driving force for the recovery of dislocations during subsequent aging treatments. The recovery of dislocations has been reported to be insignificant during the natural aging of the AA7075 alloy [55]. Therefore, a considerable proportion of the dislocations that form during the die-quenching process are presumed to be persistently present in the microstructure of the alloy in the 2NA condition. The annihilation of dislocations is expected to be more noticeable during aging at higher temperatures (*i.e.*, aging at 177°C or PBC treatment), at which dislocations go through a rearrangement or partial recovery more easily [112]. As a result of the decrease in dislocation density, the strength/hardness contribution due to dislocations is reduced in both the DQ+PA and DQ+PB conditions. To predict the microstructure and yield strength evolution during artificial ageing (such as PBC treatment) of AA7075 in the DQ+PA condition, a precipitation hardening model is developed and is detailed in section 5.2.2, based on the experimental observations reported in this section.

4.3 Summary

In this chapter, the microstructural evolution and precipitation hardening behavior of AA7xxx alloys in the WQ and DQ conditions were studied. The kinetics of precipitation and strengthening behavior during natural aging of AA7xxx-WQ alloys were discussed. The precipitation hardening behavior of the AA7075-WQ alloy during multi-step aging treatments, including pre-aging treatments, secondary natural aging, and artificial aging of the alloy in pre-aged tempers were investigated. The effects of natural aging and a multi-step aging treatment on the microstructure and hardening response of a die-quenched AA7075 alloy were evaluated, and the interactions between the precipitates and dislocations were analyzed. The acquired knowledge has been used to model the microstructural and yield strength evolution of these alloys during natural and multi-step aging treatments, which will be presented in the next chapter.

5. Modeling Analysis

The aim of this chapter is to model the precipitation kinetics and age hardening behavior of the AA7xxx alloys used in this study in the WQ and DQ conditions and during natural aging and multi-step aging treatments. The applied thermal processing histories for each section of this chapter are shown schematically in Figure 5-1.

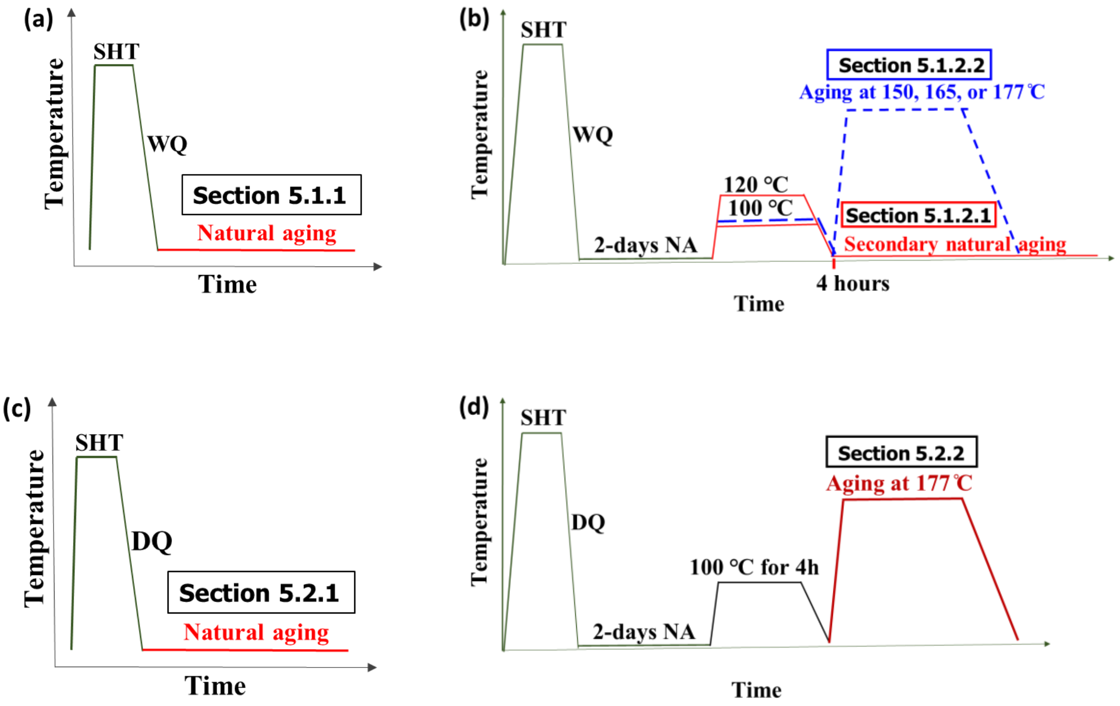

Figure 5-1 Schematic of the thermal processing routes, showing positioning of each section in this chapter.

5.1 Modeling of Precipitation Hardening in Solutionized and Water-Quenched Materials

In this section, the microstructural and yield strength evolutions during natural aging of the AA7xxx alloys in WQ condition (Section 5.1.1) and multi-step aging treatments of the AA7075 alloy in WQ condition (Section 5.1.2) are modeled.

The modeling of natural aging kinetics (Section 5.1.1) has already been published in a journal paper [123].

Yield Strength Model

The evolution of the yield strength during precipitation hardening of the WQ materials is modeled using the methodology introduced by Esmaeili *et al.*, as outlined in Table 5-1. All modeling equations used for this purpose are listed in Table 5-1. In this model, it is assumed that the shape and orientation of the hardening phases do not change during the aging process and that the precipitates act as spherical obstacles to dislocation motion. The spherical shape of the precipitates has also been assumed in previous modeling results for AA7xxx alloys [85,97]. To model the yield strength evolution during aging treatments, the strengthening components σ_{ss} and σ_{ppt} are modeled using the microstructural variable f_r.

Table 5-1 Summary of equations used in the yield strength model.

Parameter	Equation	References	Calibration parameters
σ_y	$\sigma_y = \sigma_i + \sigma_{ss} + \sigma_{ppt}$	[105]	σ_i
σ_{ss}	$\sigma_{ss} = \sigma_{0ss}(1 - f_r)^{2/3}$	[96,105]	$\sigma_{0ss} = \sigma_y^{AQ} - \sigma_i$
σ_{ppt}	Natural aging: $\sigma_{ppt} = C\ (f_r^{NA})^{1/2}$	[113]	$C = \sigma_y^{peak} - \sigma_i$
	Multi-step aging: $\sigma_{ppt} = C\ (f_r)^{3/4}$	[106]	

5.1.1 Natural Aging Kinetics of AA7xxx Alloys

Using the methodology introduced by Esmaeili *et al.* [113] for AA6xxx alloys, the strengthening relationships used to define natural aging is applied to formulate and analyze the stability of the as-quenched 7xxx alloys at room temperature. In this approach, the knowledge of the empirical linear-log relationship between yield strength and natural aging time, as well as the physically-based yield strength modeling formulation for the weak obstacle assumption [105] are used to numerically calculate the evolution of the microstructure (*i.e.,* relative volume fraction (f_r^{NA}) and size (radius, *r*) of the precipitates) that form during natural aging as follows:

$$a \ln (t_{NA}) + b = \sigma_i + C_2\, r^{1/2}\, (f_r^{NA})^{1/2} + \sigma_{0ss}\, (1 - f_r^{NA})^{2/3} \qquad \textbf{Eq. 5-1}$$

where σ_i is intrinsic strength of aluminum matrix, σ_{0ss} is the contribution from solid solution to yield strength for the as-quenched material, and C_2 is a proportionality factor related to the microstructure-strength relationship for the peak-aged (*i.e.,* long-term naturally-aged condition).

For the alloy systems with practically constant size natural aging precipitates, Eq. 5-1 reduces to a single unknown parameter equation [113]:

$$a \, ln \, (t_{NA}) + b = \sigma_i + C \, (f_r^{NA})^{1/2} + \sigma_{0ss} \, (1 - f_r^{NA})^{2/3}$$ **Eq. 5-2**

Using the experimental input parameters of a, b, C, and σ_{0ss}, Eq. 5-2 is solved to obtain f_r^{NA} as a function of t_{NA}. In Eq. 5-2, σ_i is equal to 10 MPa [97], and σ_{0ss}, and C are found as follows; assuming f_r^{NA} is 0 and 1 for the as-quenched and peak-aged conditions, respectively:

$$\sigma_{0ss} = \sigma_y^{AQ} - \sigma_i,$$ **Eq. 5-3**

$$C = \sigma_y^{peak} - \sigma_i$$ **Eq. 5-4**

For AA7075 alloy, σ_y^{peak} is assumed to be equal to $\sigma_y^{as-received\,T6}$ =498 MPa and for D-7xxx alloy, σ_y^{peak} is assumed as $\sigma_y^{2-years\ NA}$ where $\sigma_y^{2-years\ NA}$ is obtained using the logarithmic relationship in Figure 4-2 (a). The values of σ_y^{AQ} for both alloys are obtained using tensile data in Figure 4-2 (see Table 5-2 for the resultant input parameters).

Table 5-2 Input parameters for modeling of the yield strength during natural aging.

Alloys	$\boldsymbol{\sigma_{0ss}}$ (MPa)	$\boldsymbol{C}$ (MPa)	$\boldsymbol{a}$	$\boldsymbol{b}$
AA7075	130	488	20.286	282.77
D-7xxx	100	386	22.91	171.63

Following the APT observation of no significant change in the natural aging precipitate size in AA7075 APT results, Eq. 5-2 is used to reverse calculate f_r^{NA} as a function of t_{NA} for AA7075 and D-7xxx alloys. For this purpose, Eq. 5-2 is solved using Newton's numerical analysis method (in MATLAB 9.3), using the input parameters listed in Table 5-2. Table 5-2 also outlines how input parameter C is obtained from the known strength values.

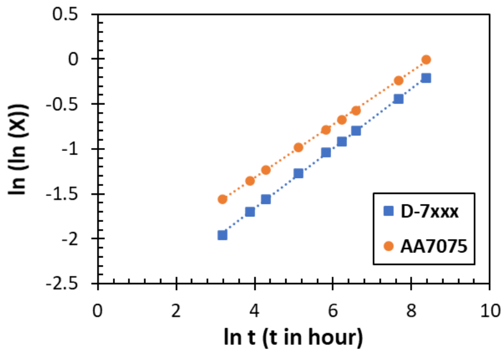

Figure 5-2 The plot of $lnln\left(\frac{1}{1-f_r^{NA}}\right)$ vs. $\ln(t_{NA})$ for the three alloys where $X = \frac{1}{1-f_r^{NA}}$ in the y-axis title.

By solving Eq. 5-2 for both alloys, f_r^{NA} is obtained as a function of t_{NA} within the range of 24 hours to 180 days. This reverse calculated data is further used to plot $lnln(\frac{1}{1-f_r^{NA}})$ vs. $ln\ (t_{NA})$. As Figure 5-2 shows, for each alloy, the plot identifies a linear relationship between $lnln(\frac{1}{1-f_r^{NA}})$ and $ln\ (t_{NA})$. These linear relationships, as in the case of AA6111 alloy [113], are indicative of the well-known JMAK equation [96,105,160], as follows:

$$f_r^{NA} = f_r = 1 - \exp\left(-kt^n\right) \quad \textbf{Eq. 5-5}$$

The kinetic parameters *n* and *k*, as obtained from Figure 5-2, are presented in Table 5-3. The two alloys have similar *n* values, suggesting similarity in the morphology of precipitates. This interpretation is consistent with the formation of the same type of precipitates, *i.e.*, spherical GP zones, during natural aging of AA7xxx alloys [46,54,161]. For better comparison, Table 5-3 also contains *n* and *k* values for three other alloys as analyzed in the next section.

Table 5-3 Natural aging kinetic parameters.

Alloys	*n*	*k* (h^{-n})
AA7075	0.3	0.08
D-7xxx	0.3	0.05
AA7050 (Ref. [69])	0.3	0.1
Al-Zn-Mg (Ref. [56])	0.3	0.04
Al-Zn-Mg (Ref. [46])	0.3	0.01

5.1.1.1 Applicability of the Reverse Calculation Approach

5.1.1.1.1 Cu-Free Al-Zn-Mg Alloys

The general applicability of the reverse calculation methodology to AA7xxx alloys is evaluated by considering the age hardening data of a Cu-free alloy (wt.%: 6.5Zn, 2.3Mg, and 0.1Zr), reported in Ref. [56]. A close examination of the hardness data for this alloy (Figure IV.2 of Ref. [56]) shows that the data falls on a single log-linear trend line when the data for the three shortest natural aging times (*i.e.*, 0.5, 1, and 2 hours) are not included. Therefore, the hardness values for the rest of the reported range (*i.e.*, 24 to 2208 hours) are used in the analysis to define the Cu-free alloy's natural aging kinetics. The input parameters used for this purpose are listed in Table 5-4.

Table 5-4 Input parameters for modeling of the yield strength during natural aging.

Alloys	$\boldsymbol{\sigma_{0ss}}$ (MPa)	$\boldsymbol{C}$ (MPa)	$\boldsymbol{a}$	$\boldsymbol{b}$	Remarks
Al-Zn-Mg (Ref. [56])	194	460	18.256	278.9	σ_y^{peak} assumed to be ≅ $\sigma_y^{peak-aged\ at\ 160℃}$ [56]. YS (MPa) is assumed to be equal to 3×hardness (HV).
Al-Zn-Mg (Ref. [46])	164	356	20.296	187.59	σ_y^{peak} is equal to $\sigma_y^{8-months\ NA}$ [46]. YS (MPa) is assumed to be equal to 3×hardness (HV).
AA7050 (Ref. [69])	160	451	23.766	228.86	σ_y^{peak} assumed as $\sigma_y^{2-years\ NA}$ [69]
AA7010 (Ref. [56])	160	540	-	-	σ_y^{peak} assumed to be ≅ σ_y^{T6} [56] Hardness (HV) is assumed to be 1/3 of the YS (MPa).
AA7108 (Ref. [5])	149	398	-	-	σ_y^{peak} assumed to be ≅ σ_y^{T6} [5] YS (MPa) is assumed to be equal to 3×hardness (HV).

Note: For all the alloys, the values of σ_{0ss} and C are obtained using the literature data as listed in Table 5-4 and Eq. 5-3 and Eq. 5-4.

The calculated f_r^{NA} values for the above ternary alloy are used to plot $lnln(\frac{1}{1-f_r^{NA}})$ vs. ln (t_{NA}) in Figure 5-3. Similar to all other cases, this plot reveals that the JMAK equation is a valid formulation to define the kinetics of natural aging. As listed in Table 5-3, the obtained *n* value for this ternary alloy is similar to the value found for AA7075 and D-7xxx alloys, while the *k* value is lower than that of the Cu-containing AA7xxx alloys in Table 5-3.

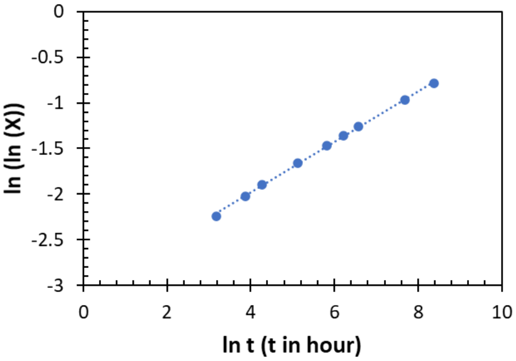

Figure 5-3 The plot of $lnln\left(\frac{1}{1-f_r}\right)$ vs. $\ln(t_{NA})$ for the Al-Zn-Mg alloy in Ref. [56] **where $X = \frac{1}{1-f_r}$ in the y-axis label.**

The validity of the JMAK formulation to define the kinetics of natural aging in AA7xxx alloys is further evaluated by using the small-angle X-ray scattering (SAXS) data for an Al-Zn-Mg alloy as reported in Figure IV.1 of Ref. [56]. Using the calculated kinetic parameters (Table 5-3), the evolution of f_r during natural aging of this alloy from 4 to 100 hours is predicted (Figure 5-4). The integrated intensity data obtained from the SAXS measurements (Q_0) is reported [162] to represent the volume fraction of precipitates ($f_{v|t}$ at time t), and thereby, the relative volume fraction of precipitates (f_r=$f_{v|t}$ /f_{peak}). Hence, the same trends for the modeled f_r and measured Q_0 with natural aging time, presented in Figure 5-4, validates the model outcome.

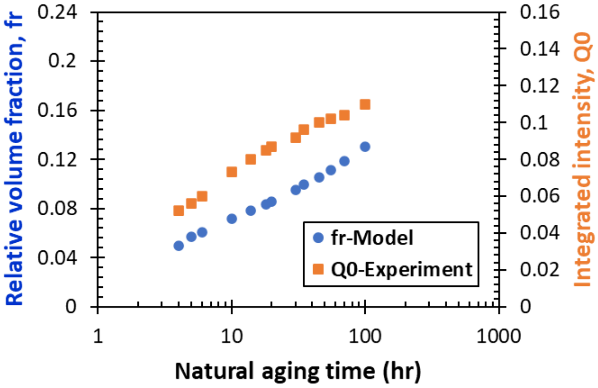

Figure 5-4 Comparison of the modeling results for f_r with the experimental data for integrated intensity obtained from Ref. [56] **for Al-Zn-Mg alloy.**

5.1.1.1.2 Copper-Containing AA7xxx Alloys

The kinetic model is also evaluated by implementing the model to predict the yield strength of the AA7010 (wt.%: 6.5Zn, 2.3Mg, 1.5Cu, 0.1Zr, 0.1Fe, and 0.1Si) alloy. The prediction results are further compared with independent data from the literature [56]. Considering the compositional characteristics, it is assumed that the AA7010 alloy has natural aging kinetic parameters similar to those of the AA7075 alloy (see Table 5-3). Using these kinetic parameters in Eq. 5-5, the evolution of f_r^{NA} during natural aging, from 6 to 648 hours, is estimated for the AA7010 alloy. The f_r^{NA} values are then used to predict YS and hardness as a function of time for the alloy. The hardness predictions are compared with the above-mentioned experimental data, as seen in Figure 5-5. The predicted and experimental results follow a similar trend, while the predictions underestimate (up to 12%) the experimental values. This underestimation may stem from the simplifying assumptions used for calculations (*i.e.*, strength-hardness conversion factor and the compositional dependence of the kinetic parameter).

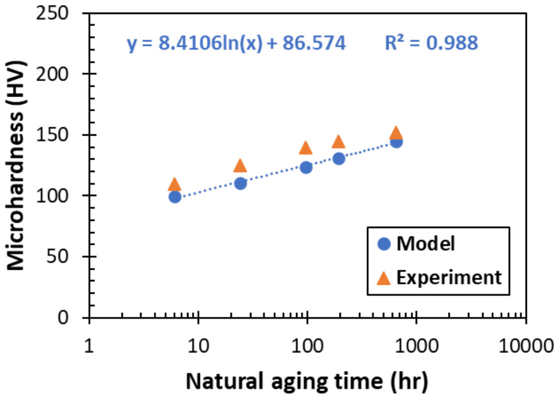

Figure 5-5 Comparison of the model predictions for the AA7010, using the kinetic parameters for AA7075, with the experimental data obtained from Ref. [38].

5.1.1.2 Influence of Composition on the Kinetics of Natural Aging in Al-Zn-Mg-(Cu) Alloys

To further investigate and compare the kinetics of natural aging in different Al-Zn-Mg-(Cu) alloys, the kinetic parameters for natural aging of copper-containing AA7050 (Figure 4-2) and a copper-free Al-Zn-Mg alloy (with a nominal composition of 4.62Zn, and 0.9Mg (wt.%)) are obtained using the yield strength and hardness data reported in references [69] and [46], respectively. The input parameters used for this purpose are listed in Table 5-4. The reverse calculation of f_r^{NA} (using Eq. 5-2) is performed for these two alloys. The calculated f_r^{NA} values for these alloys are used to plot $\ln\ln(\frac{1}{1-f_r^{NA}})$ vs. $\ln(t_{NA})$ in Figure 5-6. This figure is then used to find the natural aging kinetic parameters for the two alloys as listed in Table 5-2.

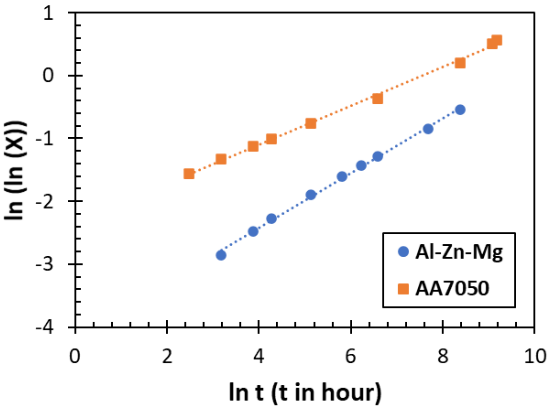

Figure 5-6 The plot of $\ln\ln\left(\frac{1}{1-f_r}\right)$ **vs.** $\ln(t_{NA})$ **for the Al-Zn-Mg alloy in Ref.** [46] **and AA7050 in Ref.** [69] **where** $X = \frac{1}{1-f_r}$ **in the y-axis label.**

As in the case of the Cu-free alloys, the estimated values for *n* are found to be 0.3. More detailed future work is necessary to elaborate on the similarity in the *n* values obtained for natural aging kinetics of AA7xxx alloys. In contrast to the similarity in the *n* values, a lower *k* value is obtained for the copper-free alloy compared to the Cu-containing AA7050 alloy. The data in Figure 5-7 shows that the *k* value increases with increasing Zn+Mg+Cu (wt.%) alloy content in the composition of these alloys. An increase in the content of the main alloying elements in the alloy results in achieving a higher supersaturation of the matrix thereby enhancing the driving force for nucleation of natural aging precipitates right after quenching. According to classical nucleation theory, an increase in the driving force for transformation will reduce the energy barrier for nucleation (ΔG^*). Consequently, the rate of nuclei formation will increase resulting in faster kinetics of natural aging.

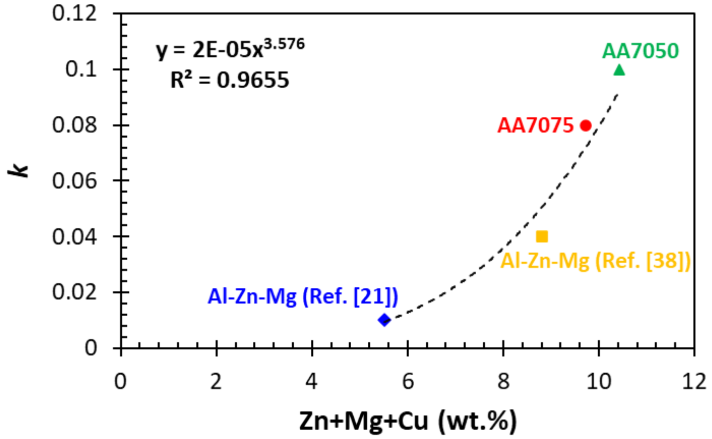

Figure 5-7 Comparison of *k* parameter vs. Zn+Mg+Cu content for the investigated AA7xxx alloys.

The variation of k with the sum of Zn+Mg+Cu (wt.%) alloy content was trial fit to a power-law (Eq. 5-6) as follows:

$$k = k_1 {C_t}^m \qquad \textbf{Eq. 5-6}$$

where C_t is the main alloying elements percentage (*i.e.*, wt.%: Zn+Mg+Cu) of the alloys and k_1, and m are constants, that were determined to be $k_1 = 0.00002$, and $m = 3.576$.

As an independent assessment of this approach to determine *k*, Eq. 5-6 is used to predict the microstructural evolution and the evolution of yield strength during natural aging of AA7108 (wt.%: 5.36Zn, 1.21Mg, 0.01Cu, 0.16Zr, 0.15Fe, and 0.08Si) using hardness and yield strength data reported in Ref. [5]. f_r^{NA} values are found using Eq. 5-5 and assuming *n*=0.3 and *k*=0.02 (according to Figure 5-7) for the alloy. The f_r^{NA} values and the parameters in Table 5-4 are then used to predict YS as a function of time during natural aging of this alloy from 24 to 672 hours. Figure 5-8 shows the predicted values for yield strength compared with the experimental data obtained from Ref. [5]. The predicted data slightly underestimates the experimental values (maximum 10%). The relatively good agreement between the predicted and experimental results for this alloy suggests that Eq. 5-6 can be used to have an approximate value for the *k* parameter, enabling natural aging predictions for various AA7xxx alloys.

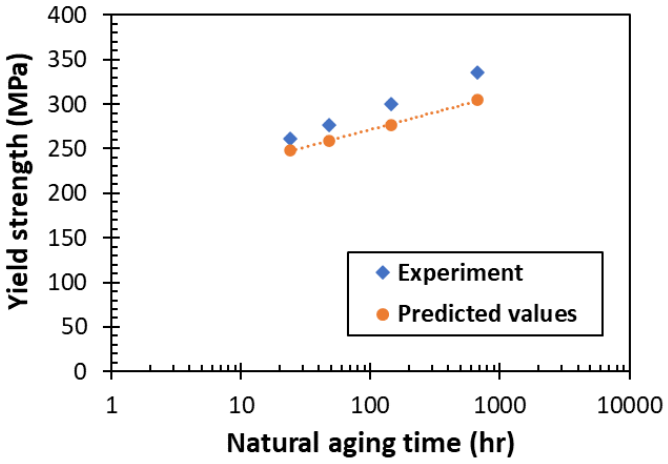

Figure 5-8 Comparison of the model-predicted yield strength values, using Equation 6, for AA7108 with the experimental data obtained from Ref. [3].

5.1.2 Multi-Step Aging Treatments of AA7075 Alloy

5.1.2.1 Secondary Natural Aging of the Pre-aged Material

5.1.2.1.1 Natural Aging Kinetics

The stability of the pre-aged samples at room temperature (secondary natural aging, SNA) is formulated and analyzed using the same approach reported for the analysis of the natural aging kinetics of the as-quenched AA7xxx alloys (Section 5.1.1). For secondary natural aging, however, the relative volume fraction of the precipitates during natural aging is assumed to be as follows:

$$f_r = f_r^0 + f_r^{SNA} \qquad \textbf{Eq. 5-7}$$

where f_r^{SNA} is the relative volume fraction of precipitates formed during secondary natural aging. In this equation, f_r^{SNA} is a function of the secondary natural aging time (t_{SNA}).

The evolution of hardness for the A7075 alloy in the PA condition follows a linear logarithmic relationship with time during secondary natural aging, as previously reported in Section 4.1.2.2.1. Therefore, it is assumed that the same trend holds for the evolution of the yield strength of the AA7075-PA during secondary natural aging as a function of t_{SNA}, as formulated in Eq. 5-2 and replacing t_{NA} with t_{SNA}. This equation is then used to numerically calculate the evolution of f_r. For secondary natural aging, as in the case of natural aging of as-water-quenched AA7075 [163], it is assumed that there is no significant change in the natural aging precipitate size during subsequent natural aging. The equations used for the back-calculation analysis to formulate f_r and the yield strength modeling equations are reported in the chart shown in Figure 5-9.

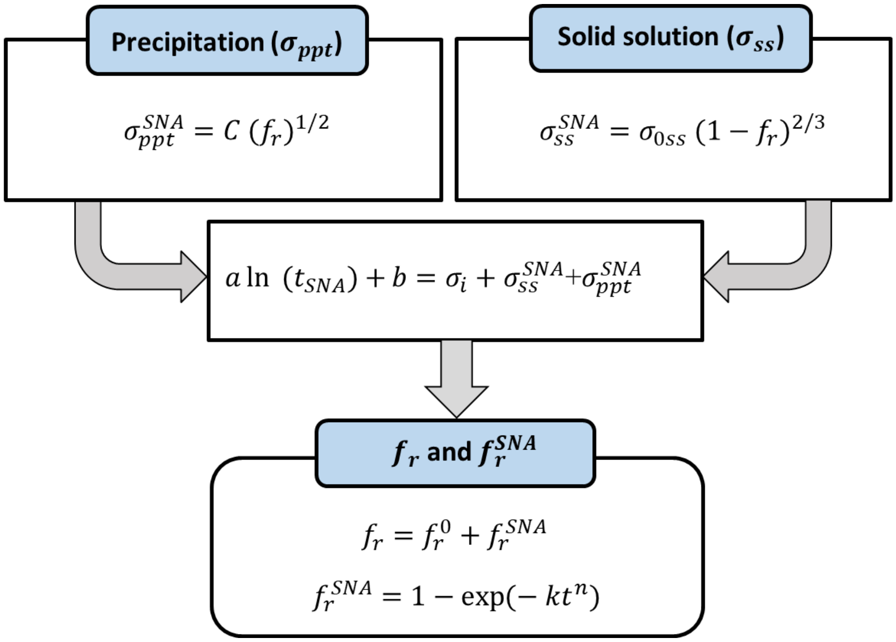

Figure 5-9 Schematic outline of the modeling of natural aging kinetics for pre-aged materials (PA=Pre-Aged, SNA= Secondary Natural Aged).

The modeling equations in Figure 5-9 are used to find f_r as a function of t_{SNA} and to analyze the kinetics of secondary natural aging for the AA7075 alloy in the PA condition. The yield strength modeling formulation (reported in Figure 5-9) is then solved using Newton's numerical analysis method (in MATLAB 9.3), and the input parameters that are listed in Table 5-5. The f_r^{SNA} values are then estimated using the calculated f_r values and the f_r^0 value for the PA condition (Figure 4.14).

Table 5-5 Input parameters for modeling of the yield strength during natural aging of the AA7075-PA.

Parameter	Value
a	7.4
b	403
C (MPa)	488
σ_{0ss}(MPa)	130
σ_i	10

Plotting $lnln(\frac{1}{1-f_r^{SNA}})$ vs. $ln\ (t_{SNA})$ yields a straight line, as shown in Figure 5-10. Therefore, the evolution of f_r^{SNA} can be formulated by using the JMAK relationship. *n* and *k* parameters for the secondary natural aging of AA7075 alloy in the PA condition are obtained as 0.3 and 0.02 $hr^{-0.3}$, respectively. The obtained *n* value is similar to the value found for the natural aging of water-quenched AA7075, whereas the *k* value is lower than that of the WQ sample (see Table 5-3). The similarity in the *n* values obtained for the evolution of natural aging of AA7075 in the PA and WQ conditions is ascribed to the similarity in the morphology of precipitates that form during secondary natural aging in the microstructure of this sample, as suggested in Section 5.1.1.1 [123] for the natural aging of as-water-quenched AA7xxx alloys.

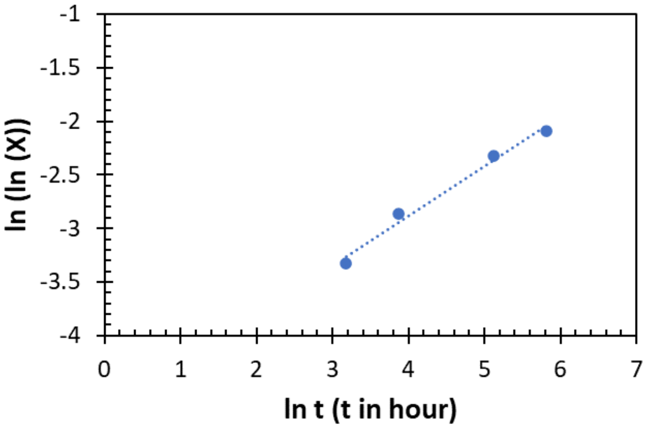

Figure 5-10 The plot of $lnln\left(\frac{1}{1-f_r^{SNA}}\right)$ vs. $\ln(t_{NSA})$ where $X = \frac{1}{1-f_r^{SNA}}$ in the y-axis label.

5.1.2.1.2 Modeling of Yield Strength

The yield strength model for the natural aging of pre-aged AA7xxx alloys has been validated by implementing it to predict the yield strength and hardness of the AA7075 alloy and comparing the results with experimental data. The evolution of f_r^{SNA} during the natural aging of the AA7075-PA (up to 2880 hours) has been predicted using the JMAK equation for the kinetic model and the kinetic parameters reported in Section 5.1.2.1.1. The evolution of f_r during secondary natural aging has been then calculated using the evolution of f_r^{SNA} and f_r^0 value for the PA condition in Eq. 5-7. The evolution of f_r and the calibrated parameters in Table 5-5 are then used in yield strength modeling formulation reported in Figure 5-9 to model the evolution of yield strength during natural aging of this alloy in the PA condition. It should be noted that σ_y^{peak} has been assumed to be equal to the peak strength of AA7075 during aging at 120°C, that is the T6 condition. The modeled yield strength values have then been converted to hardness values by assuming that the yield strength in MPa was approximately equivalent to the Vickers hardness number multiplied by 3 [56,123]. A comparison of the modeling and experimental results is shown in Figure 5-11. It is evident that the model and experimental results agree very well (up to a difference of 4 HV). The difference between the experimental and modeling results can be due to the approximations made for the calibration parameters and the simplifying assumptions used for calculations.

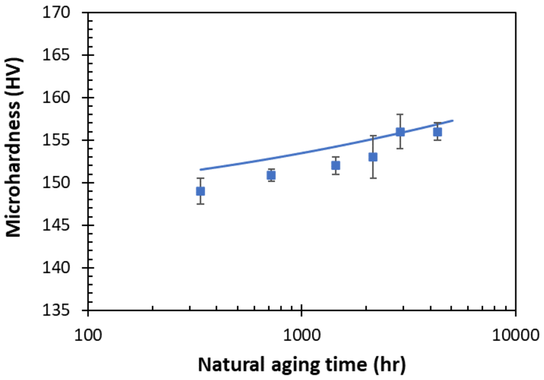

Figure 5-11 Comparison of the model-predicted hardness (line) for pre-aged AA7075 with experimental measurements (symbols).

5.1.2.2 Artificial Aging of Pre-Aged AA7075

5.1.2.2.1 Modeling of Precipitation Kinetics

The precipitation kinetics during artificial aging treatments of the alloy in the PA condition are predicted using a kinetic model developed by Esmaeili and Lloyd for AA6xxx alloys [98]. The modeling equations are listed in Table 5-6.

Table 5-6 Summary of equations used in modeling of precipitation kinetics for artificial aging of the material in the PA condition.

Equation type	Parameter	Equation	References
Modeling equation	f_r	$f_r = 1 - (1 - f_r^0)\exp(-kt)^n$	[98]
	k	$k = k_0 \exp(-Q_A/RT)$	[98]
Experimental analysis equation	f_r^0	$f_r^0 = \frac{\int_0^{t_{peak}} \left(\frac{dQ}{dt}\right) dt\vert_{AQ+AA} - \int_0^{t_{peak}} \left(\frac{dQ}{dt}\right) dt\vert_{\mathrm{PA+AA}}}{\int_0^{t_{peak}} \left(\frac{dQ}{dt}\right) dt\vert_{AQ+AA}}$	[96,105]

The kinetic parameters k and n for artificial aging treatments of the alloy in PA condition are determined by experimental measurement of f_r as a function of temperature at three different temperatures and plotting the $\ln \ln \frac{(1-f_r^0)}{1-f_r}$ vs. $\ln t$. The slop and y-axis intercept of the resultant lines (Eq. 2-7) are then used to obtain the necessary values. The experimentally obtained values for the evolution of f_r during the artificial aging of AA7075- PA, reported in Section 4.1.2.3.2, are used to calculate the k values. The resulting n values for all the three temperatures are close to unity. The resulting k values are used to obtain the kinetic parameters of k_0 and Q_A through that equation (as shown in Figure 5-12).

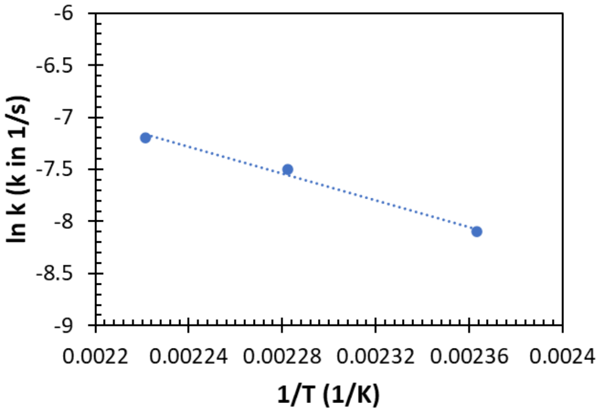

Figure 5-12 The Arrhenius plot to determine the kinetic parameters for artificial aging of AA7075 in the PA condition.

The kinetic parameters for the artificial aging of the material in the PA condition are summarized in Table 5-7. The activation energy (Q_A) compares very well with the activation energy required for the migration of Mg atoms in Al-Zn-Mg alloys (58 kJ/mol [164]). However, it is higher than the activation energy required for the migration of Zn and Zn-vacancy pairs in Al, which are 39 kJ/mol and 43 kJ/mol, respectively [164]. This finding suggests that the growth rate of precipitates during the final aging step of the pre-aged AA7075 alloy may be controlled by the migration of magnesium atoms.

Table 5-7 Kinetic parameters for artificial aging of the AA7075-PA alloy.

Parameter	Value
k_0 (1/s)	1.4×10^3
Q_A (kJ/mol)	54

5.1.2.2.2 Modeling of Yield Strength

The yield strength of the pre-aged AA7075 alloy is modeled for the third aging step using the modeling equations adapted from Ref. [98,105,106,113], as reported in the chart shown in Figure 5-13. For this purpose, the evolution of f_r is modeled during artificial aging of the pre-aged AA7075 using the equations reported in Figure 5-13 for f_r and the kinetic parameters listed in Table 5-5.

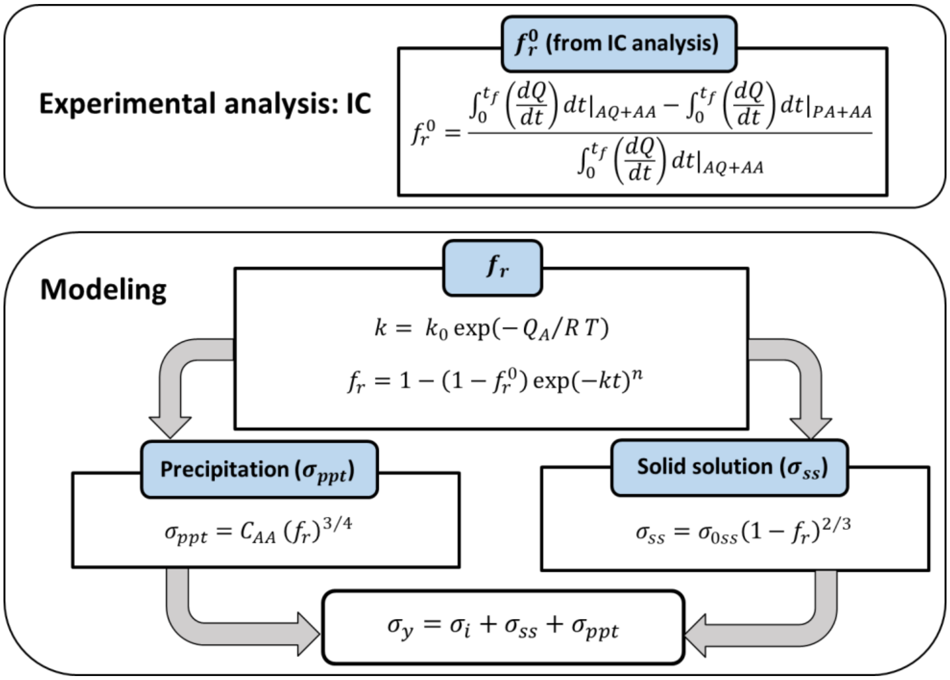

Figure 5-13 Schematic outline of yield strength modeling for pre-aged materials (PA=Pre-Aged, AA=Artificially-Aged, AQ=As-Quenched).

The evolution of yield strength in the AA7075-PA alloy during artificial aging at 177°C up to the peak-aged condition is predicted using the modified-weak obstacle assumption (as described in Section 2.4.2) for σ_{ppt}. This modeling assumption has been selected based on previous studies [106,112] where using weak obstacle assumptions resulted in a better match between predicted and experimental yield strength values for artificial aging treatments of AA7xxx alloys, compared to strong obstacle modeling results. The calibration parameters used to model the yield strength are listed in Table 4-5.

An excellent prediction of the yield strength is demonstrated, as shown in Figure 5-14. It is concluded that the modeling approaches developed by Esmaeili and co-workers [98,105] are applicable for modeling the precipitation kinetics and hardening during multi-step aging treatments of the AA7075 alloy. For the yield strength modeling, the modified-weak model ($\sigma_{ppt} = C\ (f_r)^{3/4}$) has been found to provide excellent predictions for the yield strength values of the PA sample and throughout the artificial aging process. As a result, it is recommended for use in predicting the evolution of yield strength during artificial aging treatments of AA7xxx alloys.

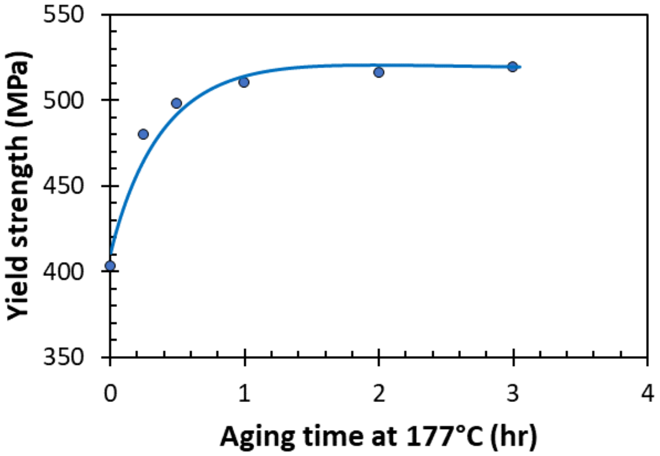

Figure 5-14 Comparison of the model-predicted yield strength (line) to experimental measurements (symbols) during aging at 177°C for the yield strength of AA7075.

5.2 Modeling of Precipitation Hardening in Die-Quenched AA7075

This section presents (a) the general yield strength model applied to model precipitation hardening, (b) the modeling of natural aging kinetics of AA7075-DQ (Section 5.2.1), and (c) the microstructural and yield strength evolution of the AA7075-DQ+PA alloy during subsequent artificial aging (Section 5.2.2), where recovery and precipitation hardening occur simultaneously.

Yield Strength Model

The evolution of yield strength during aging treatments for the DQ material is modeled using the equations for modeling listed in Table 5-8. In general yield strength modeling equation, m is a hardening exponent that increases from a value of 1 for shearable precipitates to a value of 2 for non-shearable precipitates. In this study, it is assumed that m =1. A comparison between the size of precipitates obtained from the current TEM study (Figure 4-32 (b)) and those reported by Danh *et al.* for the shearable to non-shearable transition in an AA7075 alloy (6.9$<$ R_c=13.2 nm) confirms this assumption.

To model the evolution of σ_{ss}, it is assumed that the loss of solutes during the die-quenching process (resulting from the slower quench rate compared to that of water-quenching) is negligible. This assumption is supported by experimental observations of very similar hardness values obtained for the alloy in both the as-WQ and as-FAQ conditions.

Table 5-8 Summary of equations used in the yield strength model.

Parameter	Equations	References	Calibration parameters
σ_y	$\sigma_y = \sigma_i + \sigma_{ss} + \left(\sigma_{ppt}^m + \sigma_d^m\right)^{1/m}$	[97,106,109,110]	–
σ_{ss}	$\sigma_{ss} = \sigma_{0ss}(1 - f_r)^{2/3}$	[96,105]	$\sigma_{0ss} = \sigma_y^{AQ} - \sigma_i$
σ_{ppt}	Natural aging: $\sigma_{ppt} = C\ (f_r^{NA})^{1/2}$	[113]	$C = \sqrt[m]{(\sigma_y^{Peak} - \sigma_i)^m - (\sigma_d^{peak})^m}$ where σ_d^{peak} is the contribution of dislocations to the yield strength of the alloy at peak-aged condition [106].
	Multi-step aging: $\sigma_{ppt} = C\ (f_r)^{3/4}$	[106]	
σ_d	$\sigma_d = MG\alpha b\sqrt{\rho}$	[104,165,166]	–

5.2.1 Kinetics of Natural Aging

The natural aging kinetics of the AA7075-DQ alloy are analyzed using the reverse yield strength modeling methodology described in Section 5.1.1. Using the empirical linear-log relationship for the yield strength and the yield strength modeling formulation for the DQ material (outlined in Table 5-8), the evolution of the relative volume fraction (f_r^{NA}) of precipitates that form during natural aging of the DQ material is numerically calculated as:

$$\sigma_y^{DQ+NA} = a\ln(t_{NA}) + b_1 = \sigma_i + C\ (f_r^{NA})^{1/2} + \sigma_{0ss}\ (1 - f_r^{NA})^{2/3} + MG\alpha b\sqrt{\rho_{NA}}$$ **Eq. 5-8**

Hardness values measured between 24 hours and 365 days are used to determine the natural aging kinetics. Microhardness data is utilized to estimate the evolution of yield strength during the natural aging of this alloy. It is assumed that the yield strength in MPa is approximately equivalent to the measured Vickers hardness number multiplied by 3. To obtain the evolution of f_r^{NA} as a function of t_{NA}, Eq. 5-8 is solved using Newton's numerical analysis method in MATLAB 9.3 with the calibration parameters listed in Table 5-9.

Table 5-9 Input parameters for modeling of the yield strength during natural aging of AA7075-DQ.

Parameter	Value	Remarks
σ_i (MPa)	10	-
a (MPa)	13.4	Obtained from the hardness measurements results. $\sigma_{y\ (NA)} = a \ln(t_{NA}) + b_1$
b_1 (MPa)	362.6	Obtained from the hardness measurements results
C (MPa)	407	Assumed to be equal to the value of C_{AA} for the DQ+PB condition. $C = \sigma_y^{peak} - \sigma_i - \sigma_d^{peak}$
σ_{0ss} (MPa)	130	Obtained from tensile testing experiments (Ref. [123]). $\sigma_{0ss} = \sigma_y^{as-WQ} - \sigma_i$
ρ_{NA} (m^{-2})	3.69×10^{14}	Assumed to be equal to the ρ_{PA} obtained from TEM analysis.
α	0.3	Ref. [109]
M	2	Ref. [83,167]
G (GPa)	25. 4	Ref. [109]
b (nm)	0.286	Ref. [109]

By plotting $\ln\ln\left(\frac{1}{1-f_r^{NA}}\right)$ vs. $\ln(t_{NA})$, as shown in Figure 5-15, a linear relationship is indicative of the JMAK equation [96,105,160]; *i.e.*, $f_r^{NA} = 1 - \exp(-kt^n)$. The JMAK kinetic parameters for natural aging of AA7075-DQ are *n*=0.3 and *k*=0.06. The obtained value of *n* is similar to the value found for AA7075 in the WQ condition. This similarity may suggest a similarity in the morphology of precipitates, as discussed in the context of natural aging of AA7xxx alloys in the WQ condition. The lower value of *k* obtained for the DQ sample indicates slower kinetics of natural aging compared to the AA7075-WQ (refer to Table 5-3). Excess vacancies formed during quenching facilitate the nucleation of precipitates during aging by increasing diffusion rates or relieving misfit strain energies (ΔG_s) [10]. Therefore, the reduction in the supersaturation of vacancies in the material in the as-DQ condition (as discussed in Section 4.2.1), can lead to an increase in the activation energy required for atomic migration (ΔG_m) and an increase in the energy barrier for the nucleation (ΔG^*) of natural aging precipitates. Therefore, the rate of nuclei formation for Zn-Mg precipitates will decrease during the natural aging of the material in the DQ condition. This results in a slower kinetics of natural aging compared to the WQ condition.

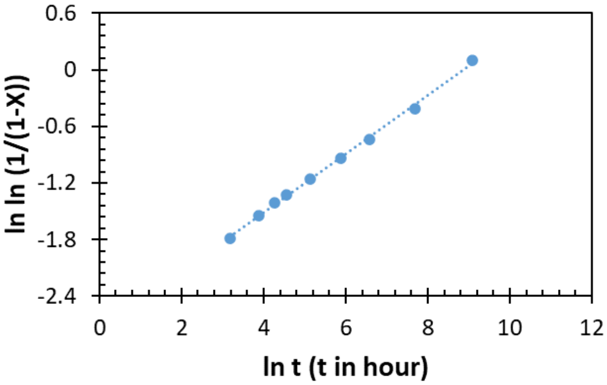

Figure 5-15 The plot of $lnln\left(\frac{1}{1-f_r^{NA}}\right)$ vs. $\ln(t_{NA})$ for AA7075-DQ where $X = \frac{1}{1-f_r^{NA}}$ in the y-axis title.

5.2.2 Artificial Aging of the Pre-Aged Material

The process model described in this section consists of (1) a microstructure model to predict the evolution of the relative volume fraction of precipitates and (2) a yield strength model to predict the strengthening response of the DQ+PA condition during subsequent artificial aging (*e.g.*, automotive PBC treatment).

5.2.2.1 Modeling of Precipitation Kinetics

The evolution of the relative volume fraction of precipitates during the artificial aging process of the material in the DQ+PA condition can be predicted by adapting the modeling equation (Eq. 2-2) that was developed for the artificial aging of AA6xxx alloys in pre-aged conditions [98]. Following Baghbanaghaei [106], who further included the effect of deformation on precipitation during artificial aging of pre-aged conditions, the evolution of f_r during artificial aging treatments of a die-quenched and pre-aged material can be found according to the following equation:

$$f_r = 1 - (1 - f_r^0) \exp\left(-k_{eff} t\right)^n \qquad \textbf{Eq. 5-9}$$

In this equation, n is assumed to be equal to unity [160], f_r^0 is the relative volume fraction of precipitates in the DQ+PA material, at the beginning of the final artificial aging step, and k_{eff} is a temperature-dependent constant that describes the precipitation rate in the presence of dislocations. According to Eq. 5-9, the residual dislocations which are primarily generated during die-quenching, can alter the precipitation kinetics in the microstructure of the pre-aged alloy by enhancing the diffusional mechanisms. The evolution of dislocation density during the artificial aging treatment of the alloy in the DQ+PA condition is estimated using modeling approaches, which will be described in the following section. The equations used for modeling the evolution of f_r in this section are listed in the chart shown in Figure 5-16.

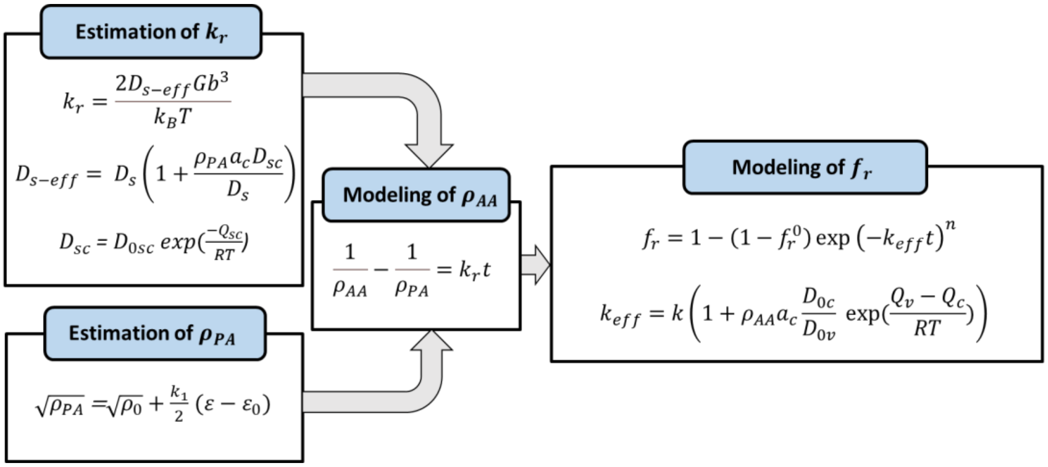

Figure 5-16 Schematic outline for modeling the evolution of relative volume fraction of precipitates during artificial aging of the material in the DQ+PA condition (Note: The calculated and the calibration parameters in this chart are defined in the next sections).

5.2.2.1.1 Estimation of Dislocation Density During Artificial Aging of the Alloy in DQ+PA Condition

During the artificial aging of the material in die-quenched+pre-aged condition (DQ+PA), static recovery and precipitation are interdependent processes that occur. To determine k_{eff}, it is necessary to model the evolution of dislocation density (ρ) during artificial aging of the alloy in the DQ+PA condition (*i.e.,* the kinetics of the reduction in dislocation density during aging).

In the current model, the commonly reported empirical relationship for predicting the kinetics of recovery during aging treatments, has been utilized [168]:

$$\frac{d\rho}{dt} = -k_r \rho^p \qquad \textbf{Eq. 5-10}$$

where k_r denotes the rate constant. p is equal to 2 for dislocation-dislocation annihilation processes and 1 for dislocation adsorption at grain boundary processes [168,169]. Based on the TEM observations of dislocations and their substructures (*i.e.*, dislocation tangles and subgrain boundaries), m is chosen to be equal to 2 in this study. Integrating Eq. 5-10 results in [168,169]:

$$\frac{1}{\rho_f} - \frac{1}{\rho_i} = k_r t \qquad \textbf{Eq. 5-11}$$

For the artificial aging of the alloy in the DQ+PA condition, the initial dislocation density (ρ_i) is equal to the dislocation density of the alloy after the pre-aging treatment (ρ_{PA}). The dislocation density in the final condition (ρ_f) represents the dislocation density of the alloy in the DQ+PA condition during the subsequent artificial aging treatment (ρ_{AA}). The recovery rate constant (k_r) is defined as [168,170]:

$$k_r = \frac{2D_s b\Gamma}{k_B T} \qquad \textbf{Eq. 5-12}$$

where D_s is the self diffusivity coefficient, k_B is Boltzmann constant and Γ is the line tension of dislocations which is given by [170]:

$$\Gamma = Gb^2 \qquad \textbf{Eq. 5-13}$$

The self diffusivity coefficient is given as [171]:

$$D_s = D_{0s}\, exp\left(\frac{-Q_s}{RT}\right) \qquad \textbf{Eq. 5-14}$$

in which D_{0s} is the pre-exponential factor for self-diffusion and Q_s is the activation energy for self-diffusion. It should be noted that Eq. 5-12 assumes that dislocation climb is the dominant mechanism controlling dislocation mobility and the kinetics of recovery [168,170]. Although different mechanisms of recovery may occur concurrently during heat treatments, such as artificial aging, the above-mentioned assumption is made to simplify the model.

In the case of a material that has been die-quenched, the self-diffusivity of the material is improved due to the presence of dislocations and their ability to enhance the diffusion mechanisms. According to Eq. 5-12, recovery process is a diffusion-controlled process. To account for the effect of dislocation density in a die-quenched and pre-aged material on the recovery rate constant, the equation proposed by Hart [172] (later modified by Frost and Ashby [173]) is used. This equation sums up the contributions from self-diffusion in the bulk (D_s) and self-diffusion through dislocation cores (D_{sc}) as:

$$D_{s-eff} = D_s\left(1 + \frac{\rho a_c D_{sc}}{D_s}\right) \qquad \textbf{Eq. 5-15}$$

where D_{s-eff} is the effective self-diffusion coefficient. The self-diffusion coefficient in the presence of dislocation cores, D_{sc}, is given as:

$$D_{sc} = D_{0sc}\, exp\, (\frac{-Q_{sc}}{RT}) \qquad \textbf{Eq. 5-16}$$

D_{0sc}, and Q_{sc} are the pre-exponential factor and activation energy for self-diffusion through the dislocation cores, respectively. In Eq. 5-12, D_s is replaced by D_{s-eff} to consider the effect of the deformation level in a die-quenched material on the recovery rate constant during subsequent aging treatments.

5.2.2.1.2 Estimation of ρ_{PA}

To estimate the dislocation density of the alloy in the DQ+PA condition (ρ_{PA}), the dislocation density of the as-DQ sample must first be predicted. Similar to the approach previously developed for predicting the evolution of immobile dislocation density in aluminum alloys [106,174], a simplified mathematical treatment of microstructural evolution is adapted using the Kocks/Mecking model (KM-model) [109,165]. According to the KM-model, the evolution of strain can be described based on the evolution of the total dislocation density ρ_i, as:

$$\frac{\partial\rho}{\partial\varepsilon} = (k_1{\rho_i}^{1/2} - k_2\rho_i) \qquad \textbf{Eq. 5-17}$$

where ε is the applied plastic strain and k_1 and k_2 are constants. In this equation, the first term pertains to the storage of dislocations resulting from the trapping of dislocations by one another, which is associated with the statically stored dislocation density). The second term, on the other hand, pertains to the annihilation of dislocations which is related to dynamic recovery. Both terms assume a uniform spatial dislocation distribution. This assumption is reasonable for the case of small strain levels, such as those applied in this study, where the accumulation of dislocations at the subgrain boundaries is not significant in the microstructure of the deformed material. To further simplify Eq. 5-17, it is assumed that dynamic recovery during the die-quenching process is negligible (*i.e.*, $k_2\rho_i = 0$). Therefore, integrating Eq. 5-17 yields:

$$\sqrt{\rho_{DQ}} = \sqrt{\rho_{i0}} + \frac{k_1}{2}(\varepsilon - \varepsilon_0) \qquad \textbf{Eq. 5-18}$$

This equation relates the applied plastic strain ε in the die-quenching process to the residual dislocation density in the as-DQ sample (ρ_{DQ}). Assuming that static recovery is negligible during the pre-aging treatment (ρ_{DQ}=ρ_{PA}), the estimated value for ρ_{DQ} from Eq. 5-18 can be used in Eq. 5-11 to predict the evolution of the dislocation density during artificial aging of the alloy in the DQ+PA condition as a function of pre-strain (during die-quenching). To examine the validity of the assumption of negligible recovery of dislocations during pre-aging and to theoretically determine the dislocation density of the AA7075-DQ+PA sample, two distinct approaches can be pursued:

(i) The difference in yield strength value between the as-WQ AA7075 sample ($\sigma_{y|as-WQ}$) and the as-DQ (15%) sample ($\sigma_{y|as-DQ}$) is assumed to be due to the contribution of dislocations to the yield strength (*i.e.*, $\sigma_{y|as-DQ} - \sigma_{y|as-WQ} = \sigma_d = 78\ MPa$). By using $\sigma_d = 78\ MPa$ in the equation for σ_d (reported in Table 5-8), the dislocation density for the as-DQ sample is found to be 3.3× $10^{14}\ m^{-2}$, which is very close to the dislocation density value for the alloy in the DQ+PA condition (ρ_{PA}), listed in Table 5-10. This finding also supports the assumption that only a negligible amount of dislocation annihilation takes place during the pre-aging process.

(ii) Using Eq. 5-10, Eq. 5-11, and the value for k_r reported in Table 5-10 and assuming $\rho_f = \rho_{PA}$ (the values listed in Table 5-11) and $\rho_i = \rho_{2NA}$, the dislocation density of the 2-day naturally aged alloy (at the beginning of intermediate aging at 100°C) is estimated as $3.7 \times 10^{14}\ m^{-2}$ (comparable to the value for ρ_{PA}, as listed in Table 5-10). This further supports the assumption that the annihilation of dislocation during artificial aging at 100°C is not significant.

5.2.2.1.3 Model Calibration

The model was calibrated using experimental data from the current study, as well as selected literature data. The calibration parameters are listed in Table 5-10. The activation energy (Q_c) has been reported to be in the range of 80-88 kJ/mol. The lower and upper limits of this range are the values of Q_c for the self-diffusion of aluminum [13,173] and the diffusion of magnesium solutes in aluminum alloys [175], respectively. The upper limit of this range has been chosen as Q_c for modeling purposes, assuming that Mg diffusion-limited growth of precipitates happens during aging of the AA7075-PA (as found in Section 5.1.2.3.2). The value of k_{eff} has been predicted using the equation for k_{eff} (listed in Figure 5-16), Eq. 5-11, and the calibration parameters provided in Table 5-11.

To estimate the rate of dislocation annihilation during artificial aging of the alloy in the DQ+PA condition, k_r is predicted using Eq. 5-12, Eq. 5-13, and the calibration parameters listed in Table 5-11. For bulk diffusivity, using Eq. 5-15 in Eq. 5-12, k_r is estimated as $1.17 \times 10^{-18}\ m^2/s$. To estimate the effect of dislocations on self-diffusivity (D_{s-eff}), using Eq. 5-15 and Eq. 5-16 in conjunction with Eq. 5-12, and the calibration parameters provided in Table 5-11, k_r is estimated as $1.6 \times 10^{-17}\ m^2/s$. Using the values of ρ_{PB} and ρ_{PA} obtained from the TEM analysis, in Eq. 5-11, k_r is experimentally determined to be $1.7 \times 10^{-18}\ m^2/s$. It has been observed that there is very good agreement between the predicted value for k_r, assuming bulk self-diffusion (D_s), and the experimental value determined from TEM analysis. In the case of D_{s-eff}, the discrepancy between the predicted and experimental values for k_r may suggest that the effect of dislocations (*i.e.,* dislocation cores) on both D_s and the kinetics of recovery should not be significant at the given aging temperature. However, this discrepancy may attributed to the simplifying assumptions and approximations utilized for the calibration parameters. For instance, the activation energy required for the kinetics of recovery may evolve during aging due to the evolution of dislocation density [168]. Moreover, the effects of grain boundaries, dispersoids, and precipitates on the kinetics of recovery (*i.e.,* their effect on dislocation pinning and retardation of recovery [176]) have not been considered in the modeling equations. For modeling purposes in this study, the experimentally obtained value for k_r is used in Eq. 5-11 to approximate the evolution of dislocation density during the aging of the alloy in the DQ+PA condition.

Eq. 5-18 is calibrated by determining a constant value of k_1, which is reported to be a characteristic of the material under investigation [109,177]. Assuming that the static recovery occurring during the pre-aging treatment is negligible, the dislocation density value of the alloy in the DQ (26%)+PA condition ($\rho_{DQ26+PA}$), as listed in Table 5-10, is assumed to be equal to ρ_{DQ26}, and is therefore used in Eq. 5-18 to determine k_1, as presented in Table 5-10. Based on Eq. 5-18, the dislocation density value for the DQ (15%) alloy (ρ_{DQ}) is estimated to be $3.48 \times 10^{14}\, m^{-2}$. It has been observed that there is a reasonable agreement between the estimated value of ρ_{DQ} obtained from the model and the value determined from the analysis of TEM results for the DQ+PA material ($3.69 \times 10^{14}\, m^{-2}$), taking into consideration the negligible recovery of dislocations that occur during the pre-aging treatment.

Table 5-10 Input parameters for modeling of f_r during artificial aging of the AA7075-DQ+PA at 177°C.

Parameter	Value	Remarks
$\rho_{i0}\ (m^{-2})$	10^{12}	Initial immobile dislocation density in Al obtained from Ref. [174].
$a_c \frac{D_{0c}}{D_{0v}}$	1.2×10^{-19}	Assumed to be similar to the experimentally obtained values for other AA7xxx alloys in Ref. [178].
Q_v (kJ/mol)	120	Assumed to be similar to the experimentally obtained values for other AA7xxx alloys in Ref. [178].
Q_c (kJ/mol)	88	From Ref. [175]
Q_s (kJ/mol)	142	From Ref. [10]

$D_{0s}\ (m^2/s)$	1.7×10^{-4}	From Ref. [173]
$a_c D_{0sc}\ (m^4$/s)	7×10^{-25}	From Ref. [173]
Q_{sc} (kJ/mol)	82	From Ref. [173]
$R\ (\frac{J}{mol.K})$	8.314	-
$k_1(m^{-1})$	2.3×10^{8}	Estimated using the values for ρ_{i0} and ρ_{DQ26} in Eq. 5-18.
$k_r\ (m^2/s)$	1.7×10^{-18}	Experimentally obtained value, using the values of ρ_{PB} and ρ_{PA}, obtained from the TEM analysis, in Eq. 5-11.
$k_B\ (\frac{m^2Kg}{s^2K})$	1.38×10^{-23}	-
k	0.0007	Found using IC on the AA7075-PA at 177°C (Section 5.1.1.1.2).
$\rho_{DQ26+PA}\ (m^{-2})$	8.9×10^{14}	$\rho_{DQ26+PA}$ is estimated using the value for $\rho_{DQ26+PB}$ and Eq. 5-11.
$\rho_{DQ26+PB}\ (m^{-2})$	2.37×10^{14}	Obtained from TEM analysis
$\rho_{PA}\ (m^{-2})$	3.69×10^{14}	Obtained from TEM analysis
$\rho_{PB}\ (m^{-2})$	1.72×10^{14}	Obtained from TEM analysis
G (GPa)	25.4	Ref. [109]
b (nm)	0.286	Ref. [109]

5.2.2.1.4 Comparison of Model Predictions and Experimental Results

The evolution of f_r during the artificial aging of the AA7075-DQ+PA at 177°C is modeled using Eq. 5-9. The results are then compared with the IC data (as reported in section 4.2.2.1.2.1) and presented in Figure 5-17. Eq. 5-9 is then applied to model the evolution of f_r, as shown in Figure 5-17. The model's predictions are in excellent agreement with the experimental data, with a maximum difference of 4%. The discrepancy between the experimental and modeling results may be attributed to potential errors arising from the application of literature data (which provides approximate values) for the Q_v, Q_c, and $a_c\frac{D_{0c}}{D_{0v}}$ parameters (*i.e.*, the effect of alloy composition on these parameters). This may also be related to the possible evolution of precipitation, as dictated by the thermodynamic and kinetic factors of the precipitation sequence during the final aging step, which has not been considered in the model.

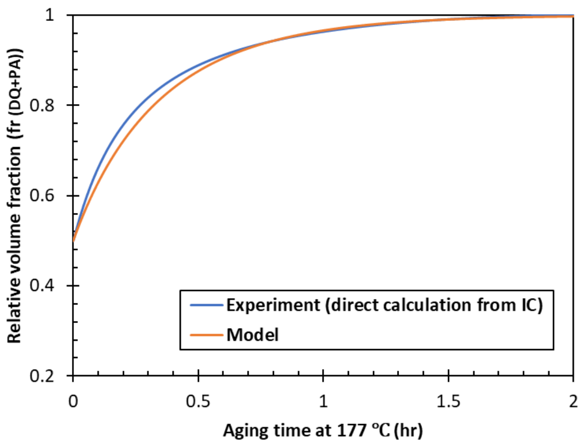

Figure 5-17 The comparison of the predicted and measured values of $f_{r\,(DQ+PA)}$ during artificial aging of the AA7075- DQ+PA at 177°C.

5.2.2.2 Modeling of Yield Strength

The equations implemented for modeling the yield strength evolution during artificial aging of the material in the DQ+PA condition (discussed in Section 5.2) are summarized in the chart shown in Figure 5-18.

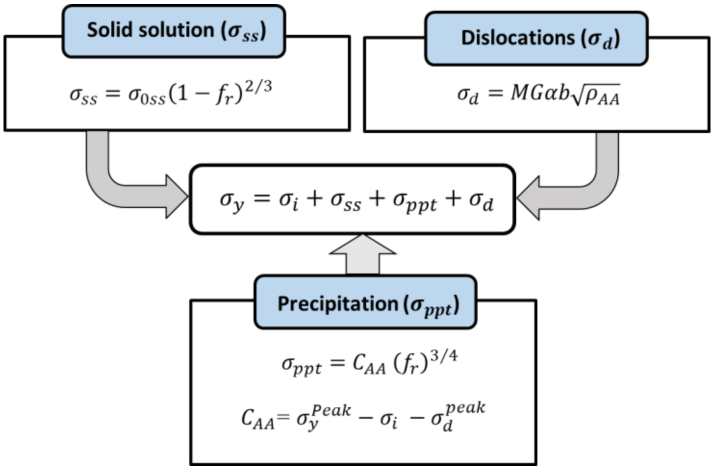

Figure 5-18 Schematic outline of yield strength modeling for artificial aging of the material in the DQ+PA condition (AA=Artificial Aging).

5.2.2.2.1 Calibration of Yield Strength Model

To determine the calibration parameter C_{AA} for the artificial aging of AA7075-DQ+PA at 177°C, the value of σ_{ppt} for the DQ+PB material is estimated. σ_{ppt}^{DQ+PB} is estimated using the estimated values of σ_{ss}^{DQ+PB} and σ_{d}^{DQ+PB} in the general yield strength modeling equation ($\sigma_y\ in$ Figure 5-18). Then, using the values of σ_{ppt}^{DQ+PB} and f_r^{DQ+PB} in the σ_{ppt} equation (reported in Figure 5-18), C_{AA} is calculated as listed in Table 5-11.

The second approach for estimating C_{AA} for artificial aging of AA7075-DQ+PA at 177°C is to use the values for peak strength (*i.e.*, σ_y^{peak}) and σ_d^{peak} (listed in Table 5-11) in the C_{AA} equation (reported in Figure 5-18). A reasonable agreement is observed between the value of C_{AA} obtained using the second approach and the value reported in Table 5-11 (*i.e.*, C_{AA}=412 MPa vs. 407 MPa).

Table 5-11 Calibration parameters for modeling the evolution of yield strength during artificial aging of the AA7075-DQ+PA at 177°C.

Parameter	Value	Remarks
α	0.3	Ref. [109]
M	2	Ref. [83,97,167]
σ_{0ss} (MPa)	130	Ref. [123]
σ_i (MPa)	10	Ref. [97]
σ_d^{PA} (MPa)	80	Calculated using the equation for σ_d in Figure 5-18 and the experimental value for ρ_{PA}.
C_{AA} (MPa)	407	-
σ_y^{Peak} (MPa)	462	Obtained from experiments.
σ_d^{peak}(MPa)	42	Calculated using the equation for σ_d in Figure 5-18 and the estimated value for ρ_{AA}^{peak}.

5.2.2.2.2 Modeling Results and Discussion

The strengthening contributions of the AA7075-DQ+PA condition during artificial aging are evaluated using the equations presented in Figure 5-18, along with the modeled evolution of f_r and ρ_{AA}. The evolution of yield strength is predicted with and without considering the recovery of dislocations (static recovery) during the final aging step. Both modeling results are then compared with experimental data, as illustrated in Figure 5-19. The maximum difference between the experiment and the model (including recovery) is ~9%. The modeling of dislocation recovery in our modeling equations is essential for accurate modeling predictions. The discrepancy between the experimental and modeling results for the as-pre-aged condition can be attributed to the effect of dislocations on the precipitation mechanisms occurring in the pre-aged material during pre-aging. The growth of precipitates is suggested to be the dominant precipitation mechanism in the pre-aged material, resulting in an enhanced precipitation hardening contribution while the model takes into account both nucleation and growth effects.

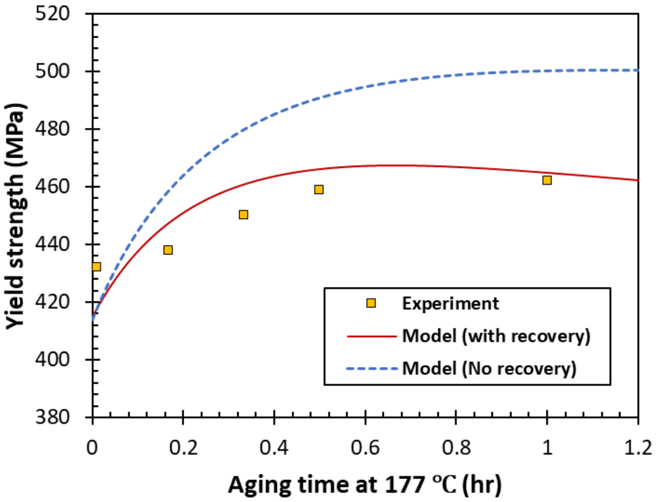

Figure 5-19 Comparison of model-predicted yield strength with and without recovery (lines) to experimental measurements (symbols) during artificial aging of the AA7075-DQ+PA at 177℃.

To gain a deeper insight into the strengthening mechanisms during artificial aging of the alloy in the DQ+PA condition, the contributions of different mechanisms to the yield strength have been plotted in Figure 5-20. This figure shows the dominant role of precipitation strengthening on the yield strength of AA7075-DQ+PA during artificial aging. The contribution of precipitates to the yield strength increases during aging up to ~1.8 hours of aging and thus, the peak strength is expected to happen around 1.8 hours of aging for the alloy in the DQ+PA condition (when $f_r = 1$ and $\sigma_{ss} = 0$). However, dislocation annihilation (partial recovery) during aging reduces the contribution of dislocations to the yield strength and prevents further increase in the yield strength of the alloy during aging, as shown in Figure 5-19. Therefore, the prediction of dislocation recovery during aging is essential for improving the accuracy of the prediction of the yield strength during artificial aging of the alloy in the DQ+PA condition. The drop in yield strength observed at aging times less than 1 hour in Figure 5-19 can be related to the possible errors coming from the simplifying assumptions made in the recovery model, such as the effect of precipitation on dislocation evolution, which has not been considered in the model.

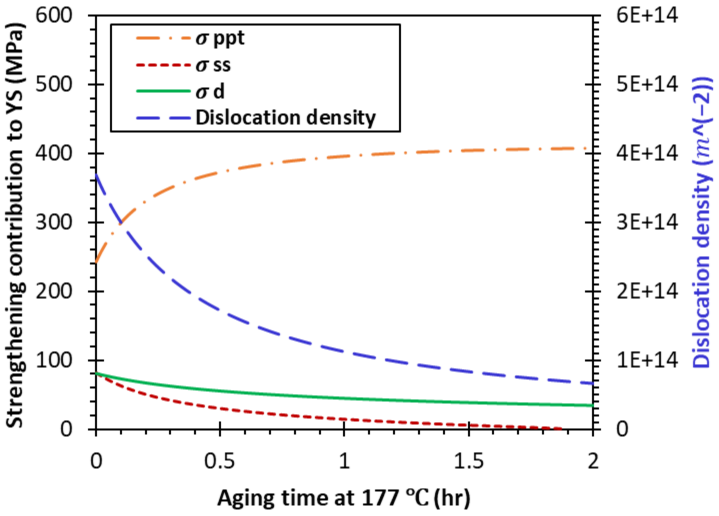

Figure 5-20 Model-predicted strengthening contributions during artificial aging of the alloy in the DQ+PA condition at 177°C (using experimental values for f_r).

5.3 Summary

In this chapter, modeling formulations have been introduced to model the microstructural and yield strength evolution of AA7xxx alloys in the WQ condition during natural aging and for AA7075-WQ during multi-step aging treatments, including pre-aging treatments, secondary natural aging, and artificial aging of the alloy in pre-aged tempers. The natural aging model introduced for the natural aging of water-quenched AA7xxx alloys has been adapted to formulate and analyze the kinetics of natural aging for AA7075-DQ alloy by incorporating the effect of dislocation strengthening on the yield strength modeling formulation. The original kinetic model for the artificial aging of water-quenched and pre-aged materials has been expanded to include the effect of dislocations and their evolution on the precipitation kinetics during the artificial aging of a die-quenched and pre-aged material. A process model for predicting the yield strength evolution during artificial aging of die-quenched and pre-aged AA7075 alloy has been developed and verified, in which the effect of dislocation recovery on the strengthening response has been incorporated. The main conclusions of the present work and the recommendations for future studies will be summarized in the next chapter.

6. Summary and Conclusions

6.1 Summary

The objectives of this study were: (1) to investigate the effects of natural aging and multi-step aging treatments on the microstructural evolution and precipitation hardening behavior of water-quenched (WQ) and die-quenched (DQ) AA7xxx alloys, and (2) to model the microstructural and yield strength evolution of these alloys for a range of both traditional and more complex multi-step aging treatments.

The thermal processing routes studied for the solutionized and water-quenched samples included (i) natural aging of AA7xxx alloys, (ii) pre-aging of AA7075, (iii) secondary natural aging of pre-aged AA7075, and (iv) artificial aging of the pre-aged AA7075.

For the die-quenched material, the thermal processing routes studied included: (i) natural aging of as-die-quenched AA7075 and (ii) artificial aging of AA7075 in the die-quenched and pre-aged conditions. To isolate the effect of the quench rate from deformation, the samples were quenched using forced-air at the same rate as in the die-quenching process. The precipitation hardening behavior of a forced-air quenched (FAQ) material was investigated during natural aging and after a pre-aging treatment and subsequent artificial aging treatment associated with automotive paint-bake cycling, and the results were compared with similarly aged die-quenched conditions.

A modeling methodology was introduced to analyze the precipitation kinetics and yield strength evolution during the natural aging of Al-Zn-Mg-(Cu) alloys for a range of process conditions. Following validation, this methodology was used to investigate the natural aging kinetics of different AA7xxx alloys in water-quenched conditions. A relationship was introduced to formulate the relative volume fraction of precipitates during the natural aging of AA7xxx alloys with pre-aging histories (secondary natural aging). The kinetics of natural aging for a pre-aged AA7075 alloy were analyzed, and the evolution of the yield strength during long-term natural aging was predicted. The kinetics of precipitation hardening during natural aging of die-quenched AA7075 were also analyzed, this time through incorporating the effect of dislocation strengthening into the yield strength modeling formulation.

A mathematical model was developed and verified to quantitatively predict the relative volume fraction of precipitates (f_r^0 values) after different times and temperatures during intermediate temperature aging in water-quenched and pre-aged conditions based on isothermal calorimetry (IC) experiments. The estimated f_r^0 values were then used to successfully calculate the yield strength of the pre-aged tempers.

The kinetics of precipitation during artificial aging of AA7075 in the PA conditions were determined in the temperature range of 150-177℃ using IC experiments and by implementing previously developed modeling approaches. The evolution of the yield strength of AA7075-PA during artificial aging at 177℃ was predicted using the modeled f_r values and a previously developed yield strength model.

A model was developed and verified to predict the evolutions of microstructure and yield strength during the artificial aging treatment of AA7075 alloy in the DQ+PA condition, up to the peak-aged condition. For this purpose, the effects of dislocation recovery on the precipitation kinetics and strengthening response were incorporated through the following steps:

- The kinetics of recovery were modeled using empirical and theoretical relationships to predict the evolution of the dislocation density during the artificial aging of the material in DQ+PA condition. For this purpose, a modeling relationship was introduced to estimate the residual dislocation density in the microstructure of the material in the as-die-quenched condition (ρ_{DQ}) as a function of the strain level applied during the die-quenching process. Methodologies were described to calibrate the model parameter ρ_{DQ+PA} (dislocation density of the alloy in the DQ+PA condition) using the predicted value for ρ_{DQ}.

- The evolution of the relative volume fraction of precipitates during artificial aging of the material in the DQ+PA condition was predicted by adapting a previously developed kinetic model. In this model, the effect of dislocation recovery (during the final aging step) on the kinetic parameter k_{eff} is incorporated.
- The evolution of the yield strength during artificial aging of AA7075-DQ+PA was modeled by adopting a linear superposition law for the individual strengthening mechanisms. The model used the relative volume fraction of the precipitates and the dislocation density as variables. Methodologies for calibrating the model parameter C_{AA} were described.

The accuracy of the modeling results for aging treatments of the WQ condition indicates that the microstructure and yield strength evolution during natural aging and multi-step aging treatments of AA7xxx alloys can be predicted using the precipitation kinetics and yield strength models introduced in this research. Likewise, the accuracy of the modeling results for the artificial aging of the material in DQ+PA condition indicates that the precipitation kinetics and strengthening behavior of the AA7075-DQ+PA alloy during artificial aging are well captured using the process model proposed in this research.

6.2 Conclusions

6.2.1 Solutionized and Water-Quenched Tempers

The combination of modeling and experimental results for the aging treatments of the WQ tempers has led to the following findings:

Natural Aging

- Three types of particles were identified in the microstructure of the as-water-quenched and naturally-aged conditions of AA7075: natural aging Zn-Mg precipitates (F particles), quenching Zn-Mg precipitates (L particles), and Cr-rich particles.

- It was found that only the population of F particle evolved (through an increase in their number density) during the natural aging of the AA7075 alloy, while no change occurred for the L- and Cr-rich particles.
- Compositional similarities in Cu-containing AA7xxx alloys, particularly the proportional contents of Zn, Mg, and Cu, resulted in similar rates of natural aging.
- Modeling analyses for the natural aging of variously processed AA7xxx alloys resulted in a JMAK-type equation for the natural aging description in all cases. The JMAK parameter n was found to be equal to 0.3 for the natural aging of the materials in the WQ, DQ, and PA conditions studied here. The similarity in the obtained n values is suggested to be due to the similarity in the morphology of the precipitates formed during natural aging. The JMAK parameter, k, for the WQ conditions, was found to be dependent on the total strengthening solute content (*i.e.*, the percentage of Zn+Mg+Cu).

Pre-Aging Treatments

- The experimental results for the pre-aged tempers revealed that GP zones and η' precipitates were present in the microstructure of AA7075-2NA after artificial aging at 120°C (PA120). The GP zones were the main precipitates in the microstructure of AA7075 pre-aged at 80 and 100°C (PA80 and PA100 conditions).
- The higher increase in hardness of the AA7075 samples pre-aged at 120°C for different times, compared to the samples pre-aged at lower temperatures (80 and 100°C), was attributed to the formation of η' precipitates.

Secondary Natural Aging

- It was found that pre-aging for the same duration at a higher temperature (*i.e.*, 120°C vs. 100°C) reduced the hardening rate during subsequent storage at room temperature. This effect was attributed to the reduction in supersaturation caused by the greater advancement in the formation of precipitates (GP zones and η') during the pre-aging treatment at higher temperatures.

Artificial Aging of the Pre-Aged Material

- The microstructure of pre-aged and paint-baked AA7075 (PB condition) was found to contain GP zones and η' precipitates. GP zones formed during the pre-aging treatment (PA condition) were found to accelerate the formation of η' precipitates during subsequent high-temperature artificial aging treatments.
- A slower drop in the yield strength evolution was observed during the aging of AA7075-PA at 150℃ compared to aging at higher temperatures, implying a slow-rate precipitate coarsening process. The absence of significant coarsening was ascribed to the small size distribution of precipitates after the pre-aging treatment, resulting from the enhanced precipitate nucleation occurring at such a low aging temperature.
- The value obtained through modeling analysis of the kinetic parameter Q_A for artificial aging of the PA material suggests that the growth rate of the precipitates during the final aging step of the pre-aged AA7075 alloy is controlled by the migration of Mg atoms.

6.2.2 Forced-Air Quenched and Die-Quenched Tempers

The analysis of the combined modeling and experimental results for the aging treatments of AA7075 alloy in FAQ and DQ tempers suggests the following findings:

- The forced-air quenching applied in this study did not cause noticeable hardening in the naturally-aged and pre-aged conditions, compared to water quenching, implying that it did not perturb the supersaturation of solutes in the as-FAQ condition or the formation of GP zones during subsequent aging treatments.
- Forced-air quenching followed by pre-aging (FAQ+PA condition) led to a lower hardness value after the PBC treatment relative to the water-quenched material. This behavior was ascribed to a decrease in the volume fraction of η' precipitates formed in the microstructure of AA7075-FAQ+PB due to the formation of fewer vacancy-rich clusters (VRCs) during or immediately after the quenching process.

- The higher hardness values obtained for the material in the as-DQ and DQ+NA conditions, relative to the WQ and FAQ conditions, were attributed to the effect of strain aging.
- The obtained value of the kinetic parameter *k* for the natural aging of AA7075-DQ was found to be smaller than that for the WQ condition. The slower kinetics of natural aging for the material in the DQ condition were proposed to be caused by the annihilation of vacancies on dislocations which reduced the rate of nuclei formation for natural aging precipitates.
- Due to the strain aging effect, die-quenching increased the material hardness after the PA treatment compared to the similarly aged material after water-quenching or forced-air quenching. However, after the final stage of aging (*i.e.,* PBC treatment), the material in the DQ+PA condition exhibited a lower hardness value than the similarly aged WQ and FAQ samples. This result was attributed to the reduced precipitation potential due to the annihilation of vacancies on dislocations, as well as the effect of dislocations on the precipitate size distribution and the annihilation and recovery of dislocations during the final aging step.
- The kinetics of precipitation hardening were accelerated by dislocation-enhanced precipitation during the artificial aging of the DQ+PA material, as compared to the WQ+PA material.
- The predicted values for the dislocation densities, based on the recovery modeling formulations, indicated that the annihilation of dislocations is negligible during the pre-aging treatment of the DQ material. The annihilation of dislocations was more noticeable during high-temperature aging, such as the PBC treatment, of the DQ+PA material, at which dislocations go through a rearrangement or partial recovery more easily.

6.3 Implications for Industry

The results of this study showcase the potential for the effective use of AA7xxx alloys in automotive applications. The development of modeling relationships that can predict the evolution of microstructure and yield strength during natural aging and multi-step aging treatments creates opportunities to design heat treatment cycles that take advantage of the alloy's age hardening potential and optimize the performance of the final product.

The presented formulations for the modeling of natural aging enable predictions of precipitation kinetics and yield strength during natural aging of variously processed Al-Zn-Mg-(Cu) alloys. For natural aging predictions of as-water-quenched AA7xxx alloys, the relative volume fraction of precipitates (f_r) can be estimated using the JMAK kinetic parameter $n = 0.3$ and an empirical relationship that approximates k as a function of the alloying element content (*i.e.,* wt% Zn+Mg+Cu). Then, by utilizing the estimated f_r values in the yield strength modeling formulations, the yield strength of the naturally-aged material can be predicted. This is beneficial for property predictions for industrial applications of these alloys, where a room-temperature delay after solution treatment and before subsequent thermomechanical steps is usually inevitable.

The pre-aging (PA) treatment identified in this research enhances the precipitation hardening capabilities of the alloy after subsequent artificial aging, resulting in hardness values (~171HV) comparable to the T6 hardness. It also accelerates the hardening response of the AA7075 alloy after the PBC treatment, compared to a single-step T6 heat treatment. The modeling framework introduced in this research can be implemented for predicting the evolution of microstructure and yield strength for the AA7075 alloy in pre-aged conditions and during subsequent aging treatments (up to peak-aged conditions). For new AA7xxx alloys, these predictions can be made by conducting limited isothermal calorimetry tests to characterize the relative volume fraction of the precipitates (f_r) at each aging step.

The experimental results for the material in the current DQ temper demonstrate that the die-quenching process, followed by pre-aging and paint bake cycle treatment, increases the hardness value of the as-quenched alloy up to 153HV. However, the final hardness value is 88% of that of AA7075-T6 (~173HV). This observation may indicate the necessity for further optimization of the final aging treatment (*i.e.,* the paint bake cycle) in order to achieve peak strength in the final manufactured parts. The process model developed in this research, which models precipitation hardening during artificial aging of die-quenched and pre-aged material, provides a useful roadmap for future process design associated with the automotive applications of AA7075 and similar alloys.

7. Recommendations for Future Work

The following section introduces areas which are identified as being important for future work related to the current research.

- For the natural aging of as-quenched AA7xxx alloys, as suggested by the findings of the current study, a more detailed future study, including a comprehensive microstructural analysis, is necessary to elucidate the similarity in the JMAK parameter n values obtained for the natural aging kinetics of AA7xxx alloys. This can also be beneficial for elucidating the effect of a pre-aging treatment on the subsequent natural aging kinetics (secondary natural aging).
- For the artificial aging of naturally-aged AA7075 alloy, the findings of this research can be used to predict the initial relative volume fraction of precipitates (*i.e.*, f_r^0) and yield strength of the alloy using the analysis of IC experiments after different pre-aging treatments. However, more detailed work is required to expand the modeling work (for the three-step aging treatments) in order to consider the effect of concurrent dissolution and formation of precipitates during the artificial aging of naturally aged alloys at higher temperatures. This can broaden the applicability of modeling formulations for predicting the microstructural and yield strength evolution over a wide range of temperatures.

For the DQ process, this study has not considered certain areas of research concerning the die-quenching process.

- It is proposed to investigate the effect of the cooling rate during die-quenching on the microstructure and strengthening response of multi-step aged AA7xxx alloys for better optimization of the thermal processing routes and mechanical properties of manufactured automotive parts.
- In the die-quenching process, the effects of non-isothermal heating and heating rate to solutionizing temperature on the microstructure evolution of AA7xxx alloys during subsequent aging treatments is another area where the application of detailed experimental work would be beneficial. The results can be invaluable for optimizing

industrial processes, including non-isothermal furnace heating and ramp heating treatments.

- The effect of high deformation levels (*e.g.*, in the corner section of a die-quenched part) in the die-quenching process on the precipitation hardening behavior of AA7xxx alloys during subsequent aging treatments is proposed. The increase in the dislocation density of the DQ parts accelerates the kinetics of precipitation and may ultimately cause coarsening of precipitates during the PBC treatments. Therefore, the precipitate hardening model for the aging of the material in the DQ+PA condition can be further extended to include the effect of precipitate coarsening during the final aging treatments. This will improve the range of applicability of the model and may also be advantageous for studying the potential application of AA7xxx alloys in die-quenched and over-aged conditions for automotive applications, due to the improved corrosion resistance of over-aged microstructures [61].
- The modeling equation for predicting the dislocation density as a function of plastic strain during die-quenching can be further improved by incorporating the effect of dynamic recovery on the residual dislocation density after die-quenching. This will result in a more accurate prediction of the dislocation density of the as-DQ material. Further investigations are proposed to elucidate the effect of dynamic recovery during die-quenching on the residual dislocation density of AA7xxx-DQ alloys.
- The DQ process model is recommended to be implemented for the non-isothermal aging treatments of AA7xxx alloys in the DQ+PA conditions. Non-isothermal paint-bake cycling and ramp heating treatments are commonly used in the automotive industry and thus the results will be valuable for mechanical property and process optimizations.

Letters of Copyright Permission

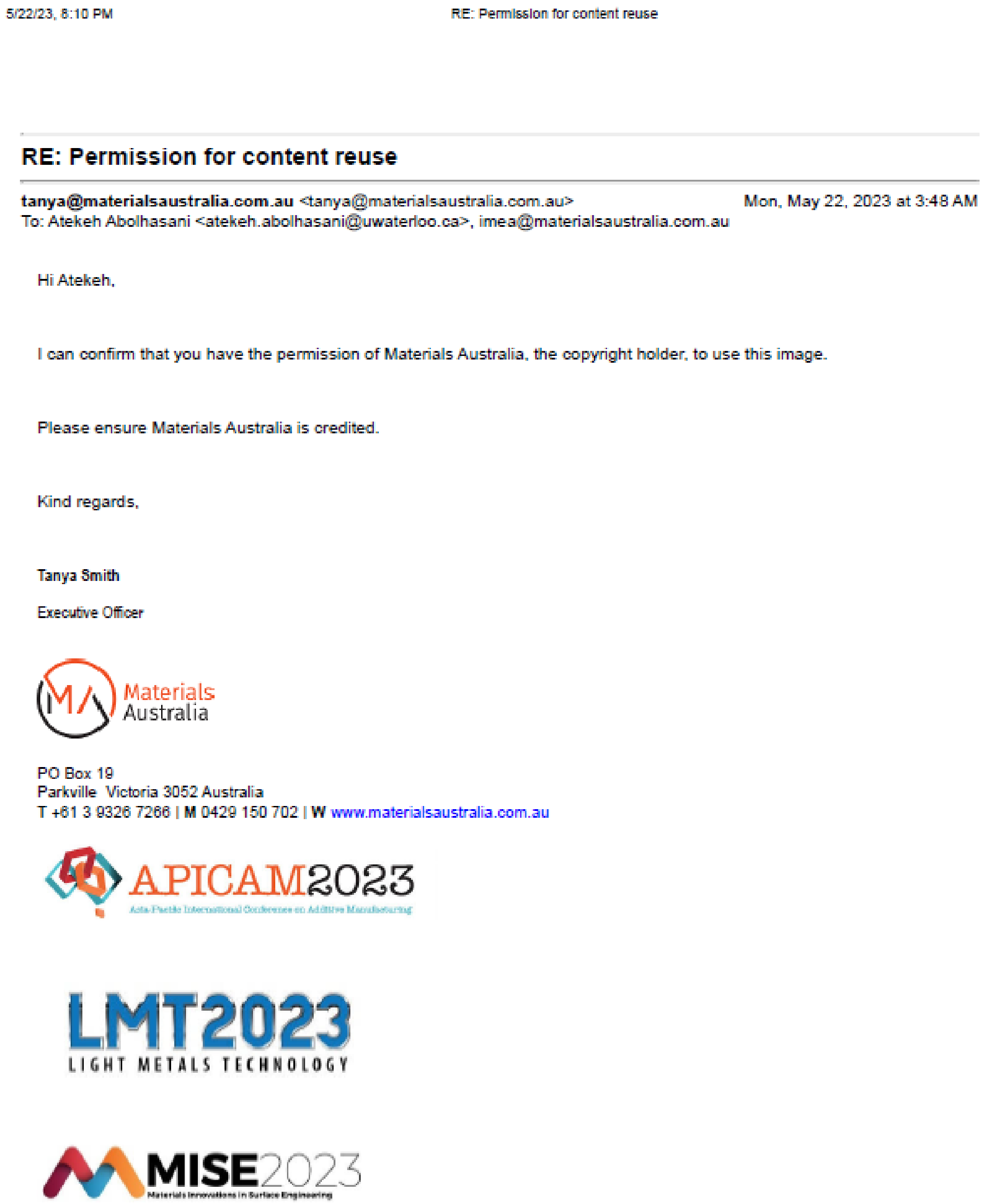

5/22/23, 8:10 PM RE: Permission for content reuse

RE: Permission for content reuse

tanya@materialsaustralia.com.au <tanya@materialsaustralia.com.au> Mon, May 22, 2023 at 3:48 AM
To: Atekeh Abolhasani <atekeh.abolhasani@uwaterloo.ca>, imea@materialsaustralia.com.au

Hi Atekeh,

I can confirm that you have the permission of Materials Australia, the copyright holder, to use this image.

Please ensure Materials Australia is credited.

Kind regards,

Tanya Smith

Executive Officer

Materials Australia

PO Box 19
Parkville Victoria 3052 Australia
T +61 3 9326 7266 | **M** 0429 150 702 | **W** www.materialsaustralia.com.au

APICAM2023
Asia-Pacific International Conference on Additive Manufacturing

LMT2023
LIGHT METALS TECHNOLOGY

MISE2023
Materials Innovations in Surface Engineering

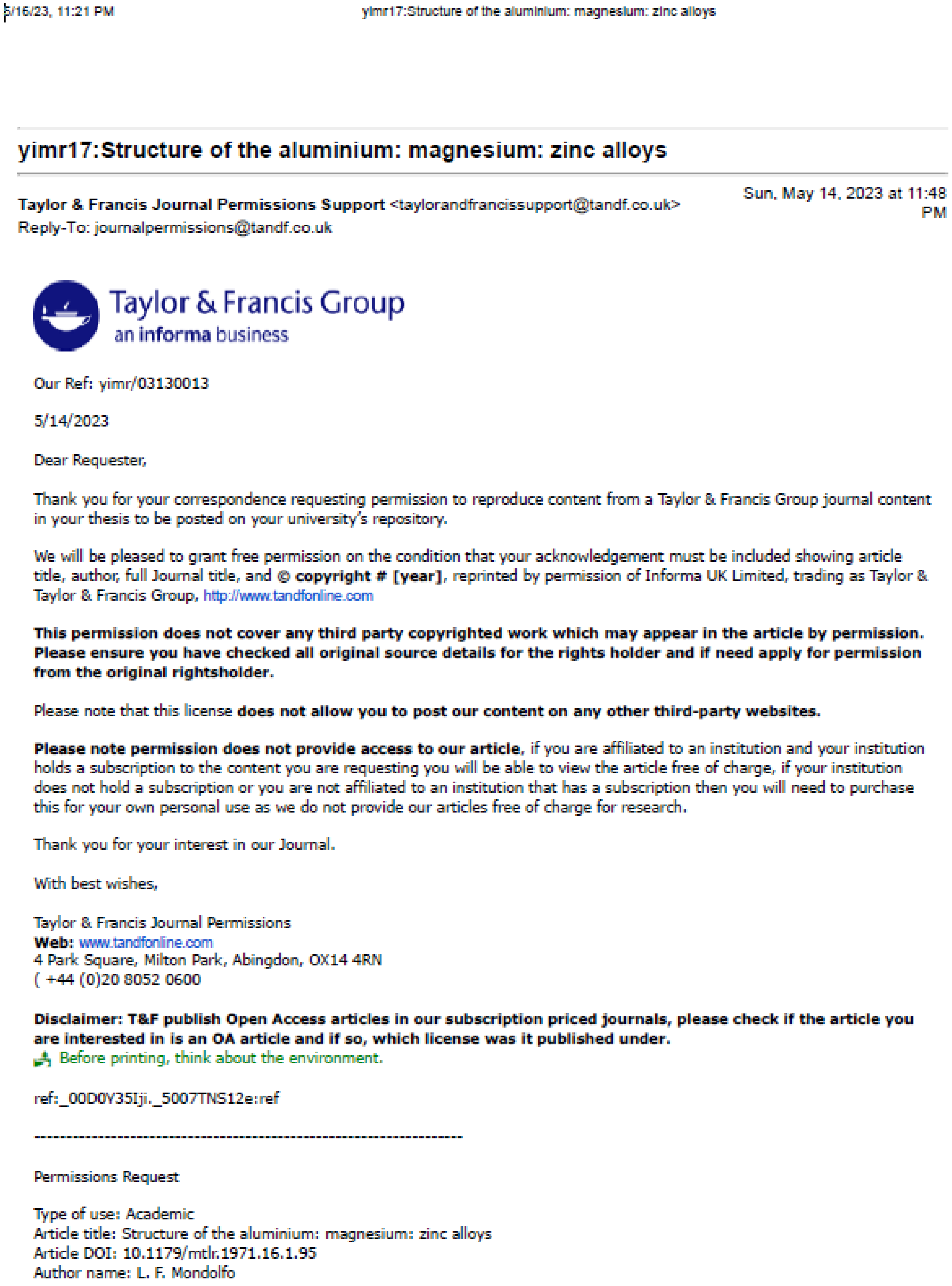

5/16/23, 11:21 PM yimr17:Structure of the aluminium: magnesium: zinc alloys

yimr17:Structure of the aluminium: magnesium: zinc alloys

Taylor & Francis Journal Permissions Support <taylorandfrancissupport@tandf.co.uk>
Reply-To: journalpermissions@tandf.co.uk

Sun, May 14, 2023 at 11:48 PM

Taylor & Francis Group
an **informa** business

Our Ref: yimr/03130013

5/14/2023

Dear Requester,

Thank you for your correspondence requesting permission to reproduce content from a Taylor & Francis Group journal content in your thesis to be posted on your university's repository.

We will be pleased to grant free permission on the condition that your acknowledgement must be included showing article title, author, full Journal title, and **© copyright # [year]**, reprinted by permission of Informa UK Limited, trading as Taylor & Taylor & Francis Group, http://www.tandfonline.com

This permission does not cover any third party copyrighted work which may appear in the article by permission. Please ensure you have checked all original source details for the rights holder and if need apply for permission from the original rightsholder.

Please note that this license **does not allow you to post our content on any other third-party websites.**

Please note permission does not provide access to our article, if you are affiliated to an institution and your institution holds a subscription to the content you are requesting you will be able to view the article free of charge, if your institution does not hold a subscription or you are not affiliated to an institution that has a subscription then you will need to purchase this for your own personal use as we do not provide our articles free of charge for research.

Thank you for your interest in our Journal.

With best wishes,

Taylor & Francis Journal Permissions
Web: www.tandfonline.com
4 Park Square, Milton Park, Abingdon, OX14 4RN
(+44 (0)20 8052 0600

Disclaimer: T&F publish Open Access articles in our subscription priced journals, please check if the article you are interested in is an OA article and if so, which license was it published under.
Before printing, think about the environment.

ref:_00D0Y35Iji._5007TNS12e:ref

Permissions Request

Type of use: Academic
Article title: Structure of the aluminium: magnesium: zinc alloys
Article DOI: 10.1179/mtlr.1971.16.1.95
Author name: L. F. Mondolfo

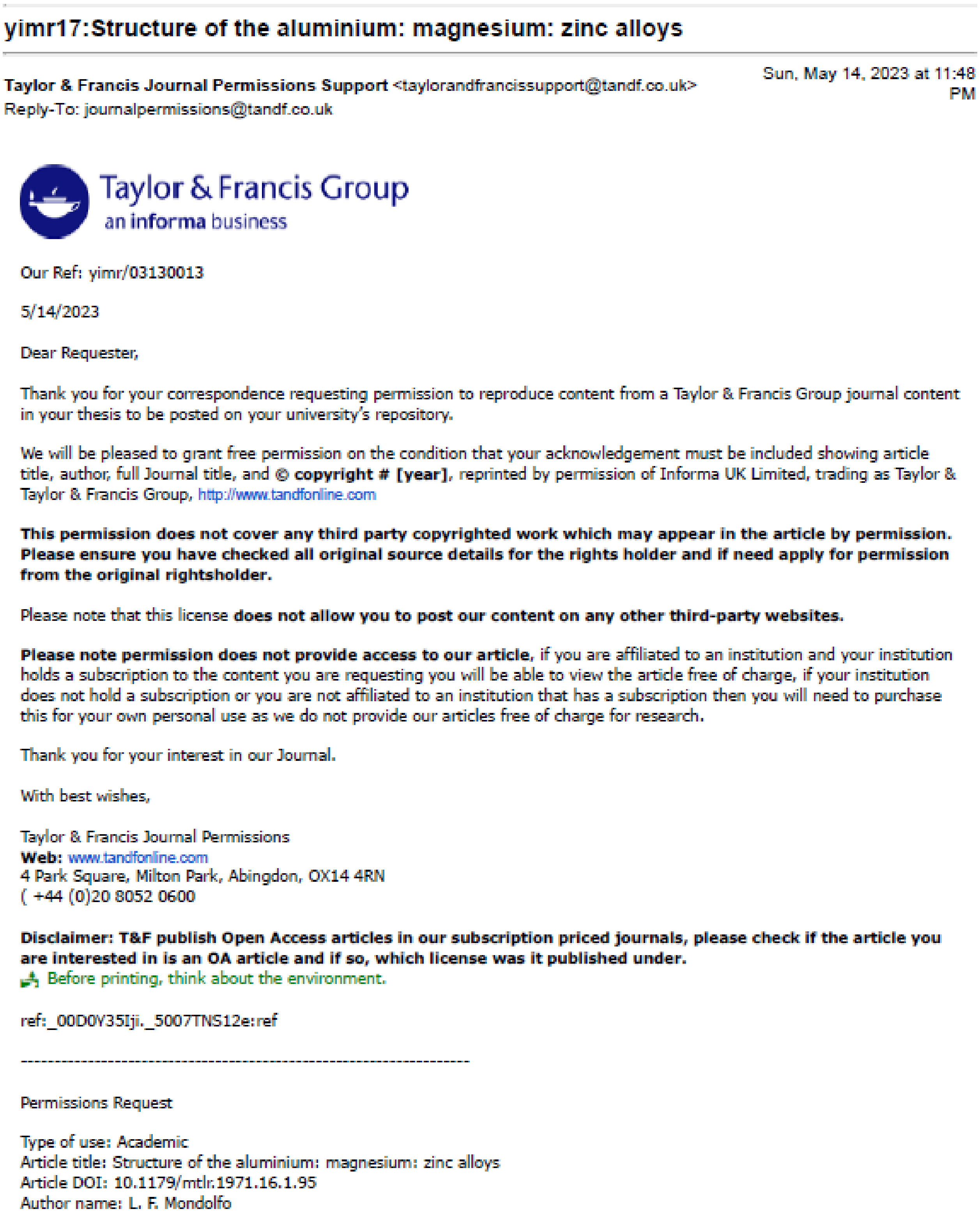

yimr17:Structure of the aluminium: magnesium: zinc alloys

Taylor & Francis Journal Permissions Support <taylorandfrancissupport@tandf.co.uk>
Reply-To: journalpermissions@tandf.co.uk

Sun, May 14, 2023 at 11:48 PM

Taylor & Francis Group
an informa business

Our Ref: yimr/03130013

5/14/2023

Dear Requester,

Thank you for your correspondence requesting permission to reproduce content from a Taylor & Francis Group journal content in your thesis to be posted on your university's repository.

We will be pleased to grant free permission on the condition that your acknowledgement must be included showing article title, author, full Journal title, and **© copyright # [year]**, reprinted by permission of Informa UK Limited, trading as Taylor & Taylor & Francis Group, http://www.tandfonline.com

This permission does not cover any third party copyrighted work which may appear in the article by permission. Please ensure you have checked all original source details for the rights holder and if need apply for permission from the original rightsholder.

Please note that this license **does not allow you to post our content on any other third-party websites.**

Please note permission does not provide access to our article, if you are affiliated to an institution and your institution holds a subscription to the content you are requesting you will be able to view the article free of charge, if your institution does not hold a subscription or you are not affiliated to an institution that has a subscription then you will need to purchase this for your own personal use as we do not provide our articles free of charge for research.

Thank you for your interest in our Journal.

With best wishes,

Taylor & Francis Journal Permissions
Web: www.tandfonline.com
4 Park Square, Milton Park, Abingdon, OX14 4RN
(+44 (0)20 8052 0600

ref:_00D0Y35Iji._5007TNS12e:ref

Permissions Request

Type of use: Academic
Article title: Structure of the aluminium: magnesium: zinc alloys
Article DOI: 10.1179/mtlr.1971.16.1.95
Author name: L. F. Mondolfo

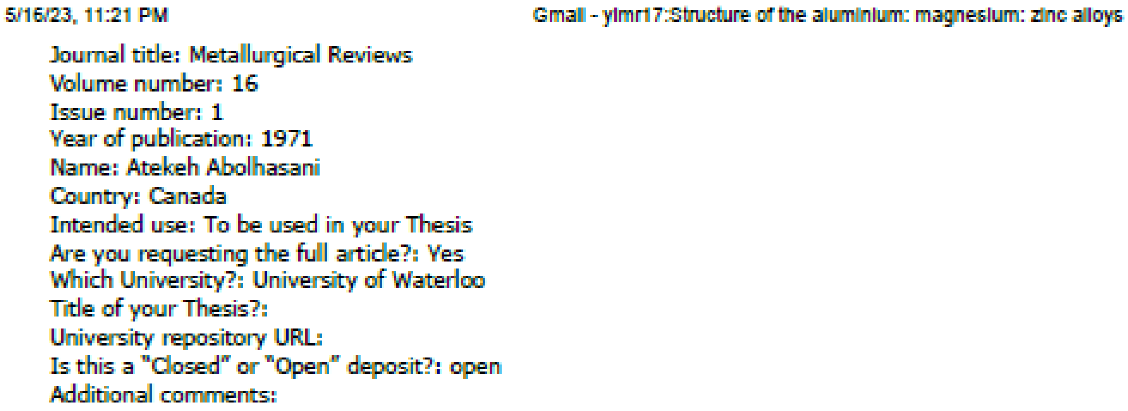

5/16/23, 11:21 PM Gmail - ylmr17:Structure of the aluminium: magnesium: zinc alloys

Journal title: Metallurgical Reviews
Volume number: 16
Issue number: 1
Year of publication: 1971
Name: Atekeh Abolhasani
Country: Canada
Intended use: To be used in your Thesis
Are you requesting the full article?: Yes
Which University?: University of Waterloo
Title of your Thesis?:
University repository URL:
Is this a "Closed" or "Open" deposit?: open
Additional comments:

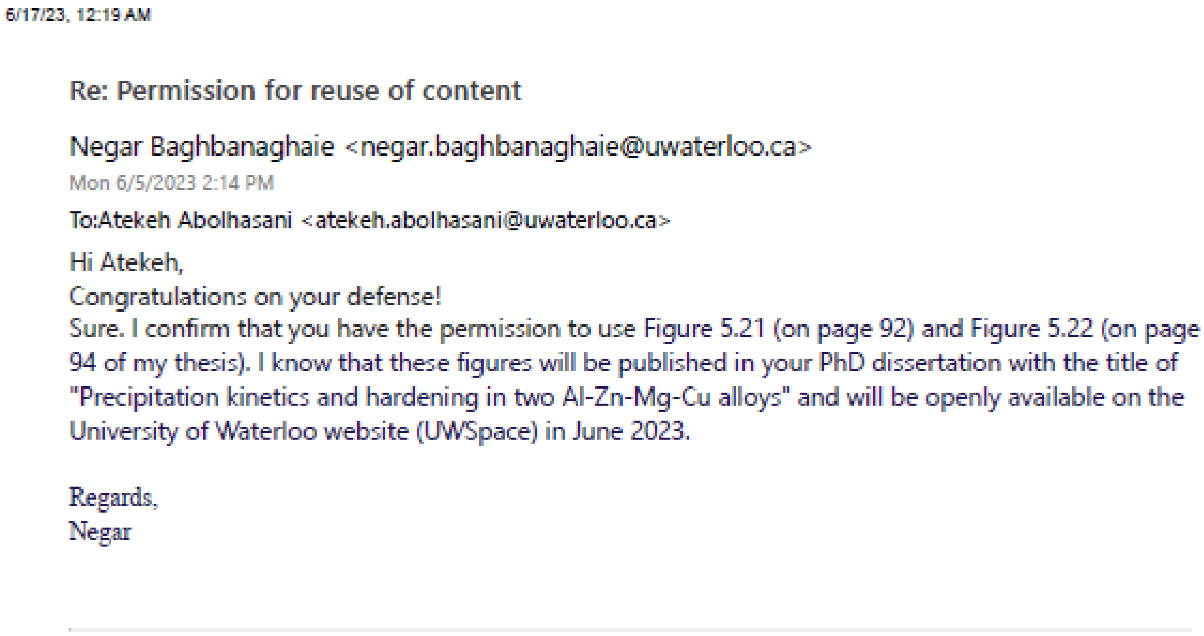

6/17/23, 12:19 AM

Re: Permission for reuse of content

Negar Baghbanaghaie <negar.baghbanaghaie@uwaterloo.ca>
Mon 6/5/2023 2:14 PM
To:Atekeh Abolhasani <atekeh.abolhasani@uwaterloo.ca>

Hi Atekeh,
Congratulations on your defense!
Sure. I confirm that you have the permission to use Figure 5.21 (on page 92) and Figure 5.22 (on page 94 of my thesis). I know that these figures will be published in your PhD dissertation with the title of "Precipitation kinetics and hardening in two Al-Zn-Mg-Cu alloys" and will be openly available on the University of Waterloo website (UWSpace) in June 2023.

Regards,
Negar

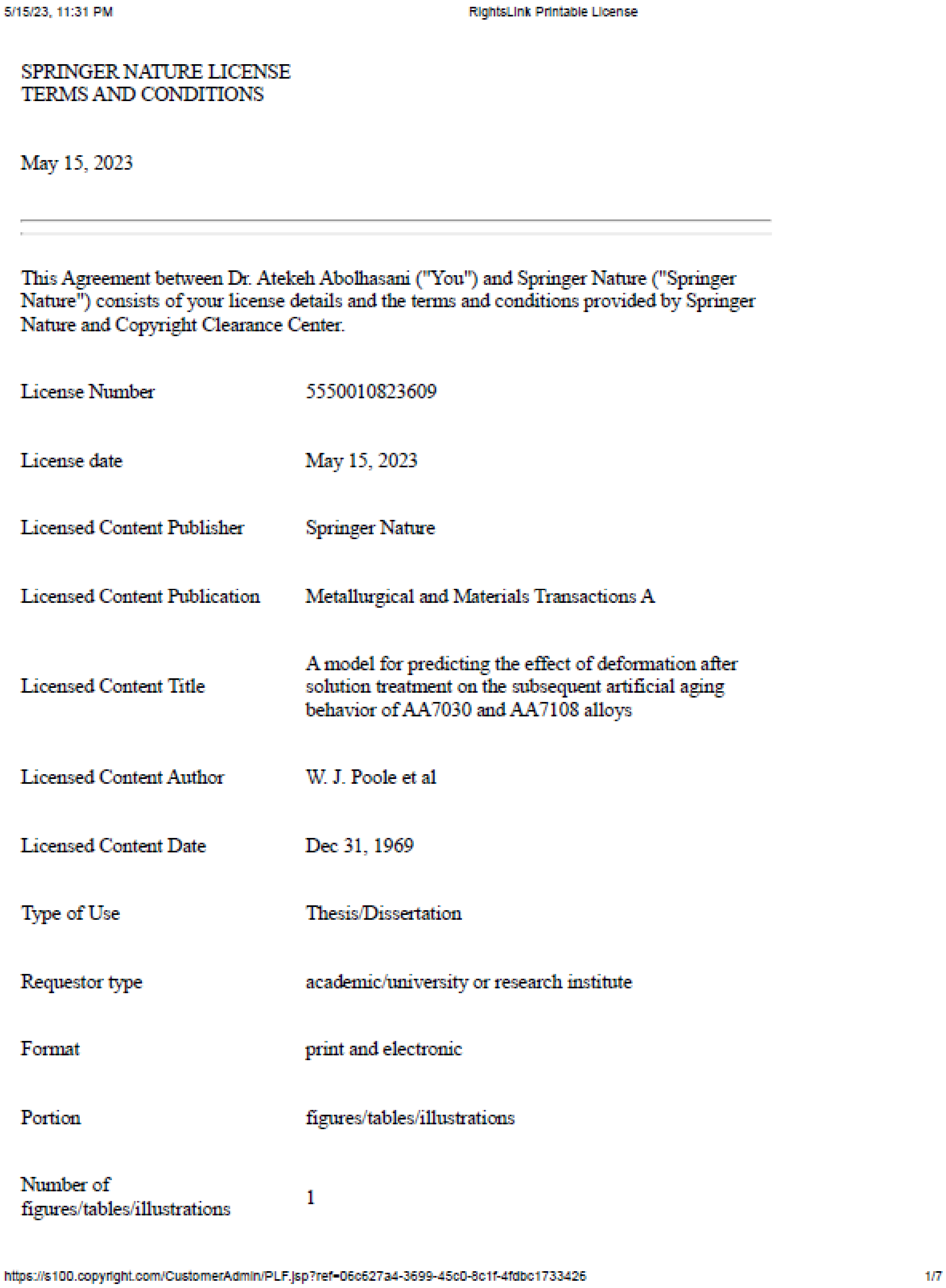

SPRINGER NATURE LICENSE
TERMS AND CONDITIONS

May 15, 2023

This Agreement between Dr. Atekeh Abolhasani ("You") and Springer Nature ("Springer Nature") consists of your license details and the terms and conditions provided by Springer Nature and Copyright Clearance Center.

License Number	5550010823609
License date	May 15, 2023
Licensed Content Publisher	Springer Nature
Licensed Content Publication	Metallurgical and Materials Transactions A
Licensed Content Title	A model for predicting the effect of deformation after solution treatment on the subsequent artificial aging behavior of AA7030 and AA7108 alloys
Licensed Content Author	W. J. Poole et al
Licensed Content Date	Dec 31, 1969
Type of Use	Thesis/Dissertation
Requestor type	academic/university or research institute
Format	print and electronic
Portion	figures/tables/illustrations
Number of figures/tables/illustrations	1

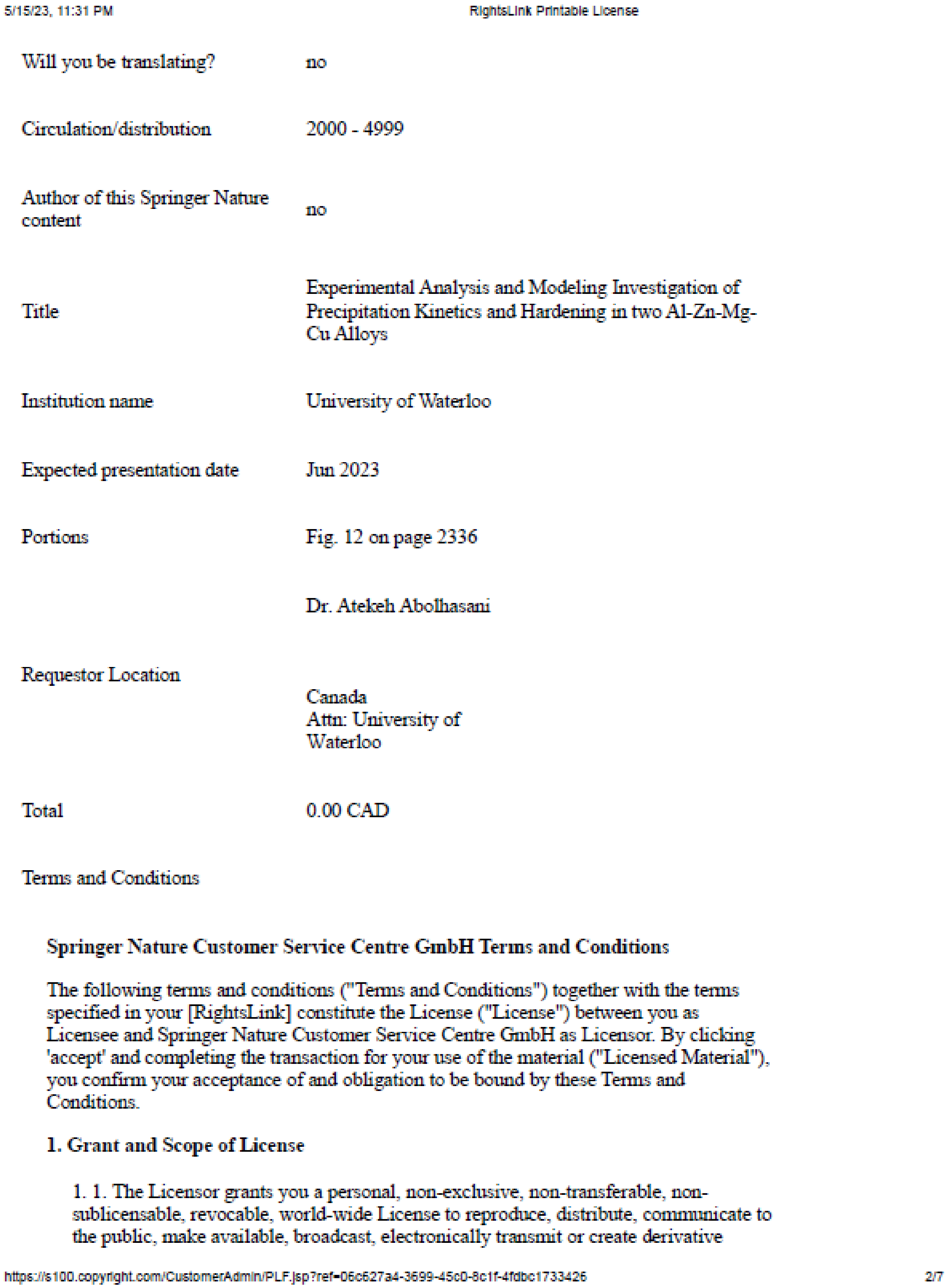

5/15/23, 11:31 PM RightsLink Printable License

Will you be translating?	no
Circulation/distribution	2000 - 4999
Author of this Springer Nature content	no
Title	Experimental Analysis and Modeling Investigation of Precipitation Kinetics and Hardening in two Al-Zn-Mg-Cu Alloys
Institution name	University of Waterloo
Expected presentation date	Jun 2023
Portions	Fig. 12 on page 2336
Requestor Location	Dr. Atekeh Abolhasani Canada Attn: University of Waterloo
Total	0.00 CAD

Terms and Conditions

Springer Nature Customer Service Centre GmbH Terms and Conditions

The following terms and conditions ("Terms and Conditions") together with the terms specified in your [RightsLink] constitute the License ("License") between you as Licensee and Springer Nature Customer Service Centre GmbH as Licensor. By clicking 'accept' and completing the transaction for your use of the material ("Licensed Material"), you confirm your acceptance of and obligation to be bound by these Terms and Conditions.

1. Grant and Scope of License

1. 1. The Licensor grants you a personal, non-exclusive, non-transferable, non-sublicensable, revocable, world-wide License to reproduce, distribute, communicate to the public, make available, broadcast, electronically transmit or create derivative

https://s100.copyright.com/CustomerAdmin/PLF.jsp?ref=06c627a4-3699-45c0-8c1f-4fdbc1733426 2/7

ELSEVIER LICENSE
TERMS AND CONDITIONS

May 15, 2023

This Agreement between Dr. Atekeh Abolhasani ("You") and Elsevier ("Elsevier") consists of your license details and the terms and conditions provided by Elsevier and Copyright Clearance Center.

License Number	5550000384193
License date	May 15, 2023
Licensed Content Publisher	Elsevier
Licensed Content Publication	Scripta Materialia
Licensed Content Title	In situ transmission electron microscopy investigation of nucleation of GP zones under natural aging in Al-Zn-Mg alloy
Licensed Content Author	Arya Chatterjee,Liang Qi,Amit Misra
Licensed Content Date	Jan 15, 2022
Licensed Content Volume	207
Licensed Content Issue	n/a
Licensed Content Pages	1
Start Page	114319
End Page	0

Type of Use	reuse in a thesis/dissertation
Portion	figures/tables/illustrations
Number of figures/tables/illustrations	1
Format	both print and electronic
Are you the author of this Elsevier article?	No
Will you be translating?	No
Title	Experimental Analysis and Modeling Investigation of Precipitation Kinetics and Hardening in two Al-Zn-Mg-Cu Alloys
Institution name	University of Waterloo
Expected presentation date	Jun 2023
Portions	Fig. 1 (d) on page 3
Requestor Location	Dr. Atekeh Abolhasani Canada Attn: University of Waterloo
Publisher Tax ID	GB 494 6272 12
Total	0.00 CAD

Terms and Conditions

INTRODUCTION

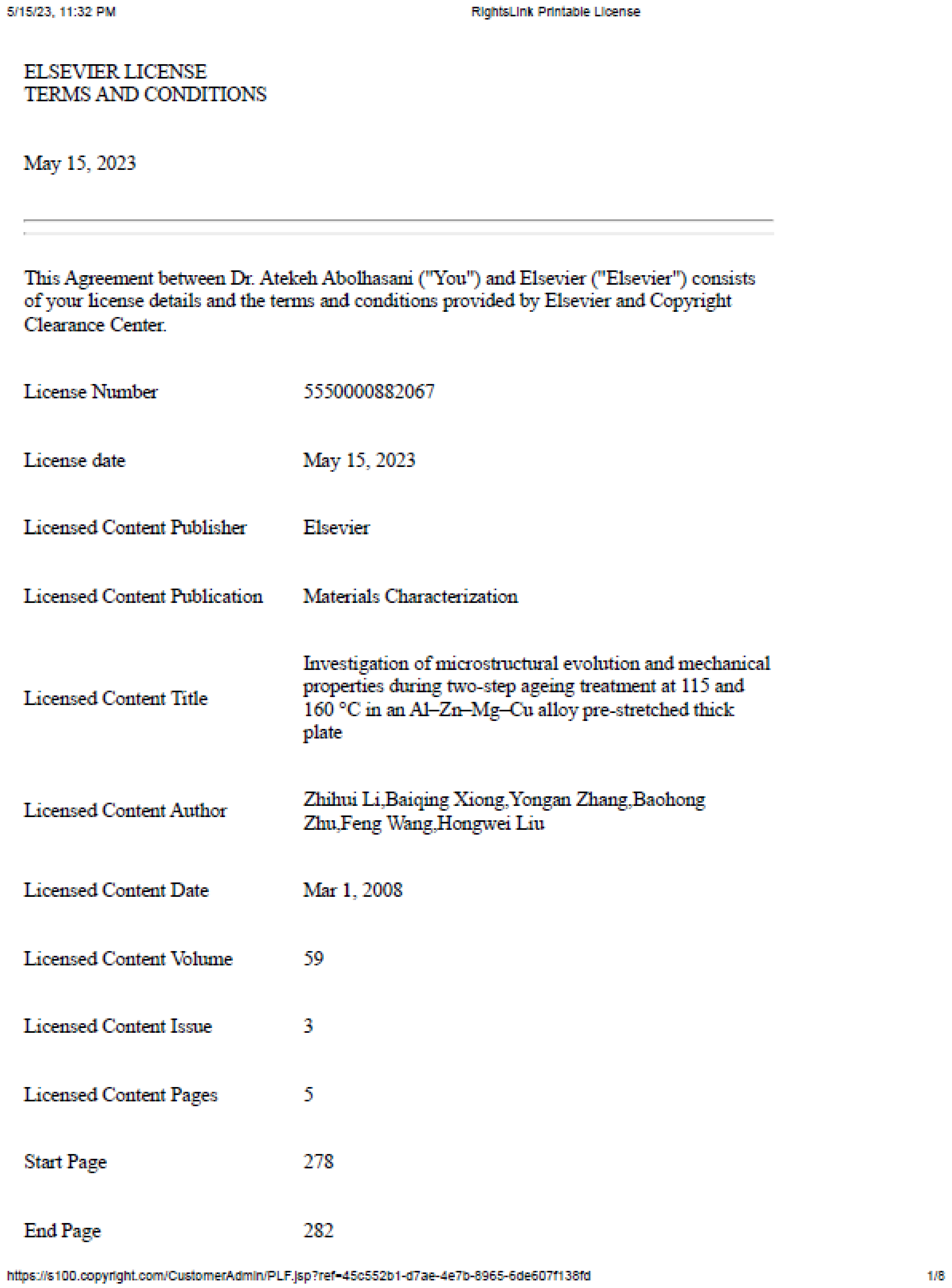

5/15/23, 11:32 PM RightsLink Printable License

ELSEVIER LICENSE
TERMS AND CONDITIONS

May 15, 2023

This Agreement between Dr. Atekeh Abolhasani ("You") and Elsevier ("Elsevier") consists of your license details and the terms and conditions provided by Elsevier and Copyright Clearance Center.

License Number	5550000882067
License date	May 15, 2023
Licensed Content Publisher	Elsevier
Licensed Content Publication	Materials Characterization
Licensed Content Title	Investigation of microstructural evolution and mechanical properties during two-step ageing treatment at 115 and 160 °C in an Al–Zn–Mg–Cu alloy pre-stretched thick plate
Licensed Content Author	Zhihui Li,Baiqing Xiong,Yongan Zhang,Baohong Zhu,Feng Wang,Hongwei Liu
Licensed Content Date	Mar 1, 2008
Licensed Content Volume	59
Licensed Content Issue	3
Licensed Content Pages	5
Start Page	278
End Page	282

https://s100.copyright.com/CustomerAdmin/PLF.jsp?ref=45c552b1-d7ae-4e7b-8965-6de607f136fd 1/8

Type of Use	reuse in a thesis/dissertation
Portion	figures/tables/illustrations
Number of figures/tables/illustrations	2
Format	both print and electronic
Are you the author of this Elsevier article?	No
Will you be translating?	No
Title	Experimental Analysis and Modeling Investigation of Precipitation Kinetics and Hardening in two Al-Zn-Mg-Cu Alloys
Institution name	University of Waterloo
Expected presentation date	Jun 2023
Portions	Fig. 2 (a) on page 279, and Fig. 5 (d) on page 280
Requestor Location	Dr. Atekeh Abolhasani Canada Attn: University of Waterloo
Publisher Tax ID	GB 494 6272 12
Total	0.00 CAD
Terms and Conditions	

INTRODUCTION

ELSEVIER LICENSE
TERMS AND CONDITIONS

May 15, 2023

This Agreement between Dr. Atekeh Abolhasani ("You") and Elsevier ("Elsevier") consists of your license details and the terms and conditions provided by Elsevier and Copyright Clearance Center.

License Number	5550001170541
License date	May 15, 2023
Licensed Content Publisher	Elsevier
Licensed Content Publication	Journal of Alloys and Compounds
Licensed Content Title	Effect of ageing temperature on microstructure, mechanical property and corrosion behavior of aluminum alloy 7085
Licensed Content Author	Yan Zou,Lingfei Cao,Xiaodong Wu,Yichang Wang,Xuan Sun,Hui Song,Malcolm J. Couper
Licensed Content Date	May 15, 2020
Licensed Content Volume	823
Licensed Content Issue	n/a
Licensed Content Pages	1
Start Page	153792
End Page	0

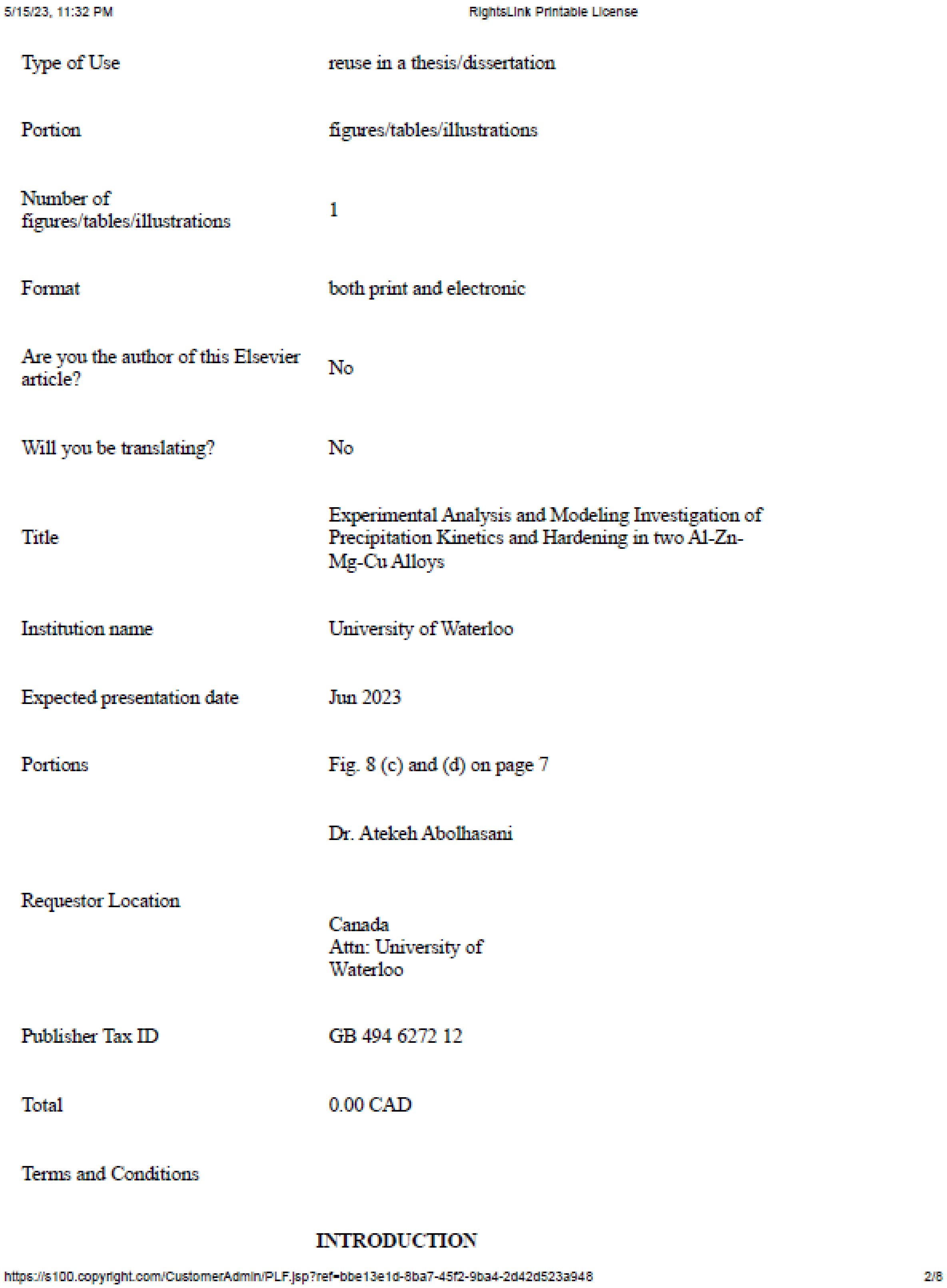

5/15/23, 11:32 PM RightsLink Printable License

Type of Use	reuse in a thesis/dissertation
Portion	figures/tables/illustrations
Number of figures/tables/illustrations	1
Format	both print and electronic
Are you the author of this Elsevier article?	No
Will you be translating?	No
Title	Experimental Analysis and Modeling Investigation of Precipitation Kinetics and Hardening in two Al-Zn-Mg-Cu Alloys
Institution name	University of Waterloo
Expected presentation date	Jun 2023
Portions	Fig. 8 (c) and (d) on page 7
Requestor Location	Dr. Atekeh Abolhasani Canada Attn: University of Waterloo
Publisher Tax ID	GB 494 6272 12
Total	0.00 CAD
Terms and Conditions	

INTRODUCTION

https://s100.copyright.com/CustomerAdmin/PLF.jsp?ref=bbe13e1d-8ba7-45f2-9ba4-2d42d523a948 2/8

ELSEVIER LICENSE
TERMS AND CONDITIONS

May 15, 2023

This Agreement between Dr. Atekeh Abolhasani ("You") and Elsevier ("Elsevier") consists of your license details and the terms and conditions provided by Elsevier and Copyright Clearance Center.

License Number	5550010104400
License date	May 15, 2023
Licensed Content Publisher	Elsevier
Licensed Content Publication	Materials Science and Engineering: A
Licensed Content Title	Precipitation strengthening in naturally aged Al–Zn–Mg–Cu alloy
Licensed Content Author	Sang-Hwa Lee,Jae-Gil Jung,Sung-Il Baik,David N. Seidman,Min-Seok Kim,Young-Kook Lee,Kwangjun Euh
Licensed Content Date	Jan 28, 2021
Licensed Content Volume	803
Licensed Content Issue	n/a
Licensed Content Pages	1
Start Page	140719
End Page	0

Type of Use	reuse in a thesis/dissertation
Portion	figures/tables/illustrations
Number of figures/tables/illustrations	1
Format	both print and electronic
Are you the author of this Elsevier article?	No
Will you be translating?	No
Title	Experimental Analysis and Modeling Investigation of Precipitation Kinetics and Hardening in two Al-Zn-Mg-Cu Alloys
Institution name	University of Waterloo
Expected presentation date	Jun 2023
Portions	Fig. 3 on page 3
Requestor Location	Dr. Atekeh Abolhasani Canada Attn: University of Waterloo
Publisher Tax ID	GB 494 6272 12
Total	0.00 CAD
Terms and Conditions	

INTRODUCTION

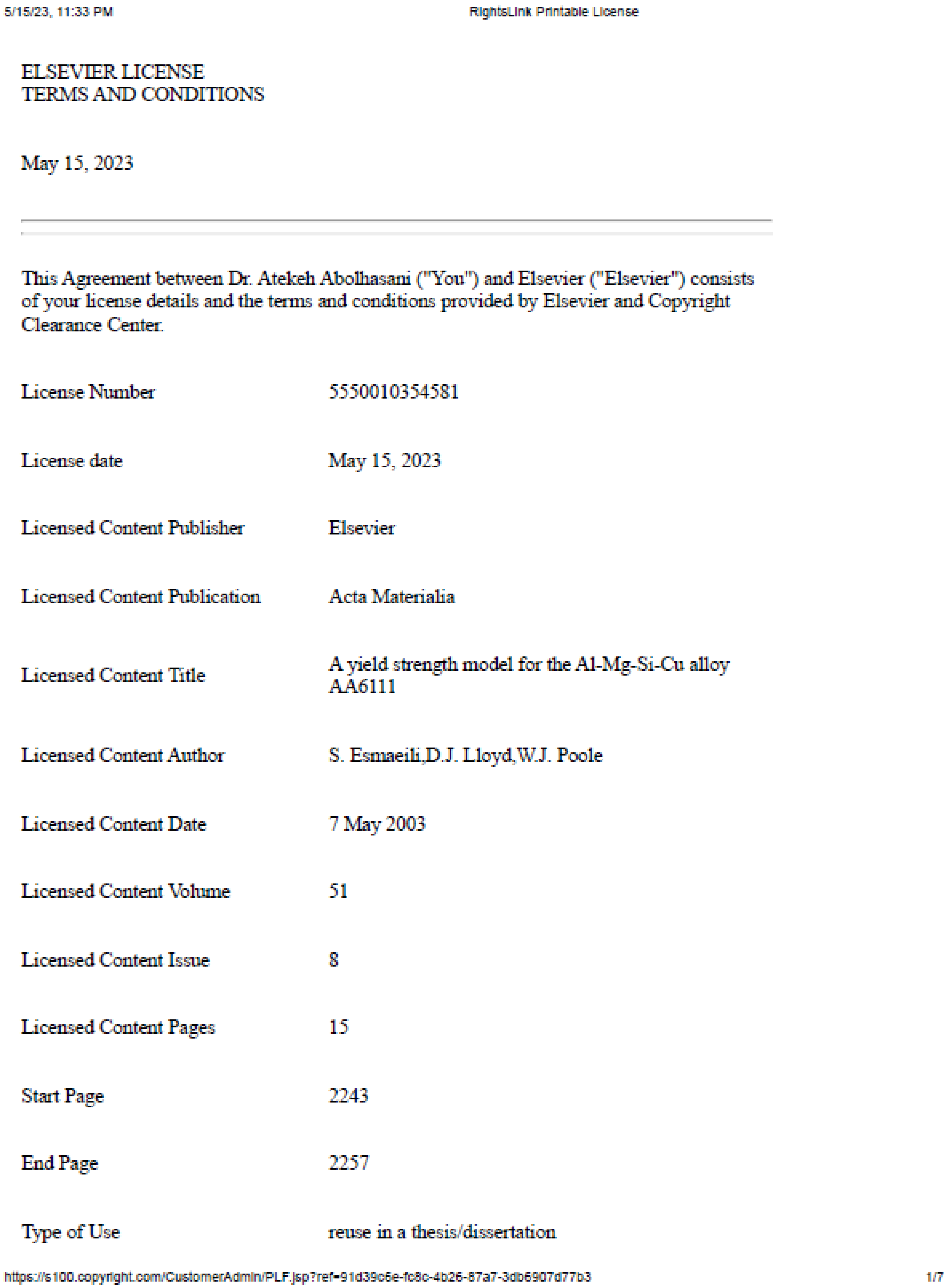

ELSEVIER LICENSE
TERMS AND CONDITIONS

May 15, 2023

This Agreement between Dr. Atekeh Abolhasani ("You") and Elsevier ("Elsevier") consists of your license details and the terms and conditions provided by Elsevier and Copyright Clearance Center.

License Number	5550010354581
License date	May 15, 2023
Licensed Content Publisher	Elsevier
Licensed Content Publication	Acta Materialia
Licensed Content Title	A yield strength model for the Al-Mg-Si-Cu alloy AA6111
Licensed Content Author	S. Esmaeili,D.J. Lloyd,W.J. Poole
Licensed Content Date	7 May 2003
Licensed Content Volume	51
Licensed Content Issue	8
Licensed Content Pages	15
Start Page	2243
End Page	2257
Type of Use	reuse in a thesis/dissertation

Portion	figures/tables/illustrations
Number of figures/tables/illustrations	1
Format	both print and electronic
Are you the author of this Elsevier article?	No
Will you be translating?	No
Title	Experimental Analysis and Modeling Investigation of Precipitation Kinetics and Hardening in two Al-Zn-Mg-Cu Alloys
Institution name	University of Waterloo
Expected presentation date	Jun 2023
Portions	Fig. 2 (b) on page 2246
Requestor Location	Dr. Atekeh Abolhasani Canada Attn: University of Waterloo
Publisher Tax ID	GB 494 6272 12
Total	0.00 CAD
Terms and Conditions	

INTRODUCTION

1. The publisher for this copyrighted material is Elsevier. By clicking "accept" in connection with completing this licensing transaction, you agree that the following terms and conditions

ELSEVIER LICENSE
TERMS AND CONDITIONS

May 15, 2023

This Agreement between Dr. Atekeh Abolhasani ("You") and Elsevier ("Elsevier") consists of your license details and the terms and conditions provided by Elsevier and Copyright Clearance Center.

License Number	5550010540116
License date	May 15, 2023
Licensed Content Publisher	Elsevier
Licensed Content Publication	Materials Science and Engineering: A
Licensed Content Title	Application of recently developed approaches to microstructural characterization and yield strength modeling of aluminum alloy AA7030
Licensed Content Author	Panthea Sepehrband,Shahrzad Esmaeili
Licensed Content Date	Jul 25, 2008
Licensed Content Volume	487
Licensed Content Issue	1-2
Licensed Content Pages	7
Start Page	309
End Page	315

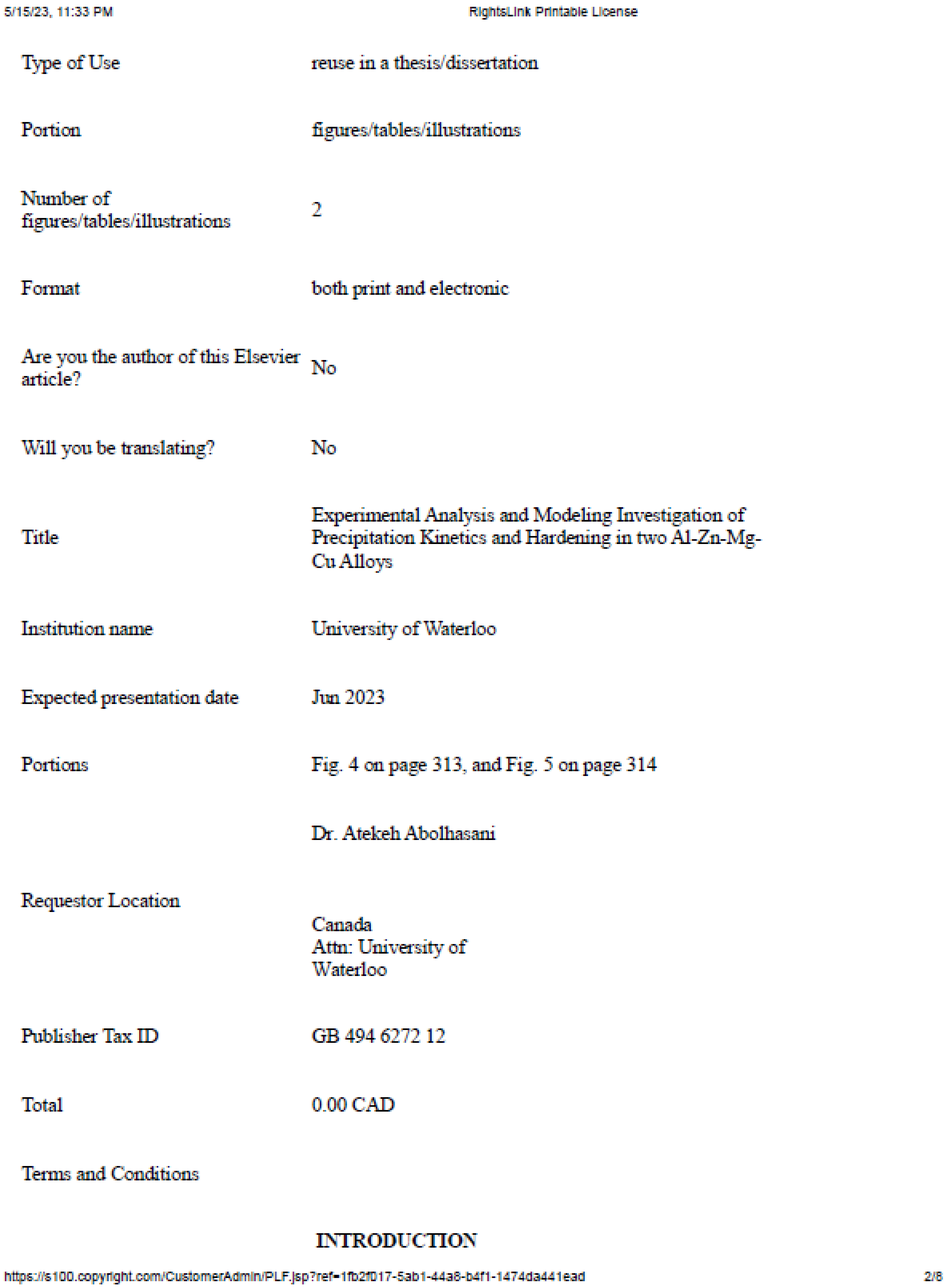

Type of Use	reuse in a thesis/dissertation
Portion	figures/tables/illustrations
Number of figures/tables/illustrations	2
Format	both print and electronic
Are you the author of this Elsevier article?	No
Will you be translating?	No
Title	Experimental Analysis and Modeling Investigation of Precipitation Kinetics and Hardening in two Al-Zn-Mg-Cu Alloys
Institution name	University of Waterloo
Expected presentation date	Jun 2023
Portions	Fig. 4 on page 313, and Fig. 5 on page 314
Requestor Location	Dr. Atekeh Abolhasani Canada Attn: University of Waterloo
Publisher Tax ID	GB 494 6272 12
Total	0.00 CAD
Terms and Conditions	

INTRODUCTION

References

[1] T. Dursun, C. Soutis, Recent developments in advanced aircraft aluminium alloys, Mater. Des. 56 (2014) 862–871. https://doi.org/10.1016/j.matdes.2013.12.002.

[2] A.C.U. Rao, V. Vasu, M. Govindaraju, K.V.S. Srinadh, Stress corrosion cracking behaviour of 7xxx aluminum alloys: A literature review, Trans. Nonferrous Met. Soc. China. 26 (2016) 1447–1471. https://doi.org/10.1016/S1003-6326(16)64220-6.

[3] M. Tisza, I. Czinege, Comparative study of the application of steels and aluminium in lightweight production of automotive parts, Int. J. Light. Mater. Manuf. 1 (2018) 229–238. https://doi.org/10.1016/j.ijlmm.2018.09.001.

[4] M. Kumar, N. Sotirov, C.M. Chimani, Investigations on warm forming of AW-7020-T6 alloy sheet, J. Mater. Process. Technol. 214 (2014) 1769–1776. https://doi.org/10.1016/j.jmatprotec.2014.03.024.

[5] G. Waterloo, V. Hansen, J. Gjønnes, S.R. Skjervold, Effect of predeformation and preaging at room temperture in Al-Zn-Mg-(Cu,Zr) alloys, Mater. Sci. Eng. A. 303 (2001) 226–233. https://doi.org/10.1016/S0921-5093(00)01883-9.

[6] M. Kumar, N.G. Ross, Investigations on the Hot Stamping of AW-7921-T4 Alloy Sheet, Adv. Mater. Sci. Eng. (2017). https://doi.org/10.1155/2017/7679219.

[7] A.J. Beaudoin, J.A. Dantzig, I.M.R. Co-pis, Development of a Two-Phase Model for the Hot Deformation of Highly-Alloyed Aluminum, 2005. https://www.osti.gov/servlets/purl/859225.

[8] H.E. Hu, L. Zhen, B.Y. Zhang, L. Yang, J.Z. Chen, Microstructure characterization of 7050 aluminum alloy during dynamic recrystallization and dynamic recovery, Mater. Charact. 59 (2008) 1185–1189. https://doi.org/10.1016/j.matchar.2007.09.010.

[9] S. Chen, K. Chen, P. Dong, S. Ye, L. Huang, Effect of heat treatment on stress corrosion cracking, fracture toughness and strength of 7085 aluminum alloy, Trans. Nonferrous Met. Soc. China. 24 (2014) 2320–2325. https://doi.org/10.1016/S1003-6326(14)63351-3.

[10] D.A. Porter, K.E. Easterling, Phase Transformations in Metals and Alloys, 1992.

[11] S. Liu, Q. Zhong, Y. Zhang, W. Liu, X. Zhang, Y. Deng, Investigation of quench sensitivity of high strength Al-Zn-Mg-Cu alloys by time-temperature-properties diagrams, Mater. Des. 31 (2010) 3116–3120. https://doi.org/10.1016/j.matdes.2009.12.038.

[12] M. Chemingui, M. Khitouni, K. Jozwiak, G. Mesmacque, A. Kolsi, Characterization of the mechanical properties changes in an Al-Zn-Mg alloy after a two-step ageing treatment at 70° and 135 °C, Mater. Des. 31 (2010) 3134–3139. https://doi.org/10.1016/j.matdes.2009.12.033.

[13] W.J. Poole, H.R. Shercliff, T. Castillo, Process modell for two step age hardening 7475 aluminum alloy, Mater. Sci. Technol. 13 (1997) 897–904. https://doi.org/10.1179/mst.1997.13.11.897.

[14] G. Sha, Y.B. Wang, X.Z. Liao, Z.C. Duan, S.P. Ringer, T.G. Langdon, Microstructural evolution of Fe-rich particles in an Al-Zn-Mg-Cu alloy during equal-channel angular pressing, Mater. Sci. Eng. A. 527 (2010) 4742–4749. https://doi.org/10.1016/j.msea.2010.04.041.

[15] S. Nandy, K. Kumar Ray, D. Das, Process model to predict yield strength of AA6063 alloy, Mater. Sci. Eng. A. 644 (2015) 413–424. https://doi.org/10.1016/j.msea.2015.07.070.

[16] J.S. Santner, A study of constituent, dispersoids and hardening particles in the fracture of 7075

aluminum alloys, Ohio, 1977.

[17] G.H. Koch, D.T. Kolijn, Aluminum Alloy 7075, J. Heat Treat. 1 (1979) 3–14.

[18] R. Ayer, J.Y. Koo, J.W. Steeds, B.K. Park, Microanalytical study of the heterogeneous phases in commercial Al-Zn-Mg-Cu alloys, Metall. Trans. A. 16 (1985) 1925–1936. https://doi.org/10.1007/BF02662393.

[19] X.J. Jiang, J. Tafto, B. Noble, B. Holme, G. Waterloo, Differential scanning calorimetry and electron diffraction investigation on low-temperature aging in Al-Zn-Mg alloys, Metall. Mater. Trans. A. 31 (2000) 339–348. https://doi.org/10.1007/s11661-000-0269-x.

[20] J. Mittra, U.D. Kulkarni, G.K. Dey, Hardness based model for determining the kinetics of precipitation, Mater. Sci. Eng. A. 500 (2009) 244–247. https://doi.org/10.1016/j.msea.2008.09.056.

[21] M.R. Ahmadi, E. Povoden-Karadeniz, K.I. Öksüz, A. Falahati, E. Kozeschnik, A model for precipitation strengthening in multi-particle systems, Comput. Mater. Sci. 91 (2014) 173–186. https://doi.org/10.1016/j.commatsci.2014.04.025.

[22] I.J. Polmear, Recent developments in light alloys, Mater. Trans. 37 (1996) 12–31. https://doi.org/10.2320/matertrans1989.37.12.

[23] Overview of materials for 7000 Series Aluminum Alloy, (n.d.). www.matweb.com.

[24] I.J. Polmear, Wrought aluminium alloys, in: Light Alloy., 2005: pp. 97–204. https://doi.org/10.1016/B978-075066371-7/50007-4.

[25] T. Ungár, J. Lendvai, I. Kovács, G. Groma, E. Kovács-Csetényi, The decomposition of the solid solution state in the temperature range 20 to 200 C in an Al-Zn-Mg alloy, J. Mater. Sci. 14 (1979) 671–679. https://doi.org/10.1007/BF00772729.

[26] W. Yang, S. Ji, M. Wang, Z. Li, Precipitation behaviour of Al-Zn-Mg-Cu alloy and diffraction analysis from η′ precipitates in four variants, J. Alloys Compd. 610 (2014) 623–629. https://doi.org/10.1016/j.jallcom.2014.05.061.

[27] C. Schmuck, P. Auger, F. Danoix, D. Blavette, Quantitative analysis of GP zones formed at room temperature in a 7150 Al-based alloy, Appl. Surf. Sci. 87–88 (1995) 228–233. https://doi.org/10.1016/0169-4332(94)00501-X.

[28] Z.W. Huang, M.H. Loretto, R.E. Smallman, J. White, The mechanism of nucleation and precipitation in 7075-0.7 Li alloy, Acta Metall. Mater. 42 (1994) 549–559. https://doi.org/10.1016/0956-7151(94)90509-6.

[29] J.M. Papazian, Calorimetric Studies of Precipitation and Dissolution Kinetics in Aluminum Alloys 2219 and 7075, Metall. Trans. A. 13 (1982) 761–769. https://doi.org/10.1007/BF02642389.

[30] M.H. Li, Y.Q. Yang, Z.Q. Feng, B. Huang, X. Luo, J.H. Lou, J.G. Ru, Precipitation sequence of η phase along low-angle grain boundaries in Al-Zn-Mg-Cu alloy during artificial aging, Trans. Nonferrous Met. Soc. China (English Ed. 24 (2014) 2061–2066. https://doi.org/10.1016/S1003-6326(14)63312-4.

[31] K. Wen, Y. Fan, G. Wang, L. Jin, X. Li, Z. Li, Y. Zhang, B. Xiong, Aging behavior and precipitate characterization of a high Zn-containing Al-Zn-Mg-Cu alloy with various tempers, Mater. Des. 101 (2016) 16–23. https://doi.org/10.1016/j.matdes.2016.03.150.

[32] T. Engdahl, V. Hansen, P.J. Warren, K. Stiller, Investigation of fine scale precipitates in Al-Zn-Mg alloys after various heat treatments, Mater. Sci. Eng. A. 327 (2002) 59–64.

https://doi.org/10.1016/S0921-5093(01)01876-7.

[33] J.C. Werenskiold, A. Deschamps, Y. Bréchet, Characterization and modeling of precipitation kinetics in an Al-Zn-Mg alloy, Mater. Sci. Eng. A. 293 (2000) 267–274. https://doi.org/10.1016/S0921-5093(00)01247-8.

[34] A. Dupasquier, R. Ferragut, M.M. Iglesias, M. Massazza, G. Riontino, P. Mengucci, G. Barucca, C.E. MacChi, A. Somoza, Hardening nanostructures in an AlZnMg alloy, Philos. Mag. 87 (2007) 3297–3323. https://doi.org/10.1080/14786430701271959.

[35] A.K. Mukhopadhyay, Guinier-Preston zones in a high-purity Al-Zn-Mg alloy, Philos. Mag. Lett. 70 (1994) 135–140. https://doi.org/10.1080/09500839408240966.

[36] L.K. Berg, G. Waterloo, D. Schryvers, L.R. Wallenberg, GP-zones in Al-Zn-Mg alloys and their role in artificial aging, 49 (2001) 3443–3451. https://doi.org/10.1016/S1359-6454(01)00251-8.

[37] B. Gueffroy, H. Löffler, On the reversion behaviour of an Al–Zn(4.5 at%)–Mg(2.0 at%) alloy, Phys. Status Solidi. 66 (1981) 585–590. https://doi.org/10.1002/pssa.2210660221.

[38] D.C.C. Magalhães, M.F. Hupalo, O.M. Cintho, Natural aging behavior of AA7050 Al alloy after cryogenic rolling, Mater. Sci. Eng. A. 593 (2014) 1–7. https://doi.org/10.1016/j.msea.2013.11.017.

[39] G. Sha, A. Cerezo, Kinetic Monte Carlo simulation of clustering in an Al-Zn-Mg-Cu alloy (7050), Acta Mater. 53 (2005) 907–917. https://doi.org/10.1016/j.actamat.2004.10.048.

[40] N. Saunders, The Modeling of Stable and Metastable Phase Formation in Multi-Component Al-Alloys, Mater. Forum. 28 (2004) 96–106.

[41] L.F. Mondolfo, Structure of the aluminium: Magnesium: Zinc alloys, Metall. Rev. 16 (1971) 95–124. https://doi.org/10.1179/mtlr.1971.16.1.95.

[42] M.M. Sharma, Microstructural and mechanical characterization of various modified 7XXX series spray formed alloys, Mater. Charact. 59 (2008) 91–99. https://doi.org/10.1016/j.matchar.2007.01.013.

[43] W.F. Smith, N.J. Grant, Effects of chromium and copper additions on precipitation in Al-Zn-Mg alloys, Metall. Trans. 2 (1971) 1333–1340. https://doi.org/10.1007/BF02913356.

[44] J. Buha, R.N. Lumley, A.G. Crosky, Secondary ageing in an aluminium alloy 7050, Mater. Sci. Eng. A. 492 (2008) 1–10. https://doi.org/10.1016/j.msea.2008.02.039.

[45] P. Priya, D.R. Johnson, M.J.M. Krane, Precipitation during cooling of 7XXX aluminum alloys, Comput. Mater. Sci. 139 (2017) 273–284. https://doi.org/10.1016/j.commatsci.2017.08.008.

[46] J. Liu, R. Hu, J. Zheng, Y. Zhang, Z. Ding, W. Liu, Y. Zhu, G. Sha, Formation of solute nanostructures in an Al–Zn–Mg alloy during long-term natural aging, J. Alloys Compd. 821 (2020) 153572. https://doi.org/10.1016/j.jallcom.2019.153572.

[47] A. Chatterjee, L. Qi, A. Misra, In situ transmission electron microscopy investigation of nucleation of GP zones under natural aging in Al-Zn-Mg alloy, Scr. Mater. 207 (2022) 114319. https://doi.org/10.1016/j.scriptamat.2021.114319.

[48] P. Zhang, K. Shi, J. Bian, J. Zhang, Y. Peng, G. Liu, A. Deschamps, J. Sun, Solute cluster evolution during deformation and high strain hardening capability in naturally aged Al–Zn–Mg alloy, Acta Mater. 207 (2021) 116682. https://doi.org/10.1016/j.actamat.2021.116682.

[49] V. Hansen, O.B. Karlsen, Y. Langsrud, J. Gjønnes, Precipitates, zones and transitions during aging of Al-Zn-Mg-Zr 7000 series alloy, Mater. Sci. Technol. 20 (2004) 185–193.

https://doi.org/10.1179/026708304225010424.

[50] G. Sha, A. Cerezo, Early-stage precipitation in Al-Zn-Mg-Cu alloy (7050), Acta Mater. 52 (2004) 4503–4516. https://doi.org/10.1016/j.actamat.2004.06.025.

[51] S. V. Emani, J. Benedyk, P. Nash, D. Chen, Double aging and thermomechanical heat treatment of AA7075 aluminum alloy extrusions, J. Mater. Sci. 44 (2009) 6384–6391. https://doi.org/10.1007/s10853-009-3879-8.

[52] H. Löffler, I. Kovacs, J. Lendvai, Review: Decomposition processes in Al-Zn-Mg alloys, J. Mater. Sci. 18 (1983) 2215–2240. https://doi.org/10.1007/BF00541825.

[53] H. Schmalzried, V. Gerold, X-ray investigations into the hardening of an aluminium-magnesium-zinc alloy, Z. Met. 49 (1958) 291–298. https://doi.org/10.1515/ijmr-1958-490603.

[54] A.K. Mukhopadhyay, K.S. Prasad, Formation of plate-shaped Guinier-Preston zones during natural aging of an Al-Zn-Mg-Cu-Zr alloy, Philos. Mag. Lett. 91 (2011) 214–222. https://doi.org/10.1080/09500839.2010.547525.

[55] S.H. Lee, J.G. Jung, S. Il Baik, D.N. Seidman, M.S. Kim, Y.K. Lee, K. Euh, Precipitation strengthening in naturally aged Al–Zn–Mg–Cu alloy, Mater. Sci. Eng. A. 803 (2021) 140719. https://doi.org/10.1016/j.msea.2020.140719.

[56] A. Deschamps, Influence of pre-strain and heat treatments on the microstructure and mechanical properties of Al-Zn-Mg-Cu alloys, Institut National Polytechnique de Grenoble, 1997.

[57] Z. Katz, N. Ryum, Precipitation kinetics in Al-alloys, Scr. Metall. 15 (1981) 265–268. https://doi.org/10.1016/0036-9748(81)90341-0.

[58] J. D. Embury, R. B. Nicholson, The Nucleation of Precipitates: The system Al-Zn-Mg, Acta Metall. 13 (1965) 403–417.

[59] X.M. Li, M.J. Starink, Identification and analysis of intermetallic phases in overaged Zr-containing and Cr-containing Al-Zn-Mg-Cu alloys, J. Alloys Compd. 509 (2011) 471–476. https://doi.org/10.1016/j.jallcom.2010.09.064.

[60] Z. Li, B. Xiong, Y. Zhang, B. Zhu, F. Wang, H. Liu, Investigation of microstructural evolution and mechanical properties during two-step ageing treatment at 115 C and 160 C in an Al-Zn-Mg-Cu alloy pre-stretched thick plate, Mater. Charact. 59 (2008) 278–282. https://doi.org/10.1016/j.matchar.2007.01.006.

[61] R. Ferragut, a Somoza, a Dupasquier, On the two-step ageing of a commercial Al - Zn - Mg alloy; a study by positron lifetime spectroscopy, J. Phys. Condens. Matter. 8 (1996) 8945–8952. https://doi.org/10.1088/0953-8984/8/45/026.

[62] G. Bergman, J.L.T. Waugh, L. Pauling, The crystal structure of the metallic phase Mg32(Al, Zn)49, Acta Crystallogr. 10 (1957) 254–259. https://doi.org/10.1107/S0365110X57000808.

[63] J. Luo, H. Luo, S. Li, R. Wang, Y. Ma, Effect of pre-ageing treatment on second nucleating of GPII zones and precipitation kinetics in an ultrafine grained 7075 aluminum alloy, Mater. Des. 187 (2020) 108402. https://doi.org/10.1016/j.matdes.2019.108402.

[64] F. Viana, A.M.P. Pinto, H.M.C. Santos, A.B. Lopes, Retrogression and re-ageing of 7075 aluminium alloy: microstructural characterization, J. Mater. Process. Technol. 92–93 (1999) 54–59. https://doi.org/10.1016/S0924-0136(99)00219-8.

[65] Y. Zou, L. Cao, X. Wu, Y. Wang, X. Sun, H. Song, M.J. Couper, Effect of ageing temperature on microstructure, mechanical property and corrosion behavior of aluminum alloy 7085, J. Alloys Compd. 823 (2020) 153792. https://doi.org/10.1016/j.jallcom.2020.153792.

[66] M. Conserva, M. Buratti, E. Di Russo, F. Gatto, Age hardening behavior of TMT processed AlZnMgCu alloy, Mater. Sci. Eng. 11 (1973) 103–112. https://doi.org/10.1016/0025-5416(73)90050-5.

[67] X.W. Nie, L.J. Zhang, Y. Du, Experiments and modeling of double-peak precipitation hardening and strengthening mechanisms in Al-Zn-Mg alloy, Trans. Nonferrous Met. Soc. China. 24 (2014) 2138–2144. https://doi.org/10.1016/S1003-6326(14)63324-0.

[68] M.J. Starink, X.M. Li, S.C. Wang, Models for the yield strength of Al-Zn-Mg-Cu alloys, Metall. Model. Alum. Alloy. - Proc. from Mater. Solut. Conf. 2003 1st Int. Symp. Metall. Model. Alum. Alloy. (2003) 105–118. https://doi.org/10.1016/S1359-6454(03)00363-X.

[69] J.T. Staley, Aging kinetics of aluminum alloy 7050, Metall. Trans. 5 (1974) 929–932. https://doi.org/10.1007/BF02643150.

[70] R. xian Yang, Z. yi Liu, P. you Ying, J. lin Li, L. hua Lin, S. min Zeng, Multistage-aging process effect on formation of GP zones and mechanical properties in Al–Zn–Mg–Cu alloy, Trans. Nonferrous Met. Soc. China (English Ed. 26 (2016) 1183–1190. https://doi.org/10.1016/S1003-6326(16)64221-8.

[71] A. Lervik, E. Thronsen, J. Friis, C.D. Marioara, S. Wenner, A. Bendo, K. Matsuda, R. Holmestad, S.J. Andersen, Atomic structure of solute clusters in Al–Zn–Mg alloys, Acta Mater. 205 (2021) 116574. https://doi.org/10.1016/j.actamat.2020.116574.

[72] S. Liu, M. Zhang, Q. Li, Q. Zhu, H. Song, X. Wu, L. Cao, M.J. Couper, Effect of quenching rate on strengthening behavior of an Al-Zn-Mg-Cu alloy during natural ageing, Mater. Sci. Eng. A. 793 (2020) 139900. https://doi.org/10.1016/j.msea.2020.139900.

[73] Y. Chen, C.Y. Liu, B. Zhang, F.C. Qin, Y.F. Hou, Precipitation behavior and mechanical properties of Al–Zn–Mg alloy with high Zn concentration, J. Alloys Compd. 825 (2020) 154005. https://doi.org/10.1016/j.jallcom.2020.154005.

[74] D. Lloyd, Advances in Industrial Materials, in: and A.A. D. S. Wilkinson, W. J. Poole (Ed.), Metall. Soc. CIM, Montreal, 1998: p. 3.

[75] J.E. Hatch, Aluminum Properties and Physical Metallurgy, ASM ,Ohio, US. (1984) 424. https://doi.org/10.1361/appm1984p001.

[76] J.A. Österreicher, G. Kirov, S.S.A. Gerstl, E. Mukeli, F. Grabner, M. Kumar, Stabilization of 7xxx aluminium alloys, J. Alloys Compd. 740 (2018) 167–173. https://doi.org/10.1016/j.jallcom.2018.01.003.

[77] L. Wan, Y.L. Deng, L.Y. Ye, Y. Zhang, The natural ageing effect on pre-ageing kinetics of Al-Zn-Mg alloy, J. Alloys Compd. 776 (2019) 469–474. https://doi.org/10.1016/j.jallcom.2018.10.338.

[78] P.K. Rout, M.M. Ghosh, K.S. Ghosh, Microstructural, mechanical and electrochemical behaviour of a 7017 Al-Zn-Mg alloy of different tempers, Mater. Charact. 104 (2015) 49–60. https://doi.org/10.1016/j.matchar.2015.03.025.

[79] J.K. Park, A.J. Ardell, Microstructures of the commercial 7075 Al alloy in the T651 and T7 tempers, Metall. Trans. A. 14 (1983) 1957–1965. https://doi.org/10.1007/BF02662363.

[80] Y. Liu, D.M. Jiang, W.J. Li, The effect of multistage ageing on microstructure and mechanical properties of 7050 alloy, J. Alloys Compd. 671 (2016) 408–418. https://doi.org/10.1016/j.jallcom.2016.01.266.

[81] C. Cao, D. Zhang, L. Zhuang, J. Zhang, Improved age-hardening response and altered

precipitation behavior of Al-5.2Mg-0.45Cu-2.0Zn (wt%) alloy with pre-aging treatment, J. Alloys Compd. 691 (2017) 40–43. https://doi.org/10.1016/j.jallcom.2016.08.206.

[82] Y.S. Lee, D.H. Koh, H.W. Kim, Y.S. Ahn, Improved bake-hardening response of Al-Zn-Mg-Cu alloy through pre-aging treatment, Scr. Mater. 147 (2018) 45–49. https://doi.org/10.1016/j.scriptamat.2017.12.030.

[83] C.R. Hutchinson, F. De Geuser, Y. Chen, A. Deschamps, Quantitative measurements of dynamic precipitation during fatigue of an Al-Zn-Mg-(Cu) alloy using small-angle X-ray scattering, Acta Mater. 74 (2014) 96–109. https://doi.org/10.1016/j.actamat.2014.04.027.

[84] A. Deschamps, G. Fribourg, Y. Bréchet, J.L. Chemin, C.R. Hutchinson, In situ evaluation of dynamic precipitation during plastic straining of an Al-Zn-Mg-Cu alloy, Acta Mater. 60 (2012) 1905–1916. https://doi.org/10.1016/j.actamat.2012.01.002.

[85] W.J. Poole, J.A. Sæter, S. Skjervold, G. Waterloo, A model for predicting the effect of deformation after solution treatment on the subsequent artificial aging behavior of AA7030 and AA7108 alloys, Metall. Mater. Trans. A. 31 (2000) 2327–2338. https://doi.org/10.1007/s11661-000-0148-5.

[86] A. Deschamps, F. Livet, Y. Bréchet, Influence of predeformation on ageing in an Al-Zn-Mg alloy-I. Microstructure evolution and mechanical properties, Acta Mater. 47 (1998) 281–292. https://doi.org/10.1016/S1359-6454(98)00293-6.

[87] A. Deschamps, F. Livet, Y. Bréchet, Influence of predeformation on ageing in an Al–Zn–Mg alloy—I. Microstructure evolution and mechanical properties, Acta Mater. 47 (1998) 281–292. https://doi.org/10.1016/S1359-6454(98)00293-6.

[88] K. Omer, A. Abolhasani, S. Kim, T. Nikdejad, C. Butcher, S. Esmaeili, M. Worswick, Process parameters for hot stamping of AA7075 and D-7xxx to achieve high performance aged products, J. Mater. Process. Technol. 257 (2018) 170–179. https://doi.org/10.1016/j.jmatprotec.2018.02.039.

[89] P. Schuster, J. Österreicher, G. Kirov, C. Sommitsch, O. Kessler, E. Mukeli, Characterisation and Comparison of Process Chains for Producing Automotive Structural Parts from 7xxx Aluminium Sheets, Metals (Basel). 9 (2019) 305. https://doi.org/10.3390/met9030305.

[90] K. Zheng, Y. Dong, J.H. Zheng, A. Foster, J. Lin, H. Dong, T.A. Dean, The effect of hot form quench (HFQ®) conditions on precipitation and mechanical properties of aluminium alloys, Mater. Sci. Eng. A. 761 (2019) 138017. https://doi.org/10.1016/j.msea.2019.06.027.

[91] L. Zhu, Z. Liu, Z. Zhang, Investigation on strengthening of 7075 aluminum alloy sheet in a new hot stamping process with pre-cooling, Int. J. Adv. Manuf. Technol. 103 (2019) 4739–4746. https://doi.org/10.1007/s00170-019-03890-0.

[92] A.N. Solonin, A.Y. Churyumov, A.V. Mikhailovskaya, M.A. Ryazantseva, M.G. Khomutov, Modeling the evolution of the structure and properties of alloys for an Al-Zn-Mg system in ageing, Russ. J. Non-Ferrous Met. 51 (2010) 471–475. https://doi.org/10.3103/S1067821210060076.

[93] K.S. Ghosh, N. Gao, Determination of kinetic parameters from calorimetric study of solid state reactions in 7150 Al-Zn-Mg alloy, Trans. Nonferrous Met. Soc. China (English Ed. 21 (2011) 1199–1209. https://doi.org/10.1016/S1003-6326(11)60843-1.

[94] W. Sha, Application of simple practical models for early stage ageing precipitation kinetics and hardening in aluminium alloys, Mater. Des. 28 (2007) 528–533. https://doi.org/10.1016/j.matdes.2005.08.012.

[95] A.R. Eivani, A.K. Taheri, Modeling age hardening kinetics of an Al-Mg-Si-Cu aluminum alloy, J. Mater. Process. Technol. 205 (2008) 388–393. https://doi.org/10.1016/j.jmatprotec.2007.11.195.

[96] S. Esmaeili, Precipitation Hardening Behaviour of AA6111, PhD Thesis, Univ. Br. Columbia. (2002). https://doi.org/10.16953/deusbed.74839.

[97] A. Deschamps, Y. Brechet, Influence of predeformation and ageing of an Al–Zn–Mg alloy—II. Modeling of precipitation kinetics and yield stress, Acta Mater. 47 (1998) 293–305. https://doi.org/10.1016/S1359-6454(98)00296-1.

[98] S. Esmaeili, D.J. Lloyd, Modeling of precipitation hardening in pre-aged AlMgSi(Cu) alloys, Acta Mater. 53 (2005) 5257–5271. https://doi.org/10.1016/j.actamat.2005.08.006.

[99] W.A. Johnson, R.F. Mehl, Reaction Kinetics in Processes of Nucleation and Growth, Trans. Am. Inst. Min. Metall. Eng. 135 (1939) 416–442.

[100] A.N. Kolmogorov, On the Statistical Theory of Crystallization of Metals, Ser. Mater. 1 (1937) 355–359.

[101] M. Avrami, Kinetics of phase change. I: General theory, J. Chem. Phys. 7 (1939) 1103–1112. https://doi.org/10.1063/1.1750380.

[102] D.A. Porter, K.E. Easterling, Phase transformtions in metals and alloys, Second, Chapman and Hall, 1992.

[103] D.H. Bratland, Grong, H. Shercliff, O.R. Myhr, S. Tjøtta, Modelling of precipitation reactions in industrial processing, Acta Mater. 45 (1997) 1–22. https://doi.org/10.1016/S1359-6454(96)00100-0.

[104] H.R. Shercliff, M.F. Ashby, A process model for age hardening of aluminium alloys-II. Applications of the model, Acta Metall. Mater. 38 (1990) 1803–1812. https://doi.org/10.1016/0956-7151(90)90292-O.

[105] S. Esmaeili, D.J. Lloyd, W.J. Poole, A yield strength model for the Al-Mg-Si-Cu alloy AA6111, Acta Mater. 51 (2003) 2243–2257. https://doi.org/10.1016/S1359-6454(03)00028-4.

[106] N. Baghbanaghaei, Characterisation and modeling of precipitation kinetics and yield strength in variously treated 7000-series aluminum alloys, University of Waterloo, 2021.

[107] H.R. Shercliff, M.F. Ashby, A process model for age hardening of aluminium alloys-I. The model, Acta Metall. Mater. 38 (1990) 1789–1802. https://doi.org/10.1016/0956-7151(90)90291-N.

[108] O. Richmond, No Title, in: Proc. Int. Conf. Alum. Technol. 89, The Institute of Materials, London, 1986: p. 615.

[109] L.M. Cheng, W.J. Poole, J.D. Embury, D.J. Lloyd, The influence of precipitation on the work-hardening behavior of the aluminum alloys AA6111 and AA7030, Metall. Mater. Trans. A. 34 A (2003) 2473–2481. https://doi.org/10.1007/s11661-003-0007-2.

[110] F. Fazeli, W.J. Poole, C.W. Sinclair, Modeling the effect of Al3Sc precipitates on the yield stress and work hardening of an Al-Mg-Sc alloy, Acta Mater. 56 (2008) 1909–1918. https://doi.org/10.1016/j.actamat.2007.12.039.

[111] A.J. Ardell, Precipitation hardening, Metall. Trans. A. 16 (1985) 2131–2165. https://doi.org/10.1007/BF02670416.

[112] P. Sepehrband, S. Esmaeili, Application of recently developed approaches to microstructural

characterization and yield strength modeling of aluminum alloy AA7030, Mater. Sci. Eng. A. 487 (2008) 309–315. https://doi.org/10.1016/j.msea.2007.10.067.

[113] S. Esmaeili, D.J. Lloyd, W.J. Poole, Modeling of precipitation hardening for the naturally aged Al-Mg-Si-Cu alloy AA6111, Acta Mater. 51 (2003) 3467–3481. https://doi.org/10.1016/S1359-6454(03)00167-8.

[114] A.S. E1097-1, Standard Guide for Determination of Various Elements by Direct Current Plasma Atomic Emission Spectrometry, ASTM Int. (2012).

[115] M. Di Ciano, S. DiCecco, S. Esmaeili, M.A. Wells, M.J. Worswick, Coarsening of AA6013-T6 Precipitates During Sheet Warm Forming Applications, J. Mater. Eng. Perform. 27 (2018) 939–947. https://doi.org/10.1007/s11665-018-3161-9.

[116] F. Kellogg, B. Butler, Gleeble Testing of Tungsten Samples, 2013.

[117] B. Gault, M.P. Moody, J.M. Cairney, S.P. Ringer, Atom Probe Microscopy, 2012.

[118] D.J. Larson, T.J. Prosa, R.M. Ulfig, B.P. Geiser, T.F. Kelly, Local electrode Atom probe tomography- A User's Guide, Springer, 2013.

[119] J.M. Hyde, E.A. Marquis, K.B. Wilford, T.J. Williams, Ultramicroscopy A sensitivity analysis of the maximum separation method for the characterisation of solute clusters, Ultramicroscopy. 111 (2011) 440–447. https://doi.org/10.1016/j.ultramic.2010.12.015.

[120] T. Malis, S.C. Cheng, R.F. Egerton, EELS log-ratio technique for specimen-thickness measurement in the TEM, J. Electron Microsc. Tech. 8 (1988) 193–200. https://doi.org/10.1002/jemt.1060080206.

[121] J. Pešička, A. Aghajani, C. Somsen, A. Hartmaier, G. Eggeler, How dislocation substructures evolve during long-term creep of a 12% Cr tempered martensitic ferritic steel, Scr. Mater. 62 (2010) 353–356. https://doi.org/10.1016/j.scriptamat.2009.10.037.

[122] Monitoring of biodiesel synthesis reactions by isothermal microcalorimetry, (n.d.). www.setaram.com.

[123] A. Abolhasani, B. Langelier, M.J. Worswick, M.A. Wells, S. Esmaeili, Experimental analysis and modelling of natural aging evolution in AA7xxx Al alloys, J. Alloys Compd. 906 (2022) 1–14. https://doi.org/10.1016/j.jallcom.2022.164344.

[124] D.J. Lloyd, A.K. Gupta, Aluminum alloys and the thermal processing associated with automotive sheet, in: Thermec 97 Proc. Int. Conf. Thermomechanical Process. Steels Other Mater., Wollongong, Australia, 1997: pp. 99–108.

[125] S. Esmaeili, D.J. Lloyd, Effect of composition on clustering reactions in AlMgSi(Cu) alloys, Scr. Mater. 50 (2004) 155–158. https://doi.org/10.1016/j.scriptamat.2003.08.030.

[126] N.Q. Chinh, J. Lendvai, D.H. Ping, K. Hono, The effect of Cu on mechanical and precipitation properties of Al-Zn-Mg alloys, J. Alloys Compd. 378 (2004) 52–60. https://doi.org/10.1016/j.jallcom.2003.11.175.

[127] P. Schloth, J.N. Wagner, J.L. Fife, A. Menzel, J.M. Drezet, H. Van Swygenhoven, Early precipitation during cooling of an Al-Zn-Mg-Cu alloy revealed by in situ small angle X-ray scattering, Appl. Phys. Lett. 105 (2014) 1–5. https://doi.org/10.1063/1.4894768.

[128] G. Riontino, M. Massazza, A differential scanning calorimetry and vickers microhardness study of phase transformations in an Al-Zn-Mg alloy, Philos. Mag. 84 (2004) 967–981. https://doi.org/10.1080/14786430310001644990.

[129] P. Schloth, A. Deschamps, C.A. Gandin, J.M. Drezet, Modeling of GP(I) zone formation during quench in an industrial AA7449 75 mm thick plate, Mater. Des. 112 (2016) 46–57. https://doi.org/10.1016/j.matdes.2016.09.052.

[130] Y. Zhang, M. Weyland, B. Milkereit, M. Reich, P.A. Rometsch, Precipitation of a new platelet phase during the quenching of an Al-Zn-Mg-Cu alloy, Sci. Rep. 6 (2016) 1–9. https://doi.org/10.1038/srep23109.

[131] Y. Zhang, D. Pelliccia, B. Milkereit, N. Kirby, M.J. Starink, P.A. Rometsch, Analysis of age hardening precipitates of Al-Zn-Mg-Cu alloys in a wide range of quenching rates using small angle X-ray scattering, Mater. Des. 142 (2018) 259–267. https://doi.org/10.1016/j.matdes.2018.01.037.

[132] S. Liu, C. Li, S. Han, Y. Deng, X. Zhang, Effect of natural aging on quench-induced inhomogeneity of microstructure and hardness in high strength 7055 aluminum alloy, J. Alloys Compd. 625 (2015) 34–43. https://doi.org/10.1016/j.jallcom.2014.10.195.

[133] S. Liu, Q. Li, H. Lin, L. Sun, T. Long, L. Ye, Y. Deng, Effect of quench-induced precipitation on microstructure and mechanical properties of 7085 aluminum alloy, Mater. Des. 132 (2017) 119–128. https://doi.org/10.1016/j.matdes.2017.06.054.

[134] L. Ding, L. Zhao, Y. Weng, D. Schryvers, Q. Liu, H. Idrissi, Atomic-scale investigation of the heterogeneous precipitation in the E (Al18Mg3Cr2) dispersoid of 7075 aluminum alloy, J. Alloys Compd. 851 (2021) 156890. https://doi.org/10.1016/j.jallcom.2020.156890.

[135] J.S. Robinson, D.A. Tanner, C.E. Truman, A.M. Paradowska, R.C. Wimpory, The influence of quench sensitivity on residual stresses in the aluminium alloys 7010 and 7075, Mater. Charact. 65 (2012) 73–85. https://doi.org/10.1016/j.matchar.2012.01.005.

[136] S. Chen, R. Gu, Q. Liu, W. Wang, X. Wei, Experimental and numerical investigation on strengthening behavior of 7075 aluminum alloy sheets in hot forming- quenching integrated process, J. Manuf. Sci. Eng. Trans. ASME. 142 (2020) 1–10. https://doi.org/10.1115/1.4046741.

[137] O.C. Hellman, J.A. Vandenbroucke, J. Rüsing, D. Isheim, D.N. Seidman, Analysis of three-dimensional atom-probe data by the proximity histogram, Microsc. Microanal. 6 (2000) 437–444. https://doi.org/10.1007/s100050010051.

[138] M.M. Shea, B.V.N. Rao, Enhanced age hardening of 7075 aluminum alloy after ultrasonic vibration, Mater. Sci. Eng. 61 (1983) 67–77. https://doi.org/10.1016/0025-5416(83)90127-1.

[139] O.N. Senkov, S. V. Senkova, M.R. Shagiev, Effect of Sc on aging kinetics in a direct chill cast Al-Zn-Mg-Cu alloy, Metall. Mater. Trans. A. 39 A (2008) 1034–1053. https://doi.org/10.1007/s11661-008-9485-6.

[140] K. Stiller, P.J. Warren, V. Hansen, J. Angenete, J. Gjønnes, Investigation of precipitation in an Al–Zn–Mg alloy after two-step ageing treatment at 100° and 150°C, Mater. Sci. Eng. A270. 270 (1999) 55–63. https://doi.org/10.1016/S0921-5093(99)00231-2.

[141] S.K. Maloney, K. Hono, I.J. Polmear, S.P. Ringer, The chemistry of precipitates in an aged Al-2.1Zn-1.7Mg at.% alloy, Acta Metall. 41 (1999) 1031–1038. https://doi.org/10.1016/S1359-6462(99)00253-5.

[142] S.R. Ortner, C.R.M. Grovenor, B.A. Shollock, On the structure and composition of G-P zones in high purity AlZnMg alloys, Scr. Metall. 22 (1988) 839–842. https://doi.org/10.1016/S0036-9748(88)80060-7.

[143] R. Gerlach, H. Loffler, Isothermal Ageing in the T Range from 0C to 180C of a Technical A1-

2.0 at.% Zn-1.3 at.% Mg Alloy after Direct Quench, J. Japanese Soc. Pediatr. Surg. 14 (1978) 1034–1035. https://doi.org/10.11164/jjsps.14.7_1034_4.

[144] V. Fallah, B. Langelier, N. Ofori-opoku, B. Raeisinia, Cluster evolution mechanisms during aging in Al – Mg – Si alloys, Acta Mater. 103 (2016) 290–300. https://doi.org/10.1016/j.actamat.2015.09.027.

[145] M. Radomsky, H. Loffler, J. Lendvai, T. Ungar, I. Kovacs, A model of the effect of R.T. preageing on the nucleation of ή-precipitation in Al-Zn-Mg alloys, Krist. Und Tech. 15 (1980) 721–725. https://doi.org/10.1002/crat.19800150615.

[146] S. Esmaeili, X. Wang, D.J. Lloyd, W.J. Poole, On the precipitation-hardening behavior of the Al-Mg-Si-Cu alloy AA6111, Metall. Mater. Trans. A Phys. Metall. Mater. Sci. 34 (2003) 751–763. https://doi.org/10.1007/s11661-003-1003-2.

[147] S. Esmaeili, D.J. Lloyd, Characterization of the evolution of the volume fraction of precipitates in aged AlMgSiCu alloys using DSC technique, Mater. Charact. 55 (2005) 307–319. https://doi.org/10.1016/j.matchar.2005.07.007.

[148] J. Chen, L. Zhen, S. Yang, W. Shao, S. Dai, Investigation of precipitation behavior and related hardening in AA 7055 aluminum alloy, Mater. Sci. Eng. A. 500 (2009) 34–42. https://doi.org/10.1016/j.msea.2008.09.065.

[149] A. Deschamps, Y. Bréchet, Influence of quench and heating rates on the ageing response of an Al–Zn–Mg–(Zr) alloy, Mater. Sci. Eng. A. 251 (1998) 200–207. https://doi.org/10.1016/S0921-5093(98)00615-7.

[150] D.S. Thompson, B.S. Subramanya, S.A. Levy, Quench rate effects in Al-Zn-Mg-Cu alloys, Metall. Trans. 2 (1971) 1149–1160. https://doi.org/10.1007/BF02664247.

[151] J. Peng, S. Bahl, A. Shyam, J.A. Haynes, D. Shin, Solute-vacancy clustering in aluminum, Acta Mater. 196 (2020) 747–758. https://doi.org/10.1016/j.actamat.2020.06.062.

[152] A. Deschamps, Y. Bréchet, P. Guyot, F. Livet, On the influence of dislocations on precipitation in an Al-Zn-Mg alloy, Zeitschrift Fuer Met. Res. Adv. Tech. 88 (1997) 601–606.

[153] X. Peng, Q. Guo, X. Liang, Y. Deng, Y. Gu, G. Xu, Z. Yin, Mechanical properties, corrosion behavior and microstructures of a non-isothermal ageing treated Al-Zn-Mg-Cu alloy, Mater. Sci. Eng. A. 688 (2017) 146–154. https://doi.org/10.1016/j.msea.2017.01.086.

[154] K. Matsuda, A. Kawai, K. Watanabe, S. Lee, C.D. Marioara, S. Wenner, K. Nishimura, T. Matsuzaki, N. Nunomura, T. Sato, R. Holmestad, S. Ikeno, Extra Electron Diffraction Spots Caused by Fine Precipitates Formed at the Early Stage of Aging in Al-Mg-X (X=Si, Ge, Zn)-Cu Alloys, Mater. Trans. 58 (2017) 167–175. https://doi.org/10.2464/jilm.67.186.

[155] M. Conserva, E. Di Russo, O. Caloni, Comparison of the influence of chromium and zirconium on the quench sensitivity of Al-Zn-Mg-Cu alloys, Metall. Trans. 2 (1971) 1227–1232. https://doi.org/10.1007/BF02664256.

[156] S. Bai, Z. Liu, P. Ying, J. Wang, A. Wang, Quantitative study of the solute clustering and precipitation in a pre-stretched Al-Cu-Mg-Ag alloy, J. Alloys Compd. 725 (2017) 1288–1296. https://doi.org/10.1016/j.jallcom.2017.07.258.

[157] T.F. Chung, Y.L. Yang, B.M. Huang, Z. Shi, J. Lin, T. Ohmura, J.R. Yang, Transmission electron microscopy investigation of separated nucleation and in-situ nucleation in AA7050 aluminium alloy, Acta Mater. 149 (2018) 377–387. https://doi.org/10.1016/j.actamat.2018.02.045.

[158] T.H. Sanders, E.A. Starke, The relationship of microstructure to monotonic and cyclic straining of two age hardening aluminum alloys, Metall. Trans. A. 7 (1976) 1407–1418. https://doi.org/10.1007/BF02658827.

[159] D. Wang, D.R. Ni, Z.Y. Ma, Effect of pre-strain and two-step aging on microstructure and stress corrosion cracking of 7050 alloy, Mater. Sci. Eng. A. 494 (2008) 360–366. https://doi.org/10.1016/j.msea.2008.04.023.

[160] J.W. Christian, The theory of transformations in metals and alloys, Third, Elsevier Ltd, 2002.

[161] S. Liu, C. Li, S. Han, Y. Deng, X. Zhang, Effect of natural aging on quench-induced inhomogeneity of microstructure and hardness in high strength 7055 aluminum alloy, J. Alloys Compd. 625 (2015) 34–43. https://doi.org/10.1016/j.jallcom.2014.10.195.

[162] A. Deschamps, Y. Bréchet, F. Livet, Influence of copper addition on precipitation kinetics and hardening in Al–Zn–Mg alloy, Mater. Sci. Technol. 15 (1999) 993–1000. https://doi.org/10.1179/026708399101506832.

[163] R.T. Shuey, F. Barlat, M.E. Karabin, D.J. Chakrabarti, Experimental and analytical investigations on plane strain toughness for 7085 aluminum alloy, Metall. Mater. Trans. A Phys. Metall. Mater. Sci. 40 (2009) 365–376. https://doi.org/10.1007/s11661-008-9703-2.

[164] S. Yannacopoulos, S.O. Kasap, A. Hedayat, A. Verma, An Experimental Study of Phase Transformations in an Al – Zn – Mg – Zr Alloy : DSC and Hot Microhardness Measurements AN EXPERIMENTAL STUDY OF PHASE TRANSFORMATIONS IN AN AI-Zn-Mg-Zr ALLOY :, 4433 (2013). https://doi.org/10.1179/cmq.1994.33.1.51.

[165] H. Mecking, U.F. Kocks, Kinetics of flow and strain-hardening, Acta Metall. 29 (1981) 1865–1875. https://doi.org/10.1016/0001-6160(81)90112-7.

[166] A. Deschamps, Y. Brechet, Influence of predeformation and ageing of an Al-Zn-Mg Alloy-II. Modeling of precipitation kinetics and yield stress, Acta Mater. 47 (1998) 293–305. https://doi.org/10.1016/S1359-6454(98)00296-1.

[167] P. Guyot, L. Cottignies, Precipitation kinetics, mechanical strength and electrical conductivity of AlZnMgCu alloys, Acta Mater. 44 (1996) 4161–4167. https://doi.org/10.1016/S1359-6454(96)00033-X.

[168] F.J. Humphreys, M. Hatherly, Recrystallization and Related Annealing Phenomena, Second, Elsevier Ltd, 2004.

[169] R.J.M. Farla, H. Kokkonen, J.D.F. Gerald, A. Barnhoorn, U.H. Faul, I. Jackson, Dislocation recovery in fine-grained polycrystalline olivine, Phys. Chem. Miner. 38 (2011) 363–377. https://doi.org/10.1007/s00269-010-0410-3.

[170] M. Militzer, W.P. Sun, J.J. Jonas, Modelling the effect of deformation-induced vacancies on segregation and precipitation, Acta Metall. Mater. 42 (1994) 133–141. https://doi.org/10.1016/0956-7151(94)90056-6.

[171] R.W. Balluffi, On Measurements of Self -Diffusion Rates, Phys. Status Solidi. 42 (1970) 11–34.

[172] E.W. Hart, On the Role of Dislocations THE, Acta Metall. 5 (1957) 597.

[173] H.J. Frost, M.F. Ashby, Deformation mechanism maps: the plasticity and creep of metals and ceramics, Pergamon press, 1982.

[174] R. Guo, J. Wu, Dislocation density based model for Al-Cu-Mg alloy during quenching with considering the quench-induced precipitates, J. Alloys Compd. 741 (2018) 432–441.

https://doi.org/10.1016/j.jallcom.2018.01.135.

[175] R.C. Picu, D. Zhang, Atomistic study of pipe diffusion in Al-Mg alloys, Acta Mater. 52 (2004) 161–171. https://doi.org/10.1016/j.actamat.2003.09.002.

[176] P. Sepehrband, Experimental Analysis and Computational Modeling of Annealing in AA6xxx Alloys, University of Waterloo, 2010.

[177] O.R. Myhr, Ø. Grong, C. Schäfer, An Extended Age-Hardening Model for Al-Mg-Si Alloys Incorporating the Room-Temperature Storage and Cold Deformation Process Stages, Metall. Mater. Trans. A Phys. Metall. Mater. Sci. 46 (2015) 6018–6039. https://doi.org/10.1007/s11661-015-3175-y.

[178] W.J. Poole, H.R. Shercliff, T. Castillo, Process model for two step age hardening of 7475 aluminium alloy, Mater. Sci. Technol. 13 (1997) 897–904. https://doi.org/10.1179/mst.1997.13.11.897.

Appendix A. TEM Results

Effect of Cr-rich particles on precipitation

In this appendix, some complementary TEM results for AA7075 samples with different thermal processing histories (reported in Section 4.2.2.1.2.2) are presented. Figure A1 shows the heterogeneous formation of nano-sized precipitates on large dispersoids. EDS results in Figure A1 show that these dispersoids are Cr-rich particles and that they are available in the microstructures of the AA7075 alloy with various thermal processing histories.

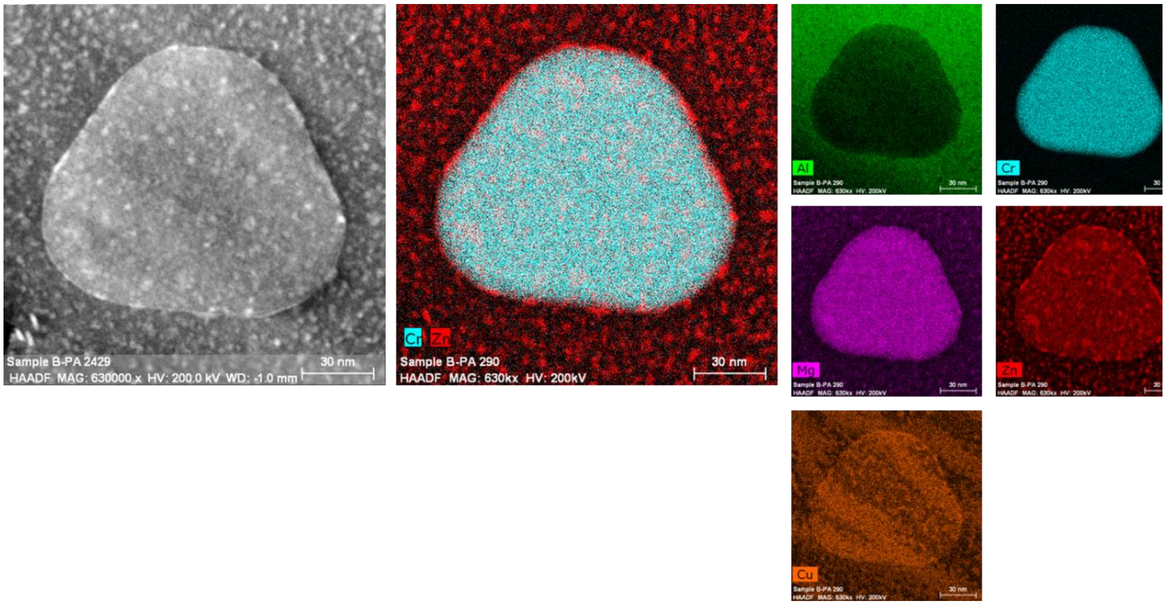

Figure A1. HAADF images and element mapping showing a Cr-rich dispersoid and a distribution of primarily precipitates enriched in Zn and Mg atoms, and to a lesser extent, Cu atoms in AA7075-PA.

As shown in Figure A2, the Cr-rich particles are coherent. These dispersoids are the main reason for the quench sensitivity of AA7xxx alloys, as reported in literature [43,59,155]. The formation of precipitates on the interfaces of these particles, as seen in the TEM results in Figure A1 and Figure A2, further supports the APT results (Section 4.1.1.3) which have shown the formation of quenching Zn-Mg precipitates in the microstructure of naturally aged AA7075.

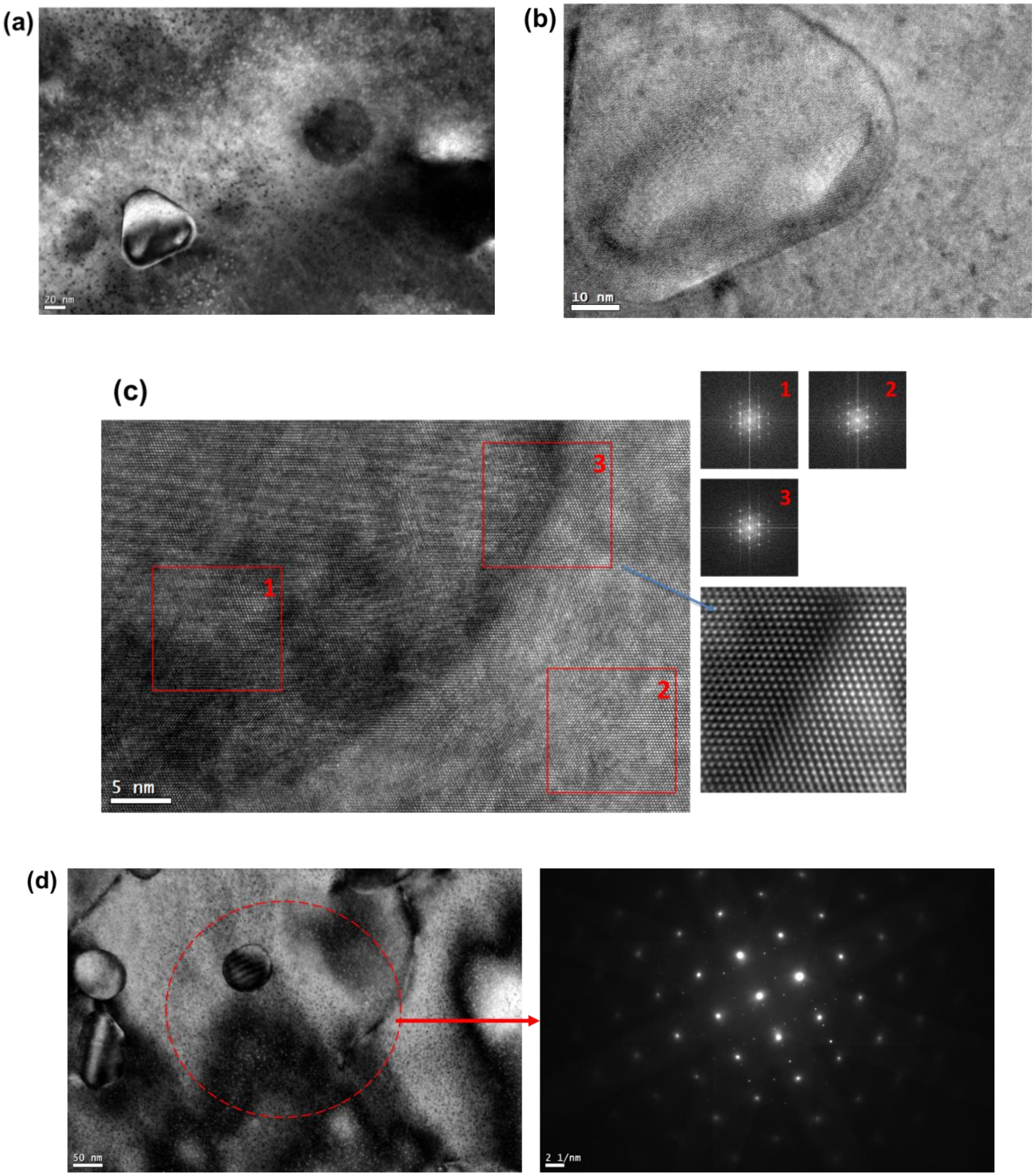

Figure A2. (a) Bright field (BF) image showing Cr-rich dispersoids in AA7075-PA (beam parallel to [011] of Al matrix)), (b) inverse fast Fourier transition (IFFT) image from Cr-rich dispersoid, (c) IFFT image from Cr-rich dispersoid and FFT patterns from (1) Al matrix, (2) dispersoid, and (3) their interface showing coherency of the Cr-rich dispersoid with Al matrix, and (d) selected area diffraction pattern from Cr-rich dispersoids showing an orientation relationship with matrix (beam parallel to [001] of Al matrix).

Figure A3 and Figure A4 also show the microstructure of AA7075 in the PB and DQ+PB conditions, respectively. Regardless of the thermal processing history, heterogeneous formation of precipitates on Cr-rich particles occurs in the microstructure of the AA7075 alloy.

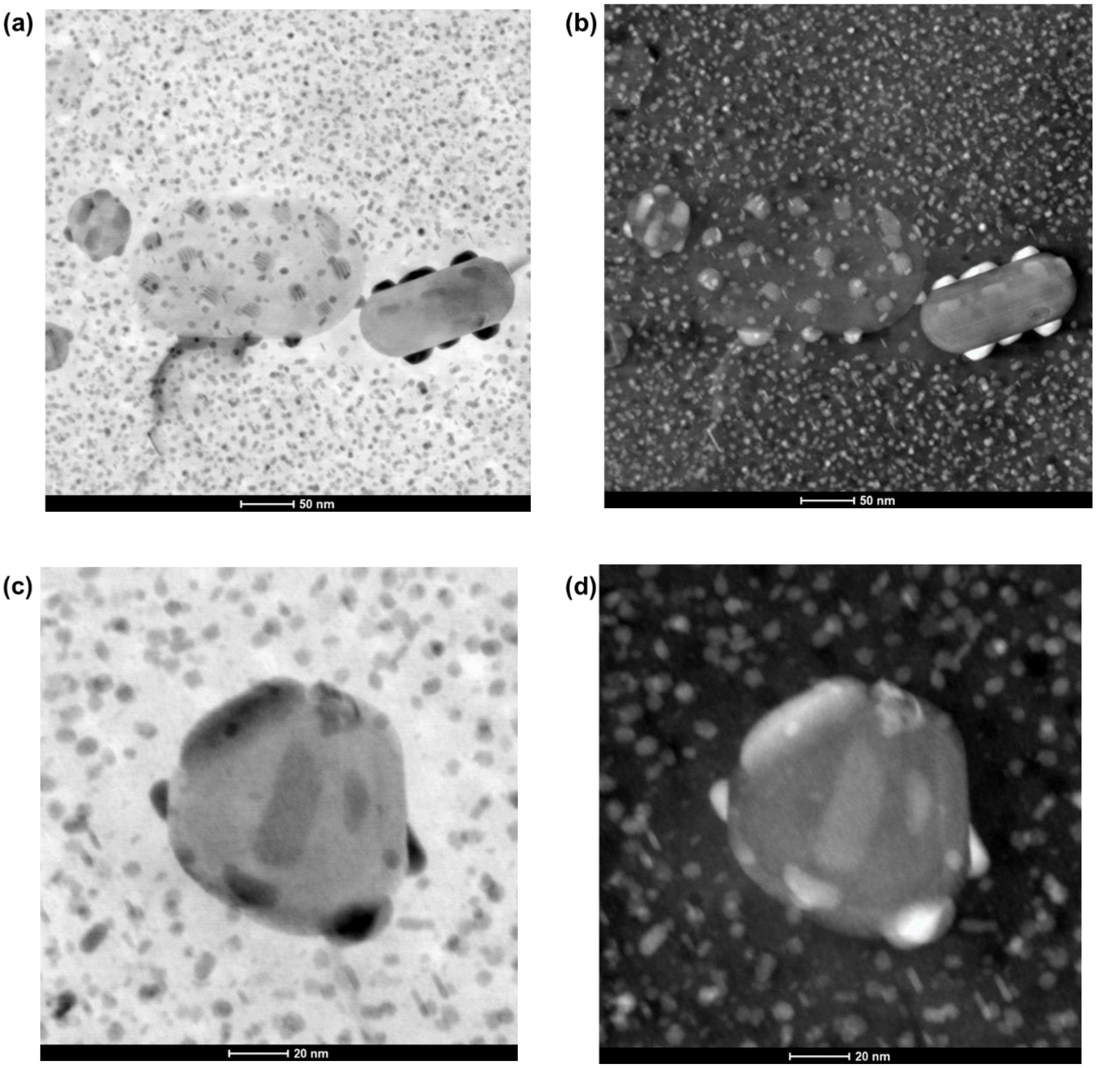

Figure A3. (a) and (c) BF and (b) and (d) HAADF TEM micrographs for the PB samples showing precipitation on Cr-rich dispersoids.

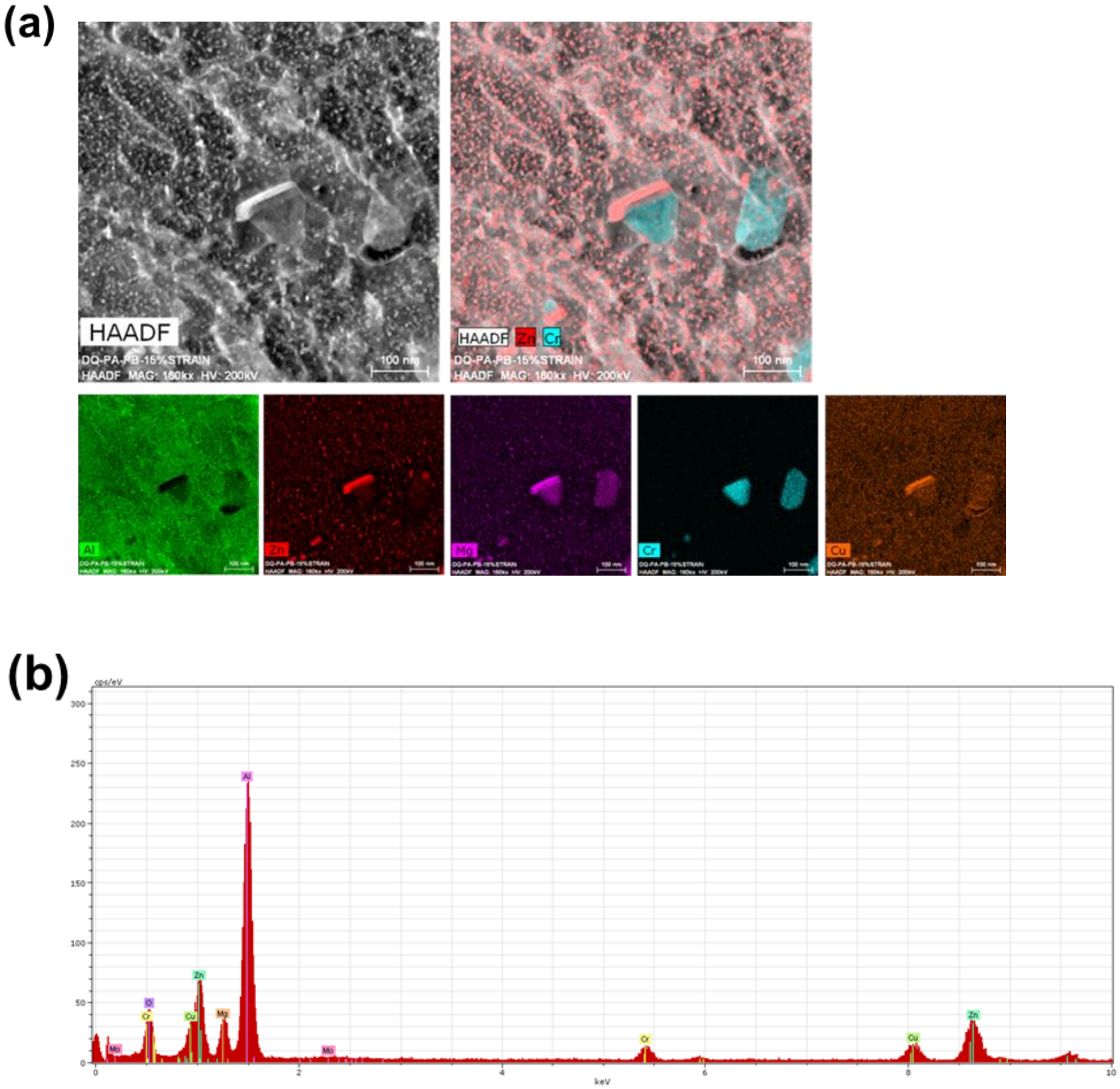

Figure A4. (a) HAADF images, and element mapping showing dislocations and primarily precipitates enriched in Zn and Mg atoms, and to a lesser extent, Cu atoms and a few Cr-rich dispersoids, and (b) energy-dispersive X-ray spectroscopy (EDS) analysis result for the alloy in the DQ+PB condition.

<u>TEM micrographs of DQ (26%)+PB sample</u>

Figure A5 shows the presence of dislocations and precipitates and their interactions in the microstructure of the AA7075 alloy in the DQ(26%)+PB condition. The TEM images of this sample have been used for the dislocation density measurements described in Section 5.2.2.1.

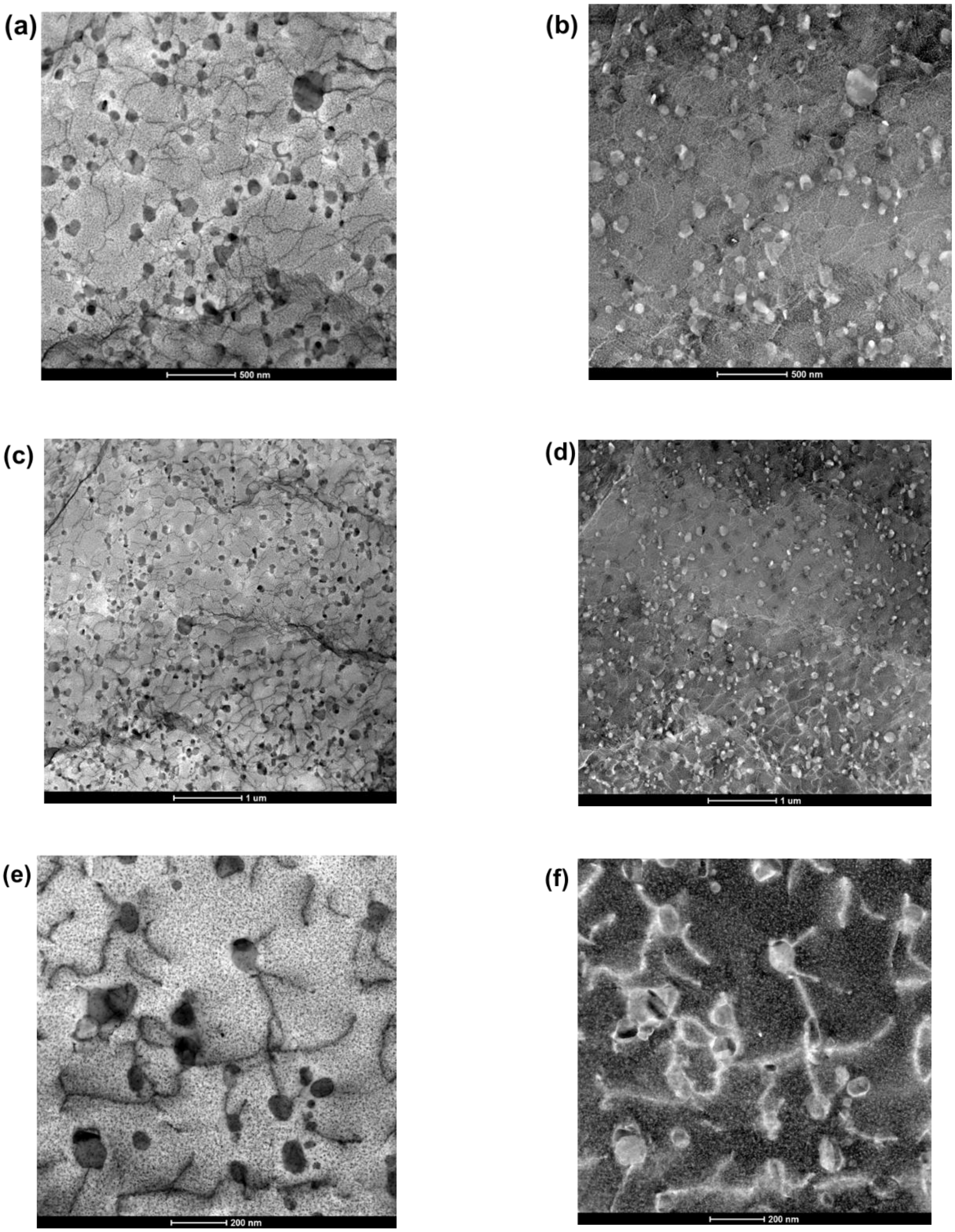

Figure A5. (a), (c), and (e) BF, and (b), (d), and (f) HAADF TEM micrographs for AA7075 samples in the DQ (26%)+PB condition showing the presence of precipitates and dislocations in the microstructure of the alloy sample.

Effect of deformation on precipitation on grain boundaries

Figure A6 and Figure A7 show the TEM micrographs of AA7075 in the DQ (26%)+PB and DQ+PB conditions. Comparing the TEM micrographs in Figure A6 and Figure A7, it is found that by increasing the amount of pre-deformation during die-quenching, the grain boundary precipitates become smaller, their distribution changes from discontinuous to continuous, and the width of the PFZ decreases. This observation can be attributed to the effect of dislocations assisting the heterogeneous nucleation of the grain boundary precipitates and providing heterogeneous nucleation sites for these precipitates. As a result, in the sample that is deformed to a higher level (*i.e.*, DQ (26%)+PB sample) grain boundary precipitates are smaller and more continuously distributed.

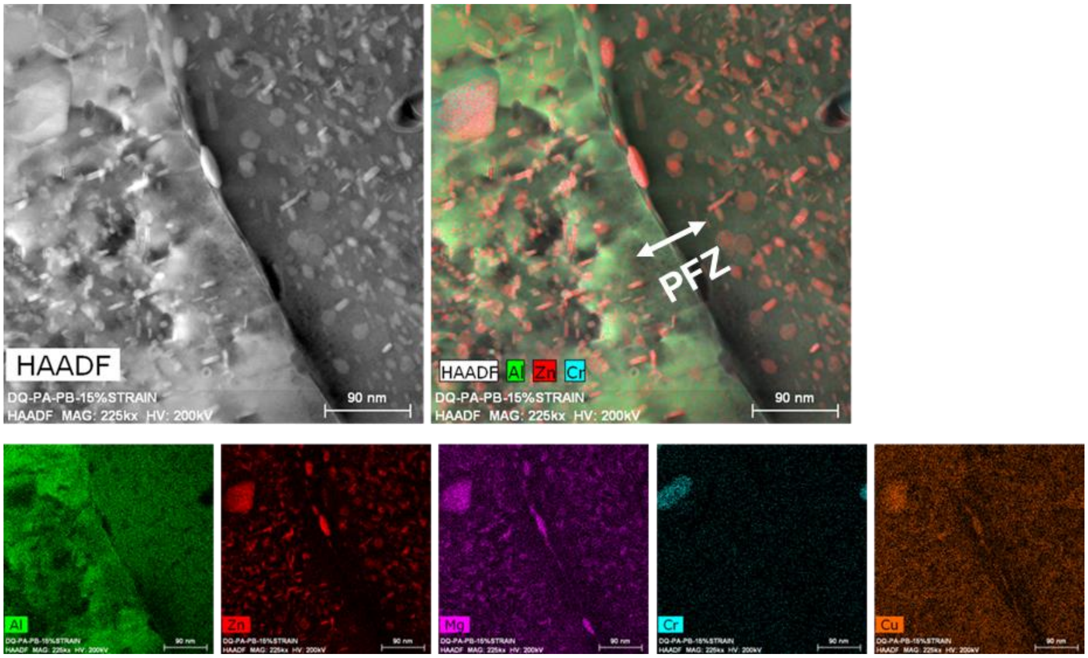

Figure A6. HAADF images, and element mapping of AA7075 in the DQ+PB condition showing primarily precipitates enriched in Zn and Mg atoms, and to a lesser extent, Cu atoms, and precipitation on a grain boundary and the PFZ around it with a width of approximately 60 nm.

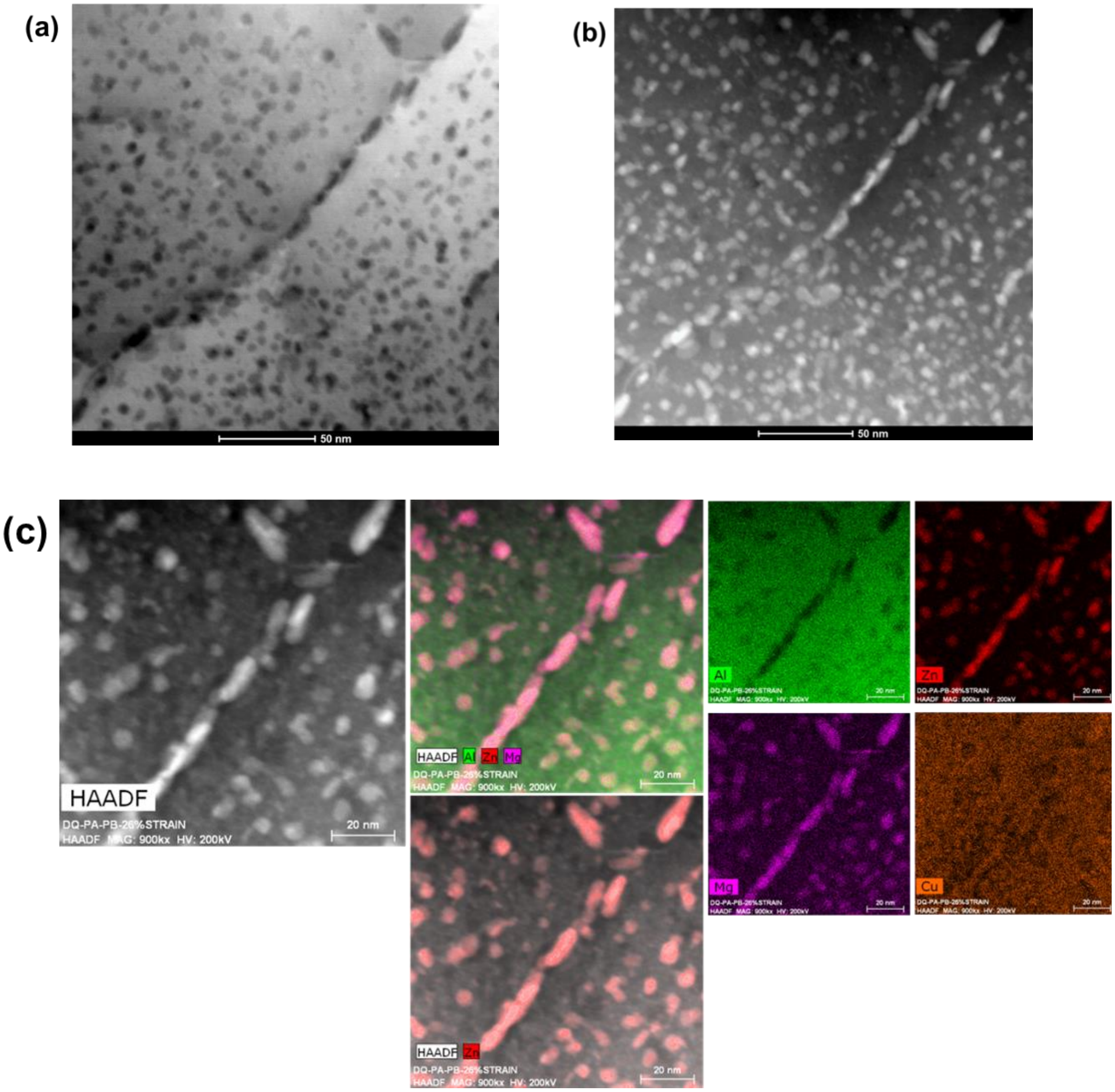

Figure A7. (a) BF, and (b) HAADF TEM micrographs for the AA7075 sample in the DQ (26%)+PB condition showing precipitation on a grain boundary and the PFZ around it with a width of approximately 31 nm, and (c) HAADF images, and element mapping showing primarily precipitates enriched in Zn and Mg atoms and to a lesser extent Cu atoms and precipitation on a grain boundary.